Titanite as an indicator mineral in porphyry systems

Thomas James Matthews

A thesis submitted for the degree of Doctor of Philosophy

Department of Earth Science and Engineering

Imperial College London

and

Department of Earth Science

Natural History Museum

March 2023

Declaration

The work presented in this thesis is my own and the work of other authors is appropriately referenced.

The copyright of this thesis rests with the author. Unless otherwise indicated, its contents are licensed under a Creative Commons Attribution-Non Commercial 4.0 International Licence (CC BY-NC).

Under this licence, you may copy and redistribute the material in any medium or format. You may also create and distribute modified versions of the work. This is on the condition that: you credit the author and do not use it, or any derivative works, for a commercial purpose.

When reusing or sharing this work, ensure you make the licence terms clear to others by naming the licence and linking to the licence text. Where a work has been adapted, you should indicate that the work has been changed and describe those changes.

Please seek permission from the copyright holder for uses of this work that are not included in this licence or permitted under UK Copyright Law.

Thomas Matthews

March 2023

Abstract

Titanite is an accessory mineral that is commonly found in rocks associated with porphyry copper deposits, either as a primary igneous or secondary alteration mineral. Compositions of titanite, with supporting whole-rock and mineral chemistry were characterised from four study sites: Strontian, Chuquicamata, Cobre Panama and Oyu Tolgoi. Titanite data from these sites were combined with data from a global sample suite and literature data, to characterise and understand signatures of titanite related to porphyry mineralisation.

Primary and secondary titanites display contrasting compositions, as exemplified by F, Al, Sc, LREE and Th contents. Primary titanite linked to mineralisation can potentially be detected using supervised learning techniques, which identify Mn and Sr concentrations, as well as Eu/Eu* ratios and lambda values as important discriminators. Igneous titanite compositions are influenced by both bulk magma chemistry and late-stage residual melt chemistry, with important implications for false positives when applying conventional techniques to mineral prospectivity studies.

Determining trace element chemistry and U-Pb isotopic compositions in both igneous and non-igneous titanite reveal the potential in recognising the presence of multiple titanite populations in the same rock. This is recommended as a means to identify porphyry titanite, allowing U-Pb ages to be related to mineralising events of a particular age. Overall, this study highlights the potential utility of titanite as an indicator mineral in porphyry copper systems.

Acknowledgements

Firstly, I would like to thank Jamie Wilkinson for his supervision and support throughout the project. I am extremely grateful to Jamie for giving me the opportunity to work at the NHM. Along with Jamie, Paul Agnew is also thanked for the inception of and funding behind the NERC CASE funded research project. The Grantham Institute and NERC SSCP DTP are also thanked for additional funding.

I am also indebted to my (formerly de facto) supervisor, and fellow Stopfordian, Matt Loader. The time spent discussing accessory minerals, mineral-melt partitioning and redox (plus Manchester and football) has been invaluable. In addition to Jamie and Matt, Simon Large and Yannick Buret are thanked not least for their assistance during manuscript preparation, but also during the PhD as a whole.

I have been lucky enough to meet, and work with, some incredible people during my PhD. I am especially grateful to Chetan Nathwani and Ethan Tonks who have invariably been there to discuss minerals, politics and football over a cappuccino or a Camden Hells (or even provide a place to crash). I am also thankful for NHM colleagues past and present: Emily, Lisa, Simon K, Chao, Francesco, Robin, Richard, Julian, Alla, and Licia with whom I have ventured to Scotland, Spain, Santiago and southern Peru.

At the Natural History Museum, special thanks go to Yannick Buret for assisting with LA ICP-MS analysis and Will Brownscombe for his help with a variety of analytical instruments. John Spratt is thanked for his time and knowledge regarding electron microprobe work. Additionally, Cindy Broderick, Tobias Salge and Innes Clathworthy are thanked for assisting with SEM analysis, as well as Callum Hatch and Tony Wighton for sample preparation. At Curtin University, Allen Kennedy is thanked for the provision of the OLT-1 titanite standard.

First Quantum Minerals and Minera Panama are thanked for facilitating sample collection from the Cobre Panama mine, with particular thanks to Tim Ireland, for both logistical and technical support, as well as Juan Burlando for collecting the samples.

Rio Tinto are thanked for their financial, logistical and technical support. In particular, Adam Pacey, Paul Agnew, Debora Araujo, Alan Kobussen are thanked for contributing ideas. Additionally, everyone at Rio Tinto in Bundoora is thanked for making me feel extremely welcome during a month-long visit, including: Ivan Semenov, Punit Kumar, Jonnaline Montesclaros, David Walsh and Will Powell. Rob Duncan is also thanked for processing a substantial amount of zircon compositional data.

Outside of academia, I would firstly like to thank Elliot, Beth and Leo for their excellent hospitality during the final few months of writing up. I am grateful to friends both in Stockport and London: Elliot, Scott, Simon, Jack, Luke and countless others, who have provided a welcome distraction with their company in fields, at pubs or gigs, and of course watching the mighty Stockport County. Additional thanks go to Beth for her support.

Last, but by no means least, I would like to thank my parents Laura and Andy, without whom none of this would have been possible. It was my mum who sparked my scientific curiosity by reading articles from biological journals when I was young- sorry for choosing granites over glucocorticoids. Thank you for facilitating my academic journey, both intellectually and financially. This thesis is dedicated to my grandparents: Pete and Trevor who were both sadly lost during the course of my PhD, and Celia who is a constant source of inspiration.

List of abbreviations

Analytical
BSE: Backscattered electron
EDS: Energy dispersive spectroscopy
EPMA: Electron probe microanalysis
LA-ICP-MS: Laser-ablation inductively coupled plasma mass spectrometry
SEM: Scanning electron microscope
WDS: Wavelength dispersive spectroscopy

Geochemical
Al^{iv}: Tetrahedral aluminium
HFSE: High field strength element
LILE: Large ion lithophile element
REE: Rare earth element
LREE: Light rare earth element
MREE: Middle rare earth element
HREE: Heavy rare earth element

Minerals
Ab: Albite
Act: Actinolite
Adr: Andradite
All: Allanite
Alm: Almandine
Am: Amphibole
Anh: Anhydrite
Ap: Apatite
Aug: Augite
Bn: Bornite
Bt: Biotite
Cc: Calcite
Chl: Chlorite
Ccp: Chalcopyrite
Epi: Epidote
Fe-Ti: Fe-Ti oxides
Kfs: K-feldspar
Mag: Magnetite
Plg: Plagioclase
Pmp: Pumpellyite
Py: Pyrite
Qz: Quartz
Rt: Rutile
Ttn: Titanite
Zrn: Zircon

Units
apfu: Atoms per formula unit
Ap-Sat: Apatite saturation temperature
***f*O_2:** Oxygen fugacity

Hz: Hertz
ICP-MS: Inductively-coupled-plasma mass spectrometry
J cm^{-2}: Joules per centimetre squared
kb: Kilobar
kV: Kilo volts
Ma: Million years ago
nA: Nano amps
ppm: Parts per million
Ttn-Sat: Titanite saturation temperature
wt.%: Weight percent
Zr-Sat: Zircon saturation temperature
µg/g: Micrograms per gram
µm: Micrometre

Geological
FMQ: Fayalite-magnetite-quartz redox buffer
MH: Magnetite-hematite redox buffer
M: Melt fraction
Ppy: Porphyry
***a*SiO_2:** Activity of silica
***a*TiO_2:** Activity of titania

Table of Contents

Declaration 2
Abstract 3
Acknowledgements 4
List of abbreviations 6
Table of Contents 8
List of Figures 13
List of Tables 16
Appendices 17
Chapter 1. Introduction 18
1.1 Introduction 18
1.2 Key features of porphyry deposits 19
1.2.1 Size 19
1.2.2 Spatial and temporal distribution 19
1.3 Porphyry Cu formation 20
1.3.1 Arc magma generation 20
1.3.2 Shallow crustal processes 21
1.3.3 Hydrothermal alteration 23
1.3.4 Mineralisation 25
1.4 Indicator minerals in porphyry systems 26
1.5 Aims, objectives and thesis outline 27
Chapter 2. Titanite literature review 28
2.1 Structure and substitutions 28
2.2 Igneous titanite 29
2.2.1 Stability and occurrence 29
2.2.2 Trace element contents and mineral-melt partitioning 31
2.2.3 Diffusion and zonation 33
2.3 Geochronology 34
2.4 Titanite occurrence in porphyry systems 34
2.5 Titanite as an indicator mineral 35
2.6 Conclusions 36
Chapter 3. Analytical Methods 37
3.1 Whole-rock chemistry 37
3.1.1 LOI, sulphur and carbon 38
3.1.2 Major elements 38
3.1.3 Trace elements 38
3.1.4 Base metals and platinum group elements 38

3.1.5 Volatile elements 38
3.1.6 Quality control 39
3.2 Titanite analysis 40
3.2.1 Identification of titanite and determination of mineral modal abundance and mineral associations 40
3.2.2 Scanning electron microscopy (SEM) 41
3.2.3 Automated scanning electron microscope (TESCAN TIMA) 42
3.2.4 Electron probe microanalysis (EPMA) 42
3.2.5 Laser ablation inductively coupled plasma mass spectrometry (LA-ICP-MS) 43
3.2.6 Geochronology 46
Chapter 4. The Strontian Intrusive Complex: petrography, thermobarometry and the influence of titanite on residual melt chemistry 49
4.1 Introduction 49
4.2 Background geology 50
4.3 Samples and methods 52
4.4 Results 54
4.4.1 Petrography 54
4.4.2 Whole-rock chemistry 57
4.4.3 Amphibole and titanite chemistry 60
4.5 Discussion 64
4.5.1 Estimation of intensive parameters 64
4.5.2 Crystallisation sequence 69
4.5.3 Trace element distribution 71
4.5.4 Evolution of the Strontian magmatic system 73
4.5.5 Trace element modelling 76
4.5.6 Wider implications 80
4.6 Conclusions 81
Chapter 5. Titanite as a recorder of magmatic evolution in the Chuquicamata district 83
5.1 Introduction 83
5.2 Geologic setting 85
5.3 Samples 85
5.4 Results 89
5.4.1 Titanite textures 89
5.4.2 U-Pb Geochronology 92
5.4.3 Geochemistry 95
5.5 Discussion 97
5.5.1 Titanite Geochronology 97
5.5.2 Comparing igneous and non-igneous titanite compositions 99

5.5.3 Titanite populations in the Este Porphyry 100
5.5.4 Titanite as an indicator of changing melt composition 103
5.5.5 Titanite textural indicators of mineralisation 106
5.6 Conclusions 107
Chapter 6. Titanite occurrence and compositions in the Cobre Panama district 109
6.1 Introduction 109
6.2 Geologic setting 109
6.3 Methods 112
6.4 Results 117
6.4.1 Titanite textures 117
6.4.2 U-Pb geochronology 120
6.4.3 Geochemistry 122
6.5 Discussion 126
6.5.1 Titanite Geochronology 126
6.5.2 Differentiating igneous and replacement titanite 127
6.5.3 Cobre Panama magmatic system 132
6.5.4 Inferring porphyry titanite compositions 133
6.6 Conclusions 136
Chapter 7. Geochronology and geochemistry of hydrothermal titanite from the Oyu Tolgoi district 138
7.1 Introduction 138
7.2 Geologic setting 139
7.2.1 Regional geology 139
7.2.2 District geology 139
7.3 Samples, previous work and methods 141
7.3.1 Samples 141
7.3.2 Previous work 144
7.3.3 Methods 146
7.4 Results 146
7.4.1 Titanite textures 146
7.4.2 U-Pb geochronology 150
7.4.3 Titanite chemistry 150
7.5 Discussion 156
7.5.1 Titanite geochronology and the presence of multiple populations 156
7.5.2 Occurrence of fluorine-bearing Permian titanite 158
7.5.3 Controls on titanite composition 163
7.6 Conclusions 166
Chapter 8. Titanite compositions and their application to porphyry exploration 167

8.1 Introduction 167
8.2 Controls on titanite composition: non-igneous 167
8.2.1 Bulk rock controls on non-igneous titanite composition 169
8.2.2 Fluid compositional controls on non-igneous titanite composition 171
8.2.3 Mineral assemblage controls on non-igneous titanite composition 171
8.3 Controls on titanite composition: igneous 173
8.3.1 Extrusive vs intrusive 173
8.3.2 Redox 175
8.3.3 Melt chemistry 176
8.4 Classification using conventional techniques 178
8.4.1 Model 1 (Igneous vs non-igneous) 178
8.4.2 Model 2 (Porphyry vs non-porphyry) 178
8.5 Classification of titanite using unsupervised and supervised learning techniques 185
8.5.1 Background 185
8.5.2 Unsupervised learning (PCA and K-means clustering) 185
8.5.3 Supervised learning (Random Forest) 186
8.6 Results of Model 1 (Igneous vs non-igneous) – unsupervised learning 189
8.7 Results of Model 1 (Igneous vs non-igneous) – Supervised learning 191
8.8 Results of Model 2 (Porphyry vs non-porphyry) – unsupervised learning 193
8.9 Results of Model 2 (Porphyry vs non-porphyry) – supervised learning 194
8.10 Use of titanite in exploration 196
8.10.1 Titanite occurrence in porphyry systems 196
8.10.2 Effects of hydrothermal alteration 196
8.10.3 Comparison of titanite with other mineral indicators 197
8.10.4 Exploration workflow 198
8.11 Conclusions 201
Chapter 9. Conclusions and future work 202
9.1 Main conclusions 202
9.1.1 The influence of titanite on residual melt chemistry 202
9.1.2 The occurrence of titanite in porphyry systems 202
9.1.3 Differentiating igneous and non-igneous titanite 203
9.1.4 Controls on compositions of non-igneous titanite 204
9.1.5 Controls on compositions of igneous titanite 204
9.1.6 Identifying igneous titanite from porphyry systems 204
9.1.7 Using titanite in mineral exploration 204
9.2 Recommendations for future work 204
9.2.1 Magmatic titanite 205

9.2.2 Hydrothermal titanite 206
References 207

List of Figures

Figure 1.1. Locations of important porphyry-related ore systems from around the world, with principal metals, deposit type and ages indicated. 20
Figure 1.2. Tectono-magmatic setting for porphyry Cu deposit formation. 21
Figure 1.3. Shallow crustal setting for porphyry Cu deposit formation. 22
Figure 1.4. Distribution of alteration zones and fluid physico-chemical conditions under which they form. 24
Figure 2.1. Titanite crystal structure projected along the c-axis showing the main structural sites. 29
Figure 2.2. Temperature vs log fO_2 plot showing titanite-absent and titanite-bearing rocks 30
Figure 2.3. Rare earth element mineral-melt partition coefficients for titanite compared to a range of important REE-bearing phases. 32
Figure 3.1. Whole-rock QA-QC for Cobre Panama and Strontian sample sets. 39
Figure 3.2. Percentage bias for whole-rock major element (**A.**) and trace element (**B.**) data. 41
Figure 3.3. RSD (%) of OLT1 titanite standard by EPMA for different species. 43
Figure 3.4. Comparison between laser-ablation (ICP-MS) and EPMA data for several elements in titanite. 45
Figure 3.5. Percentage bias calculated using repeated LA-ICP-MS analysis of secondary standard NIST-612, using NIST-610 as the primary standard. 46
Figure 3.6. Titanite lower intercept ages, 2σ error and an additional propagated 2% external uncertainty for secondary standards Fish Canyon (FCT; A.) and Grenville Skarn (OLT-1; B.). 48
Figure 4.1. Geology of the Strontian Intrusive Complex. 51
Figure 4.2. Field relationships of mafic enclaves in host granitoids. 52
Figure 4.3. Transmitted light photomicrographs and SEM backscattered electron images of amphibole, showing a range of crystal habits and mineral inclusions. 56
Figure 4.4. SEM backscattered electron images of titanite, showing a range of textures and mineral inclusions. 58
Figure 4.5. Whole-rock chemistry of the Strontian Intrusive Complex. 59
Figure 4.6. Amphibole major element chemistry. 60
Figure 4.7. Amphibole trace element maps from sample SG19. 61
Figure 4.8. Amphibole trace element maps from sample SG21. 62
Figure 4.9. Amphibole trace element ratio variations as a function of Y concentration. 63
Figure 4.10. Titanite trace element maps from sample SG21. 65
Figure 4.11. Titanite trace element ratio variations as a function of Y concentration. 66
Figure 4.12. Violin plots showing estimated intensive parameters for the Strontian magmatic system. 68
Figure 4.13. Generalised crystallisation sequence for the Strontian magmatic system. 70
Figure 4.14. Whole-rock trace element distribution between mineral phases. 73
Figure 4.15. Whole-rock chemistry showing A. Ni, B. Cr, C. Y and D. Nb vs SiO2. 75
Figure 4.16. Modelling of hypothetical amphibole compositions as a function of Y content. 79
Figure 5.1. Simplified geological map of the Chuquicamata region. 84
Figure 5.2. Quartz (Q)-Alkali(A)-Plagioclase (P) diagram (Streckeisen, 1976) for intrusive phases from the Chuquicamata district. 87
Figure 5.3. Titanite SEM-BSE images, reflected light photomicrographs and TESCAN TIMA phase maps from the Chuquicamata district. 91
Figure 5.4. Tera-Wasserburg Concordia diagrams for titanite age data 94
Figure 5.5. Chondrite-normalised (Boynton, 1984) REE plots for titanite from the Chuquicamata district 96
Figure 5.6. Trace element compositions of titanite from the Chuquicamata district. 97

Figure 5.7. Plot comparing titanite lower intercept ages for Eocene-Oligocene intrusions in the Chuquicamata district 99
Figure 5.8. Crystal from the Este Porphyry that contains both groups 1 (low Th/U) and 2 (high Th/U) titanite. 101
Figure 5.9. Tera-Wasserburg Concordia diagrams for titanite age data from groups 1 (**A.**) and 2 (**B.**) in the Este Porphyry. Displayed errors represent the 2σ error calculated from the weighted mean, with an additional propagated external uncertainty of 2%..... 101
Figure 5.10. Violin plots illustrating titanite compositions for different samples. 102
Figure 5.11. Boxplots showing calculated log fO_2 (ΔFMQ) using the zircon oxybarometer (Loucks *et al.*, 2020) for different samples. 105
Figure 5.12. Estimated melt Eu/Eu* in equilibrium with titanite in each sample. 106
Figure 6.1. Simplified maps of the Cobre Panama porphyry Cu district. 111
Figure 6.2. Selected TESCAN TIMA phase maps and photographs of the Cobre Panama sample suite. 115
Figure 6.3. Titanite petrography from the Cobre Panama district..... 118
Figure 6.4. Percentages of minerals associations with titanite in different samples. 119
Figure 6.5. Tera-Wasserburg Concordia diagrams showing titanite age data from the Cobre Panama district. 2σ error ellipses are shown, in addition to the 2σ uncertainty associated with the regression. Crystallisation ages are presented with error, which is derived from the regression, with an additional propagated external uncertainty of 2%. 121
Figure 6.6. Thorium-cobalt immobile element classification diagram (Hastie *et al.*, 2007). Analytical error was estimated to be ~2% for Co and 6% for Th. 123
Figure 6.7. Whole-rock chondrite-normalised (Boynton, 1984) REE patterns..... 124
Figure 6.8. Chondrite normalised (Boynton, 1984) REE plots for titanite from the Cobre Panama district. Average 2σ errors are smaller than symbol size. 125
Figure 6.9. Zircon trace element compositions from the Cobre Panama district. 126
Figure 6.10. Plot comparing titanite lower intercept ages with zircon Concordia ages. 127
Figure 6.11. Results of principal component analysis on titanite from the Cobre Panama district. 129
Figure 6.12. Titanite minor and trace element chemistry 130
Figure 6.13. Comparison of titanite and zircon crystallisation temperatures from the Cobre Panama district (Ferry & Watson, 2007; Hayden *et al.*, 2008). 134
Figure 6.14. Trace element compositions of titanite and hypothetical titanite that would be in equilibrium with zircon. 135
Figure 7.1. Location and geology of the Oyu Tolgoi district. 140
Figure 7.2. Selected TESCAN TIMA phase maps of the Oyu Tolgoi sample suite. 145
Figure 7.3. Titanite SEM-BSE images from the Oyu Tolgoi district..... 148
Figure 7.4. Percentages of minerals sharing grain boundaries with titanite in different samples, as determined by automated SEM analysis. 149
Figure 7.5. Tera-Wasserburg concordia diagrams for titanite age data from the Oyu Tolgoi district. 2σ error ellipses are shown, in addition to the 2σ uncertainty associated with the regression. Crystallisation ages are presented with error, which is derived from the regression, with an additional propagated external uncertainty of 2%. 152
Figure 7.6. Chondrite-normalised (Boynton, 1984) REE plots for titanite from the Oyu Tolgoi district. 153
Figure 7.7. Box plots illustrating titanite compositions for different samples. 155
Figure 7.8. Plot comparing titanite lower intercept ages in the Oyu Tolgoi district determined in this study with those of Hart-Madigan *et al.* (2020). 158
Figure 7.9. Bivariate plots illustrating titanite F contents against various trace elements for different samples..... 160
Figure 7.10. Estimated chlorite formation temperatures in the studied samples 162

Figure 7.11. Map of the Oyu Tolgoi district showing titanite U-Pb ages, from this study and (Hart-Madigan *et al.*, 2020), as well as chlorite temperatures 163
Figure 7.12. PCA biplot showing titanite compositions from OT compared to crystallisation age (**A.**) and sample number (**B.**). 164
Figure 8.1. Comparison of median non-igneous titanite compositions with the same parameter in their host rocks. 170
Figure 8.2. Median titanite F contents plotted against Al contents (**A.**) and whole-rock Al/Ti ratios (**B.**). 171
Figure 8.3. Comparison of extrusive and intrusive titanite compositions. 174
Figure 8.4. Comparison of whole-rock trace element compositions with median, minimum and maximum melt compositions inverted from titanite. 177
Figure 8.5. Titanite compositional data collected during this study and from the literature, colour coded by interpreted igneous or non-igneous origin. 179
Figure 8.6. Cumulative frequency plots comparing compositions of titanite with different porphyry scores. 181
Figure 8.7. Bivariate plots showing various potentially important indicators of magmatic fertility, colour coded by porphyry score. 183
Figure 8.8. Bivariate plots showing various potentially important indicators of magmatic fertility, colour coded by location. 184
Figure 8.9. Impact of varying K on K-means clustering outputs. 186
Figure 8.10. Illustration explaining how random forest works. 187
Figure 8.11. Results of PCA and cluster analysis for Model 1. 190
Figure 8.12. ROC curve for Model 1. 192
Figure 8.13. Results of PCA and cluster analysis for Model 2. 194
Figure 8.14. ROC curve for Models 2a and 2b. 195
Figure 8.15. Recommended exploration workflow. 200

List of Tables

Table 3.1. Whole-rock analytical methodology. 38
Table 3.2. Whole-rock certified reference materials. 40
Table 3.3. EPMA conditions and average limit of detection (LOD) and analytical error (%) for titanite EPMA analysis 42
Table 3.4. LA ICP-MS dwell times, average LOD and analytical error (%) for titanite 44
Table 4.1. Sample information, analytical techniques and number of analyses. 53
Table 4.2. Mineral modal abundances as estimated by automated SEM, or [1]CIPW norm. 55
Table 5.1. Sample information, analytical techniques and number of analyses. 86
Table 5.2. Titanite U-Pb isotopic data for the Chuquicamata district. 95
Table 6.1. Sample information, analytical techniques and number of analyses. 112
Table 6.2. Titanite and zircon U-Pb isotopic data for the Cobre Panama district. 120
Table 7.1. Sample information, alteration assemblages, analytical techniques and number of analyses. 142
Table 7.2. Titanite U-Pb dates for the same samples as reported by Hart-Madigan *et al.* (2020). 146
Table 7.3. Titanite textural features and mineral associations from the Oyu Tolgoi district. 147
Table 7.4. Titanite U-Pb isotopic data for the Oyu Tolgoi district. 150
Table 7.5. Titanite U-Pb isotopic for five samples which possibly contained multiple titanite populations. 157
Table 8.1. Sample information for the Rio Tinto sample suite and literature data. 168
Table 8.2. Titanite La/Yb ratios and whether titanite was associated with LREE-rich phases. 173
Table 8.3. Porphyry score, reasons for classification and datasets included. 180
Table 8.4. Datasets that were included in the training and test datasets for Models 1 and 2. 187
Table 8.5. Correlation matrix showing cluster analysis performance for Model 1, compared to textural classification. 191
Table 8.6. Results of random forest predictions of test dataset for Models 1, 2a and 2b. 192
Table 8.7. Gini indices for Model 1. 192
Table 8.8. Correlation matrix showing cluster analysis performance for Model 2. 193
Table 8.9. Gini index for Models 2a and 2b. 195

Appendices

Appendix 1: Whole-rock geochemistry (Excel).

Appendix 2: Titanite major element, trace element and U-Pb isotopic data (Excel).

Appendix 3: EPMA and LA-ICP-MS standard data (Excel).

Appendix 4: Amphibole major and trace element data at Strontian (Excel).

Appendix 5: Whole-rock trace element distribution at Strontian (Excel)

Appendix 6: Amphibole Rayleigh fractional crystallisation model (Excel)

Appendix 7: Cobre Panama zircon compositional and isotopic data (Excel)

Appendix 8: Melt Eu modelling at Chuquicamata (Excel)

Appendix 9: Percentage mineral association data (Excel)

Appendix 10: PCA results (Excel)

Appendix 11: Comparison of titanite and zircon compositions at Cobre Panama (Excel)

Appendix 12: Machine learning results (Excel)

Chapter 1. Introduction

1.1 Introduction

Porphyry Cu deposits are major accumulations of ore and gangue minerals in the upper crust, formed from hydrothermal fluids that alter up to 100 km^3 of rock (Sillitoe, 2010). These low-grade, high-tonnage deposits are hosted within and/or centred on porphyritic intrusions and contribute substantially to the global supply of metals (Lowell & Guilbert, 1970; Seedorff *et al.*, 2005). Forming at shallow depths (often <4 km; Singer *et al.*, 2008), porphyry deposits are typically located in continental or island arc settings, and may also be associated with skarn, carbonate-replacement and epithermal styles of mineralisation (Sillitoe, 1972; Atkinson & Einaudi, 1978; Arribas Jr *et al.*, 1995).

Porphyry deposits are typically classified by commodity, with Cu-(Mo-Au) systems supplying approximately 75% of the world's Cu, 50% of the Mo and 20% of the Au (Sillitoe, 2010). Hypogene ores in porphyry Cu deposits contain a variety of sulphides, including chalcopyrite, bornite and molybdenite, which are present in veinlets, disseminations and breccias (Gustafson & Hunt, 1975; Seedorff *et al.*, 2005). The amount of metal contained within these systems has provided the impetus for numerous academic studies attempting to understand their formation and assist exploration. Despite this, exploration expenditure has increased significantly in recent years and new discoveries have not kept pace. New deposits are increasingly likely to be located under post-mineralisation cover and at greater depth, necessitating the development of new and novel exploration techniques (Schodde, 2017; Cooke *et al.*, 2020a).

Researchers and exploration programmes are now investigating the utility of indicator minerals (i.e. phases which may indicate derivation from a mineralised system) in porphyry systems, exploiting them to understand magmatic and hydrothermal parts of the system and to develop exploration tools (Cooke *et al.*, 2017; Cooke *et al.*, 2020a). To date, porphyry indicator mineral studies have mostly focussed on either the magmatic (e.g. zircon) or hydrothermal (chlorite, epidote) portions of the system separately (Ballard *et al.*, 2002; Wilkinson *et al.*, 2015; Pizarro *et al.*, 2020). The potential of minerals with both igneous and hydrothermal origins, such as titanite, has consequently not yet been fully explored. Commonly found in porphyritic intrusions and their precursor plutons as an igneous phase (Ossandón *et al.*, 2001; Chelle-Michou *et al.*, 2014; Buret *et al.*, 2016; Loader *et al.*, 2017; Large *et al.*, 2021), titanite may also occur in potassic (Seedorff *et al.*, 2005), sodic-calcic (Carten, 1986) and propylitic (Wilkinson *et al.*, 2015; Hart-Madigan *et al.*, 2020) alteration zones. Furthermore, titanite incorporates a variety of trace elements (Frost *et al.*, 2001), meaning that it could be employed to understand melt/fluid compositions and

physico-chemical conditions throughout the porphyry environment, as well as providing an opportunity to develop multivariate exploration tools.

1.2 Key features of porphyry deposits

1.2.1 Size

The formation of porphyry Cu deposits in the Earth's crust is not an extremely rare occurrence, with a minimum of ~1000 known worldwide (Kirkham & Dunne, 2000). What is unusual, however, is the disparity in size between deposits, with the largest twenty-five porphyry deposits (Cooke *et al.*, 2005) containing approximately half of the world's porphyry Cu resources (Singer *et al.*, 2008). Consequently, porphyry deposits are classified according to size as well as by metal endowment, with the largest deposits referred to as 'behemoths' (e.g. El Teniente, Chuquicamata, Rio Blanco-Los Bronces) and increasingly smaller deposits classified as 'supergiants' (>24 Mt Cu) and 'giants' (>2 Mt Cu; Singer, 1995).

1.2.2 Spatial and temporal distribution

Most major porphyry deposits are located in magmatic arcs although some important deposits occur in post-collisional settings, especially in China (Fig. 1; Richards, 2009). However, deposits are not equally distributed between arcs, with some (e.g. the Andean arc or southwestern USA) particularly well-endowed and hosting many of the largest known deposits, whereas others (e.g. Japan) contain no significant deposits (Cooke *et al.*, 2005; Sillitoe, 2018). Within prospective arc segments, mineralisation is further restricted in both space and time, forming metallogenic belts (e.g. Andean Eocene-Oligocene and Miocene-Pleistocene belts; Fig. 1). Here, the location of individual deposits is often coincident with major crustal lineaments or faults (e.g. northern Chile; Richards *et al.*, 2001), suggesting that these structures are important in facilitating magma transport to the mid to shallow crust (Tosdal & Richards, 2001). Importantly, there are no significant known deposits of Precambrian age, presumably reflecting difficulties in preserving shallow crustal deposits in arc terranes which are often rapidly uplifted and eroded (Kesler & Wilkinson, 2006).

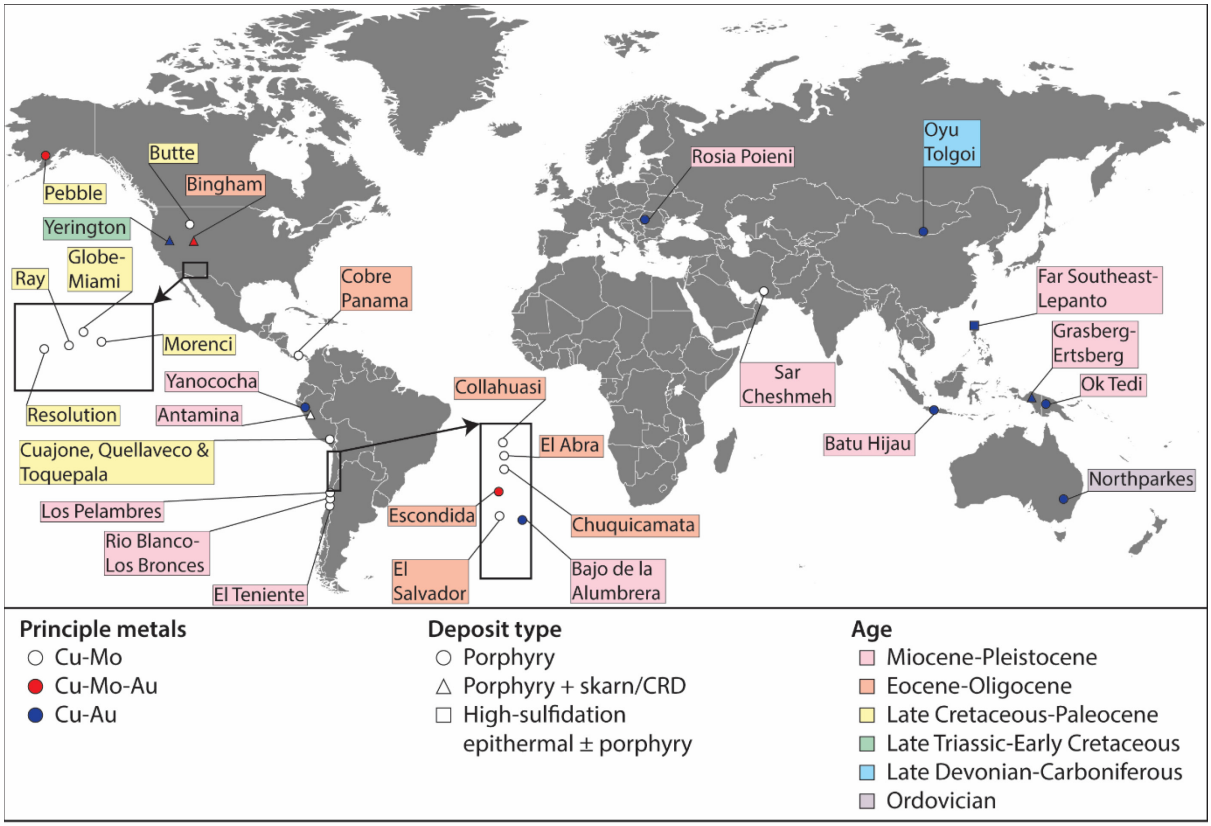


Figure 1.1. Locations of important porphyry-related ore systems from around the world, with principal metals, deposit type and ages indicated. Modified from Sillitoe (2010).

1.3 Porphyry Cu formation

1.3.1 Arc magma generation

In arc settings, primary basaltic melts are generated in the mantle wedge after metasomatism by slab-derived fluids (Peacock, 1993; Fig. 1.2). These fluids are thought to transfer important ore-forming components, such as H_2O, S (Alt *et al.*, 1993) and halogens (Ito *et al.*, 1983), as well as large ion lithophile elements (LILE; Alt *et al.*, 1993). Thereafter, primitive, hydrous melts ascend before stalling at the base of the lower crust, where they attain neutral buoyancy (Hildreth & Moorbath, 1988). Here, the geochemical characteristics of bulk magmas are believed to be locked in and more evolved compositions are produced by partial melting of the lower crust and fractional crystallisation (Annen *et al.*, 2006; Fig. 1.2).

Magmas that are associated with porphyry deposits often exhibit unusual chemical compositions, such as elevated Sr/Y, Eu/Eu*, La/Yb, V/Sc, Al_2O_3/TiO_2 and Sr/MnO ratios (Lang & Titley, 1998; Richards, 2011; Loucks, 2014; Ahmed *et al.*, 2020). Magmas that display/do not display these characteristics are referred to as 'fertile' (i.e. of the right composition to form a

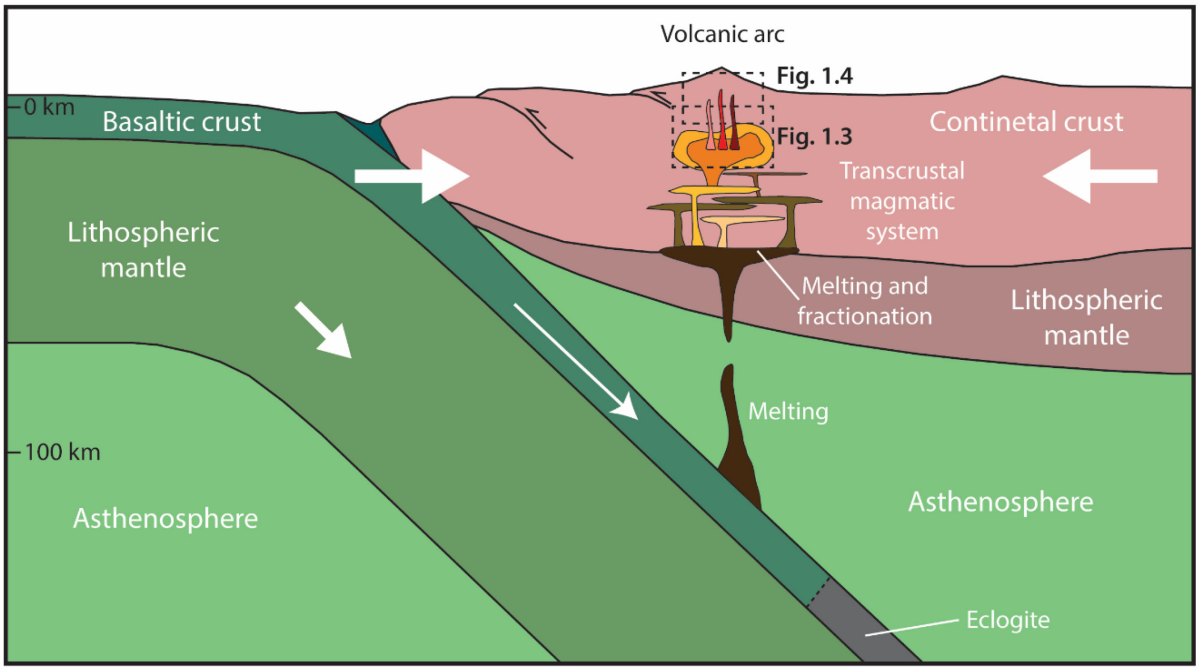


Figure 1.2. Tectono-magmatic setting for porphyry Cu deposit formation. Locations of Figures 1.3 and 1.4 are also shown. Modified from Wilkinson (2013) and Cashman et al. (2017).

deposit) and 'unfertile', respectively. These geochemical signatures are commonly ascribed to prolonged evolution in the deep crust, where repeated replenishment and crystallisation ramps up the concentrations of important ore forming components, such as water, volatiles and metals (Rohrlach & Loucks, 2005). In fact, the unique signatures of porphyry-fertile magmas are thought to dominantly reflect crystallisation of water-rich melts at high pressures, which experimental studies have shown promotes amphibole ± garnet crystallisation, and plagioclase ± magnetite suppression (Müntener *et al.*, 2001). Hence, elements that prefer to be incorporated into plagioclase (e.g. Sr and Eu^{2+}) will be enriched in the melt (Blundy & Wood, 1991), whereas elements which readily partition into amphibole and/or garnet (e.g. D_{Xx}^{Am} >1) such as Y, Eu^{3+}, Sc and Yb (Nandedkar *et al.*, 2016) will be depleted in the melt.

1.3.2 Shallow crustal processes

Dissolved volatile species and more evolved compositions promote the upwards transmission of these hydrous melts to different levels throughout the crust (Fig. 1.2), with the shallow crust comprising the uppermost portion of a transcrustal magmatic system (Cashman *et al.*, 2017). Additionally, transfer of melts may also be aided by the presence of any pre-existing faults or crustal lineaments (Richards, 2005). Indeed, prevailing stress regimes may also be important for magma ascent, with several studies identifying an association between porphyry magmatism and a relaxation in compressional stress (Richards *et al.*, 2001; Tosdal & Richards, 2001).

In the upper crust, large intrusive complexes are incrementally assembled by the repeated emplacement of small magma batches (Fig. 1.3), as evidenced by the wide range of crystallisation ages of porphyry-related precursor plutons (Ballard *et al.*, 2002; Rezeau *et al.*, 2016; Nathwani *et al.*, 2021). Mass balance calculations suggest that typical calc-alkaline arc magmas contain enough ore-forming components to produce an economic deposit (Cline & Bodnar, 1991; Richards, 2005) as long as extraction of these components is very efficient, but huge volumes of melt are likely required to produce the largest deposits (Chiaradia, 2020; Chelle-Michou & Rottier, 2021). However, the emplacement of large amounts of magma into the shallow crust can trigger voluminous volcanic eruptions, potentially stripping a system of critical ore-forming compontents to the detriment of mineralising potential (Hedenquist *et al.*, 1993; Pasteris, 1996). Coeval volcanics are sometimes associated with economic deposits (Buret *et al.*, 2017) but are typically small-scale, with favourable thermal structure and injection rate (Chelle-Michou & Rottier, 2021) or favourable tectonic conditions (Tosdal & Richards, 2001) possibly necessary to prohibit catastrophic eruption.

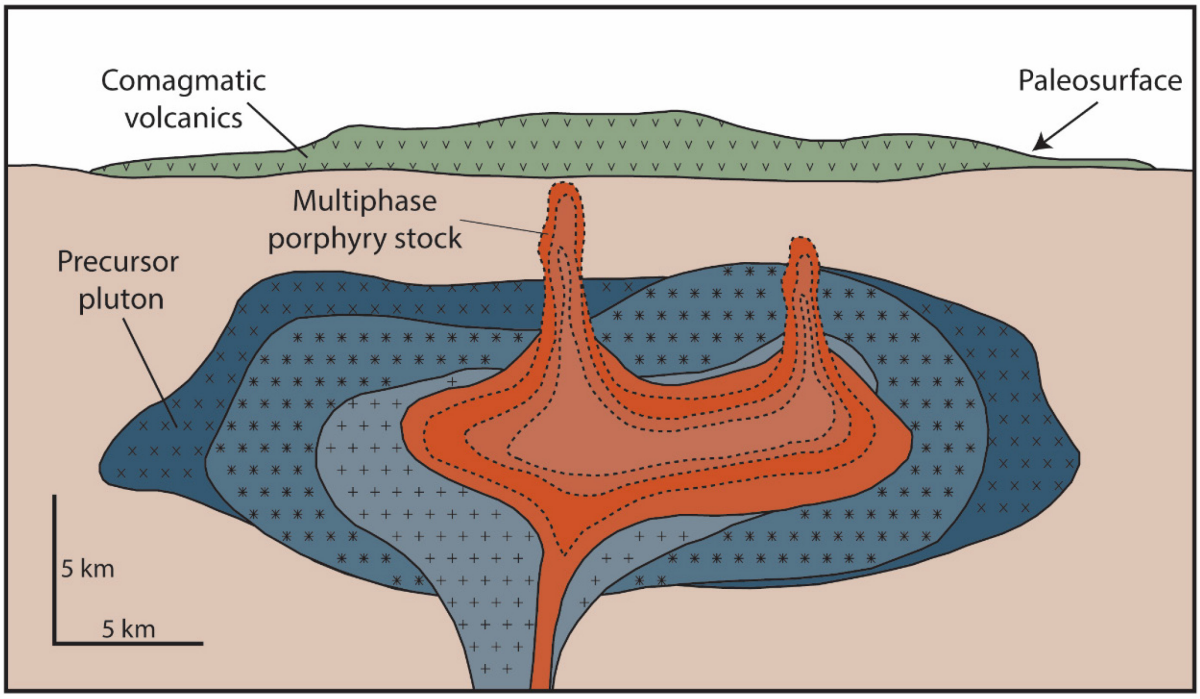


Figure 1.3. Shallow crustal setting for porphyry Cu deposit formation. Modified from Sillitoe (2010).

Porphyry intrusions are emplaced at paleodepths of 1-6 km (Seedorff *et al.*, 2005; Sillitoe, 2010), with the characteristic aplitic groundmass generally thought to be formed by quenching of the magma as a result of rapid ascent and volatile loss (Jahns & Burnham, 1969). Many porphyritic intrusions comprise a single deposit, showing a range of geometries from dykes to cylindrical stocks or domes. Porphyries are classified according to their temporal relation to mineralisation

(e.g. ‘early’, ‘intermineral’, ‘late’ and ‘postmineral’), although separate intrusions may in some instances be difficult to differentiate. Compositionally, porphyry intrusions are dominantly intermediate to silicic, calc-alkaline, I-type, and metaluminous; with more alkalic compositions chiefly associated with Cu-Au, rather than Cu-Mo systems (Seedorff *et al.*, 2005; Sillitoe, 2010).

Porphyritic intrusions act as fluid conduits, rather than being the principal source of fluids, metals and sulphur themselves. Indeed, both the porphyritic intrusions and ore-forming fluids are thought to be sourced from the large underlying magma reservoir (Fig. 1.3), yet the relationship between porphyry and parental pluton is rarely preserved (unless significant tilting or uplift has occurred, as at Yerington; Dilles, 1987).

Critical to the formation of a deposit is the exsolution of a volatile phase from the magma. Volatile exsolution is triggered by concomitant decompression and crystallisation, acting to increase melt H_2O contents and decrease water solubility, respectively (Burnham, 1979). At depth, a single, supercritical fluid of low to intermediate density will exsolve from the melt, whereas, at shallower depths, fluids either exsolving directly from the magma or decompressing supercritical fluids may intersect the solvus to form coexisting brine and low salinity vapour phases (Heinrich & Candela, 2014). Conventionally, fluids are believed to be entrained in a bubble-rich, positively buoyant melt that ascends to the top of the magma chamber (Cloos, 2001). However, the paradigm that upper crustal magma bodies are dominantly liquid (i.e. magma chambers) has been challenged in recent years (Cashman *et al.*, 2017; Jackson *et al.*, 2018), with growing evidence for the predominance of crystal-dominated or ‘mush’ reservoirs in magmatic arcs. In mush-dominated reservoirs, coalescence of bubbles into fluid channels would facilitate the upward mobility of fluid (Parmigiani *et al.*, 2017; Chelle-Michou & Rottier, 2021).

1.3.3 Hydrothermal alteration

Exsolved magmatic-hydrothermal fluids responsible for mineralisation also produce characteristic zonation patterns in terms of alteration mineral assemblages (Fig. 1.4A). In an ideal case, the spatial distribution of these zones can be used to point exploration towards the better mineralised centre of a system, though this may be complicated by the action of multiple fluid pulses or rapid uplift (Sillitoe, 2010).

Early sodic-calcic alteration may be preserved at depth (Fig. 1.4A) in some deposits (e.g. Yerington; Carten, 1986; Dilles, 1987), and is characterised by the presence of sodic plagioclase, actinolite, epidote and titanite. In the deep, potassic core of the system (Fig. 1.4A) high temperatures, high K^+/H^+ ratios and cooling fluids (Fig. 1.4B) favour cation exchange reactions ($Na/Ca \rightarrow K$), typified by the alteration of plagioclase to K-feldspar, and mafic phases to biotite.

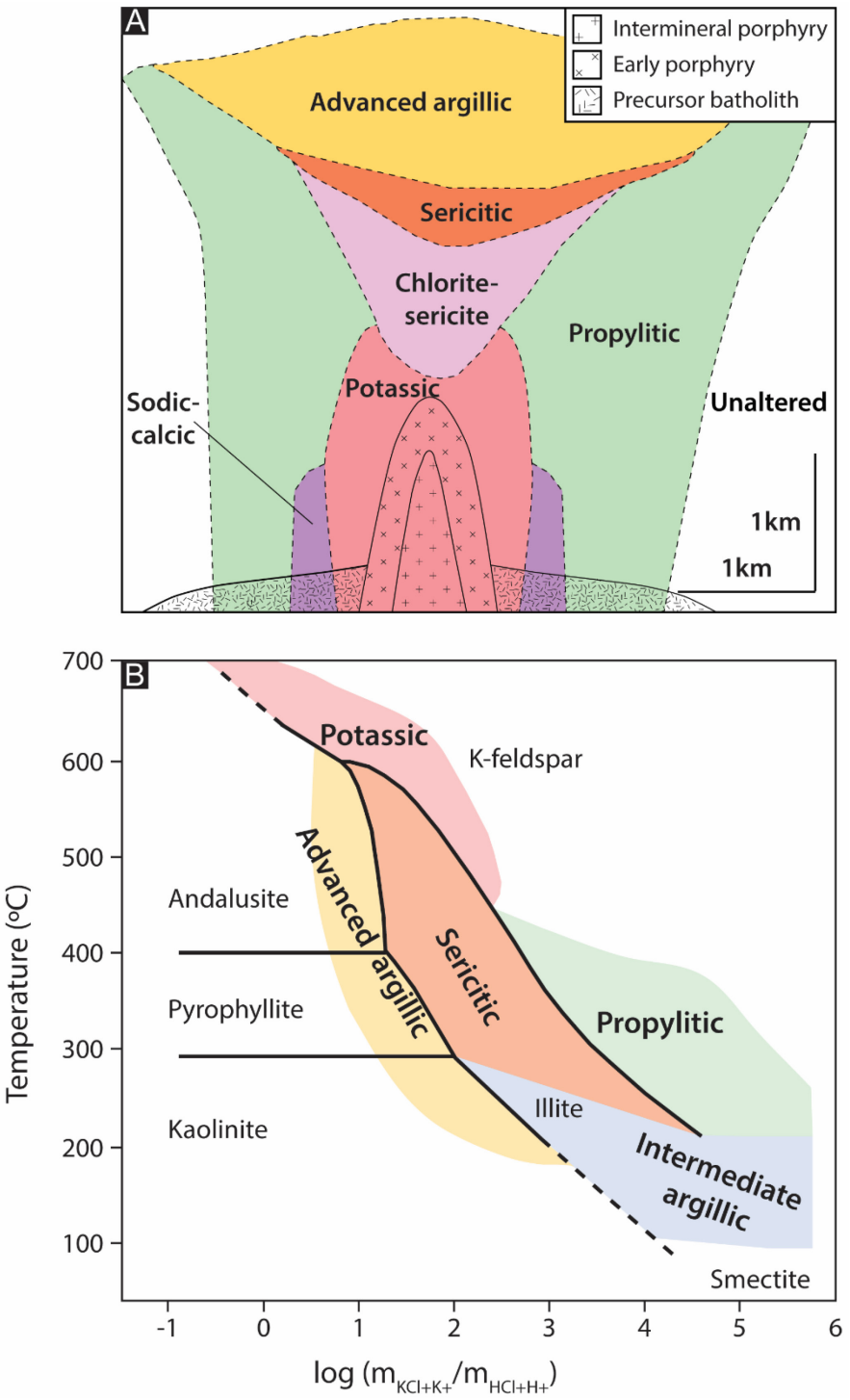


Figure 1.4. Distribution of alteration zones and fluid physico-chemical conditions under which they form. **A.** Cross section showing the distribution of alteration zones in an idealised porphyry Cu deposit. Modified from Sillitoe (2010). **B.** Phase diagram for the system K_2O-Al_2O_3-SiO_2-H_2O-KCl-HCl at $P(H_2O)$ = 1 kb. Modified from Seedorff et al. (2005).

As the dispersing fluid cools, reaction of SO_4^{2-} with reduced iron and increasing disproportionation of SO_2 generates H_2S and acid, resulting in hydrolytic (addition of H^+) reactions, together with sulphide precipitation. The decreasing buffering capacity of the host rock results in a progression through: 1) transitional chlorite-sericite alteration; 2) sericitic alteration; and 3) advanced argillic

alteration zones (Figs. 1.4A and B). Alteration of plagioclase to fine-grained muscovite (sericite), as well as addition of quartz and pyrite, characterises sericitic (phyllic) alteration, whereas alunite, pyrophyllite and kaolinite are typical of the advanced argillic zone (Lowell & Guilbert, 1970; Seedorff *et al.*, 2005; Sillitoe, 2010).

The propylitic, or green rock, domain represents the most distal expression of the magmatic-hydrothermal system (Fig. 1.4), extending for several kilometres away from the centre of the deposit (Cooke *et al.*, 2014). Green rock alteration is most well developed in mafic to intermediate rocks, which contain abundant ferromagnesian minerals to aid formation of the characteristic propylitic minerals chlorite and epidote (Lowell & Guilbert, 1970; Ballantyne, 1983). Forming contemporaneously with potassic alteration but at lower temperatures, lower fluid/rock ratios and higher K^+/H^+ (Fig. 1.4B), there is still debate about the relative importance of magmatic vs. circulating meteoric waters in producing green rocks (Norman *et al.*, 1991; Reed *et al.*, 2013; Pacey *et al.*, 2020a). Propylitic alteration is classically thought to represent the simple addition of volatile components (e.g. H_2O and CO_2; Meyer & Hemley, 1967; Halley *et al.*, 2015), although some studies have argued that significant mass transfer can take place (Ulrich & Heinrich, 2002; Pacey, 2016). In an ideal case, the propylitic domain (like the whole porphyry system) shows zonation, transitioning from a proximal actinolite subzone, through an epidote subzone, to a chlorite-dominated subzone, although chlorite is present throughout the green rock environment (Norman *et al.*, 1991; Holliday & Cooke, 2007; Cooke *et al.*, 2014). Titanite is also commonly observed in the propylitic environment (Seedorff *et al.*, 2005; Wilkinson *et al.*, 2015; Hart-Madigan *et al.*, 2020), taking up excess titanium that is liberated during the chloritisation of mafic phases (Wilkinson *et al.*, 2015).

1.3.4 Mineralisation

Precipitation of ore minerals, including Cu- and Mo-bearing sulphides, as well as Au, occurs in response to pressure decreases associated with extensive hydro-fracturing, cooling, phase separation, and fluid-rock interaction or fluid mixing (Hemley *et al.*, 1992; Fournier, 1999). Like alteration mineral assemblages, ore-minerals are zoned about the highest-grade core. Chalcopyrite and bornite are generally found in the centre, with decreasing Cu-sulphide and increasing pyrite contents through the transition into the propylitic halo (Lowell & Guilbert, 1970). Copper may also be introduced during sericitic or advanced argillic alteration, with high-sulphidation state minerals, such as enargite and covellite common in the advanced argillic zone (Sillitoe, 2010).

Significant debate still exists regarding how ore metals are transported in the hydrothermal fluids. Copper and gold are considered to be dominantly transported as Cl complexes in the brine

phase, with increasing fluid-melt partition coefficients for metals associated with higher Cl contents of the fluid (Candela & Holland, 1984; Ulrich *et al.*, 1999). However, some authors have proposed that Cu may also be transported by S-species in the vapour or lower salinity liquid phases, like Au (Heinrich *et al.*, 2004; Simon *et al.*, 2006; Seo *et al.*, 2009). Molybdenum generally precipitates in a specific event or events, spatially separate to Cu and Au (Sillitoe, 2010), reflecting differential partitioning and/or precipitation behaviour. There is a general lack of understanding of Mo complexing (Candela & Holland, 1984) but oxy-chloride complexes in the brine phase are thought to facilitate Mo transport (Ulrich & Mavrogenes, 2008).

1.4 Indicator minerals in porphyry systems

The paucity of new porphyry discoveries has led to a growing body of research into whether the textural and/or chemical characteristics of igneous and/or hydrothermal minerals (indicator minerals) can be used to infer the likely presence of, or proximity to, mineralisation (Bouzari *et al.*, 2016; Cooke *et al.*, 2017). Ideally, indicator minerals should be: i) hard, ii) easy to separate (e.g. dense or magnetic), iii) resistant to weathering and/or alteration and iv) exhibit unique geochemical compositions (McClenaghan, 2005). For example, compositions of zircons from porphyry-associated magmas are relatively distinctive, in that they exhibit elevated Eu/Eu*, Ce/Nd and Th/U ratios, in addition to low Yb/Gd ratios and Ti contents (Ballard *et al.*, 2002; Lu *et al.*, 2016; Pizarro *et al.*, 2020). High Eu/Eu* and Ce/Nd ratios in zircon are frequently attributed to crystallisation from unusually oxidised magmas (Ballard *et al.*, 2002; Dilles *et al.*, 2015), conditions which may be important for sulphur speciation and solubility (Jugo, 2009). However, these features have been shown to primarily reflect melt composition, itself affected by processes such as titanite crystallisation or plagioclase suppression (Wotzlaw *et al.*, 2013; Loader *et al.*, 2017; Nathwani *et al.*, 2021). In a study of zircon Ce/Nd ratios, Loader *et al.* (2022) suggested that the high Ce/Nd signatures of porphyry related zircons reflect enhanced partitioning of Ce at low crystallisation temperatures (inferred from the Ti-in-zircon thermometer; (Ferry & Watson, 2007), in addition to partial inheritance of melt signatures (often as a result of titanite co-crystallisation). In fact, many characteristics of porphyry-related zircons (e.g. elevated Ce/Nd and low Yb/Gd and Th/U) may result from titanite co-crystallisation, leading to questions about the validity of Ti-in-zircon temperatures and the prevalence of titanite-zircon co-crystallisation in porphyry magmas.

In terms of applying hydrothermal mineral compositions, limited work has focussed on alunite in the lithocap (silicic, argillic and advanced argillic) environment (Chang *et al.*, 2011), but much more has been directed at the propylitic alteration zone. In particular, chlorite and epidote

compositions are now routinely analysed by major mining companies with the potential to: i) indicate whether a porphyry system is nearby; ii) infer the endowment of the hydrothermal system; and iii) vector towards the mineralised centre (Wilkinson *et al.*, 2015; Cooke *et al.*, 2020b; Pacey *et al.*, 2020b).

1.5 Aims, objectives and thesis outline

This thesis aims to investigate whether titanite can be utilised as an indicator mineral in the exploration for porphyry deposits. The overarching objectives of the study are:

- Develop a methodology in which high-quality textural, geochemical and geochronological titanite data is collected
- Evaluate the extent to which titanite crystallisation impacts residual chemistry, and the compositions of other mineral phases
- Document the occurrence of igneous and non-igneous titanite in porphyry systems
- Define geochemical characteristics which differentiate igneous and non-igneous titanite
- Assess factors that control the compositions of both igneous and non-igneous titanite
- Define and understand the textural and geochemical characteristics of igneous porphyry-titanite, factoring in any temporal variation
- Utilise machine learning techniques to test whether geochemical compositions can be used to predict whether titanite originated from a magma or a hydrothermal fluid, or whether igneous titanite crystallised from a porphyry magma

Four study sites are discussed (Strontian, Chuquicamata, Cobre Panama and Oyu Tolgoi), which were chosen to address the overarching aims and objectives, encompassing both mineralised and unmineralised magmatic suites, as well as strongly altered to unaltered rocks. The study is broken down into multiple chapters, with Chapter 2 outlining what is currently known about titanite, and Chapter 3 detailing the chosen methodology for the study. Chapters 4-7 focus on the four study sites in turn, addressing the key overarching aims and objectives. Chapter 8 synthesises the results of the study and discusses how titanite could be used in the exploration for porphyry deposits. Finally, Chapter 9 summarises the most important findings and identifies areas for future work.

Chapter 2. Titanite literature review

Titanite, $CaTiSiO_4(O,OH,F)$, is an important titanium-bearing accessory mineral commonly found in igneous and metamorphic rocks (Deer *et al.*, 2013). In terms of modal abundance, titanite typically comprises less than 1% of the host rock and may exhibit a range of colours, from colourless through green to brown. Also known as **sphene**, based on the Greek *sphenos* meaning wedge, titanite is easily recognised in thin section due to its characteristic diamond or wedge-shaped cross section (Kohn, 2017). Titanite is often a key repository of trace elements (Gromet & Silver, 1983), accommodating several petrogenetically important groups of elements such as REEs, HFSEs, transition metals and LILEs (Frost *et al.*, 2001; Deer *et al.*, 2013). This compositional variability allows titanite to not only be applied to geochronologic (Storey *et al.*, 2006; Garber *et al.*, 2017; Hart-Madigan *et al.*, 2020) and thermobarometric (Hayden *et al.*, 2008) studies, but also to fingerprint environments in which it forms (Kohn, 2017; Chew *et al.*, 2020; Scibiorski & Cawood, 2022).

2.1 Structure and substitutions

Titanite is an orthosilicate mineral, comprising zig-zag chains of corner-sharing TiO_6 octahedra that run parallel to the x-axis (Fig. 2.1). Chains of TiO_6 octahedra are linked by SiO_4 tetrahedra, producing a $[TiOSiO_4]^{2-}$ framework with Ca in irregular seven-fold coordination. The O(1) oxygens in the TiO_6 octahedra are not bound to silica tetrahedra and hence are considered to be 'underbonded' (Zachariasen, 1930; Speer & Gibbs, 1976; Deer *et al.*, 2013). Chemical substitutions occur in the Ca, Ti and O(1) sites, with variation in size and charge of the crystallographic sites permitting a multitude of trace elements to be incorporated (Fig. 2.1) – in stark contrast to its relative simplicity in terms of major elements. Although Ti can substitute for Si in the tetrahedral site in other minerals (e.g. amphibole), tetrahedral Al is not accommodated by the titanite structure (Oberti *et al.*, 1991). Coupled substitutions are almost always involved, with key substitution mechanisms outlined below (Franz & Spear, 1985; Green & Pearson, 1986; Černý *et al.*, 1995):

$$Ca^{2+} + Ti^{4+} = REE^{3+} + (Al, Fe)^{3+} \quad \textbf{(Eq. 2. 1)}$$

$$Ti^{4+} + O^{2+} = (Al, Fe)^{3+} + (OH, F)^{-} \quad \textbf{(Eq. 2. 2)}$$

$$2Ti^{4+} = (Al, Fe)^{3+} + (Nb, Ta)^{5+} \quad \textbf{(Eq. 2. 3)}$$

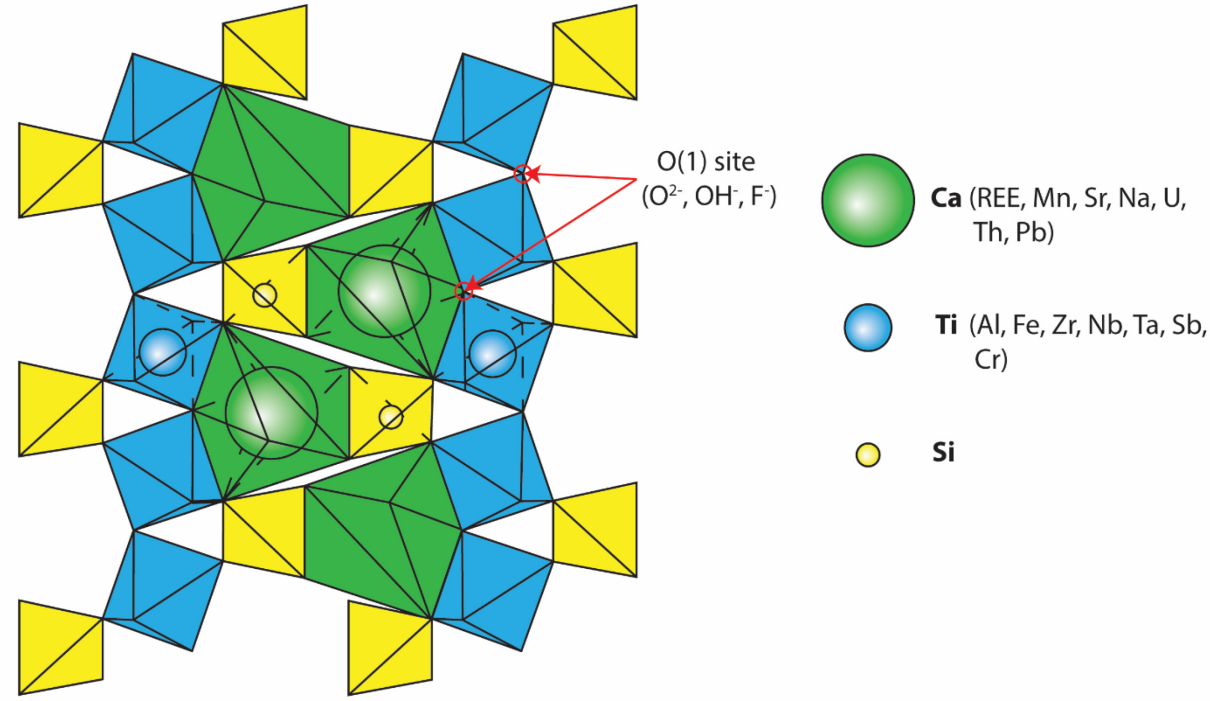


Figure 2.1. Titanite crystal structure projected along the c-axis showing the main structural sites. Commonly substituting trace elements are indicated in brackets for the different sites. Modified from Kohn (2017).

Coupled substitution with Al or Fe is thought to be important for REE incorporation (Eq. 2.1). Another important substitution mechanism is the incorporation of OH or F in the O1 site, and Al or Fe in the Ti site (Eq. 2.2). The occurrence of Al-rich (and F-rich) titanite has been documented in several environments, notably at high pressures and low temperatures (Franz & Spear, 1985; Enami *et al.*, 1993; Markl & Piazolo, 1999). This substitution mechanism has played an important role in identifying titanite formed in different environments (Nakada, 1991; Kontonikas-Charos *et al.*, 2019; Scibiorski & Cawood, 2022) and is often denoted by distinct Fe/Al or Al/Fe ratios. Additionally, coupled substitution with Al or Fe has been demonstrated to be important for the incorporation of pentavalent cations such as Nb and Ta (Eq. 2.3).

2.2 Igneous titanite

2.2.1 Stability and occurrence

In igneous rocks, titanite is most frequently found in rocks with either calc-alkaline or alkaline affinities, in the latter case comprising up to 15 modal percent (Chakhmouradian & Zaitsev, 2002; Chakhmouradian, 2004). In calc-alkaline rocks, titanite is a common accessory mineral in intermediate to felsic compositions, and, together with biotite, is likely to be the main Ti-bearing phase. Several authors have noted the tendency for titanite to be present in intrusive rather than extrusive rocks (Frost *et al.*, 2001; Kohn, 2017), although exceptions to this rule include major

explosive eruptions in the southwestern USA (e.g. Fish Canyon, Schmitz & Bowring, 2001; Kneeling Nun, Szymanowski *et al.*, 2017; Peach Springs, Colombini *et al.*, 2011). Nevertheless, the paucity of titanite in volcanic rocks is taken as evidence that titanite is a relatively late-crystallising phase (Frost *et al.*, 2001).

Despite its utility in geochemical and geochronological studies, less is known about the factors that control titanite stability in comparison to other important accessory minerals such as zircon and apatite (Watson & Harrison, 1983; Harrison & Watson, 1984; Boehnke *et al.*, 2013). However, the formation of titanite at relatively high magmatic fO_2 is widely noted (Fig. 2.2). Indeed, the assemblage titanite + magnetite + quartz is taken to indicate conditions that are more oxidising than the FMQ redox buffer (Wones, 1989), conditions which generally overlap with those encountered in magmatic arcs (Jugo, 2009).

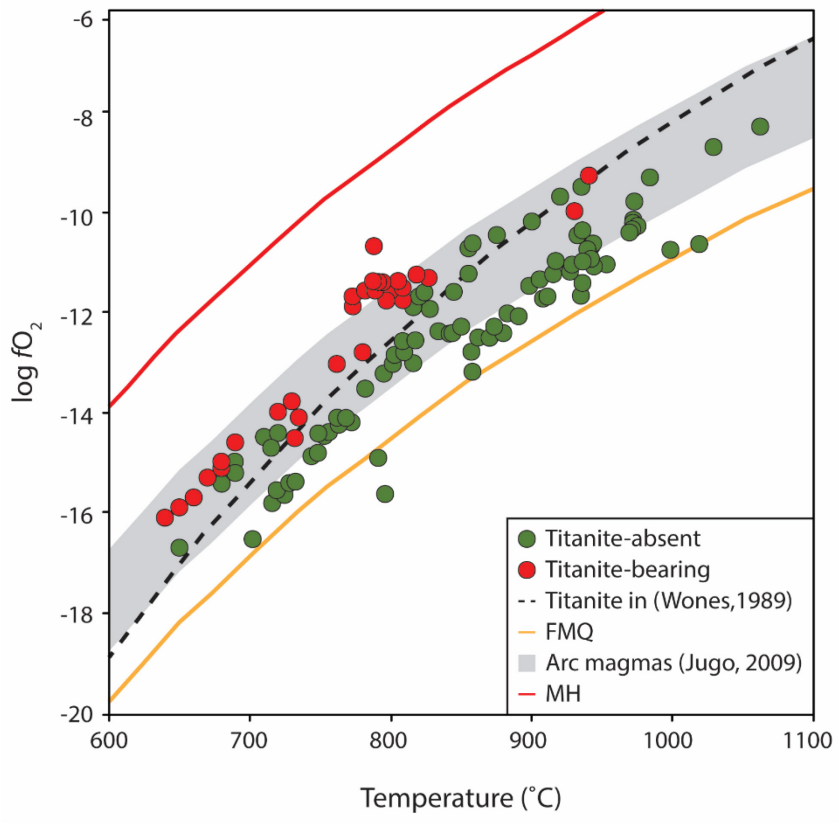


Figure 2.2. Temperature vs log fo_2 plot showing titanite-absent and titanite-bearing rocks in relation to redox buffers and typical arc magmas (Jugo, 2009). Modified from Ackerson (2011).

In addition to oxidation state, factors such as temperature and melt composition may be important in controlling titanite stability. For example, Thiéblemont *et al.* (1988) suggested that higher Ca/Al ratios, and hence sufficient Ca, may favour titanite crystallisation. More recently, Ayers *et al.* (2022) conducted experiments at various melt compositions and temperatures to explain titanite saturation, deriving an equation that is similar to those which have been generated

for apatite and zircon (Watson & Harrison, 1983; Harrison & Watson, 1984; Boehnke *et al.*, 2013). Ayers *et al.* (2022) argued that melt TiO_2 content and M (melt compositional parameter) are important parameters, with the titanite saturation temperature given as:

$$T(K) = \left({TiO_2}^{melt} - 0.978 \times M + 5.9\right) \div 0.0048 \qquad (\mathbf{Eq.\,2.4})$$

This equation allows titanite saturation temperatures to be estimated in natural systems using whole-rock chemistry, although such an application assumes that whole-rock compositions accurately reflect melt compositions, which is probably unlikely at the near-solidus conditions at which titanite saturates. The frequent association of titanite with hydrous phases such as amphibole and biotite suggests that high melt water content may also enhance titanite stability. Unlike amphibole and biotite, which have been more widely studied (Scaillet & Evans, 1999), the minimum water content to stabilise titanite is not known, although the relationship is highlighted by the following reaction (Frost *et al.*, 2001).

$$7CaFeSi_2O_6(cpx) + 3FeTiO_3(ilm) + 5SiO_2(qz) + 2H_2O = 2Ca_2Fe_5Si_8O_{22}(OH)_2(am) + 3CaTiSiO_5(ttn) \qquad (\mathbf{Eq.\,2.5})$$

2.2.2 Trace element contents and mineral-melt partitioning

Titanite has been shown to be an important trace element repository. For example, through combining mineral trace element compositions with mineral modal abundances, Gromet and Silver (1983) estimated that titanite contained over 30% of each REE in a granodiorite as a proportion of the whole-rock, and almost entirely hosted the middle to heavy REE. Such a contribution to whole-rock trace element deportment belies its modest modal abundance and is due to extremely high REE partition coefficients. Titanite, like amphibole and apatite (Fig. 2.3), preferentially incorporates middle to heavy REEs yet it does so to a much higher degree, with individual partition coefficients one to several orders of magnitude greater for titanite than other phases (Fig. 2.3) and even exceeding 1000 in some studies (Colombini *et al.*, 2011). Titanite also strongly partitions high-field strength elements and is one of the few mineral phases that fractionates Nb (D_{Nb} = 73; Colombini *et al.*, 2011) and Ta (D_{Ta} = 112; Colombini *et al.*, 2011), which are often referred to as 'geochemical twins' (Stepanov *et al.*, 2014). These partition coefficients mean that titanite crystallisation can strongly impact melt composition and hence the composition of any subsequently crystallising phases (Chelle-Michou *et al.*, 2015; Loader *et al.*, 2017; Olson *et al.*, 2017). Other compatible elements include transition metals (e.g. D_{Sc} = 23; Colombini *et al.*, 2011) and radiogenic elements (e.g. D_U = 3; Colombini *et al.*, 2011). Although LILEs are generally incompatible (e.g. D_{Sr} = 0.85; Colombini *et al.*, 2011), appreciable concentrations are still incorporated into the titanite structure.

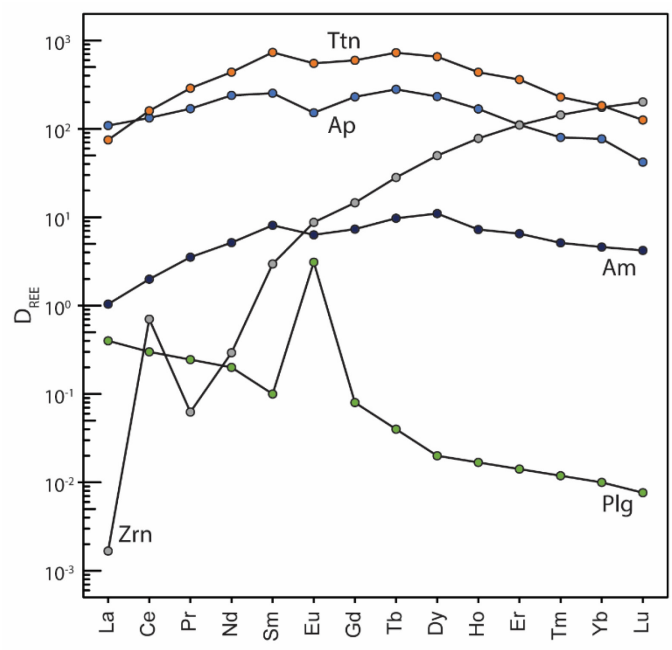


Figure 2.3. Rare earth element mineral-melt partition coefficients for titanite compared to a range of important REE-bearing phases that are commonly found in granitoids. All values are taken from Padilla and Gualda (2016) except for plagioclase which was taken from Bachmann *et al.* (2005). Interpolation of missing values (using neighbouring REEs) was undertaken where necessary.

Experimental work by Hayden *et al.* (2008) identified the temperature dependence of Zr partitioning into titanite, based on Zr^{4+} substituting for Ti^{4+} according to Equation 2.6. This forms the basis of the Zr-in-titanite thermometer, with the experimental calibration which is valid between 1000°C and solidus temperatures, given by Equation 2.7:

$$CaTiSiO_5(ttn) + ZrSiO_4(zr) + 5SiO_2(qz) + 2H_2O = CaZrSiO_5(Zr_{ttn}) + TiO_2(rt) + SiO_2(qz) \quad \textbf{(Eq. 2. 6)}$$

$$T(K) = \frac{(7708 + 960P)}{\left(10.52 - \log(\alpha_{TiO_2}) - \log(\alpha_{SiO_2}) - \log(Zr_{ttn})\right)} \quad \textbf{(Eq. 2. 7)}$$

These experiments, like those of the Ti-in-zircon thermometer (Ferry & Watson, 2007), were conducted at rutile and quartz saturation. Where these conditions are not met, a correction is necessary which involves the estimation of silica (a_{SiO_2}) and titania activity (a_{TiO_2}). Quartz saturation is generally assumed in titanite-bearing calc-alkaline systems, however, rutile is rarely observed in equilibrium with titanite (Kohn, 2017). Consequently, estimation of titania activity is required which may introduce significant uncertainty into the Zr-in-titanite thermometer. An empirical titania activity of 0.75 is often advocated for titanite-bearing systems (Claiborne *et al.*, 2010), though other authors argue for a value of 0.5 (Schiller & Finger, 2019). Nevertheless, the effect of varying α_{TiO_2} has opposing effects on calculated Zr-in-titanite and Ti-in-zircon crystallisation temperatures, with increased titania activities resulting in higher titanite and lower

zircon crystallisation temperatures (Ferry & Watson, 2007; Hayden *et al.*, 2008). Additionally, calculated titanite crystallisation temperatures are also moderately pressure dependent, unlike zircon (Eq. 2.7). Calculated titanite crystallisation temperatures in calc-alkaline rocks are generally near-solidus (e.g. <800 °C; McLeod *et al.*, 2011; Szymanowski *et al.*, 2017), suggesting that titanite saturates after a signicant amount of crystallisation has taken place (e.g. melt fraction, F<0.5; Marxer & Ulmer, 2019).

2.2.3 Diffusion and zonation

Studies investigating various species have observed that diffusion in titanite is generally slower than in apatite, but quicker than in zircon (Cherniak, 2010). Unlike many other minerals, diffusion of Zr and Pb in titanite is thought to be quicker than Sr (Cherniak, 1993; Cherniak, 1995; Cherniak, 2006; Cherniak, 2010). Nevertheless, at typical titanite crystallisation temperatures, diffusion is relatively sluggish and hence any primary igneous zonation should be preserved (Cherniak, 1993; Cherniak, 1995; Cherniak, 2006).

Zonation, as identified by changes in BSE brightness, is almost ubiquitous in igneous titanite. This zonation may manifest itself as: i) core to rim; ii) patchy; or iii) sector varieties. Patchy zoning in titanite has been noted by multiple authors (Piccoli *et al.*, 2000; McLeod *et al.*, 2011) and is often found in igneous rocks that show evidence for magma mixing. Indeed, where Fe-Ti oxide inclusions, low-REE concentrations (manifesting as dark zones in BSE mode), evidence for resorption and patchy zonation occur together, mixing with more reduced magmas is suggested to have stabilised ilmenite over titanite and decreased the amount of ferric iron available for coupled REE substitution (McLeod *et al.*, 2011).

Sector zoning is widely developed in igneous titanite, with anomalously bright sector zones often controlled by REE and HFSE enrichment (Paterson *et al.*, 1989; Paterson & Stephens, 1992). These sector zones are believed to represent crystallographically controlled differences in mineral-melt partitioning, with particular crystal faces such as [100] preferentially partitioning trace elements relative to the dominant [111] face (Paterson & Stephens, 1992). This incorporation has particular relevance when considering titanite crystallisation temperatures, with non-equilibrium Zr incorporation potentially resulting in erroneously high calculated Zr-in-titanite temperatures (Hayden *et al.*, 2008).

2.3 Geochronology

Accommodation of appreciable amounts of U into the titanite structure allows it to be dated by U-Pb geochronology. A range of closure temperatures have been suggested for titanite (Mattinson, 1978; Spear & Parrish, 1996; Kohn & Corrie, 2011), though diffusive resetting is only thought to be problematic at temperatures above the wet granite solidus (e.g. > 700 °C; Frost *et al.*, 2001). Titanite, however, incorporates non-radiogenic lead (common Pb) into its structure (Frost *et al.*, 2001), necessitating a common lead correction to account for this. There are several methods to correct for non-radiogenic lead, of which the most widely utilised is the bulk Pb evolution model of Stacey and Kramers (1975). In addition, common lead can also be constrained by repeated analyses of U poor phases (e.g. feldspar), by determination of the non-radiogenic isotope of lead (^{204}Pb), or by conducting a linear regression in ^{207}Pb/^{206}Pb vs ^{238}U/^{206}Pb space (Tera & Wasserburg, 1972; Frost *et al.*, 2001; Storey *et al.*, 2006). For Phanerozoic rocks, where the slope of the line is at a high angle to concordia, the most common method of correcting for common lead in titanite involves a regression in ^{207}Pb/^{206}Pb vs ^{238}U/^{206}Pb space (also known as Tera-Wasserburg diagrams). This is because titanite common lead compositions may differ somewhat from the terrestrial Pb evolution model (Stacey & Kramers, 1975) or U poor phases, and because ^{204}Pb is difficult to analyse due to an isobaric interference with ^{204}Hg which is prevalent in argon carrier gases (Andersen, 2002; Kirkland *et al.*, 2017). However, it should be noted that in using Tera-Wasserburg plots to determine titanite U-Pb ages, it is assumed that discrodance results from variable contamination of a single common lead composition (Storey *et al.*, 2006; Schoene, 2014; Kirkland *et al.*, 2017). Despite the need to correct for common lead, U-Pb isotopic analysis of titanite is now routine particularly in metamorphic (Aleinikoff *et al.*, 2002; Spencer *et al.*, 2013; Garber *et al.*, 2017) and hydrothermal (Hart-Madigan *et al.*, 2020) environments. Here, dating of titanite is particularly useful given the absence of easily-dated minerals that contain only radiogenic Pb (e.g. zircon).

2.4 Titanite occurrence in porphyry systems

Given that titanite is commonly observed in calc-alkaline, intrusive rocks of intermediate to felsic compositions, and titanite stability is favoured in hydrous, oxidised magmas, it is no surprise that porphyry-associated magmas often contain titanite. In particular, titanite is noted to occur in several porphyry districts, including Chuquicamata (Cabrera *et al.*, 2010), Bajo de la Alumbrera (Buret *et al.*, 2016), Bingham Canyon (Large *et al.*, 2021), Ok Tedi (Large *et al.*, 2018), Pebble (Olson *et al.*, 2017) and Yerington (Dilles, 1987). These systems represent the minimum number of titanite-bearing porphyry systems as titanite, unlike zircon, is somewhat susceptible to hydrothermal

alteration. Only where wedge-shaped pseudomorphs composed of rutile (Finlayson, 2002; van Dongen *et al.*, 2010), or intergrowths of REE-bearing minerals such as allanite and monazite (Pan *et al.*, 1993) can a titanite precursor be identified. Whilst titanite is almost certainly not resistant to hydrothermal alteration, there has been limited study of the mechanisms by which titanite is altered. Nevertheless, alteration of titanite at high partial pressures of CO_2, conditions which may be prevalent in the propylitic environment (Meyer & Hemley, 1967; Seedorff *et al.*, 2005), has been postulated; with rutile, calcite and quartz suggested as alteration products (Eq. 2.8; Hunt & Kerrick, 1977):

$$CaTiSiO_5(ttn) + CO_2 = TiO_2(rt) + CaCO_3(cc) + SiO_2(qz) \quad \textbf{(Eq. 2.8)}$$

Additionally, alteration of titanite to rutile may also occur under acidic conditions, after reaction with HCl (Eq. 2.9; Finlayson, 2002):

$$CaTiSiO_5(ttn) + HCl = TiO_2(rt) + CaCl_2 + SiO_2(qz) + H_2O \quad \textbf{(Eq. 2.9)}$$

In addition to being altered, titanite may also be formed in the porphyry environment, either occurring in veinlets or replacing other phases. Again, relatively little is known about the mechanisms by which titanite forms, or its ubiquity in various portions of the porphyry environment. In the literature, titanite is most commonly reported to occur in the propylitic domain, (Seedorff *et al.*, 2005; Wilkinson *et al.*, 2015; Hart-Madigan *et al.*, 2020), taking up excess titanium that is liberated during the chloritisation of mafic phases (Wilkinson *et al.*, 2015). Several authors have reported the occurrence of titanite in sodic-calcic alteration zones (Carten, 1986; Lynch & Ortega, 1997), however these are often the deepest and most poorly preserved parts of the porphyry system (Sillitoe, 2010), and hence are not commonly studied. The presence of titanite in potassic alteration zones has also been reported (Cao *et al.*, 2015; Celis, 2015), although the association of such potassic titanite with magmas of atypical compositions (e.g. alkalic or reduced porphyries) indicates that its formation in this environment is relatively uncommon.

2.5 Titanite as an indicator mineral

In terms of physical characteristics, titanite is well-suited to being employed as an indicator mineral. It is relatively hard (hardness = 5), dense (~3.5 g/cm^3; Deer *et al.*, 2013) and is stable during weathering and diagenesis (Morton & Hallsworth, 1999; Morton & Hallsworth, 2007; Chew *et al.*, 2020). As well as these physical traits, the chemical characteristics of titanite are particularly conducive to utilisation as a mineral indicator. For example, early geochemical studies of titanite by Franz and Spear (1985) and Nakada (1991) focussed on utilising Fe, Al and F contents in

metamorphic and igneous settings. Since then, many studies have characterised geochemical differences between igneous and metamorphic titanite (Garber *et al.*, 2017; Olierook *et al.*, 2019), with a recent study by Scibiorski and Cawood (2022) employing a support vector matrix (a machine learning technique). Similarly, compositional differences between igneous and hydrothermal titanite have been characterised by several authors (Li *et al.*, 2010; Xie *et al.*, 2010; Kontonikas-Charos *et al.*, 2019).

The occurrence of titanite in both the magmatic and hydrothermal environments, when combined with potential compositional variation and U-Pb geochronology, means there is undoubtedly potential in utilising titanite to understand how physico-chemical conditions and the geologic environment varies temporally in porphyry systems. There are few studies which have focussed on titanite in porphyry systems. However, Cao *et al.* (2015) and Cao *et al.* (2020) identified multiple titanite populations in the Baogutu and Black Mountain porphyries, respectively, with REEs, Sc, V, Sn and Cr as key discriminators. In fact, these elements, in addition to Th/U, regularly differentiate titanite from different environments. Through combining its physical and chemical characteristics, the greatest potential lies in identifying titanite from prospective porphyry intrusions in stream sediments, although most detrital work has thus far focussed on sedimentological investigations (McAteer *et al.*, 2010; Chew *et al.*, 2020). Nevertheless, a preliminary study by Celis (2015) suggested that visual characteristics may be important, with hydrothermally-altered titanites often displaying a blonde to honey-brown colouration.

2.6 Conclusions

To date, there have been a limited number of studies that have investigated the occurrence, and compositions of titanite in porphyry systems. However, from previous work it is clear that titanite exhibits a wide range of compositions that reflect intensive and extensive parameters during its formation. This, when combined with its robust character and occurrence in both magmatic and hydrothermal parts of the porphyry system make it a potentially valuable mineral for understanding and discriminating porphyry environments.

Chapter 3. Analytical Methods

A variety of analytical methods were utilised during this study, including scanning electron microscopy, determination of titanite major and minor element chemistry by electron probe microanalysis (EPMA) and major, minor and trace elements by laser ablation inductively-coupled plasma mass spectrometry (LA-ICP-MS). Mineral chemistry was augmented by U-Pb dating of titanite and whole-rock geochemistry. Limits of detection (LOD) were calculated as 3σ of the background. Accuracy and precision for the different analytical methods were estimated by repeated analysis of international reference standards. Precision was estimated through calculation of relative standard deviation, given by Equation 3.1:

$$\boldsymbol{RSD}\ (\%) = \left(\frac{\sigma i}{\bar{X}^{i}_{measured}}\right) \times 100 \qquad (\mathbf{Eq.\,3.1})$$

where σ is the standard deviation and $\bar{X}^{i}_{measured}$ is the mean concentration of element *i*. Analytical precision for data plotted in subsequent chapters is shown as +/- error bars. Accuracy is assessed through the calculation of bias, which is given by Equation 3.2:

$$\boldsymbol{Bias}\ (\%) = \left(\frac{\left(\frac{1}{n} \times \left(\sum_{i=1}^{n} X^{i}_{measured} - \sum_{i=1}^{n} X^{i}_{reference}\right)\right)}{X^{i}_{reference}}\right) \times 100 \qquad (\mathbf{Eq.\,3.2})$$

where $X^{i}_{measured}$ is the mean concentration of element *i* measured in the standard, $X^{i}_{reference}$ is the certified concentration of element *i* in the standard and *n* is the number of measurements.

3.1 Whole-rock chemistry

Whole-rock geochemical analysis for the Cobre Panama (24 samples) and Strontian study sites (21 samples) was conducted (Appendix 1) at ALS Geochemistry Perth (Lab 1) and Ireland (Lab 2) respectively, with sufficient material retained for petrographic study and *in-situ* mineral chemical analysis. Whole-rock analysis was not conducted for the Chuquicamata and Oyu Tolgoi study sites, but abundant literature data are available for these. All studied samples were first crushed and sieved to ≥ 70% passing 2 mm before being pulverised to 75 µm. Pulps were then analysed for major and trace elements, in addition to loss on ignition (LOI), sulphur and carbon. A slightly different methodology was utilised for the two study sites (Table 3.1), which is detailed below. Further details on ALS accreditation can be found at: https://www.alsenvironmental.co.uk/about-us/quality-and-accreditation.

Table 3.1. Whole-rock analytical methodology.

Study site	ALS method code					
	LOI, S and C	**Major elements**	**Trace elements**	**Base metals**	**Platinum group elements**	**Volatile elements**
Lab 1 (Cobre Panama)	OA-GRA05, S-IR08, C-IR07	ME-ICP06	ME-MS81	ME-MS61L	PGM-MS23	ME-MS42
Lab 2 (Strontian)	OA-GRA05, S-IR08, C-IR07	ME-XRF26	ME-MS81	ME-4ACD81	Not analysed	ME-MS42

3.1.1 LOI, sulphur and carbon

Loss on ignition (LOI) is a measure of the volatile species present in a rock sample. LOI was determined by measuring the weight of a sample before and after heating to 1000 °C. Total sulphur (ALS method S-IR08) and carbon (ALS method C-IR07) were determined by infrared absorption following heating in an induction furnace.

3.1.2 Major elements

Major elements (SiO_2, Al_2O_3, Fe_2O_3, CaO, MgO, Na_2O, K_2O, Cr_2O_3, TiO_2, P_2O_5, SrO, BaO) were determined by X-ray fluorescence (ALS method ME-XRF26) or by inductively-coupled atomic emission spectroscopy (ICP-AES) after fusion using a lithium borate flux (ALS method ME-ICP06).

3.1.3 Trace elements

Most trace element concentrations (Ba, Ce, Cr, Cs, Dy, Er, Eu, Ga, Gd, Hf, Ho, La, Lu, Nb, Nd, Pr, Rb, Sm, Sn, Sr, Ta, Tb, Th, Tm, U, V, W, Y, Yb, Zr) were analysed by ALS method ME-MS81, which involves preparation of a glass bead using a lithium borate flux, before acid digestion and analysis using inductively-coupled plasma mass spectrometry (ICP-MS).

3.1.4 Base metals and platinum group elements

Base metals (Ag, As, Cd, Co, Cu, Li, Mo, Ni, Pb, Sc, Tl, Zn) were determined via four-acid digestion, before analysis using either ICP-AES (ALS method ME-4ACD81) or ICP-MS (ALS method ME-MS61L). Platinum group elements (Pt, Pd, Au) were determined by fire assay with an ICP-MS finish (ALS method PGM-MS23).

3.1.5 Volatile elements

Volatile elements (Ag, As, Bi, Hg, Re, Sb, Se, Te, Tl, U) were determined by aqua-regia digestion (ALS method ME-MS42), followed by an ICP-MS finish.

3.1.6 Quality control

Concentrations of elements that were measured as both major and trace elements show strong correlations (Fig. 3.1A). Duplicate measurements of the analysed samples were also conducted, with major element concentrations in duplicate measurements generally within 10% of each other (Fig. 3.1B). The percentage difference calculated for duplicate SrO measurements of the Cobre Panama sample, however, exceeded 15%, although concentrations were just above the LOD. Consequently, concentrations of Sr, and also Ba, are only reported from the ALS method ME-MS81, which has a much lower LOD. Percentage differences between duplicate measurements for trace elements were also generally ±10% (Fig. 3.1C).

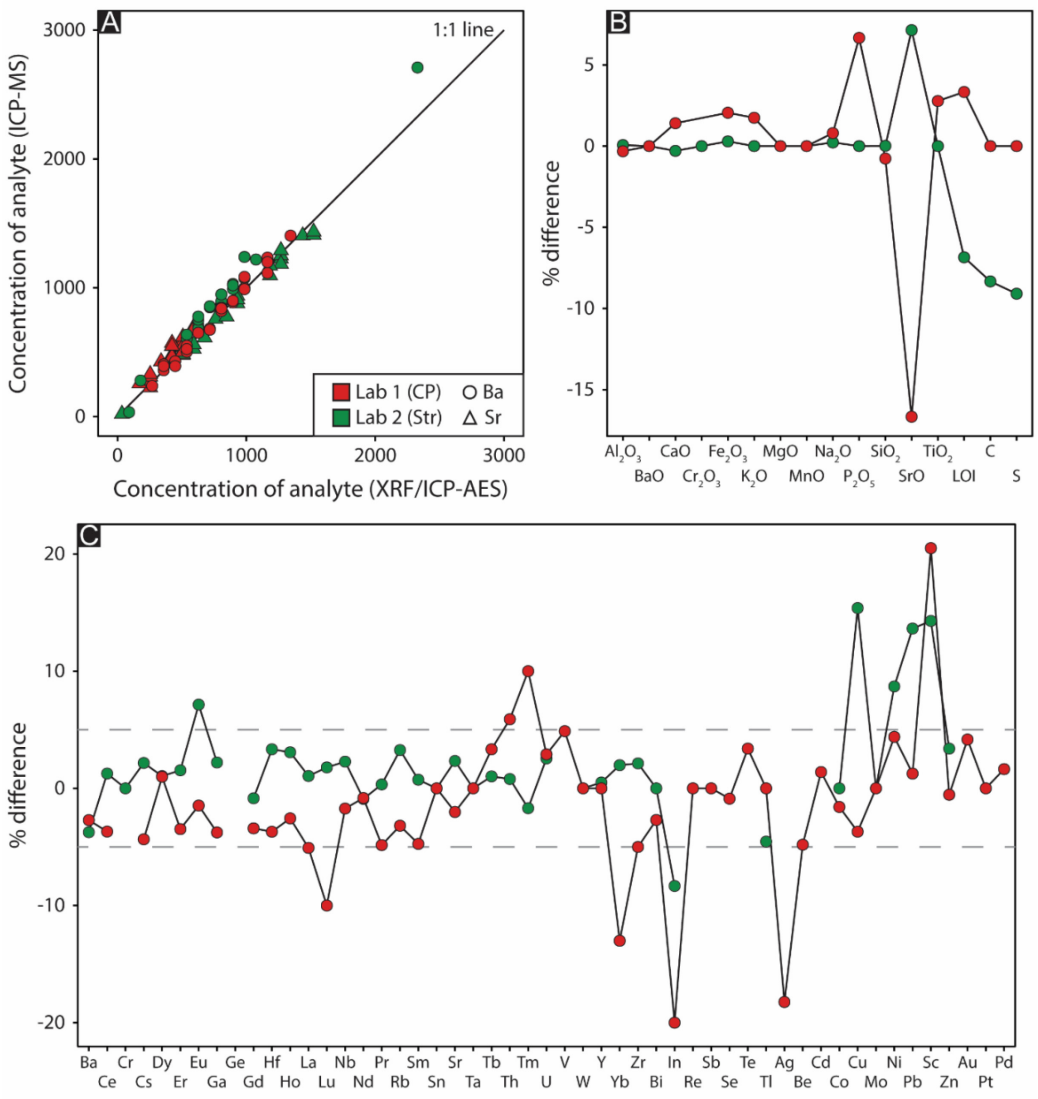


Figure 3.1. Whole-rock QA-QC for Cobre Panama and Strontian sample sets. **A.** Comparison of measured barium and strontium concentrations in unknown samples, as measured by major element and ICP-MS methods. Concentrations are given as ppm, and 2σ analytical error is smaller than the symbol size. **B.** Percentage difference between duplicate measurements for major elements, LOI, carbon and sulphur. **C.** Percentage difference between duplicate measurements for trace elements. Dashed grey line indicates ± 5%.

Percentage bias was calculated by comparing analyses of certified reference materials to published values (or those recommended by ALS; Table 3.2). For major elements, estimated bias was typically ± 10% of reference values (Fig. 3.2A). Estimated bias for BaO was greater than 10% at Lab 1; BaO and SrO at Lab 2 were both below the LOD. However, the estimated bias for Ba and Sr as determined by ALS method ME-MS81 was <3% (Fig. 3.2B) and consequently will only be presented by this method. Although the estimated bias for TiO_2 at Lab 2 was c. 30% (Fig. 3.2A), TiO_2 contents of the GIOP-96 reference material (~0.0287) are close to the LOD (0.01). The majority of trace elements exhibited an estimated bias of <15%. Estimated bias values for V exceed 15% for one run but are within 15% for the other. Where the estimated bias exceeds 15%, concentrations of these elements within certified reference materials are close to the LOD (<3x LOD). Silver shows an extremely high bias for one run, and hence will be excluded.

Table 3.2. Whole-rock certified reference materials.

Study site	ALS method code					
	LOI, S and C	**Major elements**	**Trace elements**	**Base metals**	**Platinum group elements**	**Volatile elements**
Lab 1 (Cobre Panama)	[1]ST-392, [1]GS900-5	[2]SY-4	[2]SY-4	[3]OREAS 20a	[4]OREAS 681	[5]OREAS 920
Lab 2 (Strontian)	[1]LR-LOI3, [1]GS914-5	[6]GIOP-96	[7]OREAS 102a	[1]OGGeo08	Not analysed	[2]MRGeo08

[1]ALS, [2]Jochum *et al.* (2005), [3]OREAS (2022a), [4]OREAS (2022c), [5]OREAS (2022d), [6]Geostats (2022) , [7]OREAS (2022b)

3.2 Titanite analysis

All titanite textural and geochemical data were collected in the Imaging and Analysis Centre (IAC) of the Natural History Museum. Titanite was analysed from Strontian, northern Chile (Chuquicamata and the Fortuna Complex), Cobre Panama, Oyu Tolgoi and from a global mineral separate sample suite provided by Rio Tinto. Crystals were firstly imaged, using either optical or scanning electron microscopy, before major and trace element compositions were determined by electron microprobe and laser ablation ICP-MS, respectively.

3.2.1 Identification of titanite and determination of mineral modal abundance and mineral associations

At the start of the study, optical microscopy was employed as a first step to identify titanite, as well as determine mineral associations. Titanite can be easily identified via conventional optical microscopy due to its characteristic shape in cross section, as well as its extremely high relief.

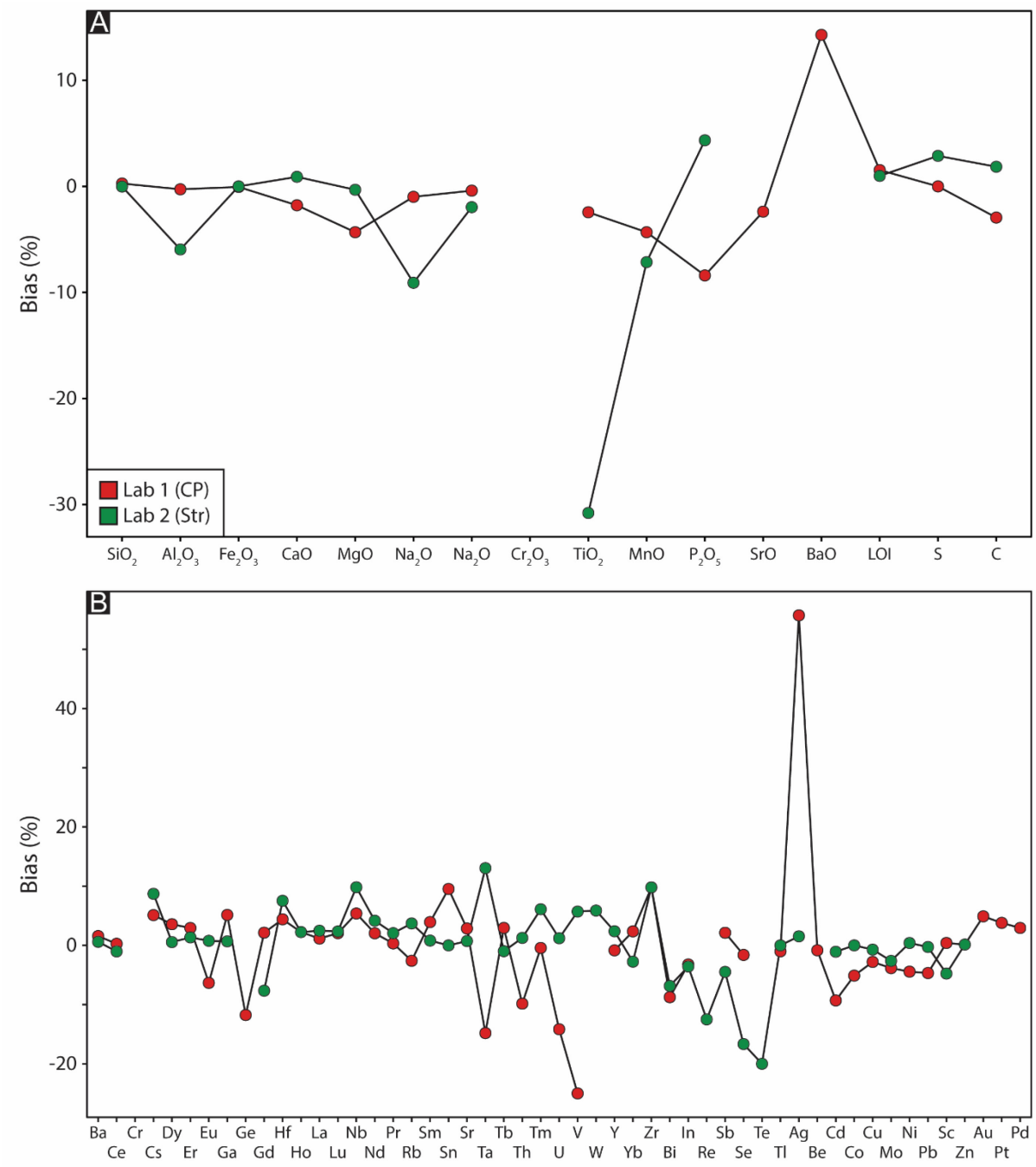


Figure 3.2. Percentage bias for whole-rock major element (**A.**) and trace element (**B.**) data. Bias calculated following analyses of certified reference materials. Bias is calculated for the different analytical runs, CP= Cobre Panama, Str= Strontian. Values for certified reference materials are from: (Jochum *et al.*, 2005).

3.2.2 Scanning electron microscopy (SEM)

Scanning electron microscopy was primarily employed to identify titanite large enough to be analysed by laser ablation (i.e. > 30 μm), as well as image intra-grain zonation, particularly in the backscattered electron mode (BSE). It was also used to determine the composition of mineral inclusions too small to identify using optical methods. SEM work was conducted using either a

Zeiss EVO SEM or using a Zeiss Ultra Plus SEM. SEM analysis was conducted with a beam current of 3-5 nA and accelerating voltage of 20 kV.

3.2.3 Automated scanning electron microscope (TESCAN TIMA)

The methods described above that were initially used for analysis of titanite were partly superseded following the acquisition of an automated scanning electron microscope, the TESCAN TIMA, at the Natural History Museum. The TIMA was able to quickly perform the same functions, in addition to easily quantifying modal abundances, determining percentages of mineral associations and generating element maps. The TIMA was operated with a beam current of ~14 nA and an accelerating voltage of 25 kV. It was set up in 'Modal Analysis' mode, which determines EDS spectra in a grid pattern. Spectra are subsequently matched to a mineral library, which was developed by modifying the in-built TIMA library to identify mineral compositions encountered during this study.

3.2.4 Electron probe microanalysis (EPMA)

Analysis of titanite via electron probe microanalysis (EPMA) was conducted using either a JEOL JXA-8530F or a Cameca SX100. All analyses were conducted using an accelerating voltage of 20 kV and beam current of 20 nA, with a spot size of 5 μm. Species analysed by EPMA were F, TiO_2, SiO_2, Nb_2O_5, Ce_2O_3, Cl, CaO, MnO, FeO, V_2O_5, Al_2O_3 (Appendix 2) using 30 seconds of on-peak and 15 seconds of background counting for all species except Cl (10 and 5, respectively). Calibration was performed according to details given in Table 3.3.

Table 3.3. EPMA conditions and average limit of detection (LOD) and analytical error (%) for titanite EPMA analysis (based on analysis of the OLT1 standard).

Species	Crystal	Line	Calibrant	Peak position (mm)	PHA mode	Background (upper, lower, slope)	Peak overlap correction	LOD (ppm)	Error (%)
F	LDE1 (1)	*Kα*	Topaz	84.376	DIFF	5, 5, 0	Ce, Fe	162	1.9
TiO_2	PETL (2)	*Kα*	Rutile	88.364	Int	1.5, 0, 1		78	0.13
SiO_2	PETL (2)	*Kα*	Wollastonite	228.258	Int	1.5, 0, 1		98	0.43
Nb_2O_5	PETL (2)	*Lα*	Niobium	183.400	Int	2, 2.5, 0		92	3.1
Ce_2O_3	PETL (2)	*Lα*	Cerium	82.266	Int	2, 0, -5.397	Ti	147	1.7
Cl	PETH (3)	*Kα*	Halite	151.421	Int	1.5, 1.772		30	95
CaO	PETH (3)	*Kα*	Wollastonite	107.445	Int	1.165, 1.391, 0		38	0.12
MnO	LIFL (4)	*Kα*	Manganese Titanium Oxide	146.11	Int	1.521, 0, -0.5		70	21
FeO	LIFL (4)	*Kα*	Hematite	134.605	Int	1.5, 0, -0.53	Mn	66	0.88
V_2O_5	LIFL (4)	*Kα*	Vanadinite	174.048	Int	5, 2.087, 0	Ti	89	7.9
Al_2O_3	TAPL (5)	*Kα*	Corundum	90.42	Int	2, 0, -4.79		54	0.37

At the time of writing, there are no published titanite major and trace element standards, due in part to the prevalence of chemical zonation. However, a titanite U-Pb dating standard known as OLT1 (Kennedy *et al.*, 2010) was kindly donated by Dr Allen Kennedy of Curtin University. The OLT1

standard is strongly zoned, although individual zones exhibit remarkably consistent concentrations when analysed by EPMA. Hence, repeat analysis of a single zone within the OLT1 standard was conducted to ensure data quality and track instrumental drift during and between analytical sessions (Appendix 3). Analytical precision for different species in the OLT1 standard was determined, with all showing an RSD of <7% except for MnO, V_2O_5 and Cl (Fig. 3.3). Chlorine concentrations in OLT1 are close to the limit of detection, hence the large RSD. Manganese and vanadium as determined by EPMA show a large RSD and hence only the LA-ICP-MS results are reported. Average limits of detection and analytical errors are given in Table 3.3, where analytical error is given as 2σ of the number of counts in an analysis peak.

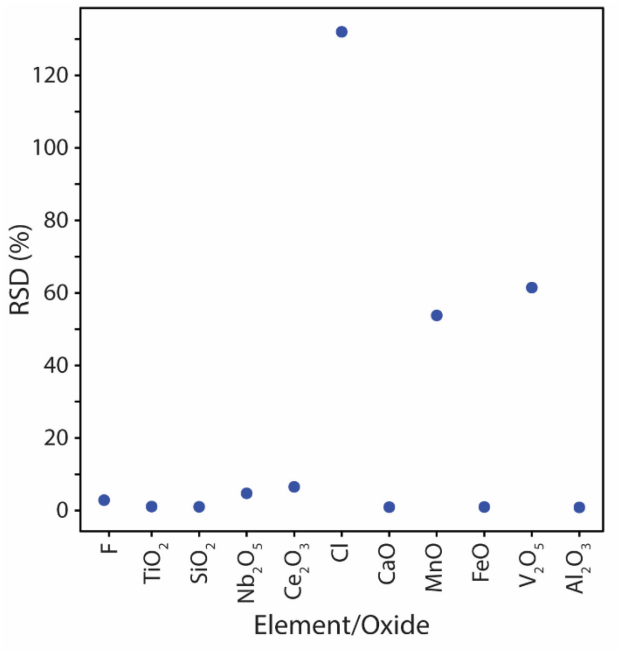


Figure 3.3. RSD (%) of OLT1 titanite standard by EPMA for different species.

3.2.5 Laser ablation inductively coupled plasma mass spectrometry (LA-ICP-MS)

Trace element concentrations of titanite were determined via laser ablation ICP-MS (Appendix 2), using either an ESI New Wave Research 193 nm excimer laser was coupled to an Agilent 7700x quadrupole ICP-MS, or using a Teledyne Iridia 193 nm laser ablation system coupled to an Agilent 8900 ICP-QQQ-MS. The laser was operated with a repetition rate of 10 Hz and a fluence of 3.5 (ESI) to 2 (Teledyne) J cm^{-2}. Initially, a total of 39 isotopes were analysed: ^{23}Na, ^{24}Mg, ^{27}Al, ^{29}Si, ^{31}P, ^{43}Ca, ^{45}Sc, ^{49}Ti, ^{51}V, ^{52}Cr, ^{55}Mn, ^{57}Fe, ^{66}Zn, ^{88}Sr, ^{89}Y, ^{90}Zr, ^{93}Nb, ^{118}Sn, ^{137}Ba, ^{139}La, ^{140}Ce, ^{141}Pr, ^{146}Nd, ^{147}Sm, ^{153}Eu, ^{157}Gd, ^{159}Tb, ^{163}Dy, ^{165}Ho, ^{166}Er, ^{169}Tm, ^{172}Yb, ^{175}Lu, ^{178}Hf, ^{181}Ta, ^{206}Pb, ^{208}Pb, ^{232}Th, ^{238}U. Following the first run, the element list was optimised to allow for the determination of titanite U-Pb ages, with ^{207}Pb also analysed. A lower fluence was utilised where trace elements

and U-Pb isotopes were determined simultaneously, as this has been shown to decrease down-hole fractionation of U-Pb isotopes (McFarlane, 2016).

Calcium was employed as the internal standard for quantification of LA-ICP-MS results, using a stoichiometric value of 19.5 wt.%. Analysis of many titanite grains via EPMA revealed that Ca contents of titanite do not significantly vary from 19.5 wt. %, with an RSD (3.3%) that is similar to typical analytical precision for elements determined by LA-ICP-MS (Table 3.4). NIST-610 was used as the primary standard and NIST-612 was used as the secondary external reference standard. Mineral ablation intervals were carefully selected to avoid contamination by mineral inclusions, with data reduction conducted using the Iolite v 3.61 software (Paton *et al.*, 2011). Dwell times, as well as average limits of detection and analytical error are shown in Table 3.4.

Comparing determined concentrations of elements that were analysed by both EPMA and LA-ICP-MS provides a check on the accuracy of the measurements (Fig. 3.4). Concentrations of Al, Mn, Nb and Ce, as determined by EPMA and LA-ICP-MS, strongly correlate. A linear regression was fitted to each of these comparisons; these show a near 1:1 correlation, in addition to r^2 values of between 0.85 and 0.94.

Table 3.4. LA ICP-MS dwell times, average LOD and analytical error (%) for titanite (based on 72 analyses of OLT-1 titanite standard).

Species	Dwell time (ms)	LOD (ppm)	Error	Species	Dwell time (ms)	LOD (ppm)	Error (%)
Na	2	47.2	14.9%	Ce	5	0.06	2.84%
Mg	10	1.23	2.56%	Pr	5	0.05	2.88%
Al	10	2.88	2.19%	Nd	5	0.25	2.89%
Si	17	1273	3.69%	Sm	5	0.32	3.42%
P	2	182	37.9%	Eu	5	0.07	3.67%
Ca	10	-	-	Gd	5	0.28	3.63%
Sc	10	0.63	14.0%	Tb	5	0.05	3.67%
Ti	2	6.58	3.20%	Dy	5	0.16	3.45%
V	10	0.35	2.41%	Ho	5	0.06	3.64%
Cr	10	4.90	21.7%	Er	5	0.16	3.70%
Mn	10	3.75	2.86%	Tm	5	0.05	4.59%
Fe	10	30.8	2.66%	Yb	5	0.23	4.29%
Zn	10	1.24	45.4%	Lu	5	0.04	5.44%
Sr	10	0.05	2.83%	Hf	20	0.08	3.02%
Y	10	0.10	2.60%	Ta	10	0.04	2.84%
Zr	20	0.06	2.38%	^{206}Pb	125	0.14	3.19%
Nb	10	0.07	2.57%	^{207}Pb	125	0.10	3.92%
Sn	10	0.57	4.30%	^{208}Pb	20	0.13	3.87%
Ba	10	0.32	56.1%	Th	10	0.06	2.92%
La	5	0.06	2.89%	U	125	0.05	2.72%

The accuracy of the laser ablation ICP-MS method was determined by repeated analysis of the certified reference material NIST-612, with NIST-610 used as the primary standard (Appendix 3). Ideally, secondary standards should be matrix matched (Günther & Hattendorf, 2005), although this was precluded by trace element heterogeneity in the OLT-1 titanite standard. Percentage bias

was ± 5% for most elements, with only Mg and Fe calculated to show greater than ± 10% bias (Fig. 3.5A). Phosphorous was also analysed although it cannot be determined quantitatively by this method. It was only used to identify contamination with phosphate minerals during signal processing and is not reported. The extreme overestimation of Fe using NIST-612 is attributed in part to the presence of an isobaric interference, likely ArOH (Hirata & Ohno, 2001). Concentrations of Mg and Fe determined by LA-ICP-MS are consequently not reported but their inclusion was still useful in order to identify contamination of LA-ICP-MS signals by other mineral phases. Titanite Fe contents as determined by EPMA, are however reported.

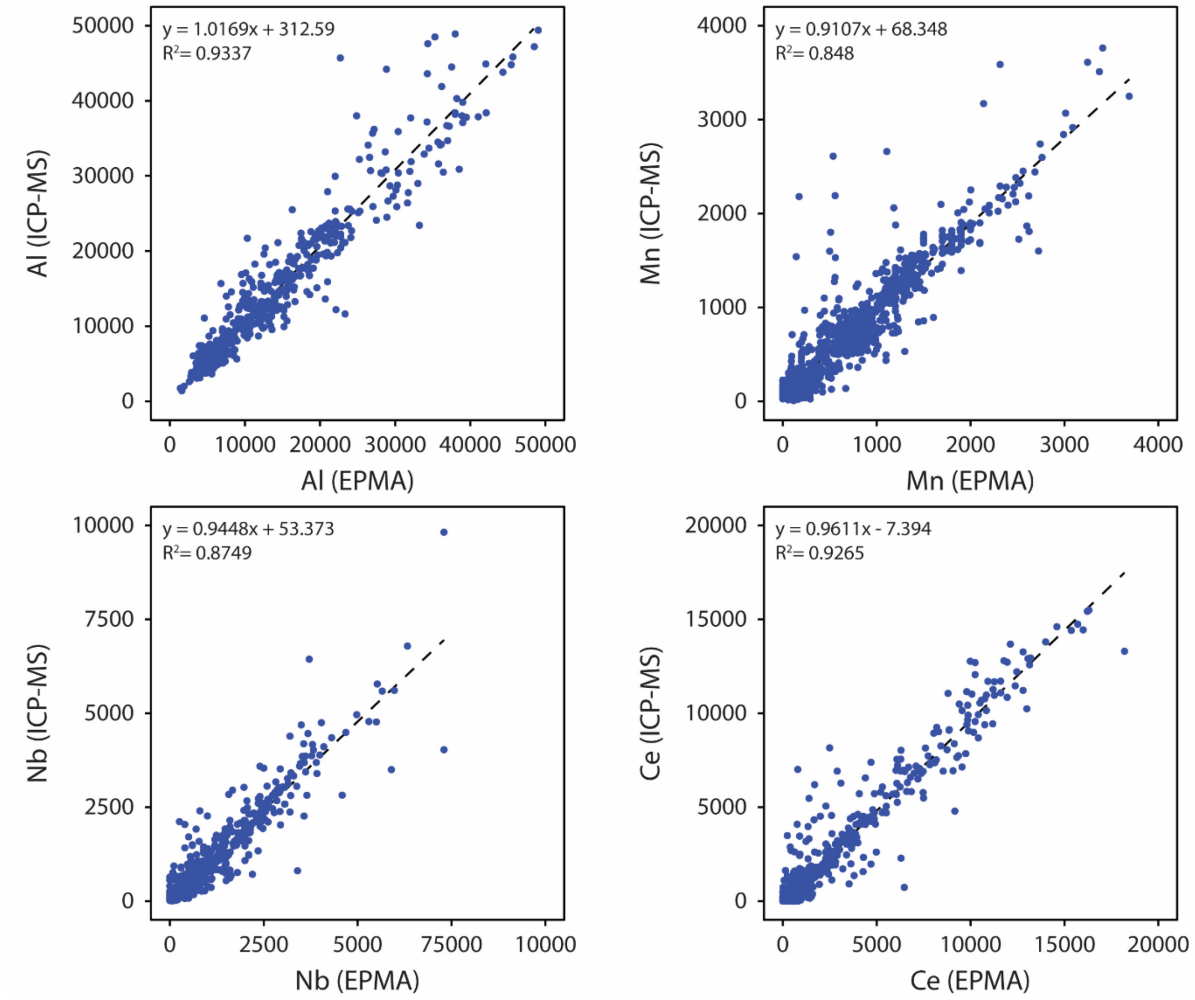


Figure 3.4. Comparison between laser-ablation (ICP-MS) and EPMA data for several elements in titanite. All concentrations are in ppm. Average 2σ uncertainty is smaller than the symbol size.

Where possible, analysis of titanite via laser ablation was conducted using a 30 µm spot size. However, small crystal size and intimate association with other mineral phases meant that applying a 30 µm spot size for all grains was not possible. In such circumstances, 20 or 15 µm spot sizes were used, in order to minimise contamination and ensure clean analyses. Accuracy was also estimated for certified reference material NIST-612 at both 30 and 15 µm spot sizes, to ensure that

reducing spot size did not compromise the data (Fig. 3.5B). It is worth noting, however, that reducing spot size did result in lower limits of detection.

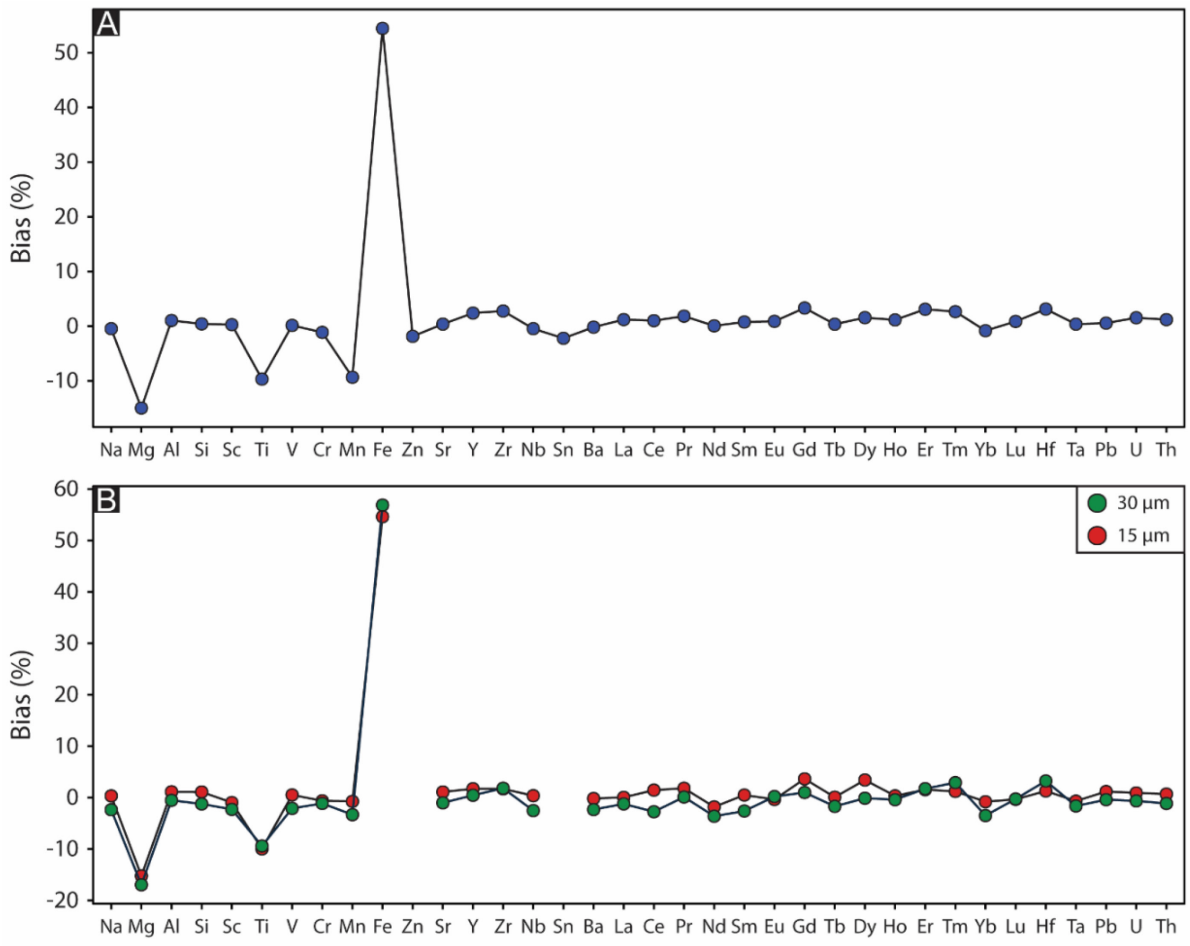


Figure 3.5. Percentage bias calculated using repeated LA-ICP-MS analysis of secondary standard NIST-612, using NIST-610 as the primary standard. Data from elements which show relatively high bias (±10%) are not reported (e.g. Mg and Fe). Additionally, P was also analysed to identify potential contamination by phosphate minerals (e.g. apatite) but was almost always below LOD and so is not displayed here. **A.** Percentage bias of all analyses. **B.** Comparison of percentage bias for analyses which used 30 and 15 µm spot sizes during the same analytical run (Cobre Panama, May 2021).

3.2.6 Geochronology

Simultaneous determination of trace elements and U-Pb isotopes in titanite was conducted by laser ablation ICP-MS according to the methodology outlined above (Appendix 2). In this study, U-Pb dating was conducted by LA-ICP-MS which allows for a large sample throughput and textural information to be retained, compared to the more precise ID-TIMS method (Schoene, 2014). Characterisation of trace elements and U-Pb isotopes simultaneously has been demonstrated for other minerals (Yuan *et al.*, 2004; Yuan *et al.*, 2008; Zeiger *et al.*, 2015), but as yet is rarely done for titanite *in-situ* (Olierook *et al.*, 2019), with studies tending to focus on either trace elements or U-Pb isotopes (Kontonikas-Charos *et al.*, 2019; Hart-Madigan *et al.*, 2020). Determination of both U-Pb isotopes and trace elements is advantageous as it allows for the identification of different

titanite populations in a temporal context but has the potential drawback that the quality of the geochronological data may be compromised.

The Khan titanite standard (522.2 ± 2.2 Ma; Heaman, 2009) was employed as the primary dating standard, with the Fish Canyon (28.395 ± 0.049 Ma; Schmitz & Bowring, 2001) and OLT1 (1014±2.0 Ma; Kennedy *et al.*, 2010) standards used as secondary dating standards in order to assess accuracy and precision. In addition to radiogenic lead, titanite often incorporates initial or common lead, necessitating the estimation of the initial lead composition to permit dating. Approaches to constrain common lead include analysing compositions of low-U phases e.g. feldspar, or by use of a bulk-Pb evolution model (Stacey & Kramers, 1975). For unknowns, linear regression in $^{206}Pb/^{238}U$ vs $^{207}Pb/^{235}U$ or Tera-Wasserburg diagrams (Tera & Wasserburg, 1972) can be utilised, from which both initial lead composition and the true age can be deduced (Aleinikoff *et al.*, 2002).

Isotopic data were plotted in IsoplotR (Vermeesch, 2018), which was used to visualise data and filter contaminated analyses. Calculations of initial lead composition, crystallisation age (based on the Tera-Wasserburg lower intercept), mean square of weighted deviates (MSWD) and uncertainty were all made in IsoplotR. The error presented below and in subsequent chapters comprises both the uncertainty associated with the regression plus an additional 2% propagated uncertainty, which may account for any systematic biases (Horstwood *et al.*, 2016).

Secondary standards FCT and OLT-1 were analysed during each run to monitor data quality (Appendix 3). The OLT-1 standard was acquired during 2020 and hence no in-house data are available prior to that. For the Fish Canyon (FCT) standard, a common lead composition ($^{207}Pb/^{206}Pb$) of 0.84 was applied based on repeated analysis of K-feldspar (Schmitz & Bowring, 2001), whereas a value of 0.91 was applied for the OLT-1 standard (Chen & Zheng, 2015). Calculated ages for the FCT standard are within 2σ uncertainty of the published ID-TIMS age (Schmitz & Bowring, 2001) apart from the first analytical session, which returned an older age (Fig. 3.6A). For the OLT-1 standard, minor variation is observed with respect to calculated ages. However, this standard displayed visible zonation when viewed in SEM-BSE mode, which may indicate variable isotopic ratios in different zones, and hence variable calculated ages. Nevertheless, all analytical runs except the March 2022 run were within 2σ uncertainty (Fig. 3.6B). During the March 2022 run, titanite from a global Rio Tinto sample suite was analysed, and as such U-Pb data were not utilised anyway.

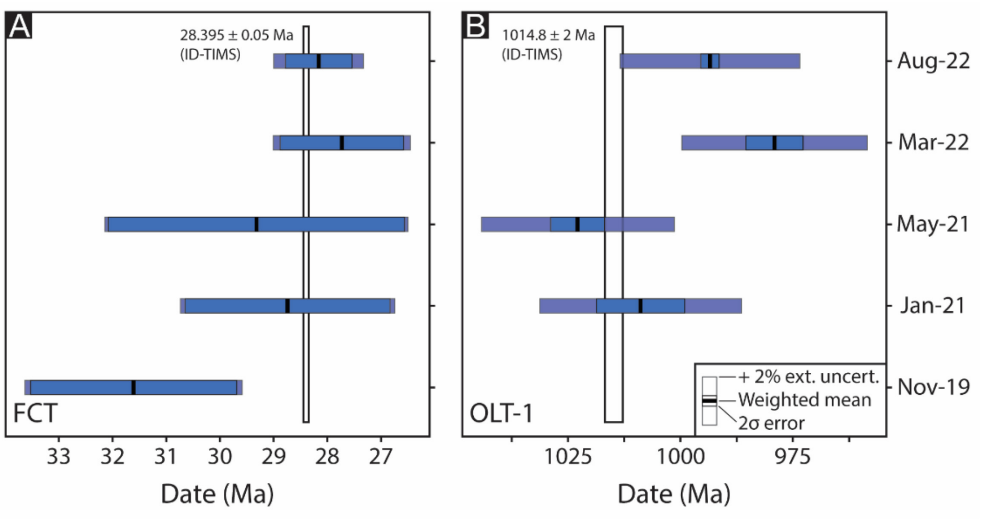


Figure 3.6. Titanite lower intercept ages, 2σ error and an additional propagated 2% external uncertainty for secondary standards Fish Canyon (FCT; A.) and Grenville Skarn (OLT-1; B.). The OLT-1 standard was acquired in 2020, and hence no data are available for the November 2019 run. Also indicated are high precision ID-TIMS ages from Schmitz and Bowring (2001) and Kennedy *et al.* (2010) respectively.

Chapter 4. The Strontian Intrusive Complex: petrography, thermobarometry and the influence of titanite on residual melt chemistry

This chapter is a modified version of a paper that was published in Journal of Petrology in September 2023 titled: **The Strontian Intrusive Complex: Petrography, Thermobarometry and the Influence of Titanite on Residual Melt Chemistry,** available at: https://doi.org/10.1093/petrology/egad059. This work is licensed under a Creative Commons Attribution 4.0 License, which permits use, sharing, adaptation, distribution and reproduction in any medium or format, as long as credit is given to the original author(s) and the source.

4.1 Introduction

The late-stage near-solidus evolution of large granitoid magma systems exerts an important control in determining the final fate of upper crustal magma bodies, including whether eruption or plutonism occurs (Annen *et al.*, 2023), or whether the magma body can concentrate economically valuable elements to generate ore bodies. One approach to understanding the late-stage evolution of these systems is to study the chemical composition of mineral phases, which may provide a record of residual melt evolution. *In-situ* crystallisation of the rock mineral assemblage may drive the residual melt chemistry away from that of the bulk magma, generating more exotic melt compositions which are inherited by subsequent mineral phases.

Of the minerals which commonly crystallise from intermediate to silicic calc-alkaline magmas, few are likely to exert such a strong control on residual melt rare earth element (REE) and high field strength element (HFSE) compositions as titanite, owing to its extremely high partition coefficients for both groups of elements (Bachmann *et al.*, 2005; Colombini *et al.*, 2011). These high partition coefficients, when coupled with the late-stage saturation of titanite (Frost *et al.*, 2001; Hayden *et al.*, 2008; Colombini *et al.*, 2011; Ayers *et al.*, 2022) and its relative abundance as an accessory phase (modal 0.5-2% in many granitoids; Gromet & Silver, 1983; Sawka, 1988; Xiao *et al.*, 2020), mean that the onset of titanite crystallisation should represent a significant event in the petrogenesis of hydrous, oxidised magmas which crystallise to near-solidus temperatures. Minerals that saturate prior to titanite and continue to concurrently crystallise, and melts which have been extracted from titanite-bearing magmas should record this event in their trace element compositions. Indeed, the effect of titanite crystallisation on some other accessory phases has been well demonstrated, especially zircon (Wotzlaw *et al.*, 2013; Loader *et al.*, 2017; Szymanowski *et al.*, 2017), in which 'false positive' porphyry signatures could be generated by titanite co-crystallisation. Despite this, the influence of titanite on the trace element composition of other

mineral phases is less well attested but has been suggested for amphibole (Chelle-Michou *et al.*, 2015) and even subsequent titanite crystallisation (Colombini *et al.*, 2011; Pamukcu *et al.*, 2013; Olson *et al.*, 2017). In this chapter, the impact of titanite crystallisation on late-stage residual melt chemistry is assessed using rocks from the Strontian Intrusive Complex, Scotland; with potential implications for porphyry prospectivity and magma provenance discussed.

4.2 Background geology

The Strontian Intrusive Complex is a composite high-K calc-alkaline granitoid pluton, with associated mafic enclaves and cross-cutting dykes, that was emplaced into metasedimentary and meta-igneous rocks of the Moine Supergroup during the late Caledonian Orogeny (Hutton, 1988). The pluton represents one of the late- to post-subduction "Newer Granites" (Read, 1961), and is part of the Argyll and Northern Highlands Suite (formerly the Argyll Suite; Stephens & Halliday, 1984). Granites of the Argyll and Northern Highlands Suite are characterised by high Ba, Sr and alkali (Na2O and K2O) contents, and high La/Yb ratios (Fowler & Henney, 1996), meaning that Strontian, like many of the granites, exhibits several geochemical indicators of a porphyry magma (Richards, 2011; Loucks, 2014). In the British and Irish Caledonides, these high Ba-Sr granites are often associated with stocks and dykes of ultramafic to intermediate composition, which exhibit many of the same geochemical characteristics (Wright & Bowes, 1979; Fowler & Henney, 1996). Recent studies have proposed that the unusual association of these rocks (historically referred to as 'appinites'; Bailey & Maufe, 1916) with the Newer Granites may be linked to slab delamination (Atherton & Ghani, 2002; Fowler *et al.*, 2008). Liquids with similar compositions to the Newer Granites could be generated by fluid fluxed melting of the granulitic lower crust, with the appinites acting as water donors (Castro, 2020) and with the timing of fluid fluxing controlling the volume and geochemical affinity of the subsequent granitic magmas (Brown *et al.*, 2008).

The pluton comprises three distinct concentric units (Fig. 4.1) with the outer two units belonging to the Loch Sunart quartz monzodiorite, and the innermost unit belonging to the Glensanda granodiorite. The Loch Sunart quartz monzodiorite (QMD) comprises two units that show a gradational contact over several metres; the outer, equigranular quartz monzodiorite (QMD_{Eq}; previously referred to as the tonalite) and the inner porphyritic quartz monzodiorite (QMD_{P}; previously referred to as the granodiorite), the latter of which contains conspicuous phenocrysts of plagioclase and K-feldspar. U-Pb dating of zircon and titanite from the equigranular quartz monzodiorite yielded overlapping crystallisation ages of 425 ± 3 Ma and 423 ± 3 Ma respectively (Rogers & Dunning, 1991). The Glensanda granodiorite (Grd; previously referred to

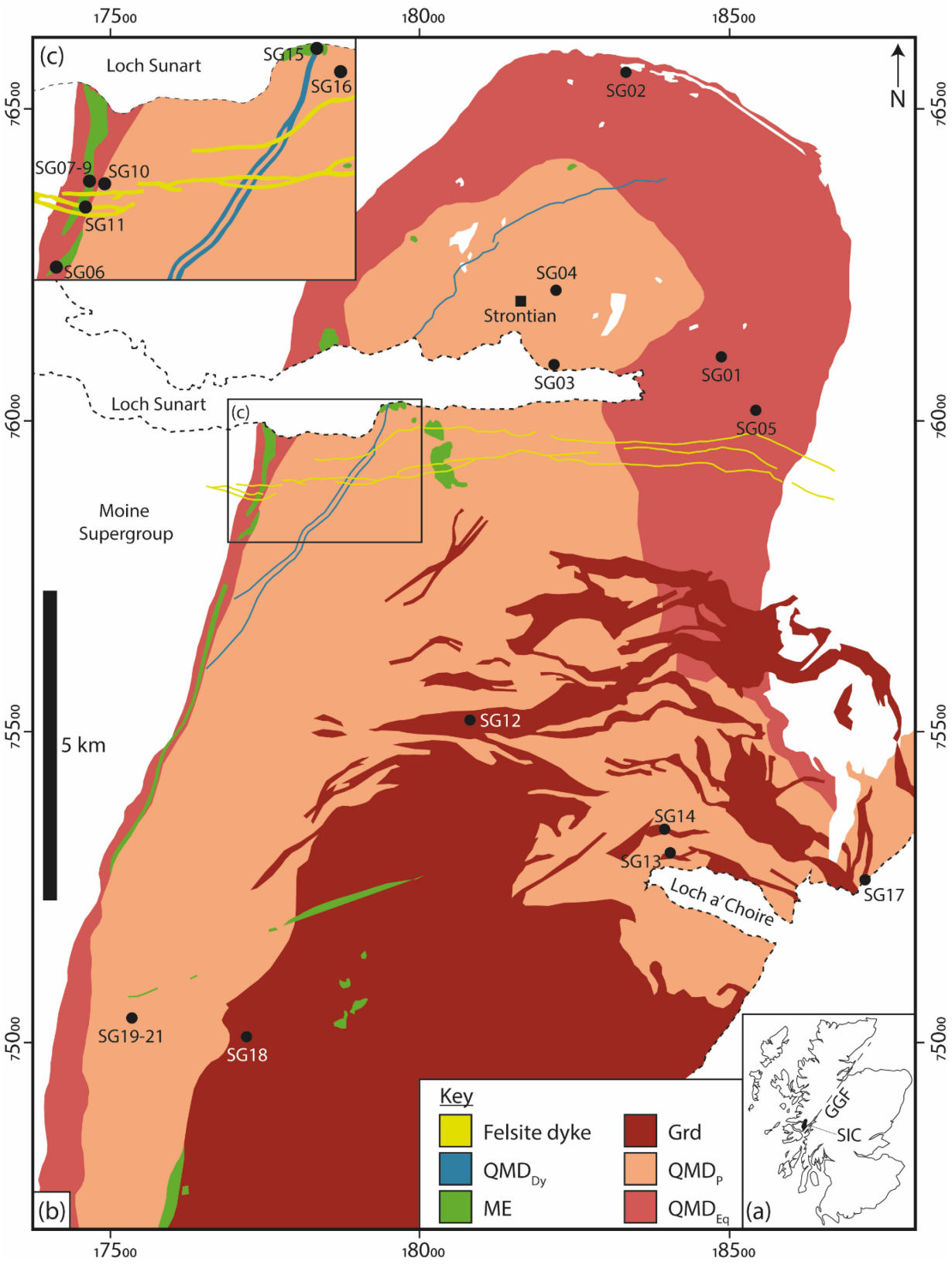


Figure 4.1. Geology of the Strontian Intrusive Complex. **A.** Locator map of the Strontian Intrusive Complex (SIC) in Scotland. **B.** Simplified geological map, including sample locations. **C.** Inset showing sampling locations in an area of high sampling density. QMD_{Dy} =quartz monzodiorite dyke; ME= Mafic enclave; Grd= Granodiorite; QMD_P= Porphyritic quartz monzodiorite; QMD_{Eq}= Equigranular quartz monzodiorite. Modified from Birt (2019).

as the biotite granite) cross-cuts the older quartz monzodiorite as sheeted, anastomosing dykes in the central part of the pluton, and as a coherent body in the southern part (Fig. 4.1). The granodiorite has been dated at 418 ± 1 Ma (Paterson *et al.*, 1993), however it is assumed to be only slightly younger than the quartz monzodiorite based on field relationships and geochemical similarity. Hutton (1988) argued that emplacement of the granodiorite was controlled by a northerly-trending dextral splay of the Great Glen Fault, providing a relatively narrow time constraint on movement along the Great Glen Fault.

A variety of mafic rocks are found in association with the pluton, either as enclaves within the host granitoids or as discrete bodies, with the latter displaying similar chemistries and textures to appinites (Stephens, 2001). Mafic enclaves (ME) show a variety of intimate mingling textures with the host granitoids (Fig. 4.2), implying that that they were broadly comagmatic. The quartz monzodiorite is also cut by a series of quartz monzodiorite dykes (QMD_{Dy}; Fig. 4.1) that display similar textures to the host. The entire intrusive complex is cut by felsic igneous intrusions emplaced during the Permian and Palaeogene, which are not discussed further.

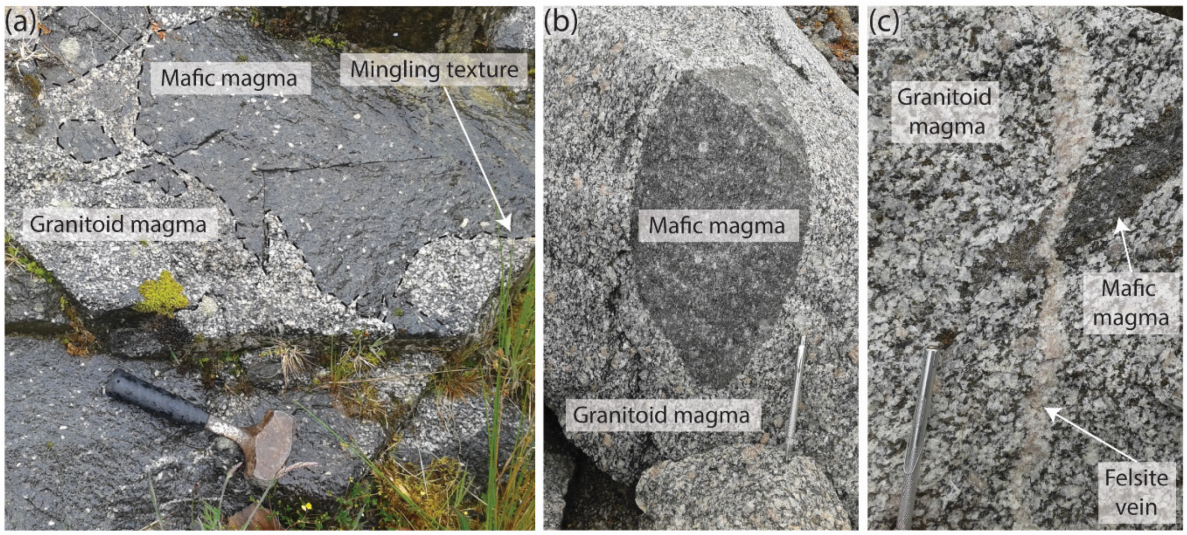


Figure 4.2. Field relationships of mafic enclaves in host granitoids. **A.** Mingling mafic and granitoid magmas, showing a cuspate contact. **B.** Ovoid mafic enclave within granitoid. **C.** Late vein cutting both the granitoid and a mafic enclave.

4.3 Samples and methods

Data presented here comes from 21 samples which were collected in 2018 to represent the lithological variation in the main intrusive units (Table 4.1). To place titanite data into context, whole-rock and amphibole compositions from the same samples are also presented.

Table 4.1. Sample information, analytical techniques and number of analyses.

Sample	Unit	Grid reference	TIMA	No. of titanite analyses	Amphibole	Whole-rock
SG18MB01	QMD_{Eq}	NM8482 6094			Y	Y
SG18MB02	QMD_{Eq}	NM8329 6554				Y
SG18MB03	QMD_{P}	NM8211 6076				Y
SG18MB04	QMD_{P}	NM8213 6202				Y
SG18MB05	QMD_{Eq}	NM8541 6008				Y
SG18MB06	ME	NM7724 5820				Y
SG18MB07	ME	NM7747 5898	Y		Y	Y
SG18MB08	ME	NM7747 5898				Y
SG18MB09	QMD_{Eq}	NM7747 5898	Y		Y	Y
SG18MB10	QMD_{P}	NM7752 5881	Y		Y	Y
SG18MB11	Felsite dyke	NM7749 5867				Y
SG18MB12	Grd	NM8081 5513				Y
SG18MB13	Grd	NM8407 5324	Y			Y
SG18MB14	Grd	NM8397 5340				Y
SG18MB15	QMD_{Dy}	NM7965 6022	Y		Y	Y
SG18MB16	ME_{Sho}	NM7985 6001	Y		Y	Y
SG18MB17	Grd	NM8721 5252				Y
SG18MB18	Grd	NM7715 5009				Y
SG18MB19	QMD_{P}	NM7532 5035	Y		Y	Y
SG18MB20	ME	NM7532 5035				Y
SG18MB21	ME	NM7532 5035	Y		Y	Y

Amphibole major element compositions were determined via wavelength dispersive spectroscopy using a JEOL JXA-8530F electron microprobe, operated with a beam current of 10 nA, a beam size of 1 mm and an accelerating voltage of 15 kV. Trace element spot analysis was conducted in the LODE Laboratory (IAC) using an ESI New Wave Research 193 nm excimer laser coupled to an Agilent 7700x quadrupole ICP-MS. The laser was operated with a repetition rate of 10 Hz, a fluence of 3.5 J cm^{-2} and a spot size of 30 μm for titanite and 35 μm for amphibole. Calcium was employed as the internal standard element with a value of 8.5 wt.% (based on microprobe analyses) for amphibole and a stoichiometric value of 19.5 wt.% for titanite. NIST-612 and NIST-610 were used as the primary standards for amphibole and titanite respectively and GSD-1G was used as the secondary external reference standard. Data reduction was conducted using an in-house Excel macro spreadsheet, during which mineral ablation intervals were selected to avoid contamination by mineral inclusions.

A representative set of amphibole and titanite crystals was selected for trace element mapping by LA-ICP-MS. Mapping was carried out using a 193 nm Teledyne Iridia laser ablation system coupled to an Agilent 8900 ICP-QQQ-MS. The selection of acquisition parameters, (e.g. repetition rate, scan speed and dwell time selection) are detailed in Petrone *et al.* (2022) and are selected following the protocols of Van Malderen *et al.* (2018), van Elteren *et al.* (2020) and Šala *et al.* (2021).

Amphibole mapping experiments were carried out using a 5 μm square beam, a fluence of 3.5 Jcm^{-2}, a repetition rate of 250 Hz and a scan speed of 125 μms^{-1}, corresponding to 10 laser pulses per 5 μm pixel (dosage). Titanite maps were constructed using a smaller spot size (3 μm square), a repetition rate of 300 Hz and a scan speed of 75 μms^{-1} corresponding to a dosage of 12. Isotopes were measured in no-gas mode, corresponding to a total ICP-MS sweep cycle of 40 ms (including settling time) for both amphibole and titanite. Isotopes measured in amphibole were: 43Ca (4.1 ms); 88Sr , 89Y, 93Nb (1.5 ms); 147Sm (3.3 ms); 153Eu, 157Gd (3.5 ms); 181Ta (4.5 ms). A similar set of isotopes were measured in titanite with the corresponding dwell times 43Ca (7.5 ms); 88Sr , 89Y (1 ms); 90Zr (2 ms); 93Nb (1 ms); 147Sm (1.2 ms); 153Eu, 157Gd, (1 ms); 181Ta (1.1 ms); 238U (1.6 ms). Compositional maps were gathered as a single acquisition in the ICP-MS for durations of between 1 and 4 hours. A gas blank (20 s) was gathered between each sample. NIST SRM 612 and NIST SRM 610 (Jochum *et al.*, 2011) was measured as a raster every four unknowns for calibration and drift correction for amphibole and titanite respectively.

Image processing and quantification were carried out using HDIP (v. 1.6). After synchronising the timestamps of the laser with the ICP-MS signal, the background of each isotope was calculated during periods the laser was not firing and subtracted from each signal. Amphibole and titanite grains were isolated from each image based on counts of 43Ca, using the labelled segments tool in HDIP. Trace element concentrations were calculated on a pixel-by-pixel basis using the sum normalisation tool in HDIP using Ca concentrations as described above for the internal standard. Compositional profiles were extracted from the calibrated maps using the "Extract Path" tool in HDIP.

4.4 Results

4.4.1 Petrography

Petrographic descriptions of intrusive rocks from Strontian have been reported previously (e.g. Sabine, 1962; and references therein) and are summarised here with the addition of new observations as appropriate (Table 4.2). All felsic units contain plagioclase, quartz, K-feldspar and biotite, with or without amphibole, as major phases. The three members of the pluton can be differentiated based on mineral proportions and grain size distribution. The equigranular quartz monzodiorite comprises 2-3 mm plagioclase, K-feldspar and quartz grains, with some plagioclase phenocrysts up to 15 mm present towards the gradational contact with the porphyritic quartz monzodiorite (e.g. SG09). In addition to these plagioclase phenocrysts, the porphyritic quartz monzodiorite contains up to 15 mm phenocrysts of microperthitic K-feldspar, allowing it to be

easily distinguished from its equigranular equivalent. Both varieties contain approximately 10-15% biotite and amphibole. In contrast to the quartz monzodiorite, phenocrysts of plagioclase are rare in the granodiorite, which is instead dominated by K-feldspar phenocrysts up to 15 mm in size in a groundmass of quartz, plagioclase and K-feldspars (~2.5 mm in size). Biotite accounts for <5 modal %, and amphibole is rare. The quartz monzodiorite dyke sample (SG15) comprises a similar modal mineralogy, albeit with a higher proportion of mafic minerals (20% amphibole and biotite). This sample consists of a fine-grained groundmass (0.5-1 mm) of quartz, plagioclase, K-feldspar, biotite, and amphibole, with phenocrysts of plagioclase approximately 6 mm in size. Mafic enclaves show considerable textural and mineralogical variability, although most can be classified as monzodiorites and quartz monzonites. These rocks comprise plagioclase, amphibole and biotite in varying proportions, with the mafic minerals comprising up to half of the assemblage (e.g. SG07). K-feldspar and quartz are typically minor phases, although sample SG16 (ME_{Sho}) contains a modest proportion of K-feldspar (15%).

Table 4.2. Mineral modal abundances as estimated by automated SEM, or [1]CIPW norm.

		Mineral modal abundances (%)								
Sample	Unit	Am	Ap[1]	Bt	Kfs	Mag	Qtz	Plg	Ttn	Zrn[1]
SG18MB07	ME	28.4	0.93	18.4	1.60	0.10	2.71	39.8	0.79	0.03
SG18MB09	QMD_{Eq}	5.81	0.83	10.6	6.03	0.04	8.06	65.8	0.87	0.04
SG18MB10	QMD_{P}	4.34	0.59	4.50	19.2	0.07	15.78	53.7	0.71	0.03
SG18MB13	Grd	0.49	0.27	1.44	28.92	0.16	25.67	40.7	0.25	0.02
SG18MB15	QMD_{Dy}	9.11	0.60	8.69	11.2	0.09	17.39	51.0	1.00	0.03
SG18MB16	ME_{Sho}	37.4	2.35	15.6	15.4	0.03	0.70	22.3	2.63	0.04
SG18MB19	QMD_{P}	4.41	0.62	9.13	14.4	0.32	10.97	57.6	0.90	0.03
SG18MB21	ME	20.1	1.52	31.0	5.52	0.49	18.19	17.1	3.27	0.06

Apatite, Fe-Ti oxides (magnetite and ilmenite ± rutile symplectites), titanite and zircon are ubiquitous. Apatite and zircon show variable modal abundances of 0.27 to 2.4 % and 0.02 to 0.06% (as estimated by CIPW norm), respectively, with lower abundances in the granodiorite (Table 4.2). In all samples, apatite is closely associated with mafic minerals. Zircon is predominantly included within biotite and more rarely in amphibole, titanite, plagioclase and K-feldspar. Trace sulphides (dominantly pyrite, with subordinate chalcopyrite and pyrrhotite) are found in the mafic enclaves and the quartz monzodiorite dyke, and in one equigranular quartz monzodiorite sample (SG01). These sulphides typically occur as fine-grained disseminations associated with mafic minerals and can also be found as larger blebs up to 2 mm in length.

Amphibole

Amphibole is found in all lithologies except the granodiorite, in which it is absent or only accounts for a small fraction of the assemblage (e.g. ~0.5 % in sample SG13). Amphibole can be divided into two textural types: small, subhedral grains forming polycrystalline aggregates, hereafter

referred to as ‘clots’, between 1 and 5 mm in diameter (Fig. 4.3A; see also Stephens, 2001); and larger euhedral to subhedral grains ~1 mm in size (Fig. 4.3B). The amphibole clots are most commonly found in the mafic enclaves but are occasionally found in the granitoids, whereas the euhedral amphiboles are predominantly found in the granitoids and are rarer in the mafic enclaves (e.g. SG07).

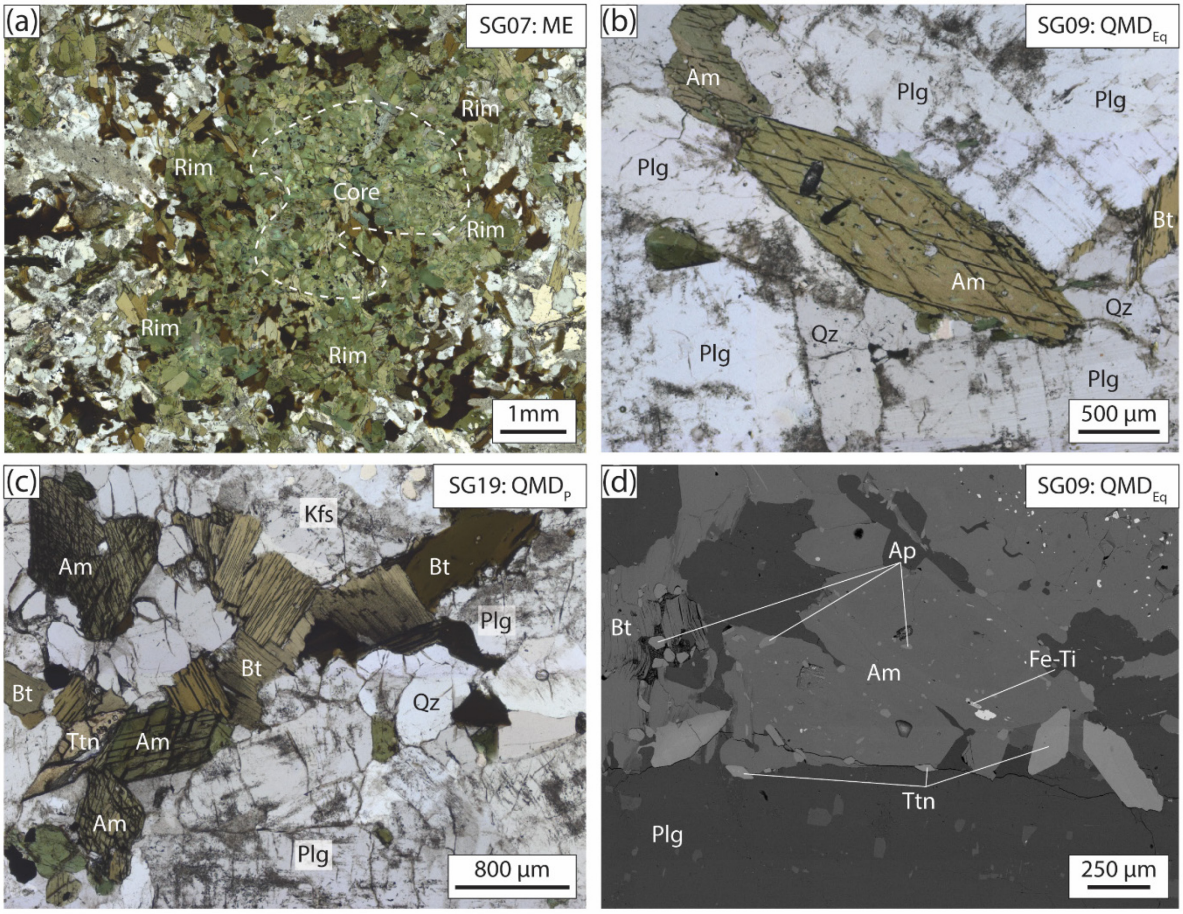


Figure 4.3. Transmitted light photomicrographs and SEM backscattered electron images of amphibole, showing a range of crystal habits and mineral inclusions. **A.** Amphibole clot showing core to rim zonation with light green granoblastic amphibole in the core and darker amphibole and biotite around the rim. **B.** Large, euhedral amphibole containing inclusions of apatite and Fe-Ti oxides. **C.** Common association of amphibole with biotite and titanite. **D.** Apatite and Fe-Ti oxide inclusions in amphibole and biotite. Titanite is associated with the rims of the amphibole crystals. Ap = apatite; Bt = biotite; Fe-Ti = Fe-Ti oxide; Am = amphibole; Kfs= K-feldspar; Plg= plagioclase; Qz= quartz; Ttn= titanite.

The amphibole clots are typically zoned, comprising a core of light green granoblastic grains ~100 µm in size, which grade outward to a zone of larger ~200-300 µm grains of intergrown darker green amphibole and biotite (Fig. 4.3A). In addition, magnetite, apatite and occasionally sulphides are found disseminated throughout the clots. These amphibole clots have previously been suggested to represent re-equilibrated restitic clinopyroxene (Stephens, 2001).

The euhedral to subhedral amphibole grains are either isolated (Fig. 4.3B), or form aggregates with biotite and accessory phases (especially titanite and apatite) that are texturally

distinct from the polycrystalline clots (Fig. 4.3C). In the granitoids, euhedral amphiboles comprise up to 10% of the rock and are mostly between 0.5 and 1.5 mm in size. The mafic enclaves and quartz monzodiorite dyke contain a greater proportion of amphibole, up to ~35%, both as clots and as large euhedral grains up to 5 mm in length. Apatite is the most common mineral inclusion in amphibole, with subordinate Fe-Ti oxides and plagioclase inclusions (Fig. 4.3D). Titanite is rarely wholly included in amphibole but is frequently intergrown with amphibole rims (Figs. 4.3C and D).

Titanite

Titanite is present in all lithologies but is rare in the granodiorite (sample SG13 only), with modal abundances generally between 0.2% and 1% and crystals ranging from 0.05 to 1.5 mm in length (Table 4.2). Generally, titanites are more euhedral and larger in the granitoids and are subhedral to anhedral and smaller in the mafic rocks. Secondary fine-grained overgrowths of titanite (~10 μm) are sometimes found where the margins of primary titanite grains are in contact with chloritized biotite and magnetite (Figs. 4.4A and B). Backscattered electron (BSE) images of titanite grains reveal that zoning is ubiquitous (Fig. 4.4), with sector (Fig. 4.4C; commonly 'fir-tree' zoning; e.g. Paterson & Stevens, 1992; Bruand *et al*., 2014; Henze *et al*., 2023), patchy (Fig. 4.4F; see also Kowallis *et al*., 2022), and concentric oscillatory zoning (Fig. 4.4D) all present. In concentrically zoned titanite, a decrease in BSE brightness from core to rim is most common (Fig. 4.4C). Apatite is the most common inclusion in titanite and is found in both cores and rims, although Fe-Ti oxide inclusions are also common in all lithologies. Sulphide inclusions (pyrite, chalcopyrite and bornite) in titanite are rare, but are present in the granitoids, quartz monzodiorite dyke, and the mafic enclaves (Figs. 4.4D-F). Both the sulphides and Fe-Ti oxide inclusions are typically associated with patchy zoning in the cores of some titanite grains, separated from oscillatory zoned rims by a resorption boundary (Figs. 4.4A, D and F; see also Kowallis *et al*., 2022). In the mafic rocks, titanite grains often show patchy zoning throughout (Fig. 4.4E).

4.4.2 Whole-rock chemistry

New analyses of Strontian whole-rock chemistry (Appendix 1) overlap with literature data from various studies (Figs. 4.5A and B). Strontian granitoids exhibit variable silica concentrations,

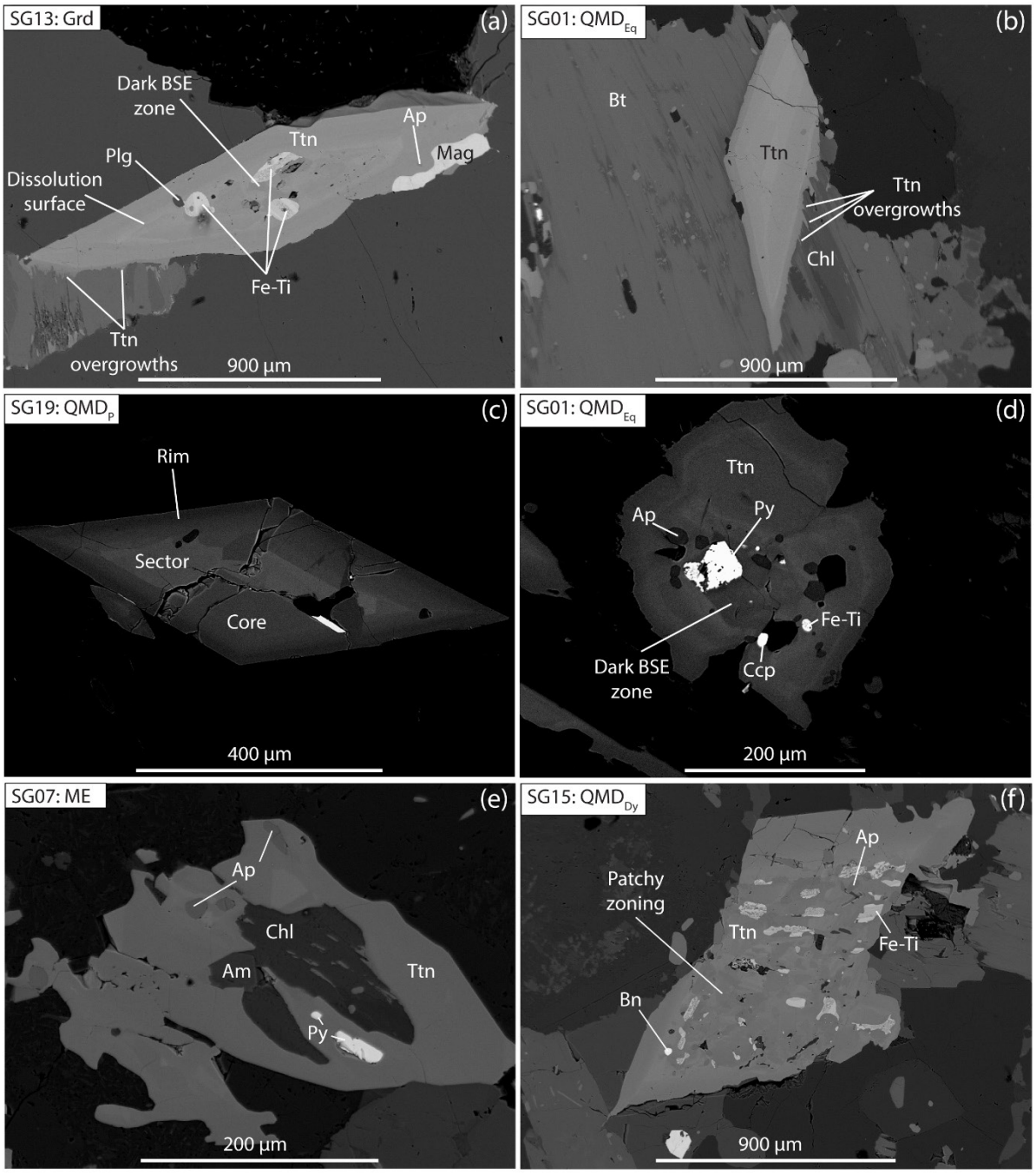


Figure 4.4. SEM backscattered electron images of titanite, showing a range of textures and mineral inclusions. **A.** Subhedral titanite exhibiting a dark BSE zone, a dissolution surface and titanite overgrowths. Apatite, plagioclase and Fe-Ti oxide inclusions are observed. **B.** Euhedral titanite with later fine overgrowths that are associated with chloritized biotite. **C.** Euhedral titanite showing core to rim and sector zoning types. **D.** Subhedral titanite showing a dark BSE zone, normal and reverse zoning and a range of inclusions (pyrite, chalcopyrite, apatite and Fe-Ti oxides). **E.** Anhedral titanite containing pyrite, apatite, chlorite and amphibole inclusions. **F.** Subhedral titanite showing partial dissolution, patchy zoning and inclusions of bornite, apatite and Fe-Ti oxides (ilmenite and titanomagnetite). Bn = bornite; Ccp = chalcopyrite; Chl = chlorite; Am = amphibole; Mag = magnetite; Py = pyrite.

ranging from ~60-75 wt.% SiO_2 and are classified as either medium-K or high-K calc-alkaline (Fig. 4.5A). The equigranular and porphyritic quartz monzodiorites have a very similar whole-rock chemical composition except for K_2O which is higher in the porphyritic type (Fig. 4.5A). Mafic enclaves show a wide range of silica contents but are mostly in the range of 45-55 wt.% SiO_2.

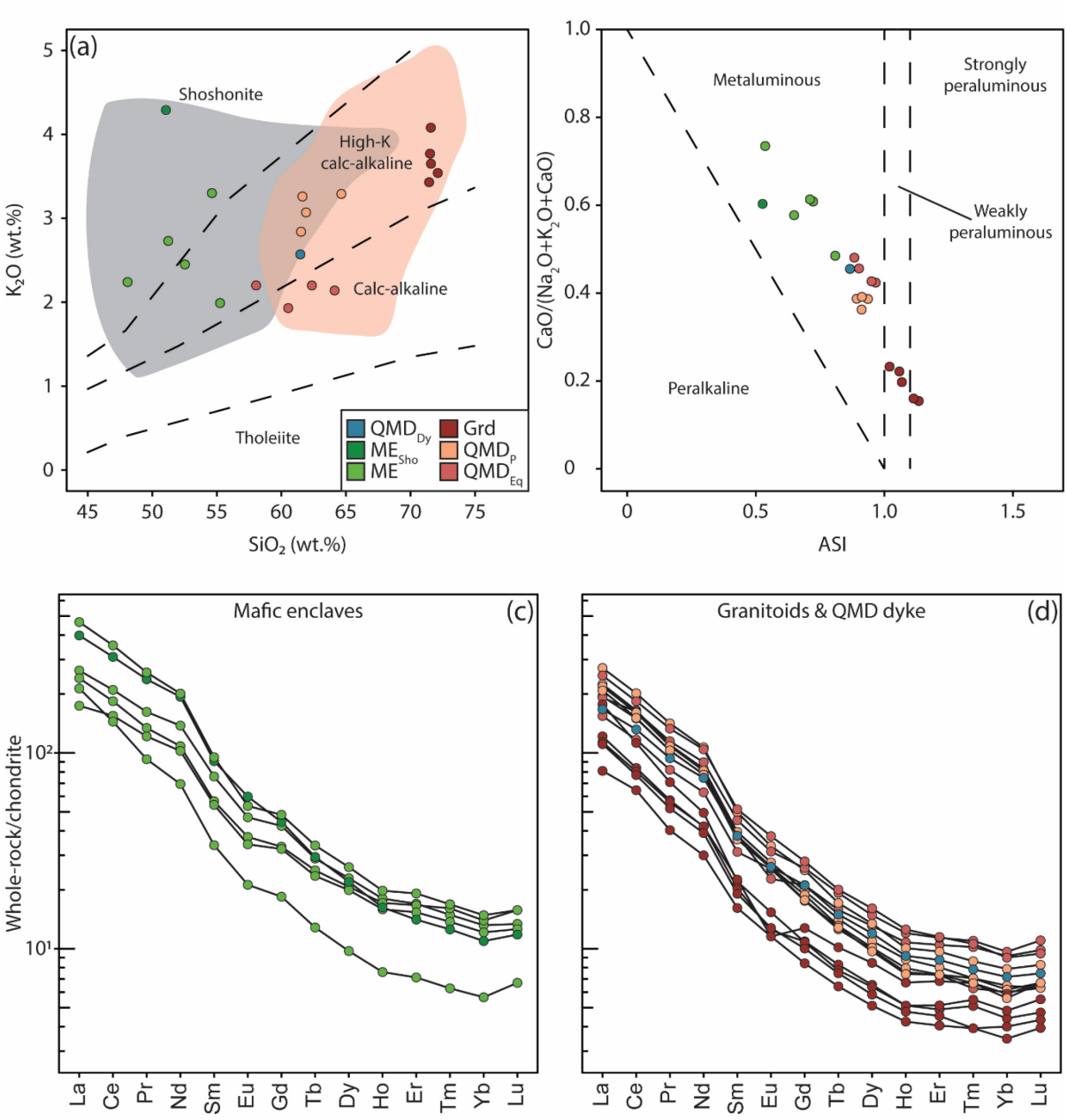


Figure 4.5. Whole-rock chemistry of the Strontian Intrusive Complex. **A.** K_2O-SiO_2 discrimination diagram (Peccerillo & Taylor, 1976). **B.** Alumina saturation diagram (Barton & Young, 2002). Shaded fields represent literature data from: Holden *et al.* (1987); Paterson (1990); Fowler *et al.* (2008). Grey and red areas represent analyses of mafic enclaves and granitoids respectively. (C and D) REE spider plots of **C.** mafic enclaves and dykes and **D.** granitoids. Chondrite normalisation values from Boynton (1984). QMD =quartz monzodiorite dyke; ME_{Sho} = Shoshonitic mafic enclave; ME= Mafic enclave; Grd= Granodiorite; QMD_P= Porphyritic quartz monzodiorite; QMD_{Eq}= Equigranular quartz monzodiorite.

Additionally, mafic enclaves show a wide range of K_2O contents, classifying as medium-K and high-K calc-alkaline, and shoshonitic (Fig. 4.5A). Almost all units are metaluminous, with the granodiorite classified as weakly peraluminous (Fig. 4.5B). The shape of chondrite-normalised whole-rock REE patterns are consistent between units, with strong light-REE (LREE) enrichments and mid- to heavy-REE depletions, with a weakly negative to absent Eu anomaly, whereas the

absolute abundance of REE decreases with increasing silica, from mafic enclaves to quartz monzodiorites and are lowest in the granodiorites (Figs. 4.5C and D).

4.4.3 Amphibole and titanite chemistry

Amphibole

Compositions of amphibole cores and rims were determined by electron microprobe and LA-ICP-MS on a total of 194 spots. Amphibole compositions are remarkably consistent between units despite varying host rock compositions and crystal habits and a large range in compositions for a given unit (Fig. 4.6). Amphiboles are exclusively calcic (> 11 wt.% CaO), with nearly all grains classifying as magnesiohornblende (Fig. 4.6A; Hawthorne *et al.*, 2012). Amphibole TiO_2 contents are also largely comparable between units, with most grains containing between 0.6 and 1.5 wt.%

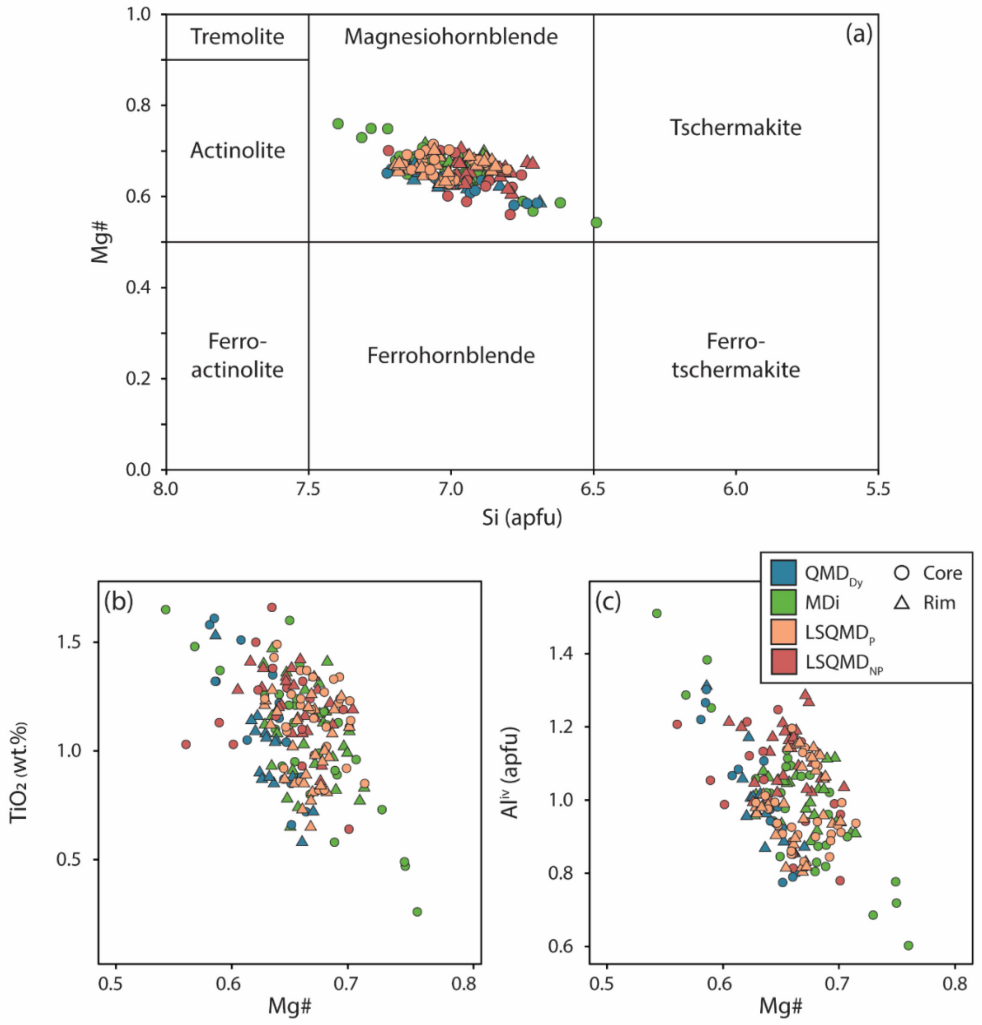


Figure 4.6. Amphibole major element chemistry. **A.** Amphibole classification diagram (Hawthorne *et al.*, 2012; using the Excel spreadsheet of Locock, 2014). **B.** TiO2 (wt.%) vs. Mg#. **C.** Aliv (apfu) vs Mg#.

(Fig. 4.6B). Al^{IV} contents in amphibole are broadly similar between units, with most grains containing between 0.8 and 1.3 Al^{IV} atoms per formula unit (apfu) (Fig. 4.6C). Amphibole Mg#

are between 0.51 and 0.72, with most analyses ~0.60. Amphibole clots and phenocrysts are mostly indistinguishable in terms of nearly all major and trace elements. However, amphibole in the cores of clots typically contain much higher Cr (≤4000 µg/g) than phenocrysts (≤500 µg/g), whereas those at the clot rims show similar Cr concentrations to phenocryst amphibole.

Laser ablation mapping of amphibole phenocrysts reveals systematic variations in trace element composition from core to rim (Figs. 4.7 and 8). Phenocrysts from both the granitoids (Fig. 4.7) and the mafic enclaves (Fig. 4.8) show narrow rims (<50 to 200 µm) with order-of- magnitude

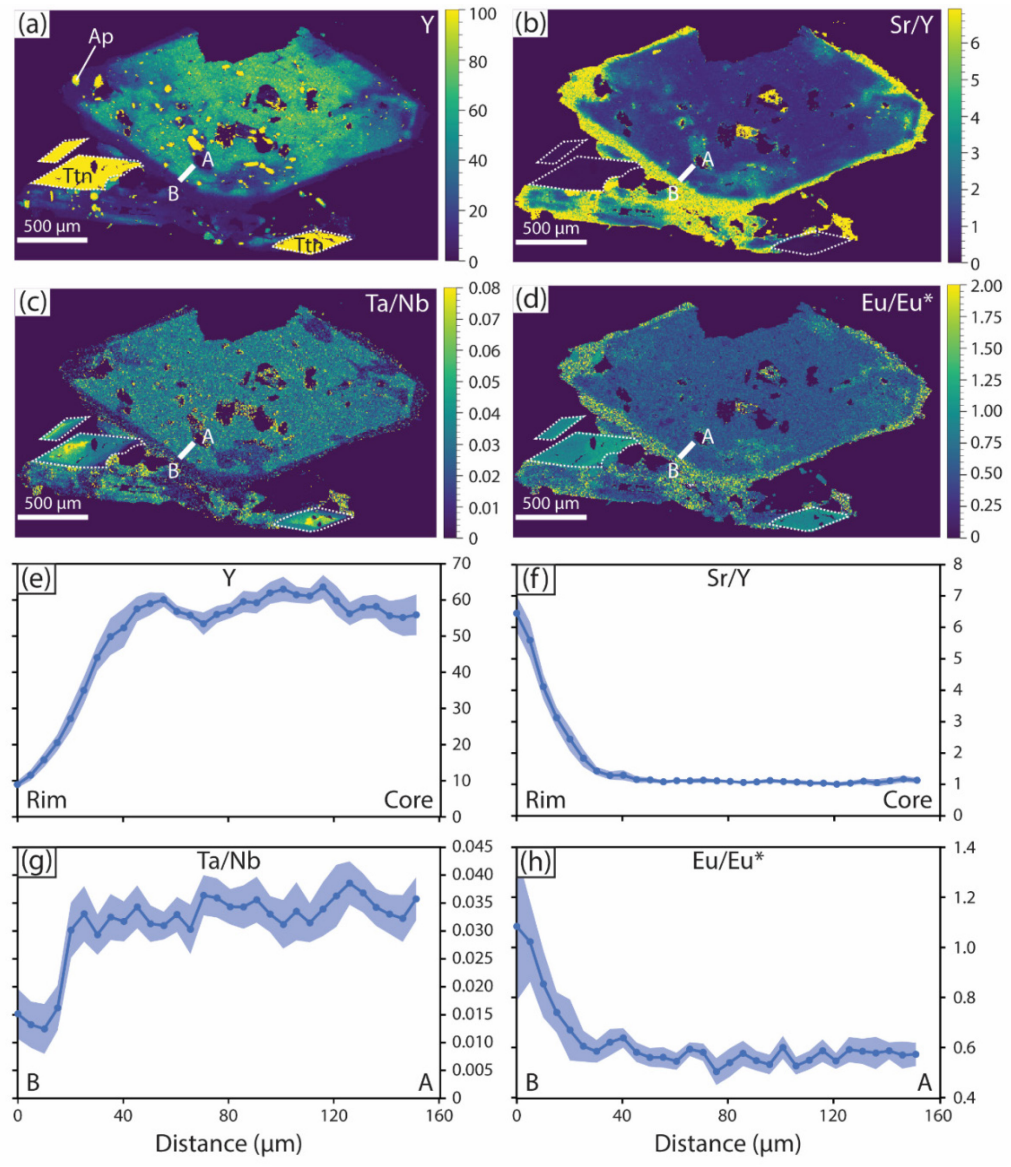


Figure 4.7. Amphibole trace element maps from sample SG19. Amphibole, apatite inclusions and associated titanite are shown, obvious mineral inclusions were removed. **A.** Y. **B.** Sr/Y. **C.** Ta/Nb. **D.** Eu/Eu*. Eu/Eu* was calculated where Eu_N, Sm_N and Gd_N are normalised (Boynton, 1984). Transects across the grain are also shown, from A-B. **E.** Y. **F.** Sr/Y. **G.** Ta/Nb. **H.** Eu/Eu*. Shaded area indicates 2σ uncertainty. Y contents are given as µg/g.

decreases in REEs (including Y), decreases in Ta, Nb, and Ta/Nb ratio, and increases in Eu/Eu* and Sr/Y (Figs. 4.7 and 8). There is no systematic change in Sr content from core to rim, so the

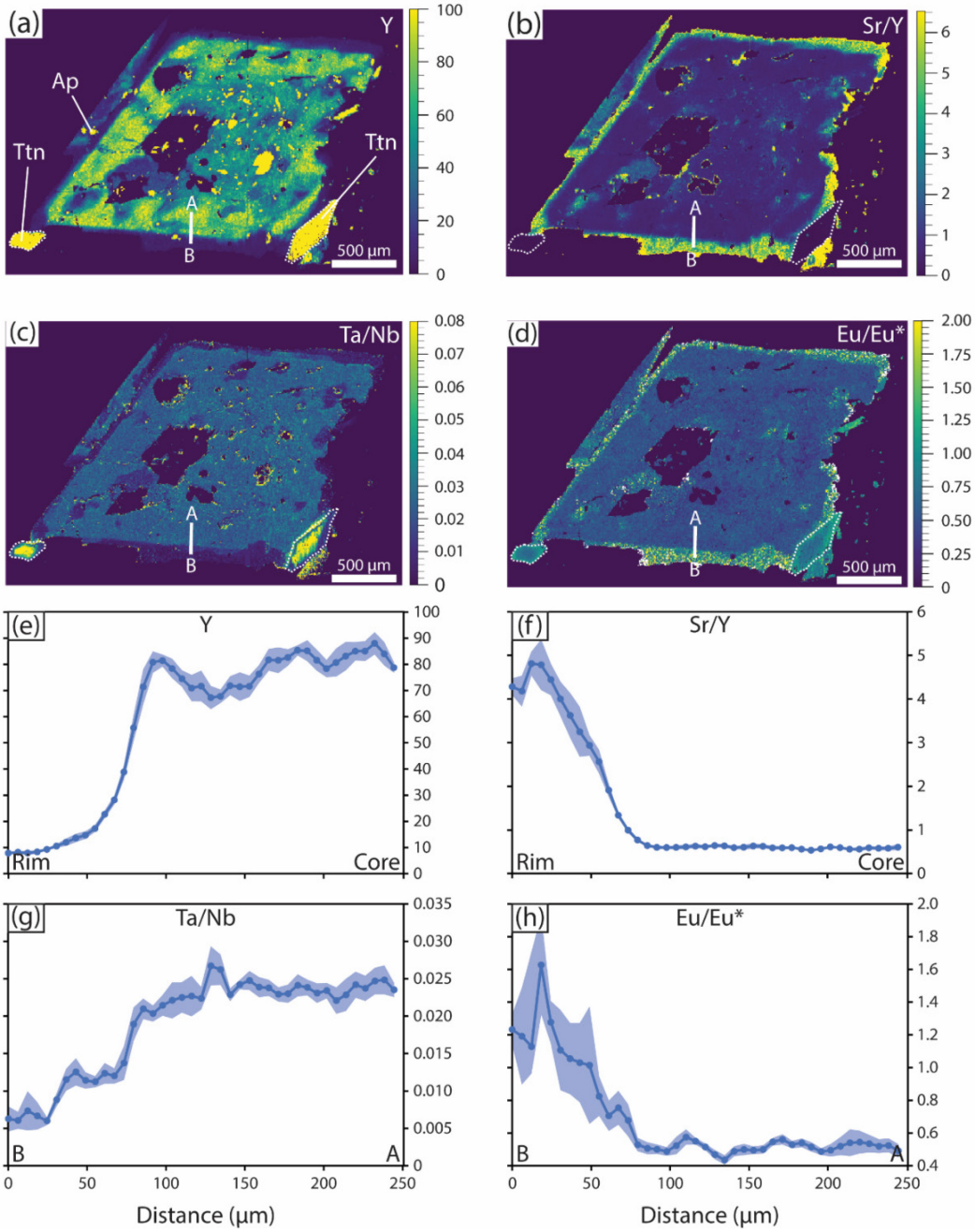


Figure 4.8. Amphibole trace element maps from sample SG21. Amphibole, apatite inclusions and associated titanite are shown, obvious mineral inclusions were removed. **A.** Y. **B.** Sr/Y. **C.** Ta/Nb. **D.** Eu/Eu*. Eu/Eu* was calculated where Eu_N, Sm_N and Gd_N are normalised (Boynton, 1984). Transects across the grain are also shown, from A-B. **E.** Y. **F.** Sr/Y. **G.** Ta/Nb. **H.** Eu/Eu*. Shaded area indicates 2σ uncertainty. Y contents are given as µg/g.

increasing Sr/Y in the rims only reflects the depletion of Y. The core-rim boundary broadly mirrors the shape of the grain but is distinctly sharp, occurring within <50 µm. There is some trace element variation within the cores, especially patches of lower Y in the vicinity of apatite inclusions which themselves contain much higher Y than the host amphibole (e.g. Fig. 4.8A). However, the within-core variability of Y in amphibole is significantly less pronounced than the core-rim variation. The amphibole rims are commonly in close association with titanite, which has much higher Y, Ta, Nb,

and Ta/Nb ratio (Figs. 4.7 and 8).A larger dataset of amphibole laser ablation spot analyses confirms the variability of trace element ratios from core to rim, using Y content as an index of fractionation (with the direction of fractionation from high to low Y; Fig 4.9) because it shows

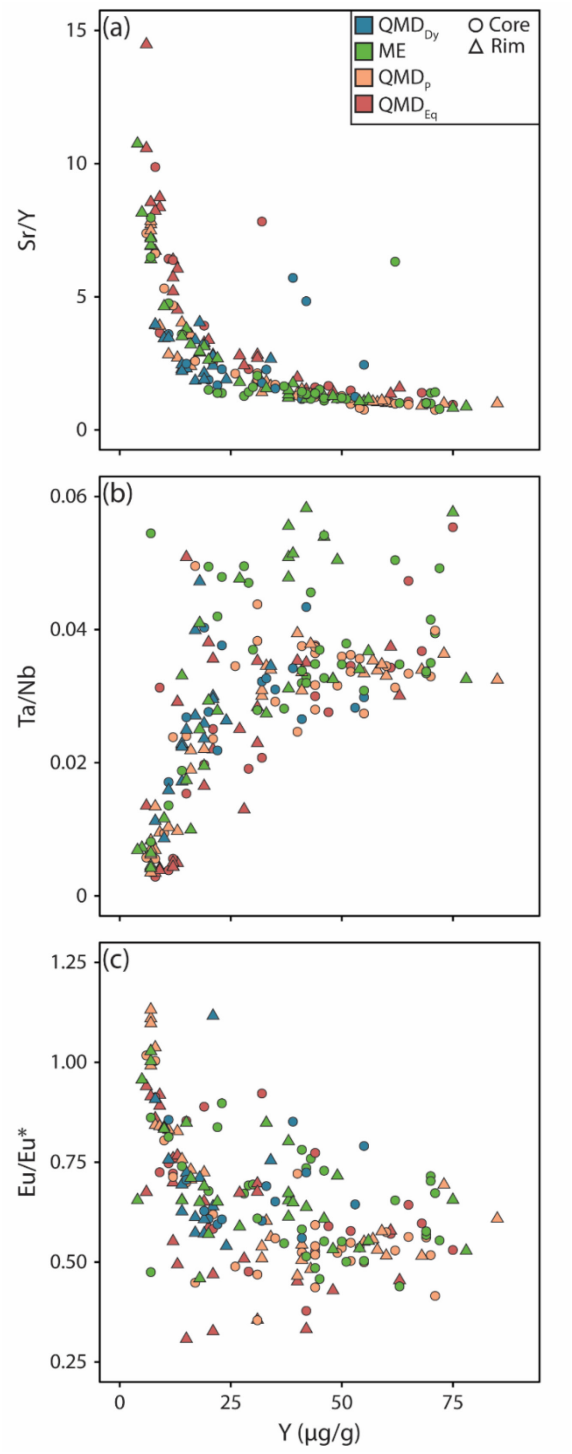


Figure 4.9. Amphibole trace element ratio variations as a function of Y concentration. **A.** Sr/Y. **B.** Ta/Nb. **C.** Eu/Eu*. Eu/Eu* was calculated where Eu_N, Sm_N and Gd_N are normalised to chondrite (Boynton, 1984).

decreases from core to rim in both amphibole and titanite (Figs. 4.7, 8 10), and therefore likely reflects compatible behaviour throughout the period of amphibole and titanite crystallisation. At Y

contents greater than ~30 µg/g the Sr/Y, Eu/Eu*, and Ta/Nb ratios are broadly similar, whereas at lower Y contents Eu/Eu* and Sr/Y show sharp increases, and Ta/Nb decreases.

Titanite

Laser ablation trace element mapping of titanite grains show similar variations as observed in amphibole, with decreasing Ta, Nb, Ta/Nb, Y, and increasing Sr/Y and Eu/Eu* from core to rim (Fig. 4.10). As with amphibole, increases in Sr/Y reflect decreases in Y; the Sr content of titanite does not change systematically from core to rim. However, the concentration of trace elements in titanite are significantly higher than amphibole, and the variations from core to rim are gradual, with no clear step change in concentrations. This is supported by a larger dataset of titanite spot analyses (Appendix 2), which broadly shows continuously increasing Eu/Eu* and decreasing Ta/Nb as a function of decreasing Y (Fig. 4.11). Trace element compositions for titanite presented here overlap with those previously reported for Strontian titanites (Bruand *et al*., 2014; Fig. 4.11).

4.5 Discussion

4.5.1 Estimation of intensive parameters

Pressure

We estimated amphibole rim crystallisation pressures using the Al-in-amphibole barometer of Mutch *et al.* (2016). This barometer is only appropriate for amphibole rim compositions which crystallised close to the solidus and in equilibrium with an assemblage of amphibole + plagioclase + biotite + quartz + K-feldspar + ilmenite/titanite + magnetite + apatite; all phases which co-crystallised with amphibole rims at Strontian. Calculated crystallisation pressures are very consistent throughout the different units and range between 200-300 MPa, corresponding to ~7.5 to 11 km depth (Fig. 4.12A). These calculated crystallisation pressures imply a slightly shallower crystallisation depth than is inferred from contact metamorphic mineral assemblages in the surrounding schists (300 to 450 MPa; Ashworth & Tyler, 1983). Nevertheless, the consistency in calculated pressures implies a majority of amphibole rims grew in the shallow crust.

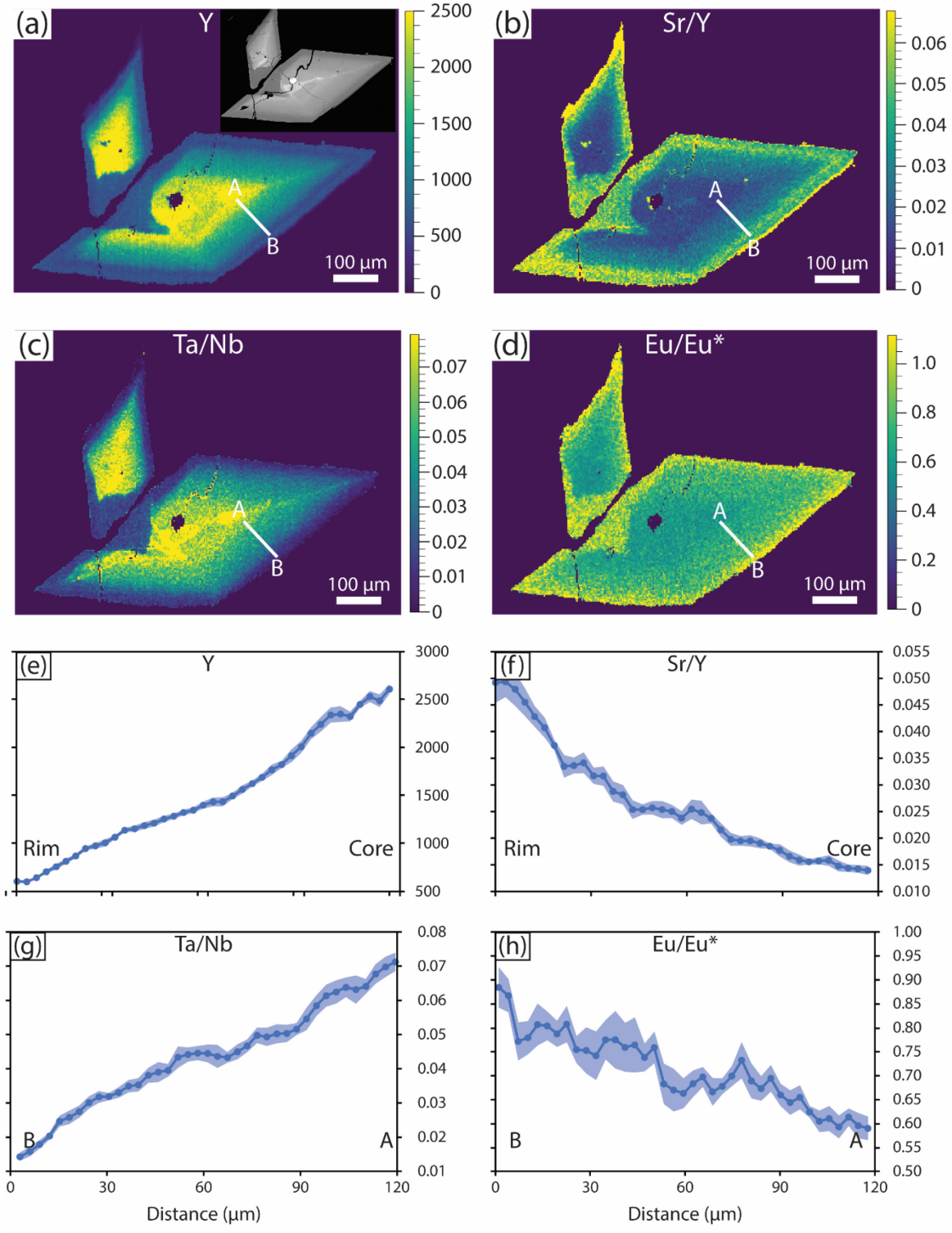


Figure 4.10. Titanite trace element maps from sample SG21. Mineral inclusions were removed. **A.** Y. **B.** Sr/Y. **C.** Ta/Nb. **D.** Eu/Eu*. Eu/Eu* was calculated where Eu_N, Sm_N and Gd_N are normalised to chondrite (Boynton, 1984). Transects across the grain are also shown, from A-B. **E.** Y. **F.** Sr/Y. **G.** Ta/Nb. **H.** Eu/Eu*. Shaded area indicates 2σ uncertainty. Y contents are given as µg/g.

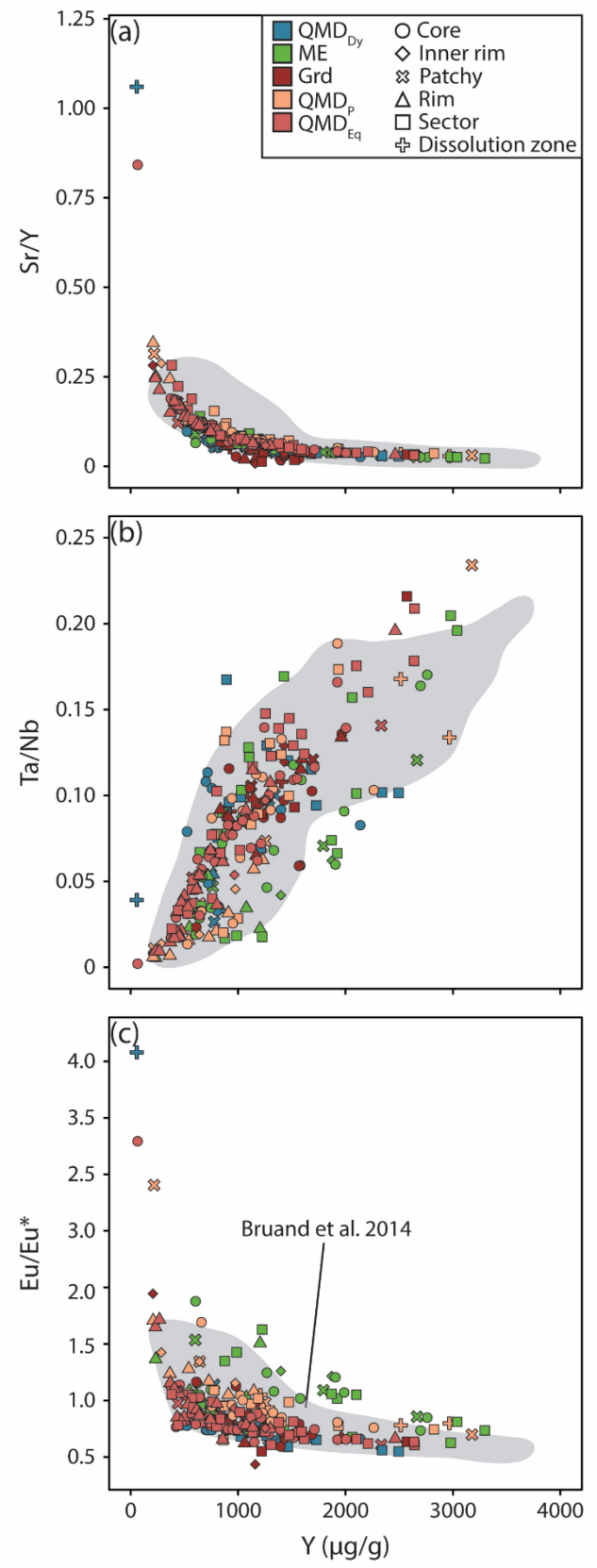


Figure 4.11. Titanite trace element ratio variations as a function of Y concentration. **A.** Sr/Y. **B.** Ta/Nb. **C.** Eu/Eu*. Eu/Eu* was calculated where Eu_N, Sm_N and Gd_N are normalised to chondrite (Boynton, 1984). Data of Bruand *et al.* (2014) are shown by the grey polygon. 2σ uncertainty is smaller than the symbols.

Temperature

Crystallisation temperatures were estimated from touching amphibole-plagioclase pairs using the thermometer of Holland and Blundy (1994). Molar proportions of anorthite (X_{An}) were approximated using the data from Paterson (1990), who found that plagioclase from Strontian granitoids shows a narrow range of X_{An} mostly between 0.25 and 0.15. Consequently, we applied the edenite-tremolite thermometer, which is relatively insensitive to X_{An}, applying a value of 0.20 and a pressure estimate of 225 MPa based on Al-in-amphibole geobarometry (Fig. 4.12A). Calculated crystallisation temperatures are mostly in the range of ~760°C to the solidus (Fig. 4.12B), with broadly comparable temperatures throughout the different lithologies. These temperature estimates are relevant only to the rims of amphiboles in contact with plagioclase, so the temperature of amphibole cores were unconstrained.

Crystallisation temperatures of titanite were calculated using the Zr-in-titanite thermometer of Hayden *et al.* (2008), which depends upon estimates of pressure and the activities of a_{SiO_2} and a_{TiO_2}. In their calculation of Zr-in-titanite temperatures at Strontian, Bruand *et al.* (2014) assumed a crystallisation depth of 13-14 km, in addition to silica and titania activities of 1. Instead, we assume an a_{TiO_2} of 0.7, as has been implemented elsewhere for titanite-bearing rocks of intermediate composition (e.g. Claiborne *et al*., 2010), in addition to a crystallisation pressure of 225 MPa based on Al-in-amphibole geobarometry. Like Bruand *et al.* (2014) we assume an a_{SiO_2} of 1 as despite variation in whole-rock SiO_2, quartz is still present in the groundmass of even the most mafic rocks. Nevertheless, if an a_{SiO_2} of 0.8 is assumed for the mafic enclaves, then calculated crystallisation temperatures would only decrease by ~12 °C We estimate that all titanites crystallised between 760 °C and the solidus, with most grains crystallising in a relatively narrow temperature range of 735-715°C, something that is remarkably consistent between units (Fig. 4.12B). Despite the different pressure and a_{TiO_2} estimates, Bruand *et al.* (2014) calculated broadly comparable crystallisation temperatures, in the range 772-682°C.

We use whole rock compositions to estimate saturation temperatures for apatite (Harrison & Watson, 1984) and titanite (Ayers *et al.*, 2022). Apatite saturation temperatures are typically ~950°C, except for mafic enclave sample SG07 (850°C). Titanite saturation temperature are mostly comparable with the highest Zr-in-titanite temperatures for a given rock and are between 750 and 725°C (Fig. 4.12C). For zircon saturation temperature estimates, we employed the equation of Watson and Harrison (1983) rather than the newer calibrations (Boehnke *et al.*, 2013), as the older calibration provides the closest match to low temperature crystallisation experiments (Marxer & Ulmer, 2019). Furthermore, we followed the method of Harrison *et al.* (2007) for estimating zircon saturation temperature, who noted that using measured whole rock Zr values leads to

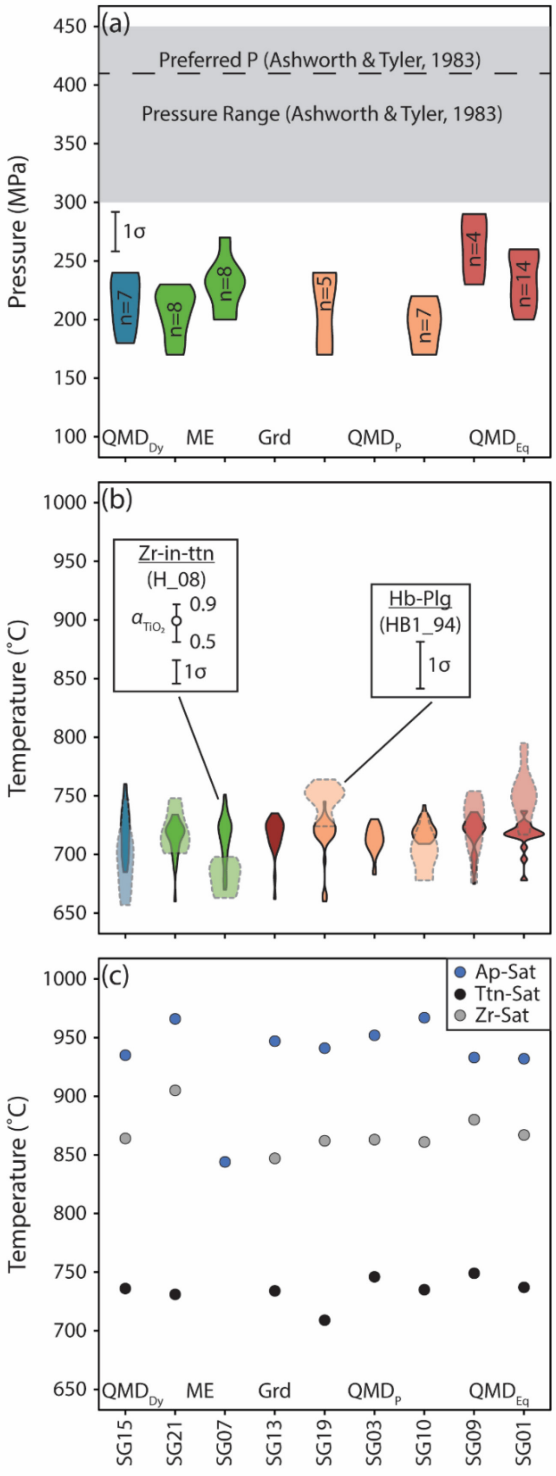


Figure 4.12. Violin plots showing estimated intensive parameters for the Strontian magmatic system. **A.** Crystallisation pressure via Mutch *et al.* (2016). Also shown are preferred and pressure ranges from Ashworth and Tyler (1983). **B.** Crystallisation temperature as calculated using the edenite-tremolite (Holland & Blundy, 1994) and Zr-in-titanite thermometers (Hayden *et al.*, 2008). **C.** Calculated saturation temperatures for apatite (Piccoli & Candela, 2002, after Harrison & Watson, 1984), titanite (Ayers *et al.*, 2022) and zircon (Watson & Harrison, 1983). The effect of changing $a\mathrm{TiO_2}$ on Zr-in-ttn temperatures are shown. N.B. No amphibole data was available for the Glensanda granodiorite because of the lack of amphibole. Titanite and zircon saturation temperatures were not valid for SG07.

underestimates. This is because significant zircon-absent crystallisation causes melt Zr contents to increase and the melt bulk compositional parameter M (the cation ratio [Na + K + 2Ca / Al × Si])

to decrease with respect to whole rock values, with concomitant effects on zircon saturation temperature. The method of Harrison *et al.* (2007) accounts for this by modelling the Zr increase due to incompatible Rayleigh fractional crystallisation, using the whole rock Zr as a starting melt composition, and by parameterising both degree of fractionation (F) and melt bulk composition (M) as a function of temperature using experimental constraints (for which we used the experiments of Marxer & Ulmer, 2019). Using this method, we estimate zircon saturation temperature to be between 862 and 880°C for the quartz monzodiorites, and 831 and 847°C for the granodiorites (Fig 4.12C).

Applying a similar method to the titanite saturation thermometer is more difficult. The change in melt TiO2 content prior to late-stage titanite saturation is harder to constrain, because (unlike Zr) the compatibility of TiO_2 in the bulk crystallising assemblage is highly variable depending on which phases crystallise, and at which temperatures. Instead, comparing the experimentally-determined liquid line of descent for TiO_2 (Marxer & Ulmer, 2019) to a temperature-dependent curve for titanite stability (Ayers *et al.*, 2022) with the 'M' compositional term parameterised as a function of temperature, yields a titanite saturation temperature of ~720°C similar to those determined using whole rock TiO_2, and consistent with our Zr-in-titanite temperature estimates. No such adjustment is required for the saturation temperatures of apatite, which crystallises close to the liquidus.

Oxygen fugacity and water content

Although mineral proportions vary between units, Strontian rocks exhibit a relatively consistent mineralogy. The assemblage of titanite, quartz and magnetite can be used to constrain a minimum fO_2 of ~FMQ+1 (where FMQ denotes the fayalite magnetite quartz buffer) at 725°C (Wones, 1989). The range of possible magmatic water contents is constrained at the lower end by the presence of amphibole, which is stable at >4.5 wt.% H_2O at 780°C and 220 MPa (Scaillet & Evans, 1999), and by water-saturated conditions at these pressures (~6 wt.% H_2O; Newman & Lowenstern, 2002).

4.5.2 Crystallisation sequence

Based on textural observations, a common crystallisation sequence of minerals may be inferred for the quartz monzodiorite samples, despite minor differences in modal mineralogy (Fig. 4.13). This crystallisation sequence can be combined with mineral thermometry and accessory mineral saturation temperature estimates (Fig. 4.12) and compared with crystallisation experiments at similar pressures and bulk compositions to provide quantitative estimates of the temperatures at which different minerals crystallised (Fig. 4.13B). Rhyolite-MELTS (Gualda *et al.*, 2012) was used to estimate the liquidus temperature of the quartz monzodiorite (c. 1050°C at 200 MPa and FMQ+2)

and our results were also compared to the crystallisation experiments of Marxer and Ulmer (2019). These experiments used a medium-K tonalite from the Adamello Batholith (Italy) as a starting composition, which is comparable to the Strontian quartz monzodiorite, and were carried out at 200 MPa which is consistent with our Al-in-amphibole barometric estimates (Fig. 4.12A).

The Strontian crystallisation sequence is broadly comparable to that observed by Marxer & Ulmer (2019), although titanite and K-feldspar were not saturated in these experiments and no pyroxene was observed at Strontian. The absence of pyroxene may be explained by the presence of the amphibole clots, which have been interpreted to represent the hydration of restitic pyroxene (Stephens, 2001). However, considering the experiments of Marxer & Ulmer (2019), we suggest instead that these clots represent the reaction of cognate pyroxene phenocrysts during the crystallisation sequence.

We propose that plagioclase, amphibole and apatite started crystallising relatively early (≥ 950°C). Textural observations suggest that Fe-Ti oxides started to crystallise later, although there is some uncertainty as to the exact temperatures. For zircon, we suggest that saturation took place between 880 and 862°C in the quartz monzodiorites, and 847 and 831°C for the granodiorites, based on zircon saturation temperatures (Watson & Harrison, 1983). Calculated Zr-in- titanite

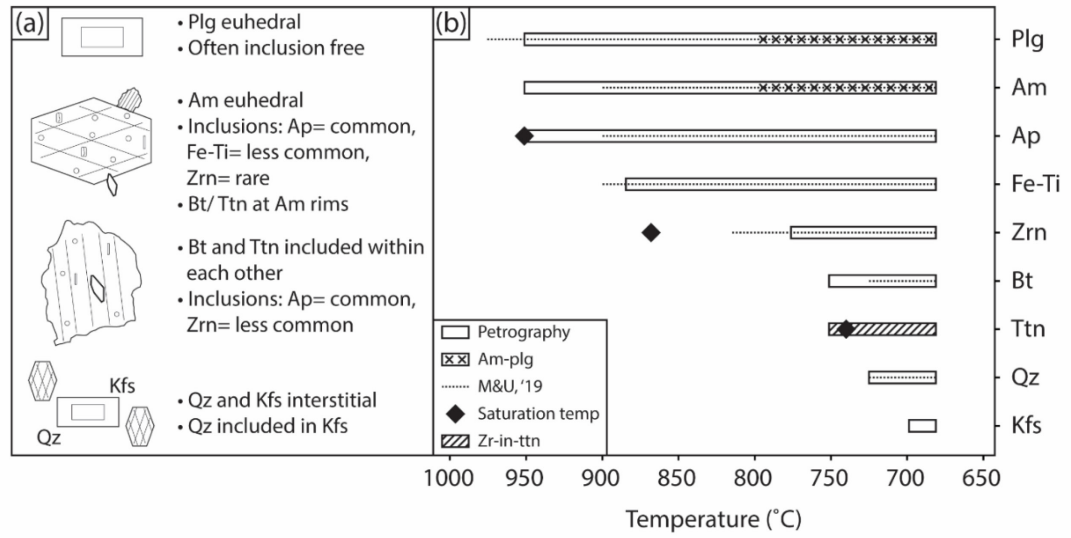


Figure 4.13. Generalised crystallisation sequence for the Strontian magmatic system. **A.** Textural relations of the various minerals. **B.** Crystallisation sequence as a function of temperature, incorporating amphibole-plagioclase pairs (Holland & Blundy, 1994), crystallisation experiments using similar starting compositions (Marxer & Ulmer, 2019) and saturation temperatures for apatite (Harrison & Watson, 1984; Piccoli & Candela, 2002) titanite (Ayers *et al.*, 2022) and zircon (Watson & Harrison, 1983). Zr-in-titanite temperatures are also shown (Hayden *et al.*, 2008).

temperatures (Hayden *et al.*, 2008) overlap with titanite saturation temperatures (Ayers *et al.*, 2022), suggesting the onset of titanite crystallisation was around 750°C. Temperature estimates for biotite, based on coeval crystallisation with titanite, are slightly higher than observed by Marxer &

Ulmer (2019), although this could be explained by earlier saturation of biotite from slightly more potassic magmas at Strontian compared to Adamello. Finally, quartz and K-feldspar likely saturated close to the water-saturated granite solidus based on textures (~680°C; e.g. Brown & Fyfe, 1970). Calculated crystallisation temperatures from amphibole-plagioclase pairs and the Zr-in-titanite thermometer overlap (Fig. 4.12B), supporting the textural evidence that titanite crystallised at the same time as amphibole rims after a protracted period of amphibole crystallisation in the absence of titanite (Fig. 4.13)

4.5.3 Trace element distribution

In order to better understand which phases are likely to impact melt chemistry, we estimated the individual mineral contributions to the rock trace element budget for two samples (SG07, a mafic enclave and SG09, an equigranular quartz monzodiorite) by combining mineral abundances (Table 4.2) with median trace element compositions (Appendix 5). Through this approach, the total contribution of each mineral to the whole-rock budget for a given element is estimated by multiplying the modal mineral fraction by the median trace element content, as has been utilised by previous authors (e.g. Gromet & Silver, 1983; Jefferies, 1985; Xiao *et al*., 2020). Median plagioclase compositions from the same samples were taken from Birt (2019), and median apatite and zircon compositions were taken from Bruand *et al.* (2014) who sampled the same units. The contributions of biotite, quartz, K-feldspar and Fe-Ti oxides to the modelled elements (Sr, Y, Nb, REEs, Hf, Ta, Pb, Th, and U) were not constrained due to a lack of data, or low concentrations of the trace elements of interest, or both (see Appendix 5 for further details).

Overall, our calculations provide a reasonable estimate of the whole-rock trace element distribution, with most elements estimated to within 20% of the measured whole-rock compositions (Figs. 4.14A and B). Furthermore, estimated chondrite-normalised REE patterns are a close match to measured whole-rock patterns (Figs. 4.14C and D). Our results confirm the findings of Gromet and Silver (1983) and Jefferies (1985) that the accessory minerals, especially titanite, are a major repository of many trace elements in granitoids. Despite comprising only a small portion of the total rock (~0.8-0.9 modal %; Table 4.2) we estimate that titanite hosts up to 80% of all REEs and the majority of several HFSEs (e.g. Nb, Ta, Th, U). Zircon contains most of the Hf and is also a minor repository of heavy-REEs and U, whereas apatite hosts only a modest proportion of trace elements, accounting for up to 20% of the whole-rock La and lesser percentages of middle- and heavy-REEs. Of the major phases, amphibole hosts the most significant proportion of the REE budget, containing up to 50% of some middle- to heavy-REEs in mafic enclave sample SG07 in which amphibole comprises ~30% of the rock (Figs. 4.14A and B). Plagioclase accounts for <10% of La and Eu, and even lesser amounts of other REEs, but dominates the Sr and Pb budgets.

There are some discrepancies between estimated and measured whole-rock trace element abundances. For example, Ta is underestimated in our calculations, with ~50% of the whole-rock Ta (0.55 µg/g shortfall) in quartz monzodiorite sample SG09 unaccounted for. This is likely due to variability in titanite Ta concentrations, which have a median value of 60 mg/g, and an interquartile range of 160 mg/g. Similarly, shortfalls in estimated whole-rock Hf concentration (~30%) are likely due to significant variability in zircon Hf contents, which range from 7010 to 11000 µg/g (Bruand *et al.*, 2014). However, underestimates in Th in mafic enclave sample SG07 (~50% of whole-rock Th unaccounted for) cannot be explained solely due to variations of Th content in titanite and may represent very small proportions of a Th-rich accessory mineral (e.g. thorite) which was not observed in thin section. For example, only 9×10^{-4} modal % thorite would be required to account for the 6.75 mg/g shortfall in Th.

Despite the absence of K-feldspar trace element data, it is plausible that this phase may concentrate sufficient Sr and Pb such that an approximation of the distribution of these elements in K-feldspar ought to be made. Estimates for K-feldspar trace element compositions in the Strontian system may be made by taking the composition of the amphibole rims (~40 µg/g Sr; ~2 µg/g Pb) and estimating first the melt and then the K-feldspar content using published partition coefficients (Bachmann *et al.*, 2005), yielding ~500 µg/g Sr and ~20 µg/g Pb. These values are similar to those reported by Bachmann *et al.* (2005) for the Fish Canyon Tuff (~700 µg/g Sr and ~25 µg/g Pb). Considering the modal abundance of K-feldspar in the quartz monzodiorite rocks in question (average = 12.7) and the average abundance of Sr and Pb in these rocks (1180 µg/g Sr and 16 µg/g Pb), K-feldspar may contain up to 5.5% of the rock Sr, and 15.5 % of the rock Pb. This may account for some of the shortfall in the estimate for Sr but adds to the overestimate in Pb for the quartz monzodiorite (Fig. 4.14B), which may be due to uncertainty in the concentration of Pb in plagioclase.

Our study confirms that titanite is a key repository for a wide variety of trace elements in calc-alkaline felsic igneous rocks. The textural and thermometric evidence demonstrates that titanite is a late-crystallising phase, implying that during *in-situ* granitoid crystallisation a significant proportion of the REE and some HFSE remain in the melt until most of the crystallisation has occurred. Consequently, the onset of titanite crystallisation represents a significant event in the trace element evolution of the residual melt, which is reflected in the compositions of resultant mineral phases.

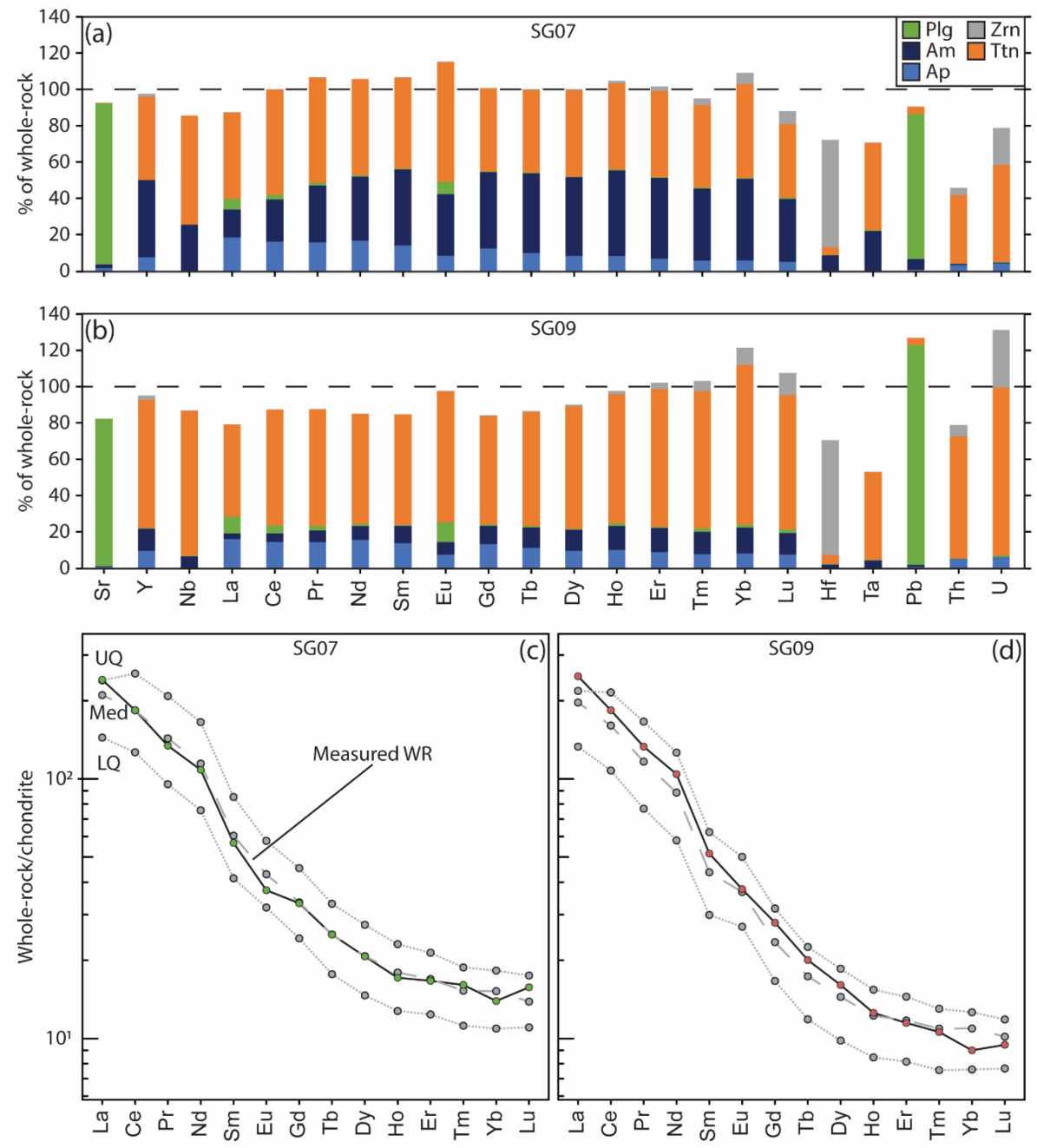


Figure 4.14. Whole-rock trace element distribution between mineral phases. Estimated percentage of various trace elements in different minerals, given as a percentage of the whole-rock. **A.** SG07. **B.** SG09. Chondrite-normalised REE plot, displaying the measured whole-rock composition against the estimated whole-rock composition using median, lower quartile and upper quartile values for different minerals. **C.** SG07. **D.** SG09.

4.5.4 Evolution of the Strontian magmatic system

The core to rim trace element variability described above (Figs. 4.7-11) was also noted by Bruand *et al.* (2014) for apatite and titanite from three samples; two quartz monzodiorite, and one mafic rock. These authors observed gradually decreasing REE, Ta and Nb concentrations and Ta/Nb ratios in grain cores followed by abrupt decreases in the rims, which they interpreted to reflect initial *in-situ* fractional crystallisation (cores) culminating in a late-stage magma mixing event

(rims). Bruand *et al.* (2014) argued that mafic magma mixing changed the trace element partitioning behaviour for both apatite and titanite, suggesting that partition coefficients for REEs, Ta, Nb, as well as D_{Ta}/D_{Nb} ratios are lower in mafic melts than in felsic melts (Prowatke & Klemme, 2005; Prowatke & Klemme, 2006). They concluded that a late-stage mixing event between the granitoid and mafic magmas would therefore lower these partition coefficients, leading to lower concentrations of these elements (and a lower Ta/Nb ratio) in the rims of resultant minerals in the granitoids. Evidence for such a mixing event is provided by the compositional similarity between the rims of titanites and apatites in the granitoids and the same minerals in the mafic rock sample.

Although the mingling of more primitive magmas with the host granitoids is attested by the presence of the mafic enclaves (Fig. 4.2), the large contrast in viscosity between the crystal-rich granitic mush and the more primitive enclave melts makes hybridisation (and chemical homogenisation) unlikely. Comparisons between the Sr-Nd isotopic compositions of enclave-host granitoid pairs at Strontian show minimal evidence for equilibration of REEs (Holden *et al.*, 1987; Holden *et al.*, 1991). This is supported by the absence of mixing arrays in whole-rock chemistry between mafic enclaves and the felsic host (Figs. 4.15A and B). For example, the quartz monzodiorite samples have a very narrow range of whole-rock Cr and Ni compositions from ~70 to 90 mg/g Cr, and 42 to 57 mg/g Ni, whereas the concentrations in the mafic enclaves are significantly higher (up to 550 mg/g Cr and 226 mg/g Ni) and mixing of even small amounts of mafic magma would be easily detected in the host granitoid compositions. Similar arguments can be made for Al_2O_3 (generally lower in the enclaves) and MgO (higher in the enclaves than the host; see Stephens 2001). Additionally, the concentrations of Y, REEs, and Nb are either similar or higher in the mafic rocks (Figs. 4.15C and D). Hence, if amphibole and titanite rims were reflecting the input of mafic magma, these elements would increase from core to rim, but they are in fact lower in the rims by up to an order of magnitude (Figs. 4.7, 8 and 10). To explain such low values by changes in partitioning behaviour alone would require more than an order of magnitude decrease in partition coefficients for these elements. Instead, partition coefficients in amphibole (like other minerals) increase towards the lower temperatures recorded by the amphibole rims (e.g. Nandedkar *et al*., 2016). Furthermore, we suggest that gradual variations in titanite trace element compositions from core to rim (Fig. 4.10) are incompatible with a sudden magma mixing event and instead indicate that *in-situ* crystallisation is the dominant process controlling residual melt chemical evolution.

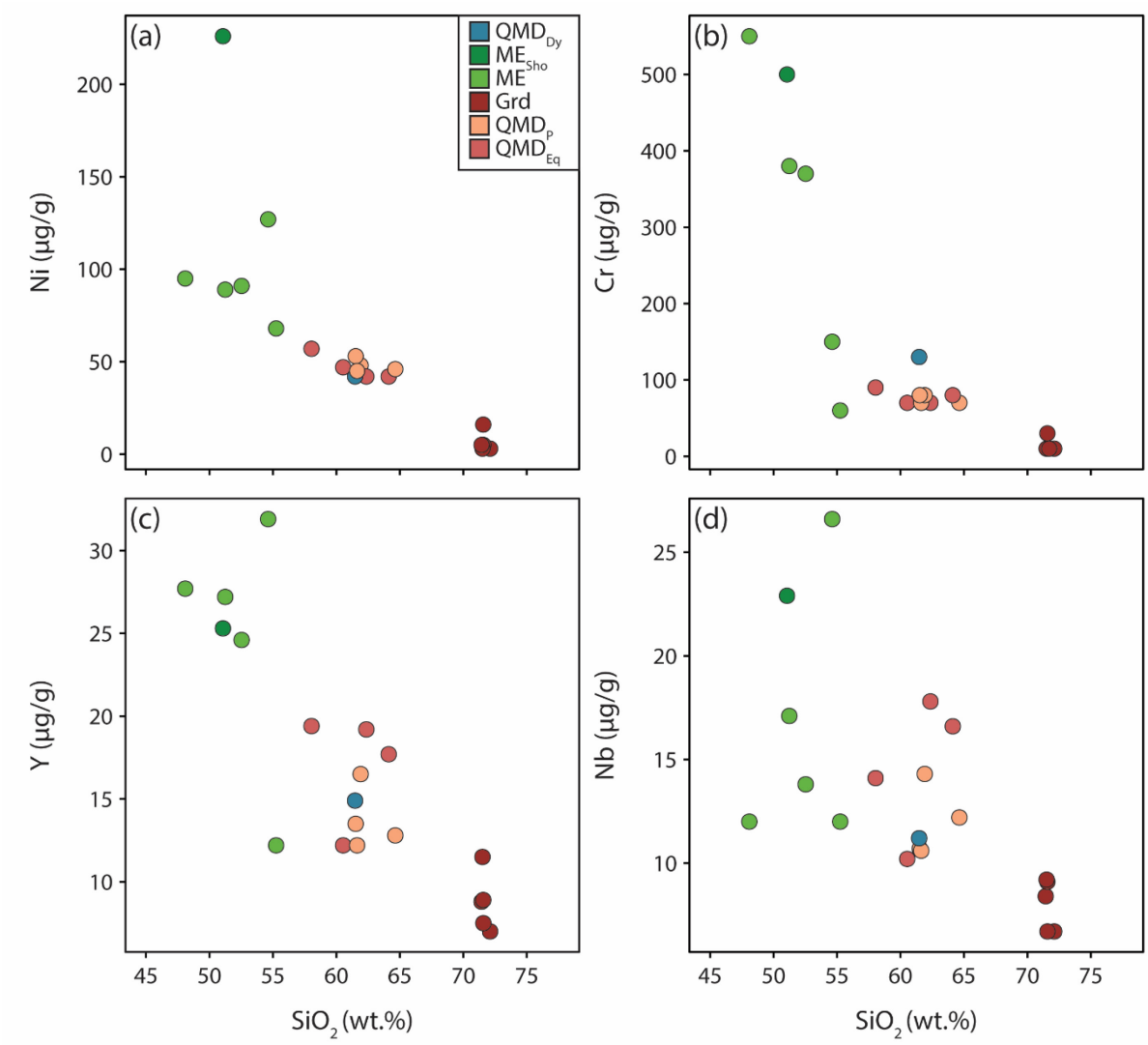


Figure 4.15. Whole-rock chemistry showing A. Ni, B. Cr, C. Y and D. Nb vs SiO2.

Another explanation for the observed rapid changes from core to rim in amphibole compositions is the late-stage crystallisation of titanite, which saturates at temperatures <780°C in granitic systems (e.g. Ayers *et al*., 2022) and is the major sink for REE and HFSE (see also Glazner *et al*., 2008; Colombini *et al*., 2011). The crystallisation of titanite at a late stage would drastically deplete the residual melt in these elements because titanite-melt partition coefficients are very high (e.g. D_Y= 633; D_{Nb}= 129; Bachmann *et al*., 2005) relative to partition coefficients for the same elements in rock forming minerals. This would also cause melt Ta/Nb to decrease (D_{Ta}/D_{Nb}= 1.2; Bachmann *et al*., 2005) and Eu/Eu* to increase (D_{Eu}/D_{Eu*}= ~0.74 at ~FMQ+2 and ~760°C; Bachmann *et al*. 2005). Titanite crystallisation has been interpreted previously to influence the composition of co-crystallising phases, including zircon (Wotzlaw *et al.*, 2013; Buret *et al.*, 2016; Loader, 2017; Szymanowski *et al.*, 2017; Large *et al.*, 2018; Rezeau *et al.*, 2019; Nathwani *et al.*, 2021; Loader *et al.*, 2022), amphibole (Chelle-Michou *et al.*, 2015), and even on subsequent titanite

growth (Colombini *et al.*, 2011; Pamukcu *et al.*, 2013; Olson *et al.*, 2017) by its influence on residual melt compositions.

4.5.5 Trace element modelling

To test whether titanite crystallisation can explain the observed variation in amphibole chemistry, we developed a Rayleigh fractional crystallisation model, with Y used as an index of fractionation (see Appendix 6 for further details). Using published trace element partition coefficients, we calculated the composition (in terms of Sr/Y, Ta/Nb and Eu/Eu*) of hypothetical amphiboles in equilibrium with model melts which, in turn, were generated by fractional crystallisation. Yttrium was used as an index of fractionation as it systematically decreases from core to rim in amphibole (Figs. 4.7-9). The model comprises two stages; Stage 1 starts at an Y-rich melt composition to model the early period of amphibole crystallisation represented by the cores, and Stage 2 starts at a lower Y composition to model the amphibole rims. The Sr, Y, Sm, Eu, Gd, Ta and Nb compositions of the starting melt from the first stage were inverted from a representative, Y-rich amphibole core composition using partition coefficients from Nandedkar *et al.* (2016). Fractional crystallisation modelling of this melt involved an assemblage of plagioclase, amphibole and apatite, matching the assemblage determined from textural and thermometric estimates (Fig. 4.13). The crystallisation of plagioclase and amphibole have competing effects on Sr/Y and Eu/Eu*, with plagioclase driving both ratios to lower values due to the compatibility of Eu and Sr, and amphibole crystallisation driving the ratios to higher values due to the compatibility of Y, and the relative compatibility of Sm and Gd over Eu at typical magmatic oxidation states (Nandedkar *et al.*, 2016). As such, the plagioclase/amphibole ratio in the crystallising assemblage exercises a key control on the evolution of Sr/Y and Eu/Eu*. Crystallisation experiments show that plagioclase/amphibole ratios vary during the period of amphibole crystallisation and become more amphibole-poor as crystallisation proceeds (Nandedkar *et al*., 2014; Marxer & Ulmer; 2019). To account for this, Stage 1 of our model comprises three separate scenarios with plagioclase/amphibole ratios between 1.3 and 3.3, matching the range observed in these experimental studies. We also included 1% apatite to match the approximate modal abundance in the granitoids (Table 4.2).

In model Stage 2, biotite, zircon and titanite were added to the assemblage. The starting melt concentration of the index of fractionation, yttrium, was estimated by assuming equilibrium with one of the highest-Y titanite core compositions (Y = 2040 mg/g; 95th percentile of the total titanite data) from which the melt composition was inverted using partition coefficients. The starting Sr/Y, Ta/Nb, and Eu/Eu* were chosen from the results of the previous model. The proportions of biotite, titanite, and zircon were increased by a factor of 2.5 compared to their

abundance in the bulk rock to account for the ~60% crystallisation predicted to occur prior to the saturation of these phases (Marxer & Ulmer, 2019).

We did not consider the crystallisation of K-feldspar, quartz, or Fe-Ti oxides in our model, as these minerals have very low partition coefficients for the elements in our model (e.g. Bachmann *et al*., 2005) and/or crystallise close to the solidus, and as such are unlikely to exercise a significant control on the late-stage melt compositions being considered. Additionally, mass balance estimates demonstrate that these phases are not a significant host of the trace elements considered in our model (Fig. 4.15). Biotite was included in the model because of the compatibility of Ta and Nb into this phase (biotite/melt: $D_{Ta} = 1$ and $D_{Nb} = 2.9$; Bachmann *et al*., 2005).

Partition coefficients for plagioclase were selected from Dohmen and Blundy (2014), assuming an anorthite content of $X_{An} = 0.3$ and a temperature of 860°C. For amphibole (Nandedkar *et al.*, 2016), apatite (Prowatke & Klemme, 2006), titanite (Colombini *et al.*, 2011), and zircon and biotite (Bachmann *et al*., 2005), partition coefficients were selected from literature sources. Bulk partition coefficients for each model were estimated by weighting the individual mineral partition coefficients relative to their abundance in the crystallising assemblage for each element. These bulk partition coefficients are listed in Appendix 6.

For each mineral, D_{Eu} was estimated using the partition coefficients for $D_{Eu^{2+}}$ and $D_{Eu^{3+}}$, and the melt $\frac{Eu^{2+}}{Eu^{3+}}$ ratio using the equation of Wilke and Behrens (1999):

$$D_{Eu} = \frac{D_{Eu^{3+}} + \left(D_{Eu^{2+}} \times \frac{Eu^{2+}}{Eu^{3+}}\right)}{\left(\frac{Eu^{2+}}{Eu^{3+}}\right) + 1} \qquad \textbf{(Eq. 4. 1)}$$

assuming $D_{Eu^{2+}} = D_{Sr}$ and $D_{Eu^{3+}} = \sqrt{(D_{Sm} \times D_{Gd})}$ and estimating melt $\frac{Eu^{2+}}{Eu^{3+}}$ using the equation of Burnham *et al.* (2015):

$$\frac{Eu^{3+}}{\sum Eu} = \frac{1}{1 + 10^{-0.25 log fO_2 - \frac{6410}{T} - 14.2\Lambda + 10.1}} \qquad \textbf{(Eq. 4. 2)}$$

where T is temperature in Kelvin, and Λ is optical basicity (effectively a measure of melt polymerisation, calculated after; Duffy, 1993) which we set at 0.55. A temperature of 850°C was chosen, although the relationship of Burnham *et al.* (2015) is not strongly sensitive to temperature.

For Stage 2 of the model, we varied melt fO_2 between FMQ and FMQ+4 to assess the effect of changing melt redox on the evolution of the Eu anomaly.

The results of our models show that the late-stage crystallisation of titanite is required to reproduce the observed amphibole compositional trends (Fig. 4.16). Crystallising the Stage 1 assemblage, dominated by amphibole and plagioclase with accessory apatite, causes Sr/Y and Eu/Eu* to remain relatively constant, or to decrease if the plagioclase/amphibole ratio is high (Figs. 4.16A and C). Recreating the high Sr/Y amphibole rim compositions without titanite would require the fractionation of an assemblage with an unrealistically low plagioclase/amphibole ratio (<1.3). Even so, such an assemblage would not be able to reproduce the decreasing Ta/Nb ratios, which modestly increase in all Stage 1 models (Fig. 4.16B). Decreasing amphibole Ta/Nb may occur if the ratio of partition coefficients for both elements (i.e. D_{Ta}/D_{Nb}) were to decrease over the period of amphibole crystallisation. In fact, experimentally determined D_{Ta}/D_{Nb} values do decrease from between 1.1 to 0.8 between 1010 and 780°C (Nandedkar *et al.*, 2016). However, amphibole Ta/Nb decreases by up to an order of magnitude from core to rim (i.e. 0.035 to 0.003; Fig. 4.16B) and the variation in D_{Ta}/D_{Nb} is likely to be small over the temperature range recorded by the core to rim transition, requiring a decrease in melt Ta/Nb to explain the observed amphibole compositional data. Stepanov *et al.* (2014) noted that titanite was one of the few minerals which could reduce Ta/Nb in the residual melt. Other minerals which may cause decreasing melt Ta/Nb include rutile (absent in the studied rocks) and ilmenite (which comprises an extremely small modal proportion; Table 4.2). To test the absence of K-feldspar and quartz in our model, we adjusted the phase proportions of the Stage 2 model to include K-feldspar and quartz with plagioclase in eutectic proportions, with significantly less amphibole and biotite than the original model (5% each) but retaining the same proportion of titanite, apatite and zircon. The results of the model are strikingly similar irrespective of the proportion of the major phases, because the crystallisation of titanite is the dominant control on the trace elements considered in our model.

Results of our Stage 2 model (light blue boxes; Fig. 16b) highlight that the addition of a small amount of titanite (~2%) into the crystallising assemblage would decrease melt Ta/Nb. The influence of varying titanite modal abundance between 1% and 5% was investigated, revealing that Sr/Y and Eu/Eu* trajectories were not significantly impacted, but lower melt fractions were required to reach equivalent trace element ratios. Modelled Ta/Nb ratios, however, are strongly impacted by titanite modal abundance, which acts to decrease melt Ta/Nb with increasing titanite. Despite this, titanite modal abundances of <5% are unable to exactly reproduce the observed trajectories. This may be explained by the literature values used for DTa/DNb , which are relatively poorly constrained and range over an order of magnitude from 1.2 to 14.4

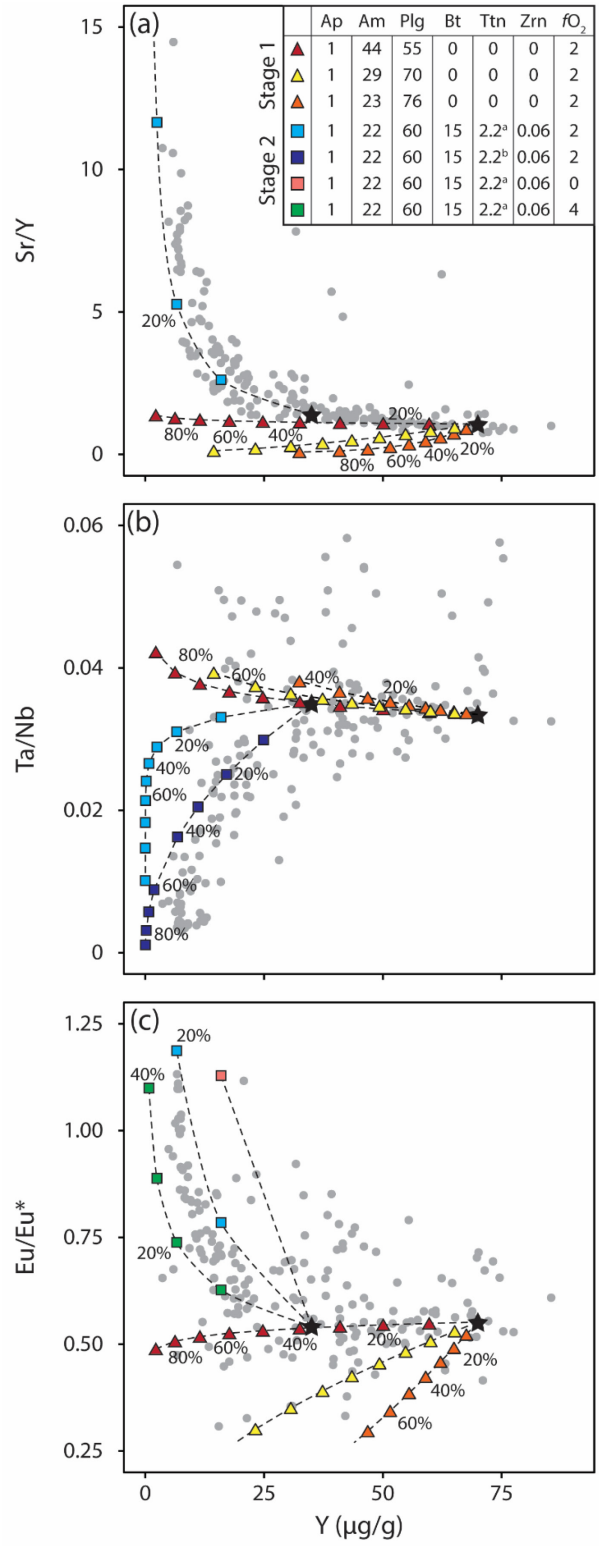


Figure 4.16. Modelling of hypothetical amphibole compositions as a function of Y content. Table denotes % of each mineral in the crystallising assemblage. Stage 1 comprises titanite-free assemblages, with variable amphibole plagioclase ratios. Stage 2 models comprise titanite-bearing assemblages. **A.** Sr/Y. **B.** Ta/Nb. Stage 2 models were also run using different titanite partitioning values [1]Colombini *et al.*, 2011. [2]Prowatke & Klemme, 2005. **C.** Eu/Eu*. Stage 2 models were also run at different oxygen fugacities (fO_2), with ΔFMQ of each assemblage noted.

(Green & Pearson, 1987; Bachmann *et al.*, 2005; Prowatke & Klemme, 2005). We note that the observed trajectories can be more accurately reproduced by utilising higher, titanite D_{Ta}/D_{Nb} ratios

(dark blue boxes; Fig. 4.16B). Nevertheless, the decreasing Ta/Nb, in addition to increasing Sr/Y and Eu/Eu* in amphibole necessitates the crystallisation of titanite and cannot be reasonably explained by other mechanisms.

Titanite crystallises from relatively oxidised magmas (Wones, 1989; Frost *et al.*, 2001), hence our models were primarily run at 2 log units above the FMQ redox buffer, within the range observed in arc-related magmas (e.g. Carmichael, 1991). To illustrate the effect of varying magmatic fO_2 on amphibole Eu/Eu*, we also ran Stage 2 models at FMQ and ΔFMQ+4 (Fig. 4.16C). The models predict that crystallisation at higher fO_2 produces a more gradual increase in Eu/Eu* for a given increment of fractionation of the titanite-bearing assemblage (Fig. 4.16C). This is because at higher oxidation states Eu^{3+} predominates in the melt, so it is more difficult to fractionate Eu from the neighbouring trivalent REEs (Sm and Gd), thereby limiting the potential to develop Eu anomalies. However, under more reducing conditions the melt Eu^{2+}/Eu^{3+} is greater, causing the mineral partitioning behaviour of Eu to differ from Sm^{3+} and Gd^{3+}. In our Stage 2 models $D_{Eu}{}^{3+} >> D_{Eu}{}^{2+}$, so more reducing conditions cause D_{Eu} to decrease relative to $D_{Sm}{}^{3+}$ and $D_{Gd}{}^{3+}$ (hence decreasing $D_{Eu/Eu*}$), resulting in a greater increase in Eu/Eu* in the residual melt for a given increment of crystallisation.

In summary, our models are unable to reproduce the observed amphibole core-rim variations without the late-stage crystallisation of titanite which, despite its modest abundance, plays a key role in controlling the near-solidus evolution of the residual melt composition. Such significant effects should be reflected in the composition of other co-crystallising minerals aside from amphibole. Thermometric and textural evidence suggests that, for example, apatite compositions would record a period of melt evolution prior to and during titanite crystallisation. Indeed, the apatite compositional data reported by Bruand *et al.* (2014) show abrupt changes from core to rim, with decreasing REE (including Y), and increasing La/Sm, Sr/Y, and Eu/Eu*; these observations are consistent with the onset of titanite crystallisation at some point after apatite saturation. In fact, the presence of continuous (rather than abrupt) trends in the same chemical parameters in titanite supports the idea that titanite passively records its own incremental crystallisation from the melt (see also Olson *et al.*, 2017).

4.5.6 Wider implications

Our results have important implications for studies that use mineral compositions to infer magmatic provenance. For example, amphibole compositions have been employed to deduce tectono-magmatic setting (Barnes & Barnes, 2020), and apatite trace element concentrations may be used to estimate host-rock compositions (Jennings *et al.*, 2011). Such studies assume that specific

signatures are unique to certain host rock compositions or tectono-magmatic settings. However, we have demonstrated that *in-situ* crystallisation of titanite can dramatically alter the trace element composition of the residual melt, and any late-crystallising minerals, concealing or exaggerating any pre-existing signatures and driving melt and mineral compositions away from that of the bulk rock.

As with amphibole and apatite, concentrations of REEs and HFSEs in zircon are used to reconstruct host rock composition (Belousova *et al.*, 2002), in addition to more empirical applications such as estimating crustal thickness (Tang *et al.*, 2019). Many studies have focussed on the use of zircon trace element signatures in the exploration for igneous rocks associated with porphyry Cu deposits (Ballard *et al.*, 2002; Pizarro *et al.*, 2020). These 'porphyry indicator' zircons are characterised by enrichments in Eu/Eu* and Ce/Nd (or Ce/Ce*) which are commonly ascribed to crystallisation from unusually oxidised magmas (Ballard *et al.*, 2002; Dilles *et al.*, 2015). However, these signatures likely reflect enrichment in the residual melt, either due to the suppression of plagioclase (Nathwani *et al.*, 2020) or due to the co-crystallisation of titanite (Loader *et al.*, 2017; Loader *et al.*, 2022), rather than high magmatic fO_2. Our results support those of previous studies (Loader *et al.*, 2017; Loader *et al.*, 2022), that the crystallisation of titanite can increase melt Eu/Eu* more efficiently than by increasing oxidation state alone. In fact, our results indicate that the generation of high melt Eu/Eu* is actually favoured by crystallisation of titanite under moderately (e.g. FMQ+2), rather than extremely oxidised conditions (e.g. FMQ+4). Indeed, many of the characteristics of porphyry indicator zircons (e.g. elevated Ce/Nd and low Yb/Gd and Th/U) can result from titanite co-crystallisation.

4.6 Conclusions

In this paper, we trace the chemical evolution of late-stage melts of the late-Caledonian Strontian magmatic system using amphibole and titanite compositions and demonstrate the following:

1) Amphibole rims record an abrupt change in the residual melt composition, characterised by decreasing Y contents and Ta/Nb ratios, and increasing Sr/Y and Eu/Eu* ratios, with similar, albeit more gradual, core-rim variations observed in titanite.
2) Early amphibole crystallisation (cores) prior to titanite saturation, followed by amphibole-titanite co-crystallisation, is evidenced by the intimate intergrowth of amphibole rims with titanite. This is corroborated by thermobarometric estimates, which indicate late-stage crystallisation of amphibole rims and titanite at relatively low temperatures (~800-680°C) in the upper crust (~7-10 km depth).

3) Estimation of the distribution of trace elements between mineral phases shows that titanite comprises a disproportionately large share of the whole-rock trace element budget, particularly for REEs and HFSEs, despite its modest modal abundance in the rock (<2 %).
4) Modelling of *in-situ* Rayleigh fractional crystallisation is consistent with an initial period of amphibole + feldspar + apatite crystallisation (represented by the amphibole cores) that was followed by a period of amphibole + plagioclase + apatite + biotite + titanite + zircon + quartz crystallisation (amphibole rims and titanite). The addition of a small amount of titanite (~2%) into the crystallising assemblage is required to produce the decreasing melt Y and Ta/Nb, as well as increasing melt Sr/Y and Eu/Eu* implied by amphibole rim compositions. Increasing the oxidation state of our model caused the melt Eu/Eu* to increase more slowly for the same degree of crystallisation, due to the differential partitioning behaviour of Eu^{2+} and Eu^{3+}.

Our study emphasises the decoupling between whole-rock compositions (whose signatures are often generated in the lower crust) and mineral compositions (which are more strongly influenced by shallow crustal processes), with important implications for the use of mineral compositions in provenance and mineral deposit prospectivity studies. In particular, caution should be exercised when interpreting the chemistry of minerals which crystallise at low temperatures (<800°C) due to the potential effects of accessory mineral crystallisation on residual melt compositions.

Chapter 5. Titanite as a recorder of magmatic evolution in the Chuquicamata district

5.1 Introduction

The Chuquicamata district is one of the largest porphyry Cu(-Mo-Au) districts in the world, being responsible for an estimated 17% of worldwide Cu production in 2011 (Rivera *et al.*, 2012). Located in the Atacama Desert, approximately 1650 km north of Santiago and 200 km northeast of Antofagasta, the district is estimated to have already produced 35.5 Mt of Cu, with a further known resource of >100 Mt. Small-scale mining in the district dates back to ~500 AD (Petersen, 2011) and persisted until the end of the 19th century, after which the Chile Exploration Company was created and subsequently purchased by the Anaconda Copper Company (Rivera *et al.*, 2012). Today, the Chuquicamata mining complex, comprising four separate open pits (Chuquicamata, Radomiro Tomic, Mina Sur and MMH) and the Toki Cluster of deposits, is wholly owned by CODELCO (Chilean state-owned mining company).

The Chuquicamata district forms part of the Andean Eocene-Oligocene Cu belt and is located within the Domeyko fault system of northern Chile, a major arc-parallel structural zone that is associated with several world-class porphyry districts including Escondida and Collahuasi (Richards *et al.*, 2001). The present-day configuration of the Chuquicamata district has been shaped by the West Fault, a strand of the Domeyko fault system, which has juxtaposed mineralised porphyritic intrusions of the Chuquicamata Intrusive Complex in the east against older, barren intrusions of the Los Picos-Fortuna Complex to the west (Fig. 5.1). Major movement along the West Fault is believed to have taken place after the mineralising event, leading to much speculation about the location of a possible missing half of the Chuquicamata deposit (Rivera *et al.*, 2012; Zentilli *et al.*, 2021). Although several authors have advocated for c. 35 km of sinistral strike-slip offset across the West Fault based on the correlation of the Fortuna Complex with the Pajonal-El Abra Complex to the north (Dilles *et al.*, 1997; Campbell *et al.*, 2006), corresponding portions of the Chuquicamata and MMH deposits have not yet been located on opposing sides of the West Fault (Rivera *et al.*, 2012).

This chapter aims to determine the extent to which titanite textures and compositions vary throughout the world class Chuquicamata porphyry Cu deposit. In particular, textural, geochemical and thermometric variations in the lead-up to the mineralising event are investigated, which could provide key insights into the formation of these magmatic-hydrothermal ore deposits. It was for this reason that Chuquicamata was chosen as a case study, given the protracted timescales (~ 10 Ma) over which magmas evolved in the district (Ballard *et al.*, 2002; Rivera *et al.*, 2012).

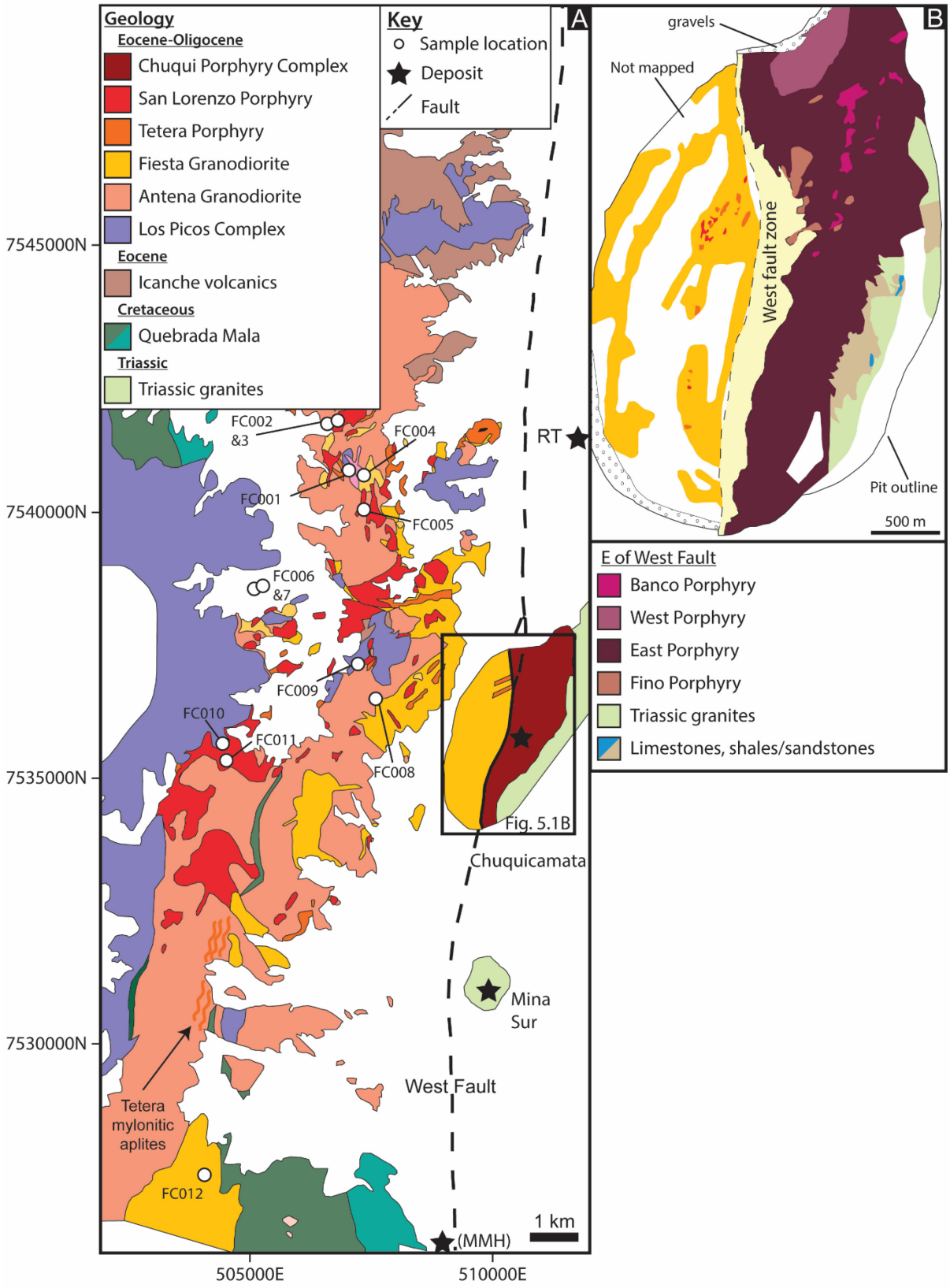


Figure 5.1. Simplified geological map of the Chuquicamata region. **A.** Regional geological map showing sample and mine locations, as well as the West Fault. Modified from Dilles *et al.* (2011). **B.** Map of the Chuquicamata open pit, units on the western side of the West Fault are the same as in Fig. 5.1A. Modified from Ossandón *et al.* (2001).

5.2 Geologic setting

The oldest rocks in the district are a series of metasedimentary to metaplutonic rocks of Precambrian to lower Paleozoic age. A variety of extrusive and intrusive rocks were emplaced between the late Paleozoic and early Mesozoic, including the Carboniferous Mesa Granite, Permo-Triassic volcano-sedimentary sequences of the Collahuasi Group and the Triassic Elena Granodiorite (Ossandón *et al.*, 2001; Campbell *et al.*, 2006; Zentilli *et al.*, 2018). Triassic granitoids are spatially coincident with (Fig. 5.1) and display similar whole-rock compositions to Eocene-Oligocene porphyry intrusions at both Chuquicamata and MMH, but may be distinguished by titanite abundance and crystal habit (Zentilli *et al.*, 2018). In the Jurassic, marine sedimentary sequences of the Caracoles Group were deposited.

To the west of the West Fault there are exposures of Cretaceous lavas and tuffs of andesitic to dacitic composition (e.g. Quebrada Mala; Fig. 5.1A), as well as continental sedimentary rocks. Magmatic activity in the Eocene-Oligocene is first recorded by volcanic breccias and conglomerates of the Icanche Formation (early-middle Eocene). Intrusive rocks of the monzonitic to dioritic Los Picos Complex (~43-42 Ma; Campbell *et al.*, 2006) were subsequently intruded into the Icanche Formation (Dilles *et al.*, 2011). The Fortuna Complex consists of four different units which (from oldest to youngest) are as follows: the Antena granodiorite (~39-38 Ma), Fiesta granodiorite (~39-38 Ma), Tetera porphyry and San Lorenzo porphyry (~38 Ma; Campbell *et al.*, 2006). The Chuquicamata Igneous Complex, which represents the youngest intrusive activity in the district, comprises three to four separate, mineralised porphyritic intrusions (Fig. 5.1B). The oldest and most extensive of these is the Este Porphyry, which is cut by the Oeste Porphyry in the north of the Chuquicamata pit, and by the Banco (and possibly Fino) Porphyry in central and western areas of the pit (Rivera *et al.*, 2012). Finally, deposition of Miocene to Holocene cover of alluvial, colluvial and aeolian sediments, as well as volcanic flows, provides evidence for rapid uplift (Campbell *et al.*, 2006; Rivera *et al.*, 2012). Despite their faulted contact with the Chuquicamata Igneous Complex, both the Los Picos and later Fortuna Complex (~42-38 Ma; Campbell *et al.*, 2006), are believed to be precursor intrusions to porphyry mineralisation, either at the El Abra deposit (Ballard *et al.*, 2002; Campbell *et al.*, 2006) or at the Toki Cluster (Barra *et al.*, 2013).

5.3 Samples

Data presented here come from 12 samples of the Los Picos-Fortuna Complex, the igneous complex that predates mineralisation, and 11 samples from the Chuquicamata open pit which were

donated to the NHM by Marcos Zentilli (Table 5.1). All of the main intrusive phases are represented in the sample suite. Titanite was analysed (Appendix 2) in both mineral separates and *in-situ* for some samples, but in one of either mineral separates or *in-situ* for others (Table 5.1). Ten samples of the main intrusive phases were selected for automated SEM analysis using the TESCAN TIMA. Zircon chemistry from all samples (Loader, unpublished data) and whole-rock chemistry (Loader, unpublished data) from the Los Picos-Fortuna Complex was also utilised (Table 5.1; Loader, unpublished data). Zircon compositional data were collected by laser ablation ICP-MS at the Natural History Museum and whole-rock major element and trace element compositions were determined at ALS (Loughrea, Ireland), via methods ME-IPC06 and ME-MS81.

Table 5.1. Sample information, analytical techniques and number of analyses.

Sample	Unit	Grid reference*	Alteration	TIMA	No. of titanite analyses (Min-Sep)	Zircon	Whole-rock
FC001	Antena Grd	507037, 754080	Propylitic (weak)	N	32 (32)	Y	Y
FC002	Antena Grd	506800, 754168	Fresh	Y	59 (42)	Y	Y
FC003	Antena Grd (mafic)	506597, 754167	Fresh	N	-	Y	Y
FC004	Antena Grd	507348, 754068	Propylitic (weak)	N	26 (26)	Y	Y
FC005	Antena Grd	507348, 754007	Propylitic (weak)	N	46 (46)	Y	Y
FC006	Los Picos	505104, 753856	Sericitic (weak)	Y	5 (5)	Y	Y
FC007	Los Picos (fine)	505083, 753857	Fresh	N	-	Y	Y
FC008	Antena Grd	507604, 753651	Potassic (locally)	Y	49 (39)	Y	Y
FC009	San Lorenzo	507235, 753715	Potassic	Y	11 (0)	Y	Y
FC010	Los Picos	504480, 753562	Propylitic	N	6 (6)	Y	Y
FC011	San Lorenzo	504536, 753536	Propylitic	N	-	Y	Y
FC012	Fiesta Grd	504053, 752757	Potassic	Y	-	Y	Y
CH001	Banco Ppy	-	Int argillic after potassic	Y	-	Y	N
CH002	Elena Grd (Triassic)	-		N	-	Y	N
CH003	Elena Grd (Triassic)	-	Chlorite-sericite	Y	11 (0)	Y	N
CH004	Este Ppy	-		N	-	Y	N
CH005	Este Ppy	-	Propylitic	Y	13 (0)	Y	N
CH006	Este Ppy	-		N	-	Y	N
CH007	Este Ppy	-	Propylitic	Y	35 (0)	Y	N
CH008	Este Ppy	-		N	-	Y	N
CH009	Felsic dyke (Triassic)	-		N	-	Y	N
CH010	Oeste Ppy	-		N	-	Y	N
CH011	Oeste Ppy	-	Potassic	Y	-	Y	N

*CH001-CH011 come from the eastern side of the Chuquicamata open pit.

All studied samples contain, or likely contained prior to hydrothermal alteration, quartz, K-feldspar, plagioclase, amphibole and biotite as major minerals, with Fe-Ti oxides (magnetite, ilmenite and rutile), apatite, zircon and titanite as accessory phases. Despite varied absolute abundances, relative proportions of quartz, alkali feldspar and plagioclase are fairly consistent, with all samples besides the Oeste Porphyry (monzogranite) classified as granodiorites (Fig. 5.2). For the Oeste Porphyry sample, addition of K-feldspar during potassic alteration is likely responsible for classification as a monzogranite. Mafic minerals, principally biotite and amphibole, comprise

<10 % of the rocks, although modal abundances of igneous minerals are difficult to reconstruct in samples which have been intensely hydrothermally altered (e.g. CH011). The occurrence of apatite and zircon throughout the studied rocks is fairly consistent, with apatite (0.1-0.3 modal%) disseminated throughout samples and zircon (<0.01-0.04 modal%) often associated with mafic minerals (in addition to Fe-Ti oxides, apatite and titanite). Magnetite is the dominant Fe-Ti oxide phase, with subordinate ilmenite present in samples FC002 (Antena Granodiorite) and FC006 (Los Picos Complex), and hydrothermal rutile present in more strongly altered rocks. In terms of felsic minerals, plagioclase often exhibits euhedral crystal forms and displays normal or reverse zonation, with quartz and K-feldspar typically interstitial. Despite these similarities, there is significant textural variation between units which, in addition to the impacts of hydrothermal alteration, will be outlined below.

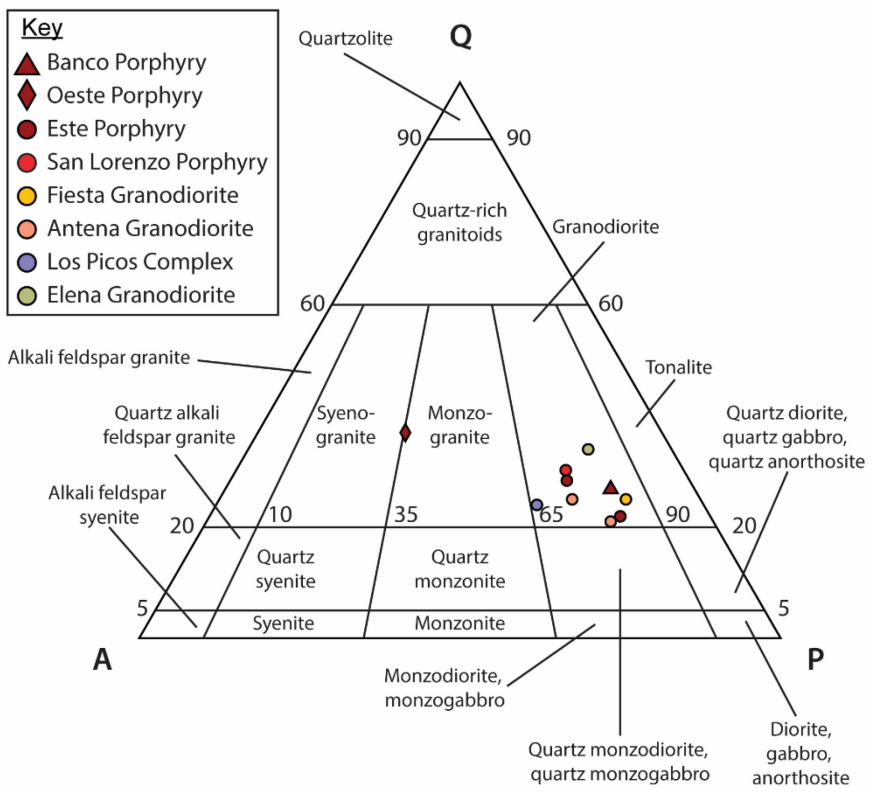


Figure 5.2. Quartz (Q)-Alkali(A)-Plagioclase (P) diagram (Streckeisen, 1976) for intrusive phases from the Chuquicamata district. Classification based on automated SEM mapping of thin sections. All intrusions classify as granodiorites except for the Oeste Porphyry sample, to which significant quartz and alkali feldspar has been added during potassic alteration.

Elena Granodiorite (CH003)

The Triassic Elena Granodiorite (sample CH003) exhibits many of the same characteristics as the Eocene-Oligocene intrusions. It is an equigranular rock (average grain size of ~1-2 mm) consisting of euhedral to subhedral plagioclase and amphibole, anhedral biotite, interstitial quartz and K-feldspar, with accessory apatite, titanite and zircon. Both mafic and felsic minerals are moderately

altered. Plagioclase has been altered to muscovite, kaolinite and epidote, and mafic minerals to chlorite with subordinate epidote, Fe-Ti oxides, apatite, allanite and titanite. Finally, partial replacement of mafic phases by calcite is sometimes observed close to late-stage calcite veins.

Los Picos Complex (FC006)

Los Picos sample FC006 is also equigranular, with an average crystal size of 1-2 mm. Unlike other samples, it contains small amounts (~2%) of euhedral to subhedral clinopyroxene (diopside-hedenbergite). These pyroxenes are 0.2-0.5 mm in diameter and are often intimately associated with amphibole, possibly indicating that pyroxenes were hydrated to form amphibole. Additionally, minor chloritisation of subhedral to anhedral amphibole is observed in some areas. Based on quartz, K-feldspar and plagioclase modal abundances, this sample would be classified as a granodiorite, although it plots close to the monzogranite boundary (Fig. 5.2).

Antena Granodiorite (FC002 & FC008)

Plagioclase, forming laths up to 5 mm in length, is the most abundant mineral in the Antena Granodiorite, comprising 40-50% of the rock. These plagioclase crystals show variable core to rim zonation, including normal, reverse or patchy zoning types, in addition to an abundance of mineral inclusions (amphibole, apatite and Fe-Ti oxide) in some crystals. Amphibole (0.1-3.5 mm) and biotite (0.3-1.2 mm) are generally unaltered, exhibiting euhedral to anhedral crystal forms.

Fiesta Granodiorite (FC012)

Unlike earlier intrusions, the Fiesta Granodiorite shows a porphyritic texture, containing phenocrysts of plagioclase (1-4 mm) and amphibole (0.5-2 mm) in a groundmass of quartz and K-feldspar. Amphibole phenocrysts have been completely replaced by secondary biotite, and a paucity of crystals with typical biotite habits suggest that amphibole was the dominant primary mafic mineral. Significant sulphur has been added to this sample, as evidenced by disseminated anhydrite (0.4 %) and celestine ($SrSO_4$; 0.05%). These sulphates are concentrated in a K-feldspar vein which is also associated with chlorite and biotitised amphibole phenocrysts.

San Lorenzo Porphyry (FC009)

The San Lorenzo Porphyry consists of plagioclase (1-4.5 mm), quartz (0.65- 1.5 mm), amphibole (0.5-2 mm) and biotite (<2.5 mm) phenocrysts in an alkali feldspar-quartz groundmass. Despite significant hydrothermal alteration, primary zonation can still be identified in plagioclase, which displays oscillatory as well as normal and reverse types. Amphibole phenocrysts are completely biotitised and biotite in some areas is partly chloritized.

Este Porphyry (CH005 & CH007)

The Este porphyry can be distinguished from the earlier San Lorenzo by its larger phenocryst size, with plagioclase phenocrysts 2-7 mm in length, and by the presence of rare K-feldspar phenocrysts. Hydrothermal alteration in these samples is characterised by the partial to complete chloritisation of mafic minerals and the partial to complete replacement of plagioclase by muscovite, kaolinite and K-feldspar.

Banco Porphyry (CH001)

The Banco Porphyry sample (CH001) contains quartz (0.1-3.5 mm), plagioclase (1-4.5 mm) and mafic phenocrysts (<0.9 mm) in a groundmass of K-feldspar and quartz. Hydrothermal alteration is characterised by complete replacement of mafic minerals by biotite (and also partial chloritisation of biotite), in addition to the partial alteration of plagioclase to muscovite and kaolinite. Minor sulphides, in the form of pyrite and chalcopyrite, are disseminated throughout the rock and pyrite is also present in K-feldspar + biotite veinlets.

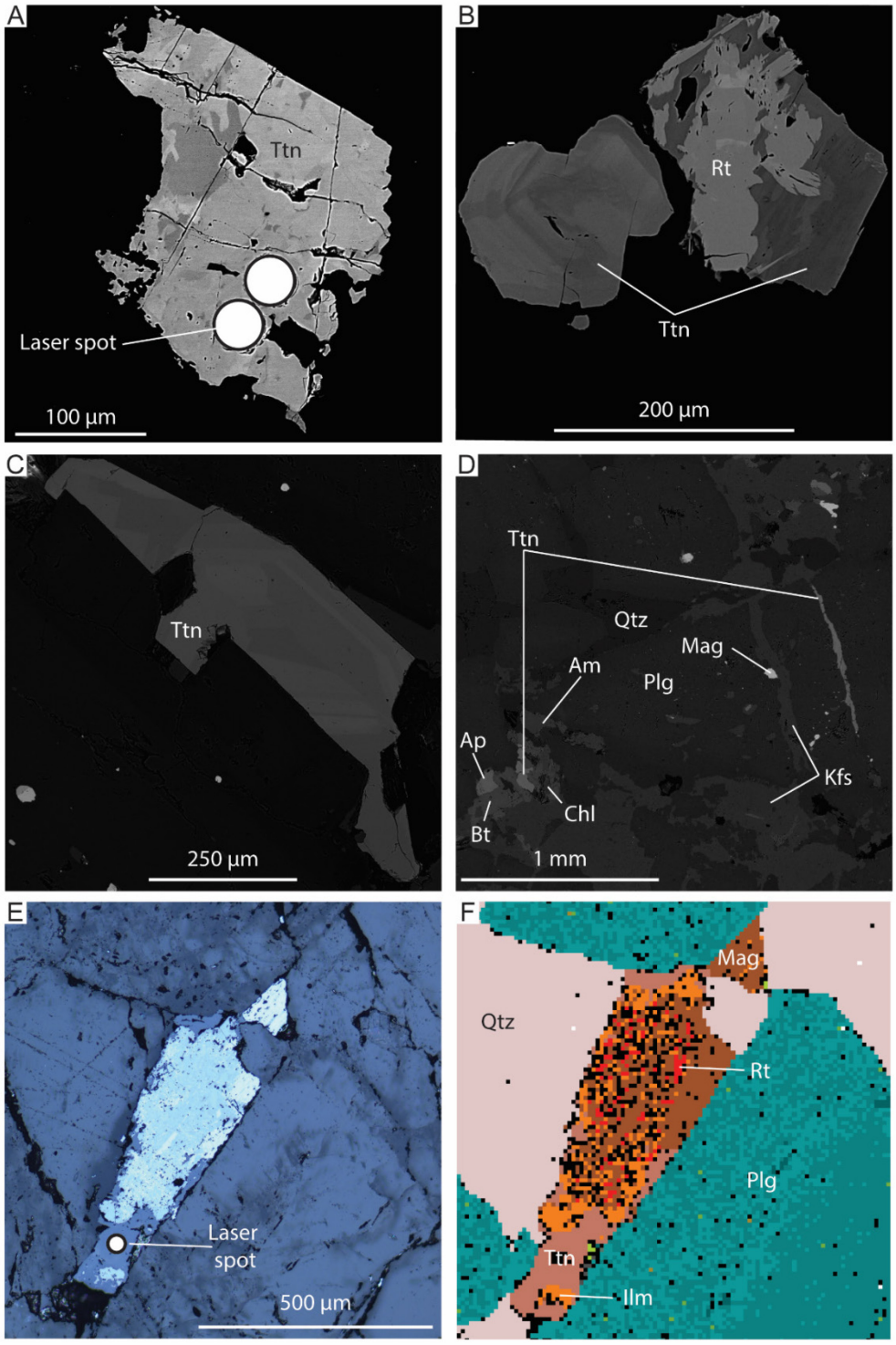
Oeste Porphyry (CH011)

The sample of Oeste Porphyry is an intensely potassically altered, quartz-, plagioclase- and biotite-phyric rock, showing pervasive K-feldspar alteration and multiple generations of veining. Quartz veinlets (~1 mm) contain molybdenite, chalcopyrite and anhydrite with a K-feldspar selvage. Plagioclase is partially altered to kaolinite and sericite; mafic phenocrysts are completely biotitised.

5.4 Results

5.4.1 Titanite textures

Titanite from the Chuquicamata district shows a range of textures, with significant variation between different units and even different samples from the same unit. Each grain selected for further analysis was initially classified as igneous, altered, replacement or vein titanite, meaning that igneous signatures could be isolated, and the magmatic evolution of the system could be traced through time, in addition to providing a sense of how igneous titanite compositions may be modified during hydrothermal alteration. Grains were classified based on shape, size and mineral associations, with the characteristics of various titanite textural types detailed in Chapter 6. At Chuquicamata, titanite with both igneous and hydrothermal origins may be found in the same sample. For example, in the Triassic Elena Granodiorite titanite occurs interstitially in subhedral to anhedral crystal forms (Fig. 5.3A), with an interpreted altered igneous origin,


A
Ttn
Laser spot
100 µm
B
Rt
Ttn
200 µm
C
Ttn
250 µm
D
Ttn
Qtz
Mag
Am
Plg
Ap
Kfs
Chl
Bt
1 mm
E
Laser
spot
500 µm
F
Mag
Qtz
Rt
Plg
Ttn
Ilm

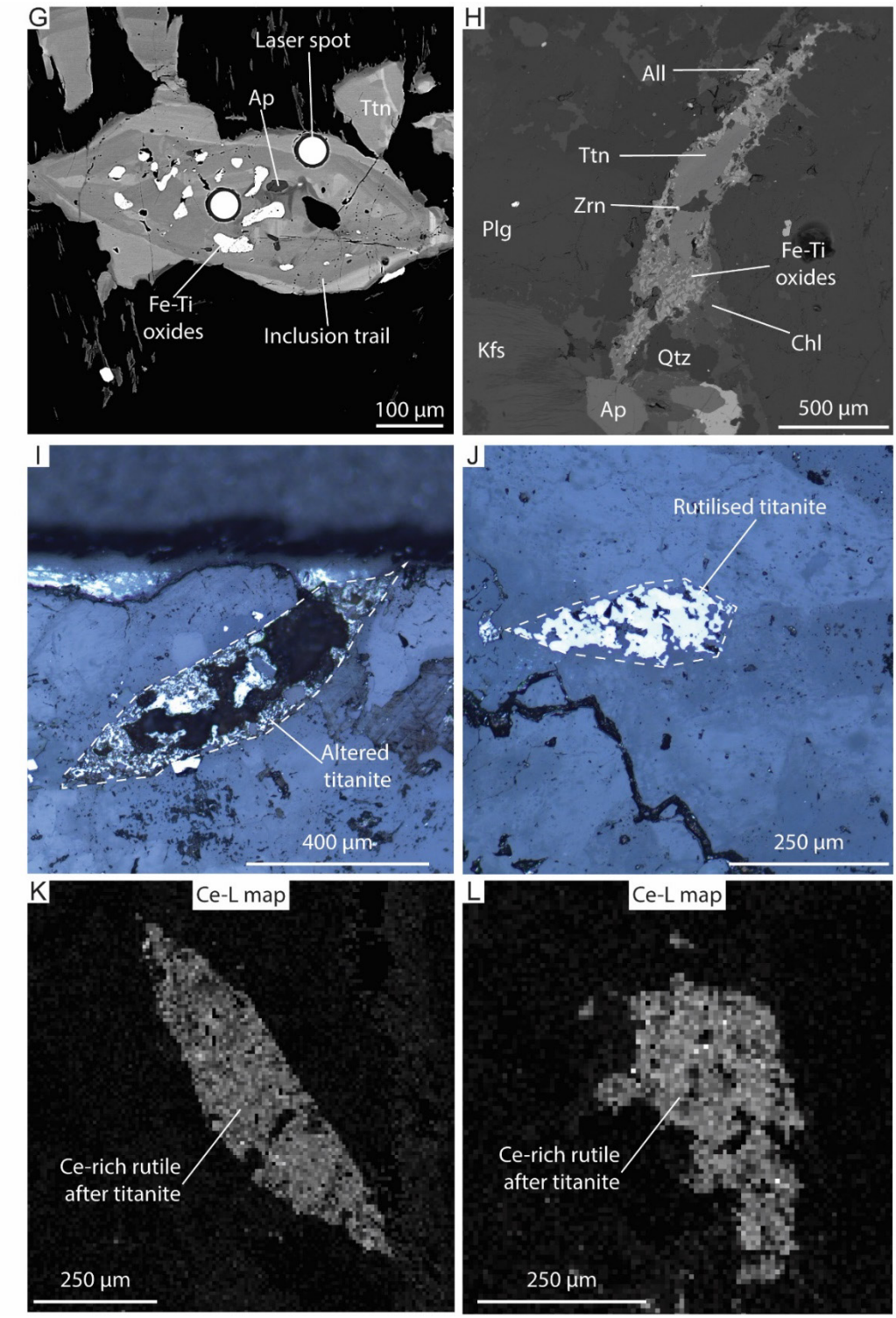


Figure 5.3. Titanite SEM-BSE images, reflected light photomicrographs and TESCAN TIMA phase maps from the Chuquicamata district. A-D: SEM-BSE images from the Elena Granodiorite (**A.**), Los Picos Complex (**B.**) and Antena Granodiorite (**C-D.**). Reflected light photomicrograph (**E.**) and TESCAN TIMA phase map (**F.**) of a partially altered titanite crystal from the San Lorenzo Porphyry. **G-H**. SEM-BSE images from the Este Porphyry. **I-J.** Reflected light photomicrographs of pseudomorphed titanite from the Banco (**I.**) and Oeste (**J.**) porphyries. **K-L.** Rutile pseudomorphs after titanite, displaying high Ce contents from the Banco (**K.**) and Este (**L.**) porphyries.

and also in association with chloritized mafic minerals, suggesting a hydrothermal (or replacement) origin.

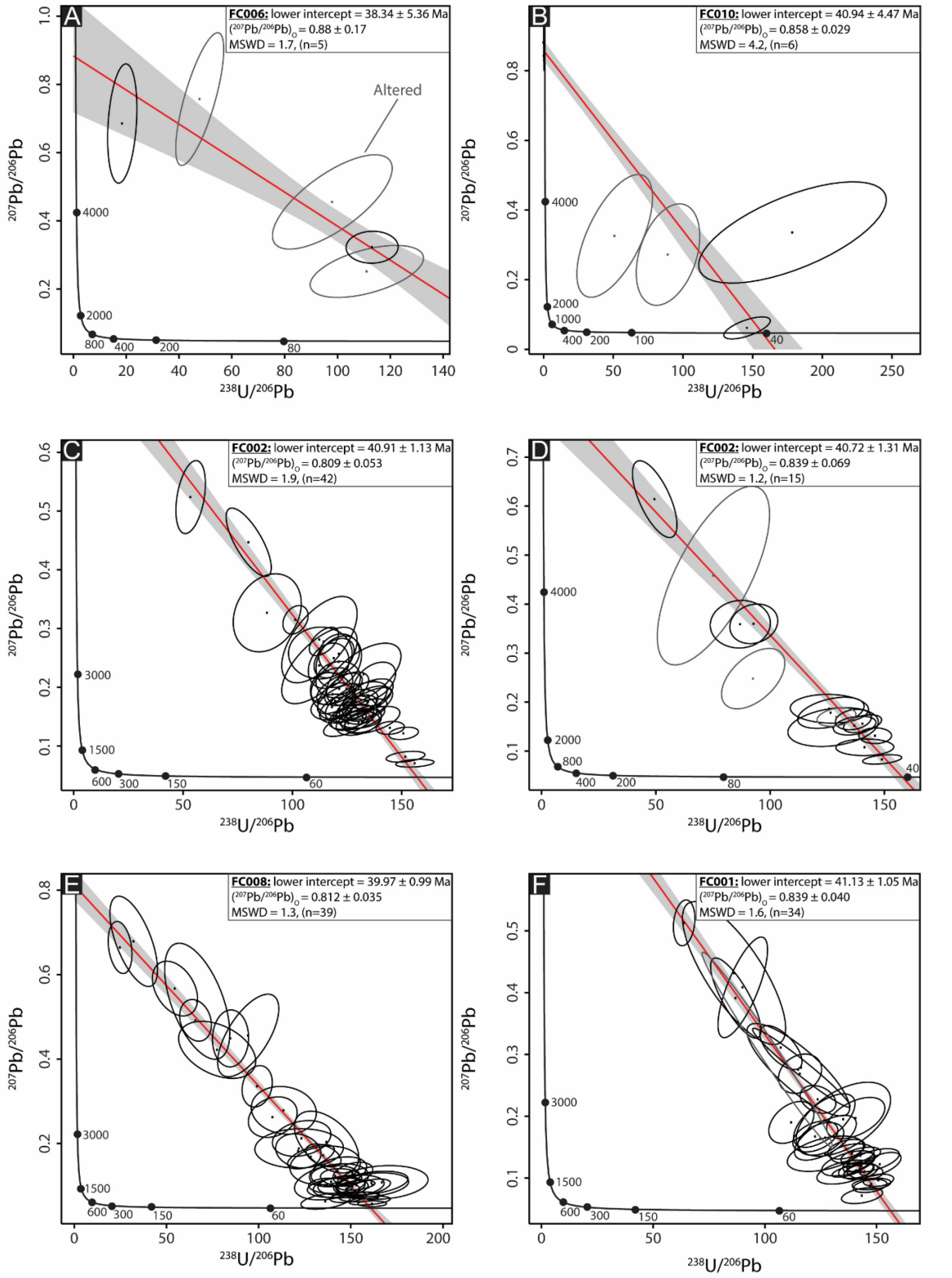
In the Los Picos Complex, titanite (<0.1 mm) is rarely found *in-situ*, with all analyses coming from mineral separates. Here, titanite is exclusively irregularly zoned and is either found as: i) anhedral grains associated with amphibole, apatite and magnetite; or ii) in irregular associations with rutile, magnetite and ilmenite (Fig. 5.3B). Similarly, titanite from the Antena Granodiorite is often irregularly zoned, although it is more abundant (~0.05-0.1%) and shows more euhedral crystal forms (Fig. 5.3C) than in the Los Picos Complex. The occurrence of titanite varies significantly between samples of the Antena Granodiorite. For example, in FC002 titanite is located either interstitially (Fig. 5.3C), or in Fe-Ti oxide + apatite aggregates, whereas in FC008 it is found in either K-feldspar + titanite + amphibole ± biotite veins, as thin rims on magnetite, or in association with chlorite (Fig. 5.3D). In the San Lorenzo Porphyry, titanite is found either as partially replaced microphenocrysts (<0.5 mm) or intergrown with chlorite. In this sample, titanite has been altered to a rutile + ilmenite + quartz ± plagioclase ± allanite ± magnetite assemblage (Figs. 5.3E, F). In the Fiesta Granodiorite, titanite is rare (<0.01 %) and no unambiguous titanite pseudomorphs were identified. Titanite from the Este Porphyry is euhedral to subhedral, moderately sized (<0.25 mm) and often contains inclusion trails (Fig. 5.3G) as well as mineral inclusions of apatite, zircon and Fe-Ti oxides. Titanite is more abundant (~0.2%) and relatively unaltered in sample CH007. These crystals generally show clear zonation, often from a patchy or sector-zoned core to a bright rim (Fig. 5.3G). In sample CH005, titanite is less abundant (~0.05%) and has been either i) partially to completely replaced by an assemblage of rutile + ilmenite ± chlorite ± allanite ± magnetite (Fig. 5.3H); or occurs in albite + K-feldspar + quartz veinlets.

Unequivocal euhedral titanite pseudomorphs, up to 1 mm in length, are observed in the Banco and Oeste porphyries, with relict titanite sometimes present in the core. In the Banco Porphyry (CH001), large (0.2-1 mm) titanite microphenocrysts (Fig. 5.3I) constitute 0.3% of the rock and have been altered to rutile + ilmenite ± quartz ± chlorite ± magnetite. In the Oeste Porphyry (CH011), however, titanite pseudomorphs are smaller (<200 μm), less abundant (~0.1%) and have been altered almost entirely to rutile (Fig. 5.3J). Secondary rutile after titanite contains elevated trace element contents, including Ce (Figs. 5.3K and L).

5.4.2 U-Pb Geochronology

A total of 293 spots were analysed from 11 samples in two separate runs (Appendix 2; Table 5.2), both *in-situ* and in mineral separates, to determine titanite major and trace element compositions as well as U-Pb isotopes. Contaminated analyses or those which returned high errors (e.g. >20%) were removed, leaving 236 valid analyses (Table 5.2). Titanite U-Pb data were subsequently plotted on Tera-Wasserburg diagrams (Fig. 5.4) and an MSWD was calculated for each sample, with all

samples besides CH003 (MSWD = 0.4) returning values of >1 (Table 5.2). Additionally, acceptable MSWD values based on the number of analyses were also calculated (Wendt & Carl, 1991).



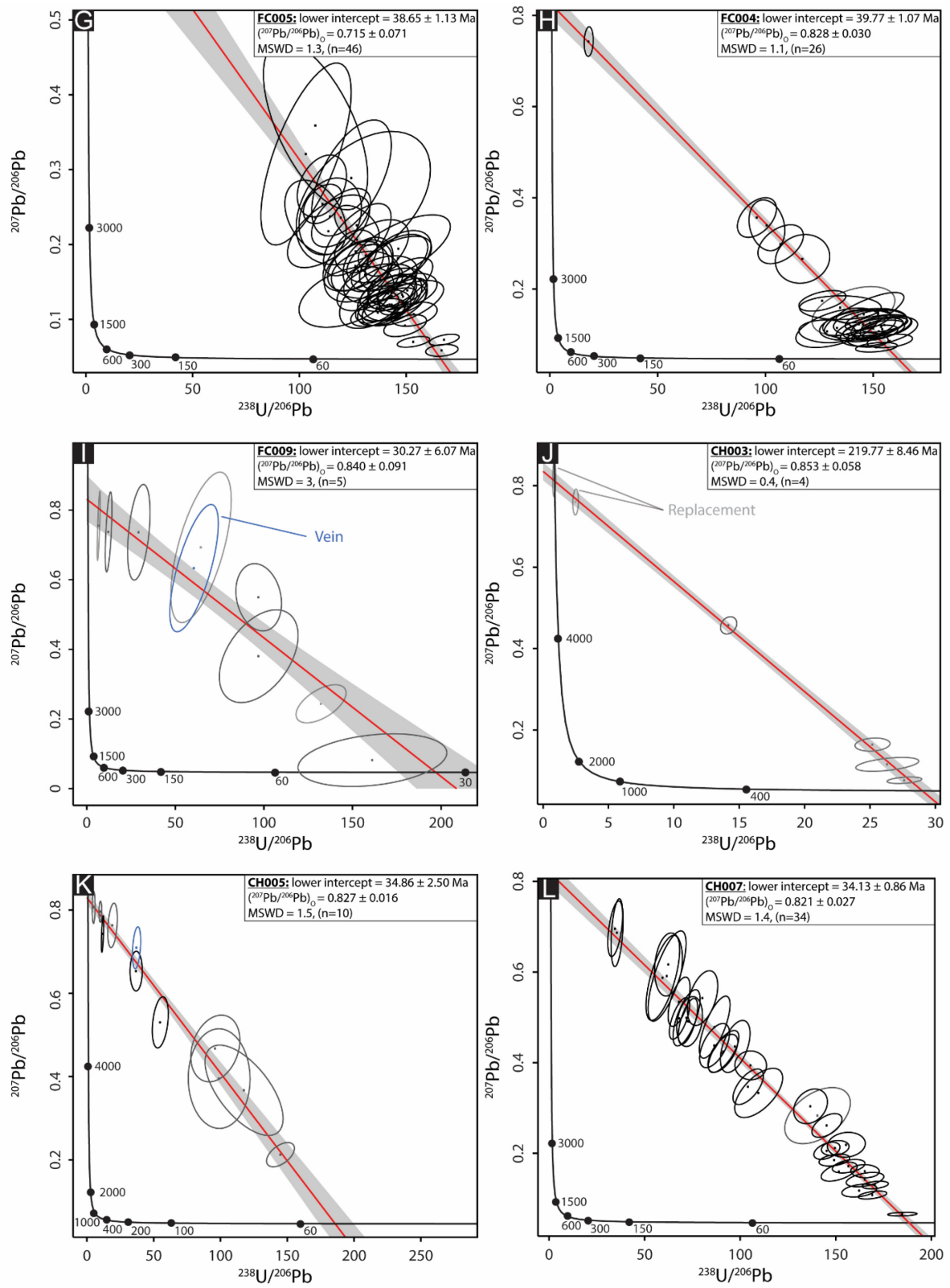


Figure 5.4. Tera-Wasserburg Concordia diagrams for titanite age data from the Los Picos Complex (**A-B.**), Antena Granodiorite (**C-H.**), San Lorenzo Porphyry (**I.**), Elena Granodiorite (**J.**) and Este Porphyry (**K, L.**). 2σ error ellipses are shown, in addition to the 2σ uncertainty associated with the regression. Crystallisation ages are presented with error, which is derived from the regression, with an additional propagated external uncertainty of 2%.

Table 5.2. Titanite U-Pb isotopic data for the Chuquicamata district. Titanite lower intercept ages, 2σ error and an additional propagated 2% external uncertainty, as well as MSWD and acceptable MSWD are shown. Acceptable MSWD is calculated using the equation of Wendt and Carl (1991).

Sample	Unit	Min-Sep/ In-Situ	n	Age (Ma)	2σ error	2σ +2% ext. uncert)	MSWD	Acceptable MSWD*
FC001	Antena Grd	Min-Sep	34	41.13	0.65	1.05	1.5	1.6
FC002	Antena Grd	Min-Sep	42	40.91	0.78	1.13	1.9	1.4
FC002	Antena Grd	In-Situ	15	40.72	1.03	1.31	1.2	1.8
FC004	Antena Grd	Min-Sep	2	39.77	0.72	1.07	1.1	1.6
FC005	Antena Grd	Min-Sep	46	38.65	0.82	1.13	1.3	1.4
FC006	Los Picos	Min-Sep	5	38.34	5.30	5.36	1.7	2.4
FC008	Antena Grd	Min-Sep	39	39.97	0.58	0.99	1.3	1.5
FC008	Antena Grd	In-Situ	7	36.50	2.17	2.29	2.5	2.2
FC009	San Lorenzo	In-Situ	5	30.27	6.04	6.07	3.0	2.4
FC010	Los Picos	Min-Sep	6	40.94	4.39	4.47	4.2	2.3
CH003	Elena Grd	In-Situ	4	219.8	7.2	8.5	0.4	2.6
CH005	Este Ppy	In-Situ	10	34.86	2.40	2.50	1.5	1.9
CH007	Este Ppy	In-Situ	34	34.13	0.53	0.86	1.4	1.5

5.4.3 Geochemistry

Titanite in the Triassic Elena Granodiorite was predominantly classified as altered igneous, with chondrite-normalised titanite REE patterns that are generally flat to positively sloping (Fig. 5.5A), exhibiting a more negative Eu anomaly compared to its host rock. Analyses of replacement titanite in the Elena Granodiorite exhibit either similar patterns to altered igneous titanite, or a strongly negatively sloping pattern (Fig. 5.5A), although only a small number of successful analyses were possible. Similarly, only a few successful analyses were possible for the Los Picos Complex, which contained both igneous and altered igneous titanite. Despite the variable influence of hydrothermal alteration, Los Picos titanite exhibits a consistent REE pattern, with a pronounced hump in the light to middle REEs and a moderately negative Eu anomaly like its whole-rock composition (Fig. 5.5B). Antena Granodiorite titanite shows similar REE patterns to the Los Picos Complex, albeit with a slightly less humped LREE pattern and greater REE content (Fig. 5.5C). San Lorenzo Porphyry titanite grains were classified as either replacement or altered igneous types, with an igneous signature (i.e. comparable to titanite from other units; Fig. 5.5D) retained in two altered igneous titanites (Fig. 5.5D). REE compositions are much more variable compared to other units and differ significantly to the host-rock composition. For the Este Porphyry, the two samples display a depletion in MREEs, resulting in the development of the listric-shaped REE pattern that often characterises porphyry-associated whole-rocks (Figs. 5.5E, F). There are some notable differences between the two Este Porphyry samples, with CH005 containing several altered igneous titanites, which often exhibit positive Eu anomalies, and significant HREE depletion in some instances (Fig. 5.5E).

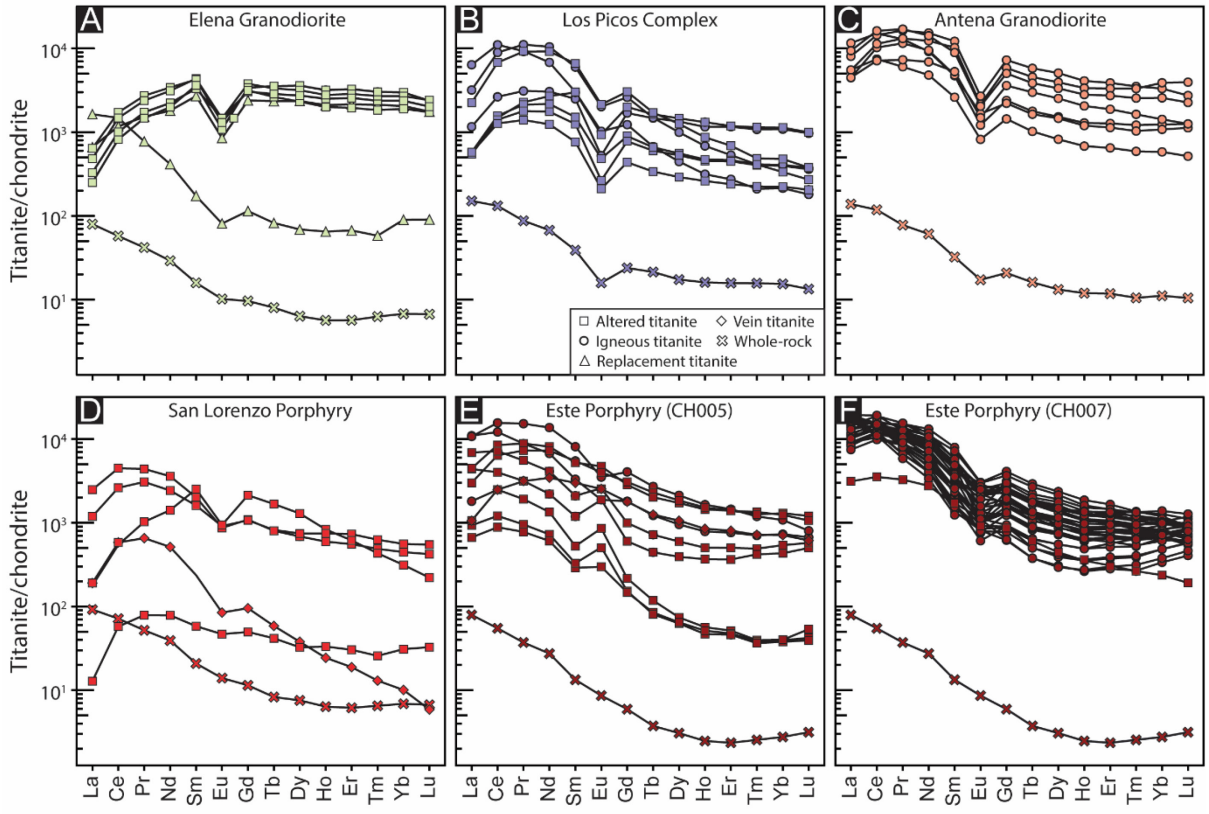


Figure 5.5. Chondrite-normalised (Boynton, 1984) REE plots for titanite from the Chuquicamata district , designated as igneous, replacement, altered igneous or vein-hosted on textural grounds. Also shown are average whole-rock compositions from the Los Picos-Fortuna Complex (Loader, unpublished data), as well as the Elena Granodorite (Zentilli *et al.*, 2018) and Este Porphyry (Ballard, 2001). **A.** Elena Granodiorite. **B.** Los Picos Complex. **C.** Antena Granodiorite. Because of the abundance of analyses from the Antena Granodiorite, only median values for individual samples are displayed. **D.** San Lorenzo Porphyry. **E.** Este Porphyry (CH005). **F.** Este Porphyry (CH005). Average 2σ analytical error is smaller than symbol size.

Bivariate plots of REE and trace element ratios better illustrate titanite compositional variation. Various trace element ratios are plotted against Th/U, which has been shown to differentiate titanite formed in different environments (Gao *et al.*, 2012; Deng *et al.*, 2015; Scibiorski & Cawood, 2022). Igneous titanite tends to cluster at low Eu/Eu* (<0.6), low Th/U (<2), low La/Yb (<20), low La/Ce (<0.4) and moderate Dy/Yb ratios (0.8-2). However, significant variation is observed within igneous titanite from the Este Porphyry, with two clear trends identified: i) one which is characterised by low Th/U, low Dy/Yb, moderate Eu/Eu*, high La/Yb and high La/Ce; and ii) a high Th/U, moderate Eu/Eu*, moderate La/Yb, moderate La/Ce, high Dy/Yb trend (Fig. 5.6). The signatures of non-igneous, either as altered igneous, replacement or vein titanite, are much more variable but are often characterised by anomalously high (>1) Eu/Eu* or low Th/U (<0.5) ratios (Fig. 5.6A).

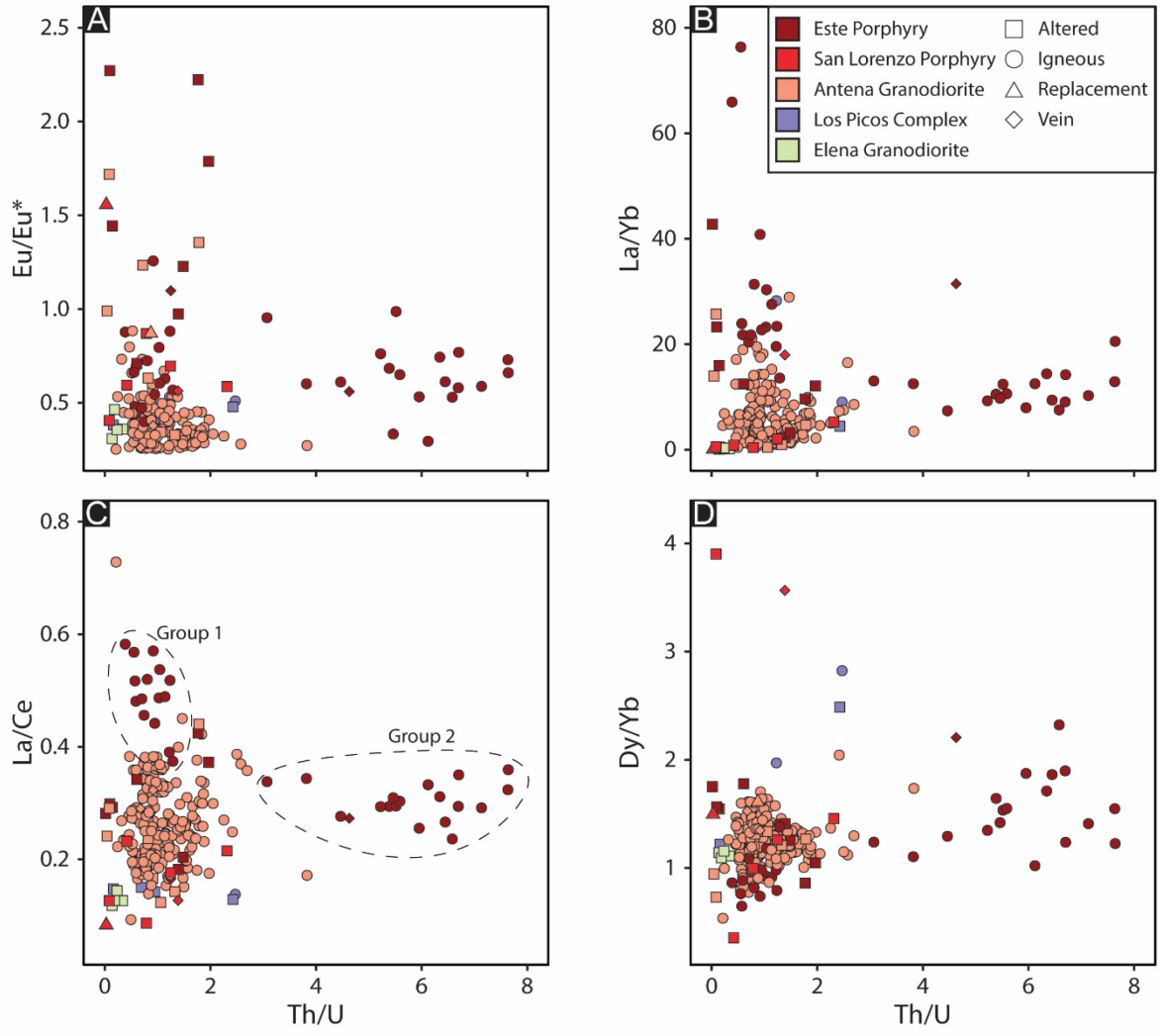


Figure 5.6. Trace element compositions of titanite from the Chuquicamata district. **A.** Eu/Eu* vs Th/U. **B.** La/Yb vs Th/U. **C.** La/Ce vs Th/U. **D.** Dy/Yb vs Th/U. Eu/Eu*, La/Yb and Dy/Yb ratios are chondrite normalised (Boynton, 1984). Average 2σ errors are smaller than symbol size.

5.5 Discussion

5.5.1 Titanite Geochronology

Of the analysed titanite, only three samples (FC006, FC009 and FC010) returned errors that were larger than 10% of the age. In these samples, large errors can be explained by the limited amount of data due to a paucity of suitable analytical sites, with relatively small crystals that are commonly intergrown with other mineral phases. Calculated ages for the FCT secondary standard were outside of published reference values for the first analytical run (see Chapter 3). However, agreement

between different analytical runs (e.g. sample FC002) and with published zircon U-Pb data (Campbell *et al.*, 2006) suggests that the data from the first analytical run are robust. More successful analyses were conducted on titanite from mineral separates, with reduced errors and MSWDs that were typically within the acceptable range (Table 5.2). For sample FC002, in which titanite was analysed both *in-situ* and from mineral separates, calculated ages overlap within the 2σ error. However, mineral separate titanite from FC002 was overdispersed compared to the acceptable MSWD (Table 5.2) suggesting that, in this sample, there may be different age populations. Distinct ages are calculated for mineral separate and *in-situ* titanite analysis in Antena Granodiorite sample FC008, although *in-situ* analysis returned a relatively large error (~10%), likely reflecting the limited number of suitable analytical sites.

Crystals which were analysed *in-situ* included altered igneous, replacement and vein-hosted titanite. All analyses were plotted on Tera-Wasserburg diagrams, although replacement and vein-hosted titanite were not utilised (igneous and altered igneous were) in the calculation of crystallisation ages. Calculated crystallisation ages which included altered igneous titanite were not significantly different to those calculated using igneous titanite alone, except for increasing 2σ error, and particularly in cases where only a small number of analyses (<10) were possible. Similar U-Pb data between igneous and altered igneous titanite suggests that U-Pb isotopic compositions were not modified by hydrothermal alteration. Moreover, U-Pb compositions of replacement and vein-hosted titanite do not significantly differ from igneous titanite in the same samples. In fact, replacement and vein-hosted titanite often contain low initial U, and hence often help to constrain common Pb compositions of the sample.

Crystallisation ages of titanite from the Chuquicamata district are all Eocene-Oligocene, with the exception of CH003 which returned a late Triassic age, broadly coeval with emplacement of this rock as part of the plutonic basement host sequence. This indicates that titanite in the Triassic Elena Granodiorite was not overprinted by the younger Eocene-Oligocene event. Titanite U-Pb data for the Eocene-Oligocene intrusions generally overlaps (within uncertainty) with zircon U-Pb data for the same units from literature sources (Campbell *et al.*, 2006) and from the same rocks (Loader, unpublished data; Fig. 5.7). The San Lorenzo Porphyry and Los Picos Complex return titanite ages with large errors (>10%), likely due to the small number of successful analyses. Este Porphyry sample CH007 returns a titanite U-Pb age which is younger than a zircon U-Pb age from the same sample (Fig. 5.7). However, the calculated titanite U-Pb age is consistent with zircon crystallisation ages from the literature (Ballard *et al.*, 2001; Campbell *et al.*, 2006), possibly indicating that some older zircons may have been included in the calculation of crystallisation ages in that sample.

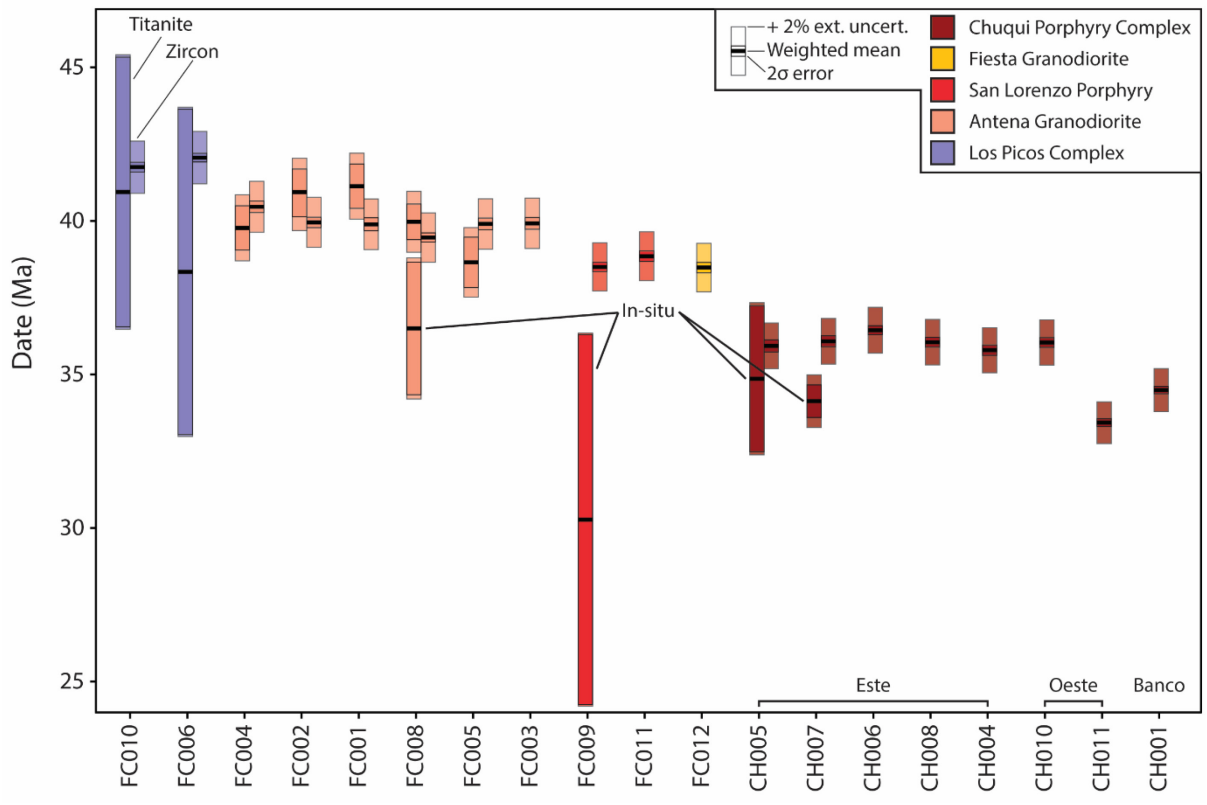


Figure 5.7. Plot comparing titanite lower intercept ages for Eocene-Oligocene intrusions in the Chuquicamata district , as well as 2σ error with ±2% external uncertainty. Shown for comparison are $^{206}Pb/^{238}U$ weighted mean ages for zircon from the same samples (Loader, unpublished data). Only zircon ages are shown for some samples due to an absence of titanite analyses.

5.5.2 Comparing igneous and non-igneous titanite compositions

In samples where titanite was analysed both *in-situ* and in mineral separates (e.g. Antena Granodiorite samples FC002 and FC008), most mineral separate titanite was classified as igneous, whereas a higher proportion of non-igneous (e.g. altered igneous, replacement and vein-hosted) titanite was identified *in-situ.* This may in part be due to increased likelihood of identifying non-igneous titanite where the chemical context of the rock has been retained. However, most titanites in the Antena Granodiorite which were classified as igneous cluster, with non-igneous often exhibiting anomalous compositions (Fig. 5.6). This suggests that there has been minimal misclassification of non-igneous as igneous titanite, and that igneous titanite may be preferentially selected during mineral separation. Preferential concentration of igneous, relative to non-igneous titanite during mineral separation may reflect varying crystal sizes and intergrowths with other mineral phases of different properties and densities. This may introduce selection bias, and hence future studies should be designed with particular textural types in mind. Through comparing igneous and altered igneous titanite compositions it is possible to assess the extent to which igneous titanite compositions may be modified during hydrothermal alteration. For example, in Este

Porphyry sample CH005 altered igneous titanite (which is partially replaced by Fe-Ti oxides ± allanite; Fig. 5.3H) exhibits weakly negative to strongly positive Eu anomalies, compared to unaltered igneous titanite from the same sample (Figs. 5.5 and 5.6). Similarly high Eu/Eu* ratios in altered titanites have been observed by other authors (Horie *et al.*, 2008; Cao *et al.*, 2020) and may be favoured by the breakdown of Eu-enriched phases such as feldspar. TESCAN TIMA phase maps reveal that plagioclase is partially to completely replaced by sericite, kaolinite and K-feldspar in this sample, potentially liberating Eu which may explain enrichment in Eu relative to neighbouring REEs. Low Th/U ratios (<1) may also characterise altered igneous titanite, as is observed in the Antena Granodiorite, San Lorenzo Porphyry and Este Porphyry (Fig. 5.6). In all instances, these low Th/U ratios are predominantly driven by low Th, rather than high U contents, indicating that Th is removed during hydrothermal alteration. This loss of Th probably represents redistribution within the sample, with minor (<0.01 modal %) thorite identified. Despite this, some visibly altered titanite may retain an igneous signature (Fig. 5.5B), and even vein-hosted titanite may show comparable compositions to igneous titanite, likely reflecting the similarities between low-temperature magmatic and high-temperature hydrothermal environments.

5.5.3 Titanite populations in the Este Porphyry

Considerable compositional variation is observed in the Este Porphyry (Figs. 5.5 and 5.6), with igneous titanite classified into two groups based on Th/U ratios (Fig. 5.6); a parameter which has been utilised to identify multiple titanite populations in other porphyry deposits (e.g. Bajo de la Alumbrera; Buret *et al.*, 2016). Texturally, Este Porphyry groups 1 and 2 are similar, showing comparable mineral associations and crystal habits. However, group 1 titanite often exhibits angular internal zonation (e.g. Fig. 5.3C), whereas group 2 often displays irregular internal (possibly sector) zonation. One titanite crystal contains both groups 1 and 2 titanite (Fig. 5.8), with a resorption surface separating the two geochemical groups. Group 2 titanite is located in the crystal core, whereas group 1 titanite is located at the rim, on the opposite side of the resorption surface. Crystallisation temperatures were calculated using the Zr-in-titanite thermometer (Hayden *et al.*, 2008), applying an $a\mathrm{SiO_2}$ of 1, an $a\mathrm{TiO_2}$ of 0.7 and a crystallisation pressure of 1.5 kb (Dahlström *et al.*, 2022) for all units. A slightly lower crystallisation temperature is observed for the group 1 (rim) analysis, although it is within error of the group 2 (core) analysis. Plotting the two Este Porphyry groups on a Tera-Wasserburg diagram does not reveal distinct crystallisation ages (Fig.

5.9), although group 1 (low Th/U) contains a larger proportion of titanite with high initial U contents, reducing 2σ error relative to group 2 (high Th/U; Fig. 5.9).

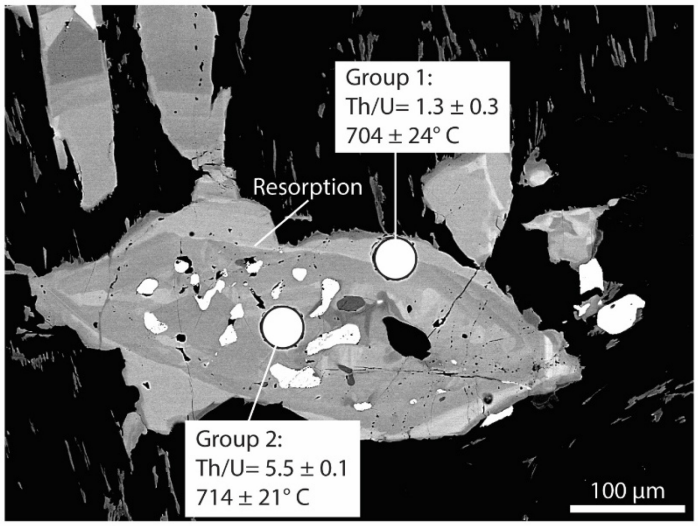


Figure 5.8. Crystal from the Este Porphyry that contains both groups 1 (low Th/U) and 2 (high Th/U) titanite.

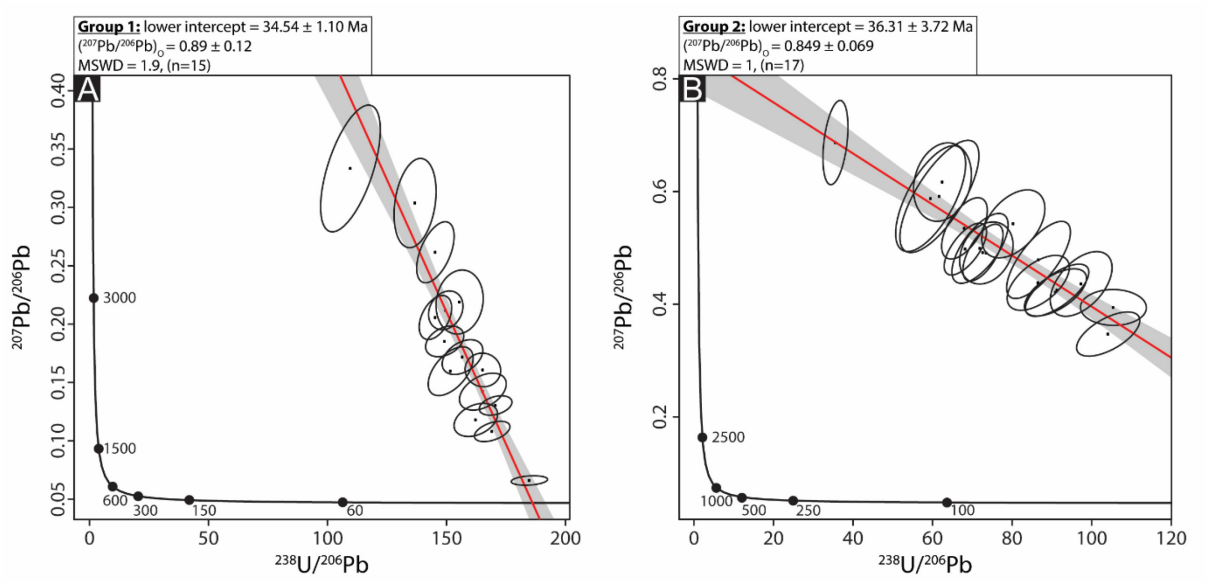


Figure 5.9. Tera-Wasserburg Concordia diagrams for titanite age data from groups 1 (**A.**) and 2 (**B.**) in the Este Porphyry. Displayed errors represent the 2σ error calculated from the weighted mean, with an additional propagated external uncertainty of 2%.

Compositions of the two Este Porphyry groups, along with igneous titanite from other units, are subsequently compared using violin plots (Fig. 5.10). Violin plots better illustrate

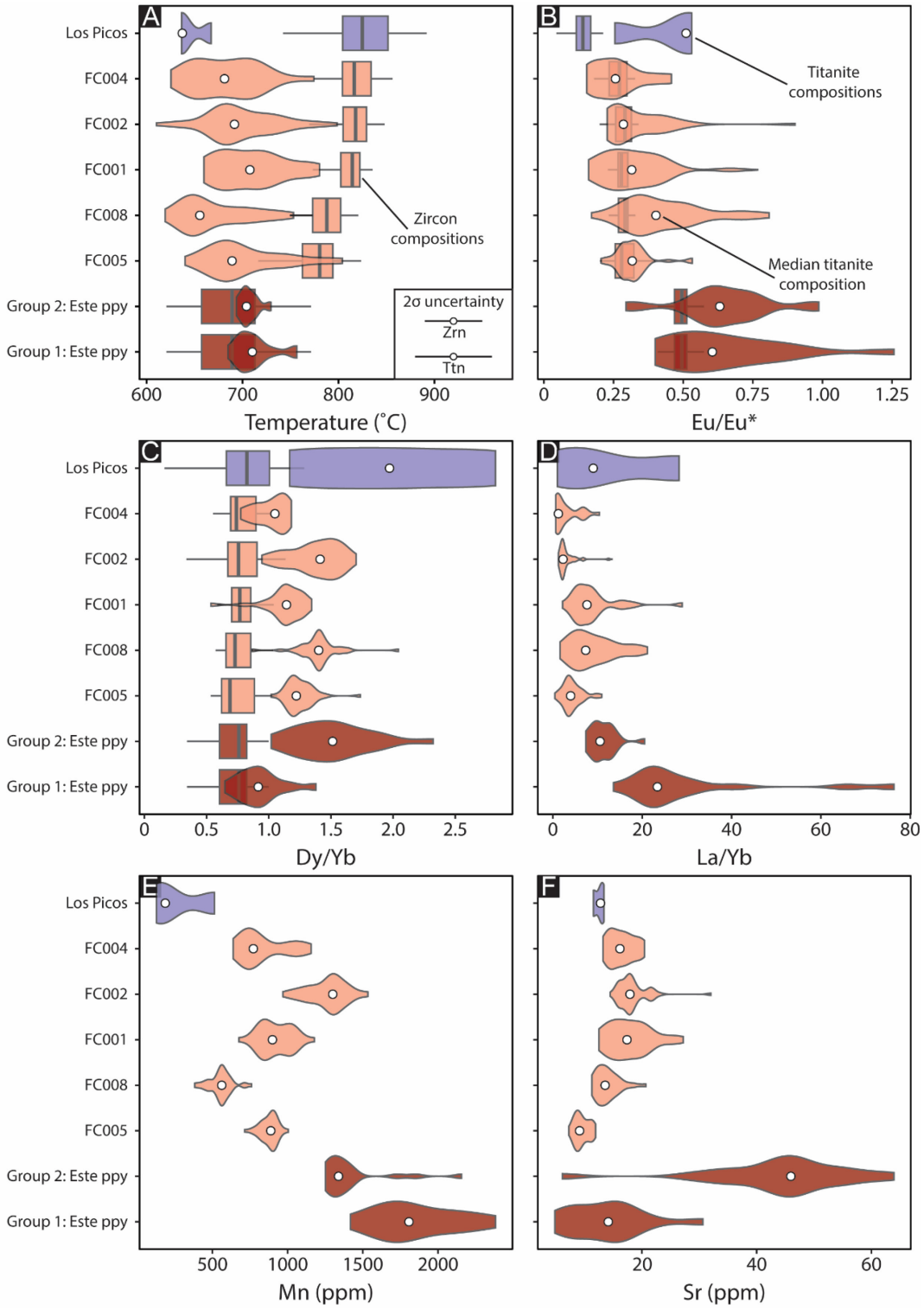


Figure 5.10. Violin plots illustrating titanite compositions for different samples. Samples are arranged top to bottom in terms of decreasing age based on cross-cutting relationships between units and using titanite crystallisation ages within units. Also shown are zircon compositions (**A-D**) from the same samples (Loader, unpublished data). All zircon data are displayed for the Este Porphyry. **A.** Crystallisation temperature (Hayden et *al*., 2008) assuming a crystallisation pressure of 1.5 kb, $\alpha SiO_2 = 1$ and $aTiO_2 = 0.7$. Calculated zircon crystallisation temperatures (Ferry & Watson, 2007) use the same $aSiO_2$ and $aTiO_2$. 2σ uncertainty for the calculation of both titanite and zircon temperatures is displayed. **B.** Eu/Eu* (Boynton, 1984). **C.** Dy/Yb. **D.** La/Yb. **E.** Mn (ppm). **F.** Sr (ppm). For plots B-F, average 2σ analytical error is 3-5%.

compositional differences between the groups, which exhibit more variation both within and between populations than zircon from the same samples (Fig. 5.10). Overall, Este Porphyry groups

two titanite populations of differing compositions can be explained by: i) misclassification of non-igneous titanite; ii) mafic recharge or wall rock contamination; or iii) by derivation from melts with distinct compositions.

Este Porphyry titanite groups 1 and 2 are unlikely to have a non-igneous origin, given either the presence of magmatic zonation or their association with igneous minerals such as amphibole and zircon. Furthermore, calculated Zr-in-titanite crystallisation temperatures, in the range of 750-700°C, are consistent with an igneous origin. Mixing with a more primitive, hotter melt, or wall-rock assimilation could alter both bulk melt composition and thermal conditions, with implications for mineral-melt partitioning and melt chemistry. However, titanite crystallisation temperatures are generally consistent between the two groups, and no evidence of magma mixing, or wall-rock assimilation has been identified by the numerous previous studies (Ossandón *et al.*, 2001; Ballard *et al.*, 2002; Campbell *et al.*, 2006). Instead, it is argued that the two titanite populations represent distinct melt compositions, probably reflecting derivation from isolated melt pockets of varying composition. Similar geochemical signatures have been noted in other porphyry districts, including Ok Tedi, Papua New Guinea, where multiple zircon populations were identified, also on the basis of Th/U ratios (Large *et al.*, 2018). Here, the authors argue that a low Th/U zircon population, which is usually sector zoned, is derived from a different melt reservoir. A similar process may be envisaged with the two titanite populations, which is evidenced by the overgrowth of group 2 by group 1 titanite (Fig. 5.8). Compositions of group 1 titanite are generally consistent with a melt that crystallised titanite (e.g. low Th/U, La/Yb and Dy/Yb; Colombini *et al.*, 2011) and plagioclase (e.g. low Sr; Blundy & Wood, 1991), with extensive plagioclase crystallisation potentially buffering titanite, to ensure that melt Eu/Eu* stays relatively constant.

The occurrence of igneous titanite with both elevated Eu/Eu* (> 0.75) and low Dy/Yb (<1) ratios (e.g. Este Porphyry group 1) may be an important indicator of the fertility of the magmatic system, given that such whole-rock (Richards, 2011) and zircon signatures (Lu et al., 2016; Pizarro et al., 2020) are often linked to mineralisation. Interestingly, group 1 titanite displays many geochemical characteristics of a porphyry fertile magma, excluding the relative enrichment in Mn, which is often observed to exhibit low concentrations in porphyry-associated whole-rocks (Ahmed et al., 2020; Nathwani et al., 2022).

5.5.4 Titanite as an indicator of changing melt composition

Considering only igneous crystals, titanite compositions can be employed to understand key physicochemical changes of the magmatic system in the lead up to mineralisation (Fig. 5.9). For the Eocene-Oligocene intrusions, calculated titanite crystallisation temperatures may slightly

increase (when factoring in uncertainty), from ~650°C in the Los Picos Complex, through to 650-750°C for both the Antena Granodiorite and Este Porphyry. Like titanite, Ti-in-zircon temperatures can be calculated where assumptions are made for $a\mathrm{SiO_2}$ and $a\mathrm{TiO_2}$ (Ferry & Watson, 2007). In this case, values of 1 and 0.7 for $a\mathrm{SiO_2}$ and $a\mathrm{TiO_2}$ respectively, which are consistent with those applied to the Zr-in-titanite thermometer. Calculated zircon crystallisation temperatures decrease through time, from ~800°C for Los Picos and Antena zircons, to ~700°C in the Este Porphyry, resulting in overlapping titanite and zircon temperatures for this unit (Fig. 5.9A). Although individual zircon and titanite temperatures in the same sample may overlap within uncertainty, overlapping median temperatures are only observed in the Este Porphyry. This implies zircon saturation occurred significantly before titanite in the earlier stages of evolution but that these two phases were concurrent in the later, mineralising stage.

Titanite and zircon Eu anomalies increase through time, with titanite ranging from ~0.25-0.4 in the Los Picos-Fortuna Complex to ~0.55-0.8 in the Este porphyry (Fig. 5.9B). These trends, along with increasing zircon Ce anomalies, were first noted in a landmark study by Ballard *et al.* (2002) who postulated that this reflected higher proportions of Eu^{3+} and Ce^{4+} in the melt due to high magmatic oxidation state. Current orthodoxy maintains that porphyry magmas are unusually oxidised, yet the importance of oxidation state in governing zircon Eu/Eu* and Ce/Ce* ratios is now strongly debated (Loader *et al.*, 2017; Loader *et al.*, 2022).

Magmatic oxidation state can be estimated using the zircon trace element oxybarometer of Loucks *et al.* (2020). Zircon compositional data (Loader, unpublished) from the sample suite is utilised to estimate $f\mathrm{O_2}$ (as ΔFMQ; Fig. 5.11). From this, it is evident that the magmatic oxidation state of the Eocene-Oligocene intrusions from the San Lorenzo onwards increased through time. Values of ~FMQ are estimated for the Los Picos intrusions, transitioning to ~FMQ+0.5-1 for the Fortuna Complex, and finally to ~FMQ+1.5-2.5 for the Chuqui Porphyry Complex. Hence, it is plausible that increasing $f\mathrm{O_2}$ is controlling both titanite and zircon Eu anomalies. To assess the importance of magmatic oxidation state in controlling titanite Eu/Eu*, melt compositions that would have been in equilibrium with titanite are back calculated. Titanite-melt partition coefficients for Eu (D_{Eu}) are calculated after $f\mathrm{O_2}$ was estimated for each of the samples/units, allowing titanite compositions to be related to those of the melt. For the Los Picos Complex and Antena Granodiorite samples minimum $f\mathrm{O_2}$ values are used, which are based on the occurrence of the titanite + magnetite + quartz assemblage. Average titanite crystallisation temperatures are used in the estimation of $\log f\mathrm{O_2}$ for the Antena Granodiorite and Este Porphyry samples, with solidus temperatures assumed for the Los Picos Complex. For the Este Porphyry samples, calculated zircon and titanite

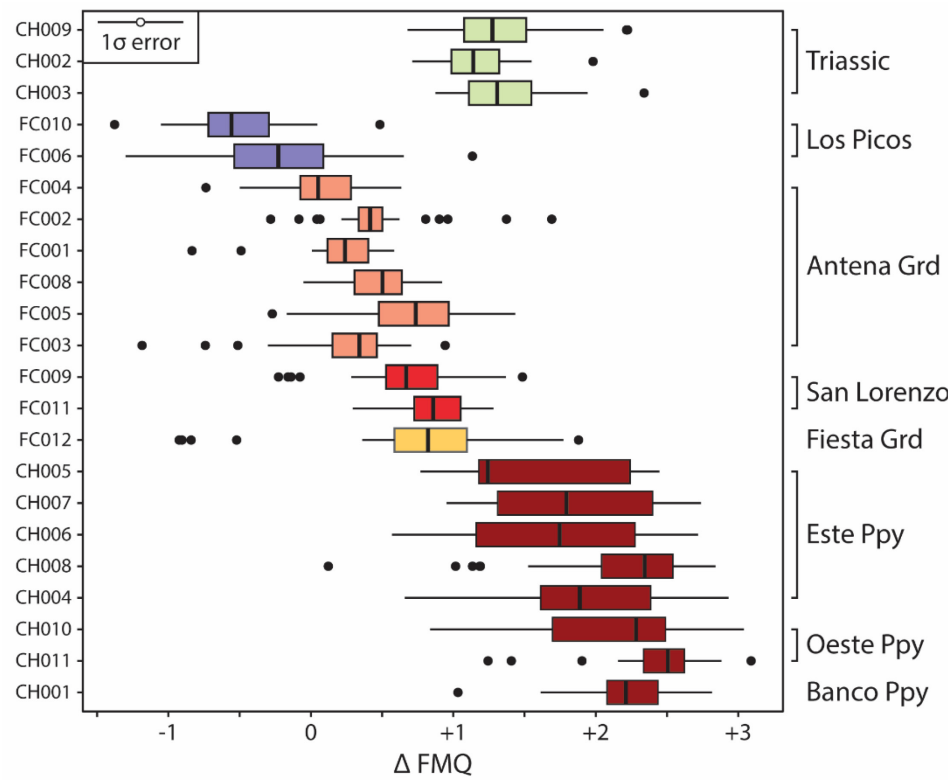


Figure 5.11. Boxplots showing calculated log fO_2 (ΔFMQ) using the zircon oxybarometer (Loucks *et al.*, 2020) for different samples. Zircons that were identified as inherited were removed from the calculation. Outliers are denoted by black points. 1σ uncertainty associated with the calculation is displayed.

crystallisation temperatures are comparable, suggesting titanite and zircon are coeval. Hence, the average fO_2 for each Este Porphyry sample, as estimated using the zircon oxybarometer (Loucks *et al.*, 2020) was applied. Titanite D_{Eu} was estimated using the equations of Wilke and Behrens (1999) and Burnham *et al.* (2015), using an optical basicity of 0.55. All partition coefficients (Sr^{2+}, Sm^{3+}, Gd^{3+} and Eu^{3+}) were derived from Colombini *et al.* (2011) and Sr was used to approximate for D_{Eu}^{2+}. Propagating the error associated with the zircon oxybarometer calculation resulted in errors of ~15% for the melt Eu/Eu* calculation.

The modelled melt Eu anomaly increases from chiefly ~0.5-0.7 in the Los Picos-Fortuna Complex to ~0.9-1.1 in the Este porphyry (Appendix 7; Fig. 5.12), implying that melt compositional evolution is also likely to have played a role. An increasing melt Eu/Eu* through time is consistent with the progressively rising whole-rock Eu anomaly (Fig. 5.12). Hence, this contradicts the hypothesis of Ballard *et al.* (2002), that oxidation state alone is responsible for progressively increasing Eu/Eu* in zircon at Chuquicamata. Instead it is more likely that zircon (and titanite) compositions are dominantly controlled by melt chemistry. Additionally, the median modelled melt Eu/Eu* (via titanite) transitions from being greater than whole-rock Eu/Eu* in the Los Picos Complex through to being coincident with whole-rock compositions in the Este Porphyry, possibly indicating progressively earlier titanite saturation.

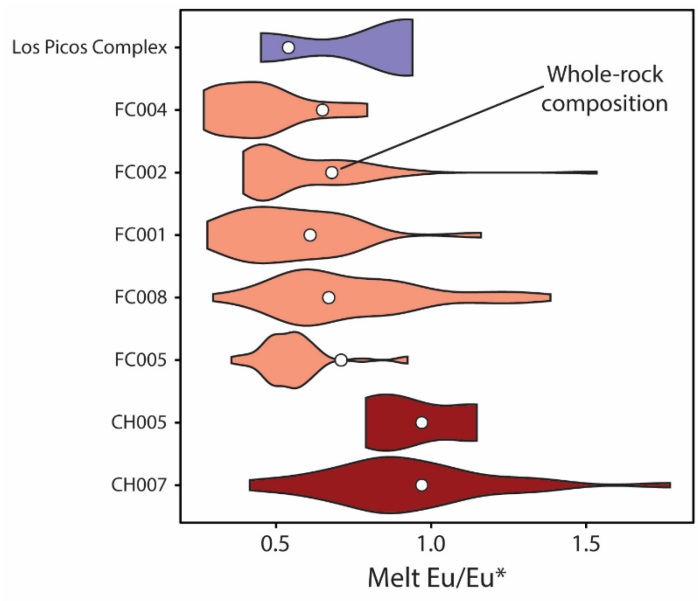


Figure 5.12. Estimated melt Eu/Eu* in equilibrium with titanite in each sample. Median oxidation states, as estimated using the Loucks *et al.* (2020) oxybarometer, were used to estimate D_{Eu} in each sample. Also shown are whole-rock Eu/Eu* values from the Los Picos-Fortuna Complex (Loader, unpublished data), as well as the Este Porphyry (Ballard, 2001).

5.5.5 Titanite textural indicators of mineralisation

Textural examination of the Eocene-Oligocene rocks from the Chuquicamata district reveals that titanite became increasingly more abundant and euhedral through time. Furthermore, the paucity of large, euhedral titanite in the Elena Granodiorite, a Triassic intrusion which displays many of the same geochemical characteristics as the porphyry intrusions (Zentilli *et al.*, 2018), suggests that the occurrence of titanite is an important marker for porphyry-fertile magmas in the district. Titanite has been reported to occur in numerous porphyry-associated magmas from other deposits, including Bajo de la Alumbrera (Buret *et al.*, 2016), Bingham Canyon (Large *et al.*, 2021), Ok Tedi (Large *et al.*, 2018), Pebble (Olson *et al.*, 2017) and Yerington (Dilles, 1987). Although primary titanite is commonly altered during intense hydrothermal alteration, the presence of titanite may be inferred from rutile pseudomorphs, which may even partially inherit titanite trace element signatures (e.g. Ce inheritance; Figs. 5. 3K and L). The exact mechanism of this inheritance is unclear, although exchange reactions between fluid and precursor titanite seem the most likely explanation.

In the Chuquicamata district, a progressive oxidation of melts over time (Fig. 5.10) may have led to enhanced titanite stability (Wones, 1989; Frost *et al.*, 2001; Ackerson, 2011). Elevated melt TiO_2 contents have also been identified as an important control on titanite stability (Ayers *et al.*, 2022), however porphyry magmas are often depleted in TiO_2 due to extensive lower crustal amphibole fractionation (Loucks, 2014). Indeed, low Ti contents are observed in porphyry zircons from Chuquicamata (e.g. Fig. 5.10A), resulting in low calculated crystallisation temperatures

(Ferry & Watson, 2007). Melt Ti contents, nevertheless, do not necessarily reflect titania activity ($a\mathrm{TiO_2}$), which may be higher in relatively oxidised magmas (Schiller & Finger, 2019). The common occurrence of titanite in porphyry magmas may, hence, simply reflect derivation from relatively oxidised magmas. However, increased oxidation state alone cannot explain the distribution of titanite in the Chuquicamata district, as the Triassic granites (e.g. Elena granodiorite) are relatively oxidised compared to the Los Picos-Fortuna Complex, and yet contain much less titanite. Elevated water contents are another potential control on titanite stability, as highlighted by the frequent association of titanite with hydrous phases, and reactions involving the hydration of clinopyroxene, ilmenite and quartz to form titanite and Ca-amphibole (e.g. Equation 2.5; Frost *et al.*, 2001). An essential requirement of a porphyry magma is that it contains sufficient dissolved water contents to saturate a magmatic volatile phase in the upper crust, with elevated water contents of porphyry magmas attested to by various whole-rock trace element compositions (Rohrlach & Loucks, 2005; Richards, 2011; Loucks, 2014). Therefore, progressively increasing magmatic water contents are invoked to explain the enhanced stability of titanite prior to, and during, formation of the world class Chuquicamata porphyry copper deposit.

Titanite textures may also provide useful information about whether an intrusion saturated in an aqueous phase. For instance, titanite from the mineralised Este Porphyry almost ubiquitously shows fluid inclusion trails, which are readily identified using an SEM. These inclusion trails crosscut igneous zonation (e.g. Fig. 5.3G) and hence are interpreted to be secondary, representing the passage of hydrothermal fluids through titanite. By contrast, fluid inclusion trails in titanite from other units are almost completely absent. Textural study of these rocks indicates that the Este Porphyry titanites are also more pervasively altered compared to the Los Picos-Fortuna Complex. Hence, the presence of fluid inclusion trails, for example in titanite from stream sediments, could give an indication of proximity to an intrusion (of the right composition) through which a large volume of hydrothermal fluid has passed. Additionally, the potential of rutile as a recorder of primary titanite compositions should be investigated. For the mineralised Oeste and Este porphyries, clear rutile pseudomorphs after titanite contain elevated Ce contents, suggesting that titanite signature may be inherited by rutile, which may be of particular importance in rocks where primary titanite has been completely destroyed.

5.6 Conclusions

Titanite textural, geochronological and geochemical data have been employed to understand the evolution of the magmatic system which formed a supergiant porphyry Cu deposit in northern Chile. Reliable titanite crystallisation ages, which are consistent with zircon, are obtained given a

suitable number of uncontaminated analyses. Various types of titanite are identified in the Chuquicamata district, including: igneous, altered igneous, replacement and vein-hosted. Compositions of non-igneous titanite generally differ from those of igneous titanite and are characterised by high Eu/Eu* and low Th/U ratios, although altered igneous crystals may exhibit similar compositions to igneous titanite in some instances. Two igneous titanite populations are identified in the Este Porphyry, on the basis of Th/U ratios, likely representing origination from melts of different composition, with group 1 titanite exhibiting many of the characteristics of porphyry-fertile magmas (e.g. high Eu/Eu* and low Dy/Yb).

Progressively increasing titanite Eu anomalies are observed through time, culminating in slightly negative to positive anomalies in the mineralised Este Porphyry. Zircon trace element compositions are utilised to estimate magmatic oxidation state in the district, which is then applied to model melt Eu/Eu* values. Modelling results are consistent with step-by-step increases in melt Eu anomalies, indicating that titanite in the Este Porphyry crystallised from a high Eu/Eu*, low Dy/Yb and Th/U melt; trace element signatures are consistent with derivation from porphyry fertile magmas, as identified in zircon and whole-rock. Furthermore, the greater abundance of, and increasingly euhedral crystal habit of, titanite, potentially due to increasing magmatic water content, may itself be an indicator of proclivity to form a deposit. This, when coupled with an abundance of fluid inclusion bearing titanite, may imply proximity to a hydrothermal system that is associated with porphyry fertile magmas.

Chapter 6. Titanite occurrence and compositions in the Cobre Panama district

6.1 Introduction

The Cobre Panama porphyry copper district is located in Colón province, Panama, approximately 120 km west of Panama City and 20 km south of the Caribbean coast (Fig. 6.1A). Mineralisation in the Cobre Panama region was first discovered in the late 1960's following a United Nations Development Programme, with the first concentrate produced in 2017 (Gray et al. 2019). Numerous porphyry centres are found in the district, occurring in two NW-SE trends at the southern end of the Petaquilla batholith. These porphyry centres, including the Botija, Colina, Valle Grande, Botija-Abajo, Balboa and Medio deposits, as well as several prospects (Fig. 6.1) contain a total measured plus indicated resource of 3,657 Mt at 0.37% Cu, 0.006% Mo, 0.07 g/t Au and 1.34 g/t Ag (Gray *et al.*, 2019). Mineralisation is associated with a series of dioritic to granodioritic porphyry dykes and stocks, dated at 29-28 Ma (Baker *et al.*, 2016; Sepp & Dilles, 2018), similar to the adjacent batholith. Typical hydrothermal alteration assemblages present at Cobre Panama include potassic, propylitic, silica-chlorite, sericitic and argillic types (Gray *et al.*, 2019). However, mineralisation and alteration zoning is generally more laterally extensive than typical for porphyry systems, likely due to post-mineralisation faulting (Sepp & Dilles, 2018). Currently, the mine is owned by Minera Panama, which itself is owned by First Quantum Minerals (90%) and Korea Mine Rehabilitation and Mineral Resources Corporation (10%).

This chapter aims to understand the occurrence and chemical compositions of both igneous and hydrothermal replacement titanite from the giant Cobre Panama porphyry Cu district, Panama. Through combining textural and geochemical data, key characteristics of igneous and non-igneous titanite can be identified, allowing for a greater understanding of the factors that control titanite chemistry.

6.2 Geologic setting

The Isthmus of Panama is a narrow land strip located at the intersection of the Caribbean, Cocos, Nazca, North and South American plates. Here, arc magmatism was thought to have been initiated in the late Cretaceous along the southwestern edge of the Caribbean plate, in response to northward subduction of the Farallon plate (Buchs *et al.*, 2010; Wegner *et al.*, 2011; Redwood *et al.*, 2021). Since the Eocene, the collision of Panama with the South American plate has resulted in anticlockwise rotation, oroclinal bending, and left-lateral offset of volcanic arc terranes (Kerr & Tarney, 2005; Lissinna, 2005; Montes *et al.*, 2012). Thick vegetation throughout much of Panama

has made exploration challenging, yet other porphyry deposits have been identified. Limited research has been conducted on the Rio Pito and Cerro Colorado deposits, but geochronological studies suggest that they are older and younger than the Eocene mineralisation at Cobre Panama respectively (Clark *et al.*, 1977; Kesler *et al.*, 1977; Gray *et al.*, 2019).

The oldest rocks in the district are a series of lavas, tuffs and volcaniclastic units of mafic to intermediate composition (Baker *et al.*, 2016; Sepp & Dilles, 2018; Gray *et al.*, 2019). These are generally mapped as undifferentiated andesite (Fig. 6.1), although Cr-rich basalts have also been identified around the Botija deposit. Despite their association with mineralisation, the age of these rocks is relatively poorly constrained, although faunal evidence from intercalated limestone beds suggests a late Eocene age (Redwood *et al.*, 2021). These volcanic units were subsequently intruded by the c. 20 km long Petaquilla batholith, which becomes younger and more evolved to the south, transitioning from dominantly dioritic compositions close to the Caribbean coast, to a dominantly granodioritic composition in the south (Baker *et al.*, 2016). The Petaquilla batholith can also be split into three domains based on zircon U-Pb ages: >30 Ma in the north; ~30 Ma in the central portion; and 29-28 Ma in the south (Fig. 6.1B; Baker *et al*. 2016; Sepp & Dilles, 2018). Thermobarometric estimates from amphibole suggest a depth of emplacement of ~6-8 km (Sepp & Dilles, 2018). Zircon U-Pb studies of the porphyry intrusions indicate overlapping crystallisation ages with the southern portion of the batholith (Baker *et al.*, 2016) which, in addition to their spatial association and paucity of cross-cutting relationships, suggests an intimate association between them. Finally, volumetrically minor late-stage basaltic to andesitic dykes crosscut all earlier intrusions (Baker *et al.*, 2016; Sepp & Dilles, 2018).

The structural geology of the district is relatively complex, with several generations of faulting. Gray *et al.* (2019) proposed that there are three generations of faults, including i) early E-W trending, moderately dipping reverse faults, which may be genetically linked to the emplacement of the porphyritic intrusions, ii) a set of conjugate NW-SE trending sinistral and NE-SW trending dextral strike slip faults and iii) late-stage E-W and NE-SW trending normal faults that cross-cut earlier structures.

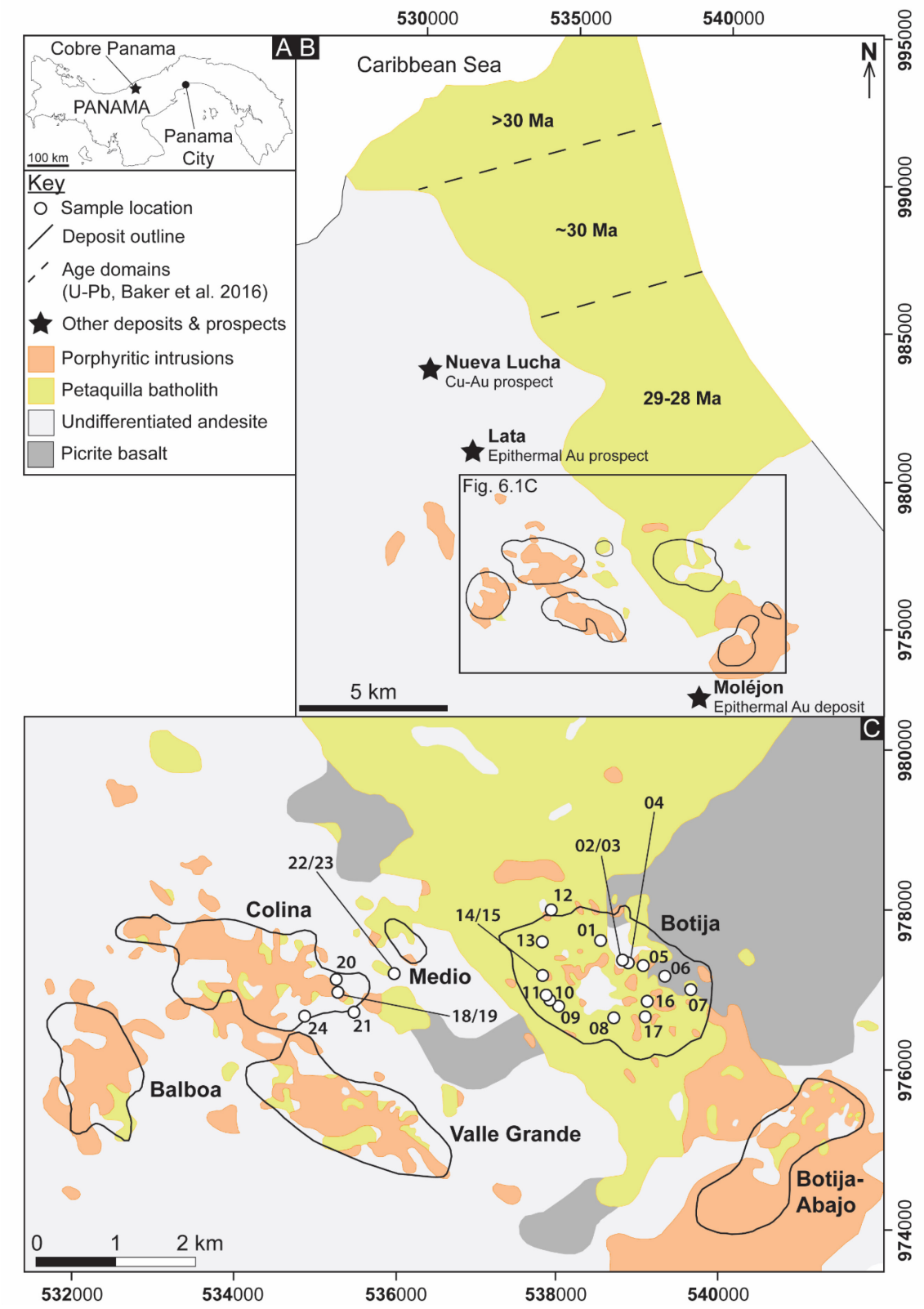


Figure 6.1. Simplified maps of the Cobre Panama porphyry Cu district. **A.** Location of the study area within Panama. **B.** Simplified geological map of the Cobre Panama district showing other deposits and prospects, in addition to age domains of the Petaquilla batholith. Modified from Sepp and Dilles (2018), after Baker *et al.* (2016), Nobel and Benavides (2013) and Speidel *et al.* (2001). **C.** Local geological map showing outlines of the major porphyry copper deposits and sample locations, modified from Redwood *et al.* (2021), after Speidel *et al.* (2001) and First Quantum Minerals Ltd.

6.3 Methods

Data presented here comes from 24 samples which were collected in 2021 by Juan Burlando, including 17 mine surface samples from the Botija open pit and 7 drillcore samples from the Colina deposit (Table 6.1). Samples were selected to encompass a range of lithologies, with a particular focus on intrusive phases that are spatially and temporally associated with mineralisation. In addition to whole-rock (Appendix 1) and titanite (Appendix 2) analysis, of which the methodology is outlined in Chapter 3, zircon compositions (Appendix 8) and U-Pb isotopic data were also collected from Cobre Panama samples, with the methodology outlined below. Prior to whole-rock analysis, samples were crushed at ALS Laboratories and coarse reject material was sent to Geotrack International, where heavy mineral separation was conducted to produce zircon rich concentrates. Zircon was successfully separated from all but two samples (IMP003 and IMP021), allowing for determination of trace element and U-Pb isotopic data at Rio Tinto Exploration, Bundoora, Australia, by laser-ablation ICP-MS. GSD-1G was employed as the primary reference material, with a stoichiometric value of 15.3 wt.% Si used as the internal standard. For U-Pb isotopes, GJ-1 was used as the standard (Jackson *et al.*, 2004). Additionally, BCR-2G and 91500 were analysed as secondary standards for trace elements and U-Pb isotopes, to provide a check on data quality.

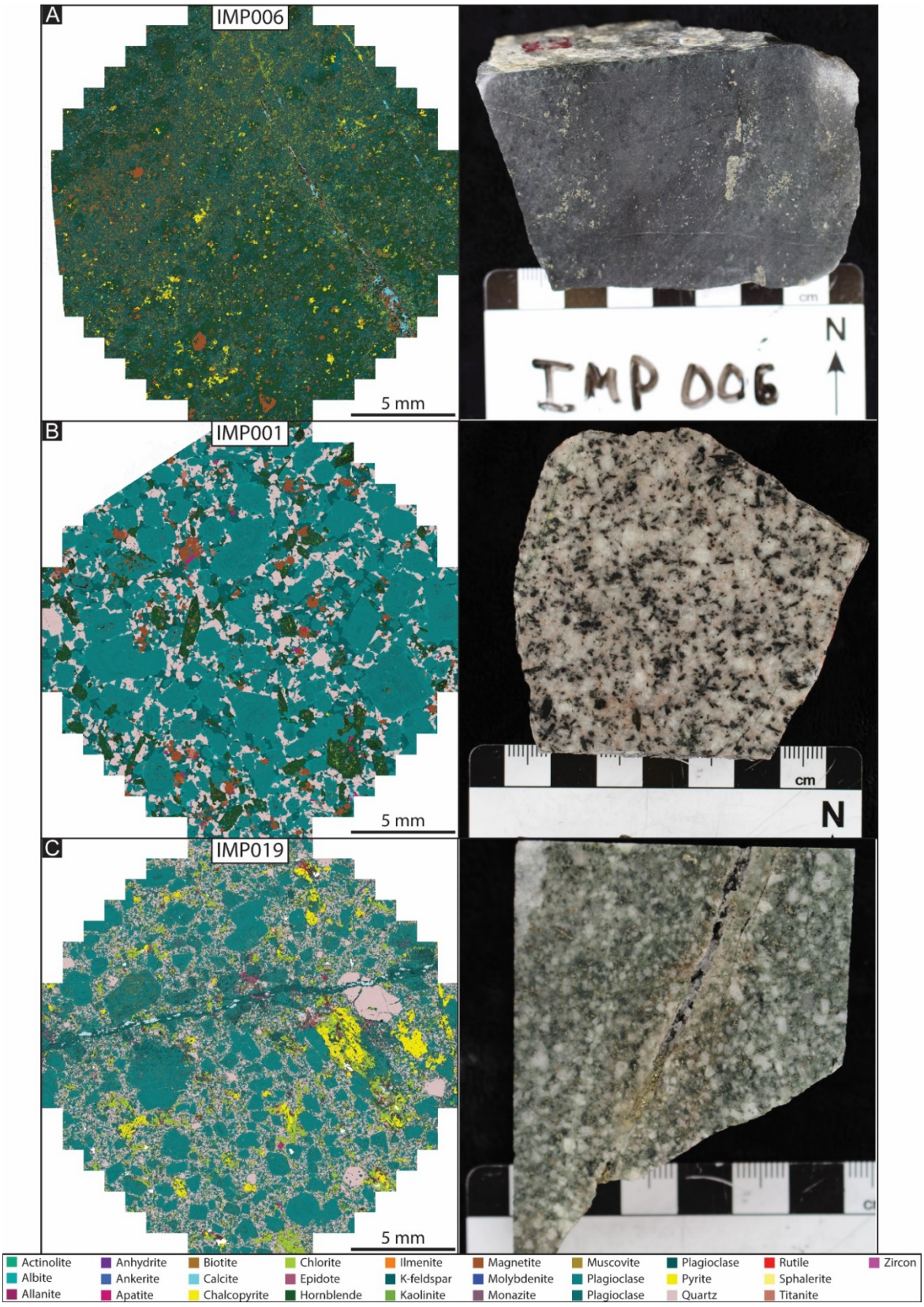
Table 6.1. Sample information, analytical techniques and number of analyses. And= Andesite, Pq Grd= Petaquilla granodiorite, Ppy-Ea= Early-mineral porphyry, Ppy-In= Inter-mineral porphyry, Ppy-La= Inter-mineral porphyry, Ppy-La= Late-mineral porphyry, Ppy-Po= Post-mineral porphyry, M-Dy= Post-mineral mafic dyke.

Sample	Unit	Grid reference (depth)	Alteration	TIMA	No. of ttn analyses	Zircon	Whole-rock
IMP001	Pq Grd	538356, 977616	Propylitic	Y	31	Y	Y
IMP002	Ppy-La	538638, 977377	Propylitic	Y	-	Y	Y
IMP003	And	538630, 977376	Propylitic	Y	-	N	Y
IMP004	M-Dy	538698, 977345	Propylitic	Y	16	Y	Y
IMP005	Pq Grd	538886, 977308	Propylitic after potassic?	Y	24	Y	Y
IMP006	And	539153, 977177	Propylitic after potassic?	Y	9	Y	Y
IMP007	Pq Grd	539473, 977012	Propylitic	Y	19	Y	Y
IMP008	Pq Grd	538521, 976664	Propylitic after potassic?	Y	15	Y	Y
IMP009	M-Dy	537837, 976810	Propylitic	Y	-	Y	Y
IMP010	Pq Grd	537723, 976888	Propylitic	Y	23	Y	Y
IMP011	Ppy-Ea	537684, 976944	Propylitic after potassic?	Y	13	Y	Y
IMP012	Ppy-La	537746, 977996	Propylitic	Y	15	Y	Y
IMP013	Ppy-Ea	537633, 977600	Propylitic	Y	10	Y	Y
IMP014	Pq Grd	537642, 977190	Propylitic after potassic?	Y	13	Y	Y
IMP015	Ppy-Ea	537634, 977186	Propylitic	Y	14	Y	Y
IMP016	Ppy-In	538938, 976868	Potassic/sericitic?	Y	-	Y	Y
IMP017	Ppy-Ea	538911, 976680	Propylitic	Y	-	Y	Y
IMP018	Ppy-Ea	535100, 976980 (30m)	Propylitic	Y	-	Y	Y
IMP019	Ppy-Ea	535100, 976980 (51m)	Propylitic after potassic?	Y	9	Y	Y
IMP020	Ppy-La	535080, 977140 (116m)	Propylitic	Y	8	Y	Y
IMP021	Ppy-Po	535297, 976732 (138m)	Propylitic	Y	9	N	Y
IMP022	Ppy-Ea	535801, 977211 (90m)	Propylitic after potassic?	Y	10	Y	Y
IMP023	Ppy-Ea	535801, 977211 (208m)	Propylitic after potassic?	Y	13	Y	Y
IMP024	Ppy-La	534686, 976682 (148m)	Propylitic	Y	12	Y	Y

In order to ensure data quality, a subset of the raw zircon laser-ablation data was provided by Rio Tinto. This was processed using the Iolite v 3.61 software (Paton *et al.*, 2011) at the Natural History Museum, before being compared to data from the same samples that was provided by Rio Tinto. Calculated crystallisation ages from the same samples (IMP002, IMP004) are consistent within uncertainty, and secondary standards (91500, Wiedenbeck *et al.*, 2004; Plešovice, Sláma *et al.*, 2008) are within uncertainty of published ages (Appendix 3). Literature data, both whole-rock and zircon geochronology from Baker *et al.* (2016) is also presented for comparison. Studied samples from the Cobre Panama porphyry Cu district comprise both extrusive and intrusive igneous rocks (Fig. 6.2). Intrusive rocks from the district include both the batholith and porphyritic intrusions, as well as post-mineral mafic dykes (Fig. 6.2). Studied samples typically contain plagioclase, quartz, amphibole, Fe-Ti oxides and apatite in varying proportions, with K-feldspar and zircon also present in all but the most mafic samples. The dominant alteration style observed in the studied samples is silica-chlorite, which is characterised by chloritisation of mafic phenocrysts and addition of quartz to the groundmass. Pervasive potassic alteration is not observed, rather potassic alteration manifests as veinlet selvages localised around K-feldspar veinlets (Fig. 6.2C). Pyrite and chalcopyrite are the most abundant sulphides, with minor bornite, molybdenite and sphalerite.

Andesite (IMP003 & IMP006)

Sampled volcanic rocks are porphyritic, containing magnetite (2.5%) and plagioclase phenocrysts in a fine-grained, plagioclase (more anorthitic) rich groundmass (Fig. 6.2A). Studied andesite samples differ in their modal mineralogy and phenocryst assemblage. Sample IMP003 is more felsic, containing an abundance of quartz (~25%) and minor apatite (0.5%) in the groundmass, whereas IMP006 contains an abundance of amphibole phenocrysts (~20%). Both samples are mineralised, containing chalcopyrite and pyrite as disseminations and veinlets. Sample IMP003 is intensely veined, containing a stockwork of sericite + chlorite + quartz + sulphide veinlets, with the abundance of quartz possibly reflecting hydrothermal rather than igneous processes. Hydrothermal alteration of sample IMP006 is patchy, with the dominant mafic replacement mineral alternating between biotite and chlorite throughout the sample. Veinlets of calcite + albite + chlorite + quartz ± sulphides ± titanite are observed, although sulphides are dominantly found as disseminations, with veinlets only comprising a volumetrically small proportion (Fig. 6.2A).


A
IMP006
5 mm
IMP 006
N
B
IMP001
5 mm
cm
N
C
IMP019
5 mm
Actinolite
Albite
Allanite
Anhydrite
Ankerite
Apatite
Biotite
Calcite
Chalcopyrite
Chlorite
Epidote
Hornblende
Ilmenite
K-feldspar
Kaolinite
Magnetite
Molybdenite
Monazite
Muscovite
Plagioclase
Plagioclase
Plagioclase
Plagioclase
Pyrite
Quartz
Rutile
Sphalerite
Titanite
Zircon

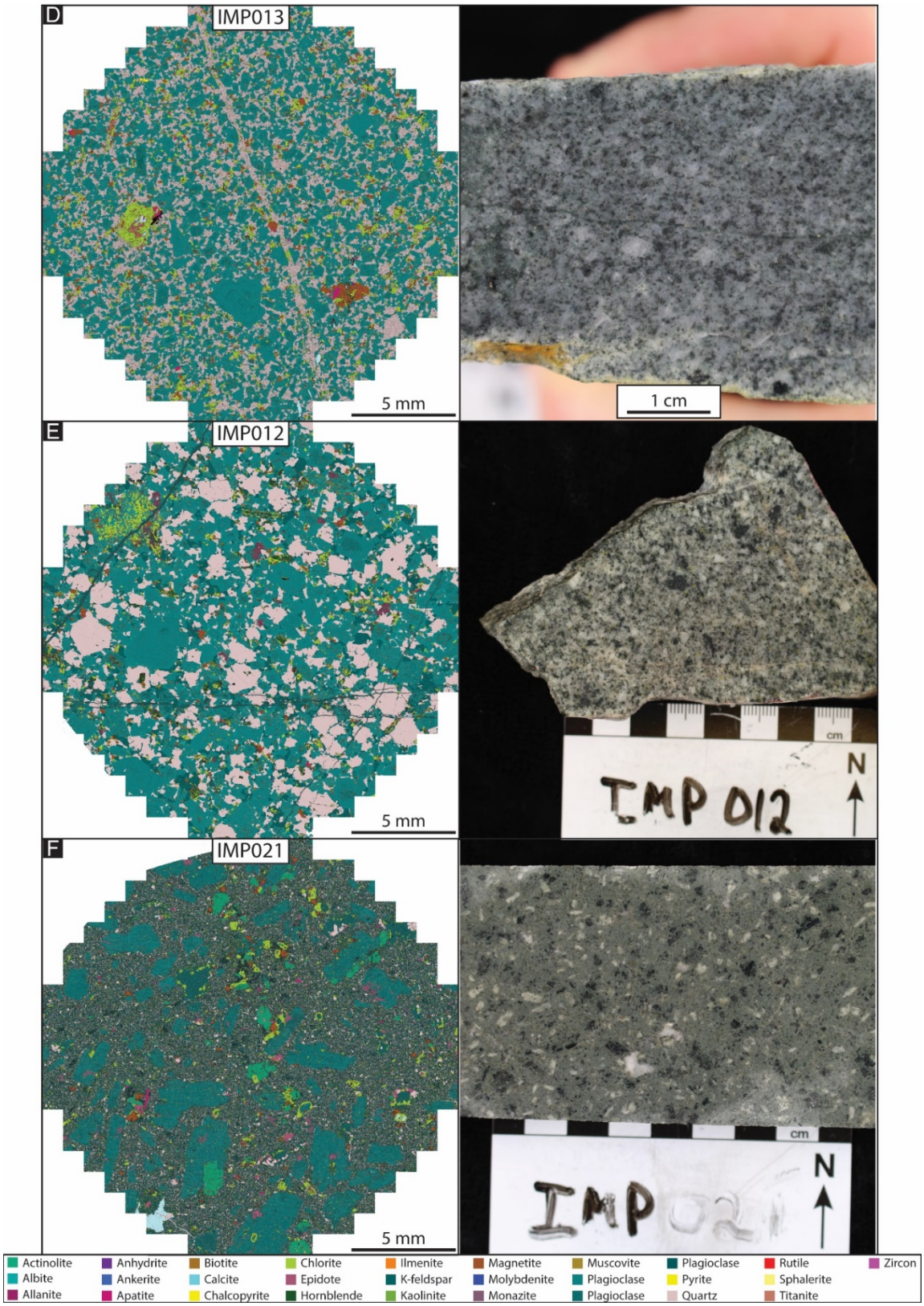


Figure 6.2. Selected TESCAN TIMA phase maps and photographs of the Cobre Panama sample suite. **A.** Andesite. **B.** Unaltered Petaquilla granodiorite. **C.** Early-mineral porphyry. **D.** Early-mineral porphyry. **E.** Late-mineral porphyry. **F.** Post-mineral porphyry. For the TIMA phase maps, darker plagioclase colours represent increasing anorthite content. Note, each increment of the scale bar in the photographs indicates 1 cm.

Petaquilla granodiorite

The Petaquilla granodiorite is an equigranular rock (average crystal size of ~1-2 mm) containing euhedral to subhedral plagioclase (~50%), amphibole (~4%) and magnetite (~1.5%), with interstitial quartz (~20%) and K-feldspar (~12%; Fig. 6.2B). Accessory phases, including apatite (~0.3%), titanite (0.1-0.5%) and zircon (~0.01%) are ubiquitous, and are often associated with magnetite or amphibole. Petaquilla granodiorite samples have undergone varying degrees of hydrothermal alteration, ranging from relatively unaltered (IMP001) through to moderately altered (IMP014). Hydrothermal alteration is characterised by addition of quartz, chloritisation of amphiboles, and alteration of plagioclase to albite and sericite. Subordinate alteration minerals include biotite, epidote, calcite and pyrite, either in veinlets or in association with altered amphiboles.

Porphyritic intrusions

Mine geologists differentiate porphyry intrusions using the phenocryst assemblage, characterising three separate intrusions: a i) feldspar-hornblende-quartz porphyry, a ii) feldspar-quartz porphyry and a iii) feldspar-hornblende porphyry (Gray *et al.*, 2019). However, the intrusions sampled during the present study are much more visually and texturally diverse, displaying a range of colours, from black through green to light grey, in addition to both crowded (i.e. phenocrysts > 50 modal %) and uncrowded (i.e. phenocrysts < 50 modal %) textures (Figs. 6.2C-F). As a result, porphyries are classified according to their timing in relation to mineralisation (early-mineral, post-mineral etc.). All porphyry intrusions contain well-formed plagioclase phenocrysts (~0.5 mm to ≤ 8 mm in length), which constitute the phenocryst assemblages of the porphyries in addition to either quartz (0.7-3mm), amphibole (0.8-4mm), or both quartz and amphibole. Crystal sizes of the groundmass differ considerably, with some samples showing an almost equigranular texture with occasional large phenocrysts (Fig. 6.2D). Alteration mineralogy and intensity varies between samples, though primary plagioclase is typically altered to secondary albite or sericite (or K-feldspar and epidote in rare cases). Similarly, amphibole is often chloritized, but can be replaced by biotite, epidote, titanite, pyrite or magnetite depending on the sample. Compared to other porphyry intrusions, the post-mineral porphyry (IMP021) is texturally distinct, containing irregularly shaped plagioclase (Fig. 6.2F), and actinolite (after amphibole) phenocrysts (≤1mm).

Post-mineral mafic dykes (IMP004, IMP009)

The two-studied post-mineral mafic dyke samples are both porphyritic but show different phenocryst assemblages and sizes. Sample IMP004 is slightly more evolved, containing quartz (0.5-2.5mm), plagioclase (0.4-3mm), magnetite (0.15-0.3mm) and chlorite-calcite (0.4-1.5 mm;

likely after amphibole) phenocrysts, in addition to quartz-calcite veins. The other studied sample, IMP009, contains phenocrysts of clinopyroxene (≤ 0.6mm) and another mineral which has been altered to calcite. Small chromite crystals (~200 μm) are found within these calcite phenocrysts, suggesting that the phenocrysts may have been chromites prior to hydrothermal alteration.

6.4 Results

6.4.1 Titanite textures

Titanite of a suitable size for analysis (e.g. Fig. 6.3) was identified in 75% of studied samples. Samples with no identifiable titanite were either from host volcanic sequence andesites, post-mineralisation mafic dykes or intensely-altered porphyries (Fig. 6.3). Titanite can be split into three groups based on mineral associations, grain morphology and chemical zonation. The first is commonly observed in rocks of the Petaquilla batholith, and in the porphyries is only found in sample IMP012, a weakly-altered late-mineral porphyry. This group is characterized by relatively large grains, sometimes up to a millimetre in length, that are intergrown with common igneous minerals such as zircon, hornblende and apatite (Fig. 6.3A). Additionally, this group can also be distinguished by the presence of sector zoning (Fig. 6.3B), or through increasing or decreasing BSE brightness from core to rim. Depending on the degree of hydrothermal alteration in the sample, titanite-hosted fluid inclusion trails are observed, with a higher abundance of fluid inclusion trails found in more strongly altered samples (Figs. 6.3A, C). An igneous origin is interpreted for this group.

The second group is predominantly observed in samples from the porphyry intrusions and is characterized by small (<30 μm) grains that show patchy zonation in BSE images. Titanite is typically associated with chlorite, epidote, allanite and calcite (Figs. 6.3C, D). Generally, this group exhibits anhedral, often angular morphologies, although titanite from the post-mineral porphyry (sample IMP021) instead shows an unusual, rounded and mottled morphology, in association with chlorite, epidote and actinolite (Fig. 6.3E). This group is inferred to have replaced earlier formed mafic minerals such as amphibole (Fig. 6.3F) and is subsequently referred to as replacement titanite.

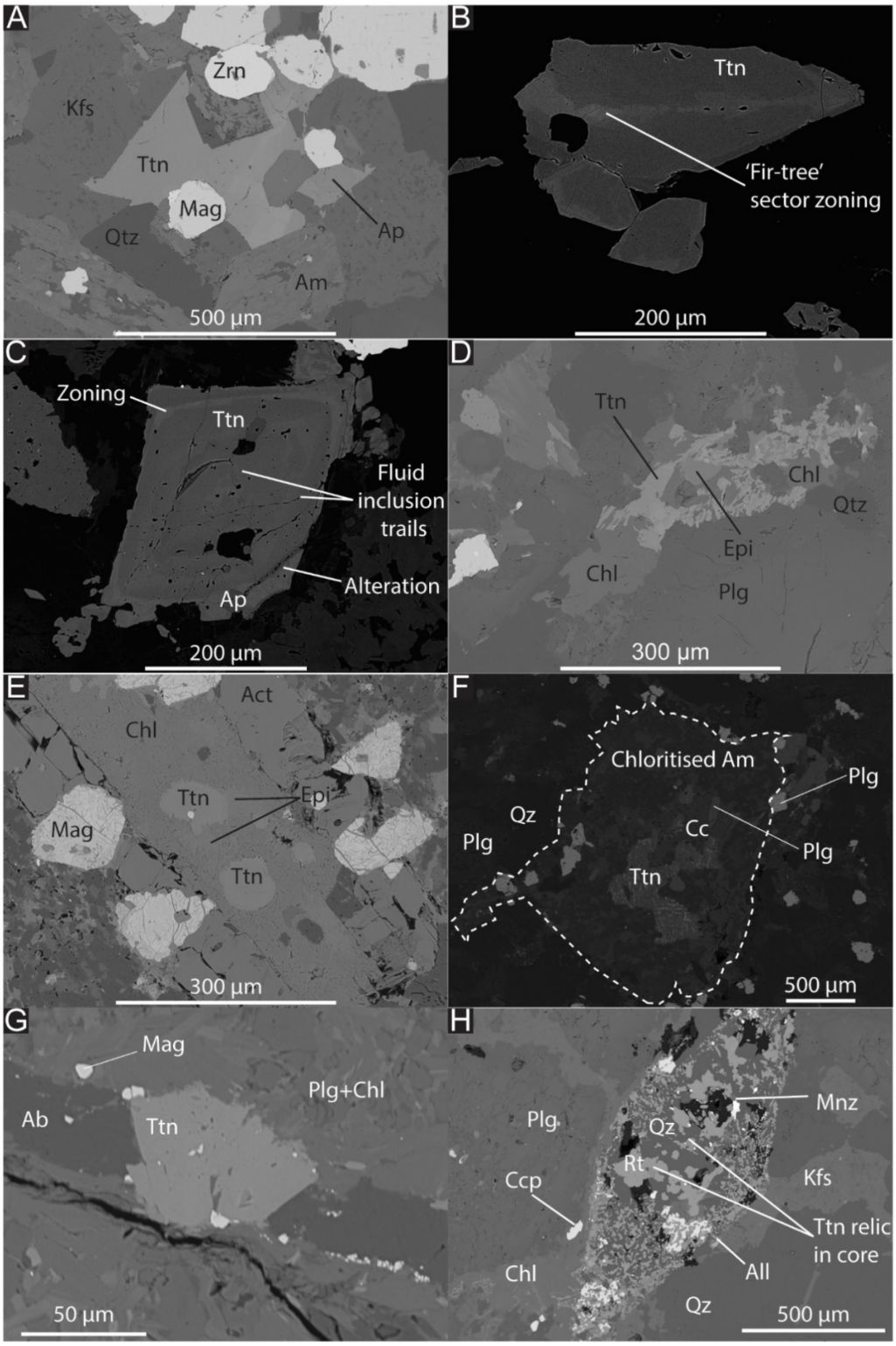


Figure 6.3. Titanite petrography from the Cobre Panama district. **A.** Typical mineral associations of igneous titanite (IMP001). **B.** Igneous titanite showing sector zoning (IMP010). **C.** Altered, zoned igneous titanite containing many fluid inclusion trails (IMP005). **D.** Typical replacement titanite, in association with chlorite and epidote (IMP011). **E.** Titanite from the post-mineral dacite porphyry (IMP021). **F.** Replacement titanite associated with altered amphibole phenocryst (IMP013). **G.** Vein-hosted titanite in albite vein (IMP006). **H.** Altered titanite phenocryst with altered titanite in the core (IMP017).

A final, volumetrically minor group - vein-hosted titanite (Fig. 6.3G) occurring with albite in veins) – was observed in one sample of the host andesite (IMP006). In addition to these groups,

clear pseudomorphs after titanite are observed in some of the altered porphyries (e.g. IMP017; Fig. 6.3H), in which relic titanite is observed in association with REE-bearing phases (e.g. allanite and monazite), rutile, chalcopyrite and quartz. Each grain that was targeted for analysis was classified as one of the three groups (igneous, replacement and vein-hosted), to enable subsequent comparison of chemical signatures.

Automated SEM analysis was used to estimate the volume percentages of minerals that are sharing grain boundaries with titanite (Appendix 9; Fig. 6.4). The dominant mineral assemblage strongly correlates with the degree of hydrothermal alteration, and on the dominant titanite group in the sample. For example, in a relatively unaltered sample where titanite is almost entirely

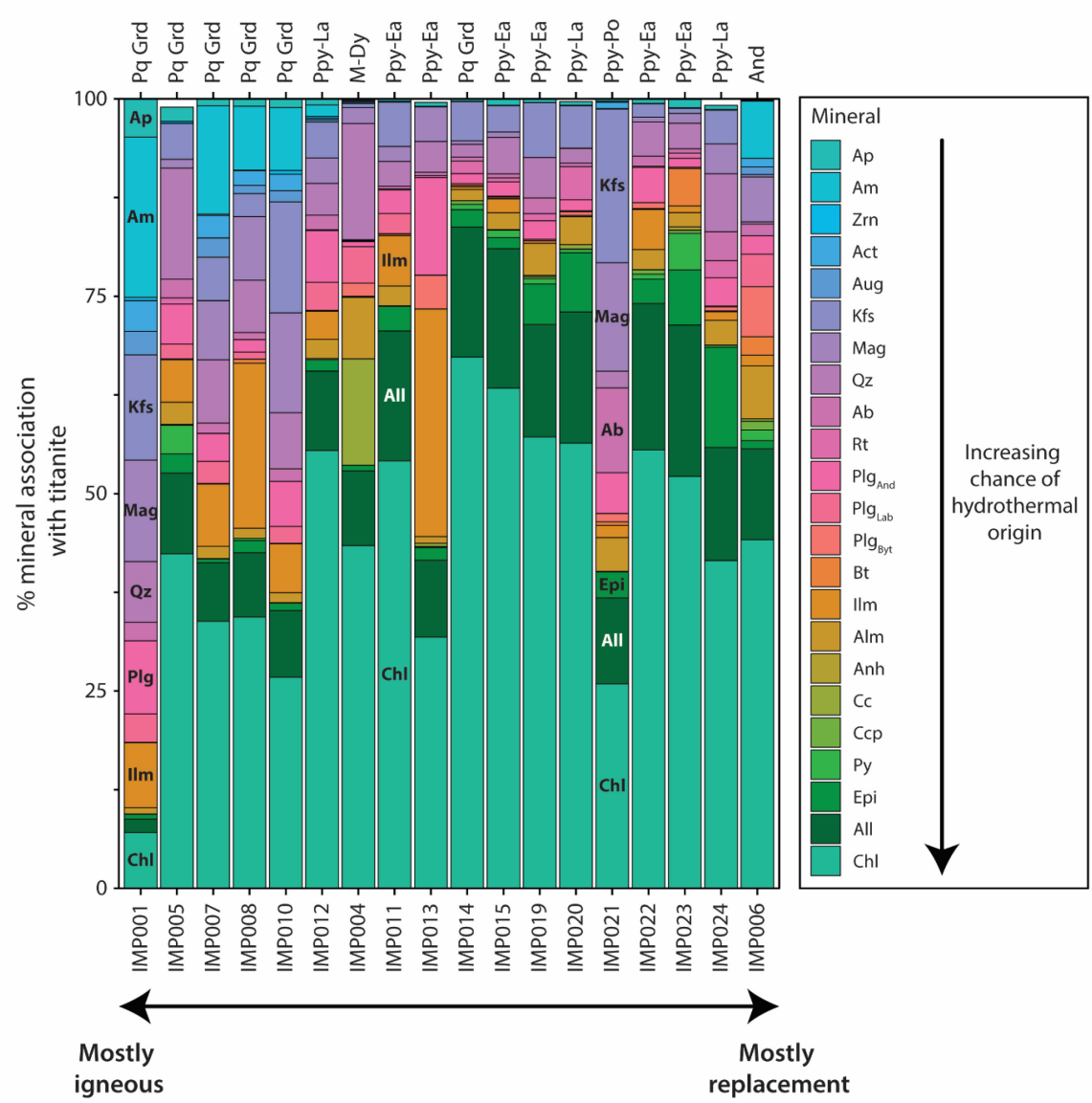


Figure 6.4. Percentages of minerals associations with titanite in different samples.

classified as igneous (IMP001), titanite is associated with amphibole + K-feldspar + magnetite + plagioclase. Oppositely, in moderately altered samples where titanite is dominantly classified as

replacement (IMP011), titanite is chiefly associated with chlorite and allanite (Fig. 6.4). Chlorite and allanite are the key minerals associated with titanite in replacement-dominated samples, although the abundances of these minerals increase in samples IMP005, IMP007, IMP008 and IMP010, in which titanite was dominantly classified as igneous. Of the samples which were dominated by replacement titanite, only IMP013 and IMP021 show some variation in the titanite associated mineral assemblage. Sample IMP013 contains an abundance of ilmenite, and IMP021 displays a K-feldspar + magnetite + albite + epidote + allanite + chlorite assemblage (Fig. 6.4).

6.4.2 U-Pb geochronology

Titanite U-Pb geochronology is only presented where a 30 μm spot size was employed during the analyses. Although applying a variable spot size does not have a major impact upon trace element analysis where concentrations may vary by orders of magnitude, using a variable spot size for U-Pb isotopic data may result in isotopic fractionation and hence biased data, due to varying transport properties (Horn *et al.*, 2000; Liu *et al.*, 2011). Hence, only 110 titanite analyses from 6 samples are presented (Fig. 6.5; Table 6.2). In addition to titanite, a total of 1054 zircon analyses in 21 samples were conducted at Rio Tinto Exploration (Table 6.2).

Table 6.2. Titanite and zircon U-Pb isotopic data for the Cobre Panama district. Titanite lower intercept ages, 2σ error and an additional propagated 2% external uncertainty, as well as MSWD and acceptable MSWD are shown. Acceptable MSWD is calculated using the equation of Wendt and Carl (1991).

Sample	Unit	Mineral	n	Age (Ma)	2σ error	2σ +2% ext. uncert)	MSWD	Acceptable MSWD*
IMP001	Pq Grd	Ttn	29	29.18	0.72	0.93	1.7	1.5
IMP001	Pq Grd	Zrn	50	28.87	0.38	0.69	1.7	1.4
IMP002	Ppy-La	Zrn	54	27.94	0.28	0.63	1.1	1.4
IMP004	M-Dy	Zrn	59	28.19	0.31	0.64	1.4	1.4
IMP005	Pq Grd	Ttn	23	30.52	0.95	1.13	2.2	1.6
IMP005	Pq Grd	Zrn	25	29.13	0.49	0.76	1.5	1.6
IMP007	Pq Grd	Ttn	16	29.72	2.41	2.48	1.9	1.7
IMP007	Pq Grd	Zrn	31	29.14	0.37	0.69	1.3	1.5
IMP008	Pq Grd	Ttn	9	28.43	1.35	1.46	1.1	2.0
IMP008	Pq Grd	Zrn	66	28.71	0.33	0.66	1.4	1.4
IMP009	M-Dy	Zrn	43	29.10	0.44	0.73	1.5	1.4
IMP010	Pq Grd	Ttn	22	29.91	0.98	1.15	1	1.6
IMP010	Pq Grd	Zrn	46	28.95	0.37	0.69	1.0	1.4
IMP011	Ppy-Ea	Zrn	54	28.82	0.38	0.69	1.5	1.4
IMP012	Ppy-La	Ttn	11	29.92	0.78	0.98	0.7	1.9
IMP012	Ppy-La	Zrn	63	28.27	0.36	0.67	3.4	1.4
IMP013	Ppy-Ea	Zrn	59	28.51	0.37	0.68	2.0	1.4
IMP014	Pq Grd	Zrn	67	29.15	0.35	0.68	1.6	1.3
IMP015	Ppy-Ea	Zrn	67	28.87	0.44	0.73	1.8	1.3
IMP016	Ppy-In	Zrn	46	28.32	0.48	0.74	1.5	1.4
IMP017	Ppy-Ea	Zrn	39	28.73	0.55	0.80	1.5	1.5
IMP018	Ppy-Ea	Zrn	61	29.09	0.35	0.68	1.7	1.4
IMP019	Ppy-Ea	Zrn	44	27.37	0.26	0.61	1.1	1.4
IMP020	Ppy-La	Zrn	53	28.61	0.36	0.68	1.7	1.4
IMP022	Ppy-Ea	Zrn	36	28.73	0.30	0.65	1.1	1.5
IMP023	Ppy-Ea	Zrn	52	28.73	0.42	0.71	2.2	1.4

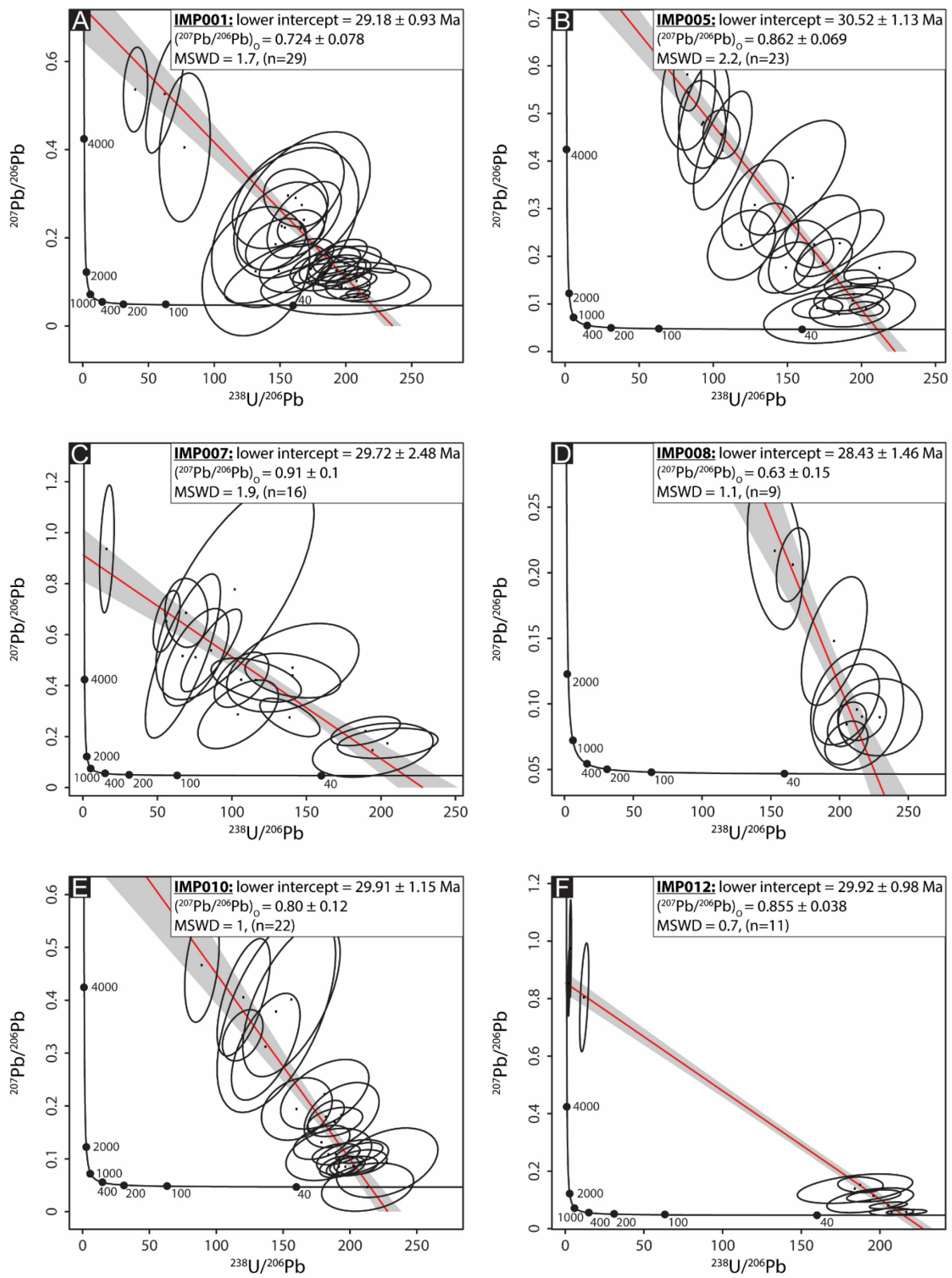


Figure 6.5. Tera-Wasserburg Concordia diagrams showing titanite age data from the Cobre Panama district. 2σ error ellipses are shown, in addition to the 2σ uncertainty associated with the regression. Crystallisation ages are presented with error, which is derived from the regression, with an additional propagated external uncertainty of 2%.

6.4.3 Geochemistry

Whole-rock

Whole-rock geochemistry of all studied samples was determined at ALS Laboratories (as outlined in Chapter 3). Intensity of hydrothermal alteration in the studied samples is variable, ranging from relatively unaltered (IMP001; Fig. 6.2A) to intensely altered (e.g. IMP016). Igneous classification diagrams commonly utilise mineral modal proportions (Streckeisen, 1976), or concentrations of alkali elements, such as K and Na (Peccerillo & Taylor, 1976; Barton & Young, 2002). However, alkali elements are extremely mobile during alteration, and mineral modal abundances, particularly of quartz, alkali feldspar and plagioclase, are likely to be affected by hydrothermal alteration. Consequently, classification diagrams which use immobile elements are better suited to hydrothermally altered rocks (Halley, 2020). Based on the Th-Co diagram of Hastie *et al.* (2007), all rocks have a calc-alkaline affinity. Most samples, particularly the Petaquilla granodiorite and the porphyries, have an intermediate to felsic composition (Fig. 6.6), although one sample of the Petaquilla granodiorite was significantly more mafic. Despite being termed 'andesites', the studied volcanic samples classify as basalts according to the diagram of Hastie et al., (2007) (Fig. 6.6), suggesting that the abundance of quartz in IMP003 may result from hydrothermal alteration. Furthermore, post-mineral mafic dyke sample IMP004 has an intermediate composition, although it is close the boundary with mafic compositions. In spite of the misclassification, unit names as determined by the mine are retained for ease.

Chondrite-normalised whole-rock REE patterns of the andesites are relatively flat, with a weak enrichment in LREEs relative to HREEs, and a weakly negative Eu anomaly (Fig. 6.7A). Studied samples of the Petaquilla granodiorite and porphyritic intrusions show a remarkably consistent REE signature, with a strongly negatively sloping, listric REE pattern, in addition to a weakly negative to positive Eu anomaly (Figs. 6.7B, C). The only sample which deviates from this signature is IMP021, which shows slightly higher LREE concentrations, but significantly higher HREE concentrations (resulting in lower La/Yb ratios), as well as a more negative Eu/Eu* relative to the other porphyries (Fig. 6.7C). Post-mineral mafic dykes show transitional compositions between the andesites, and Petaquilla granodiorite/porphyries (Fig. 6.7D). The more mafic sample (IMP009) exhibits a similar pattern to the andesites, whereas IMP004 (more felsic) is starting to develop the LREE enrichment and HREE depletion that characterises the batholith and porphyritic intrusions (Fig. 6.7). REE compositions determined in this study generally agree with published compositions for the same units (Baker *et al*. 2016; Figs. 6.7E, F). In fact, REE compositions of

the Petaquilla granodiorite determined in this study are similar to those from the southern portion of the batholith (Fig. 6.7E). However, key differences are observed compared to the older portions

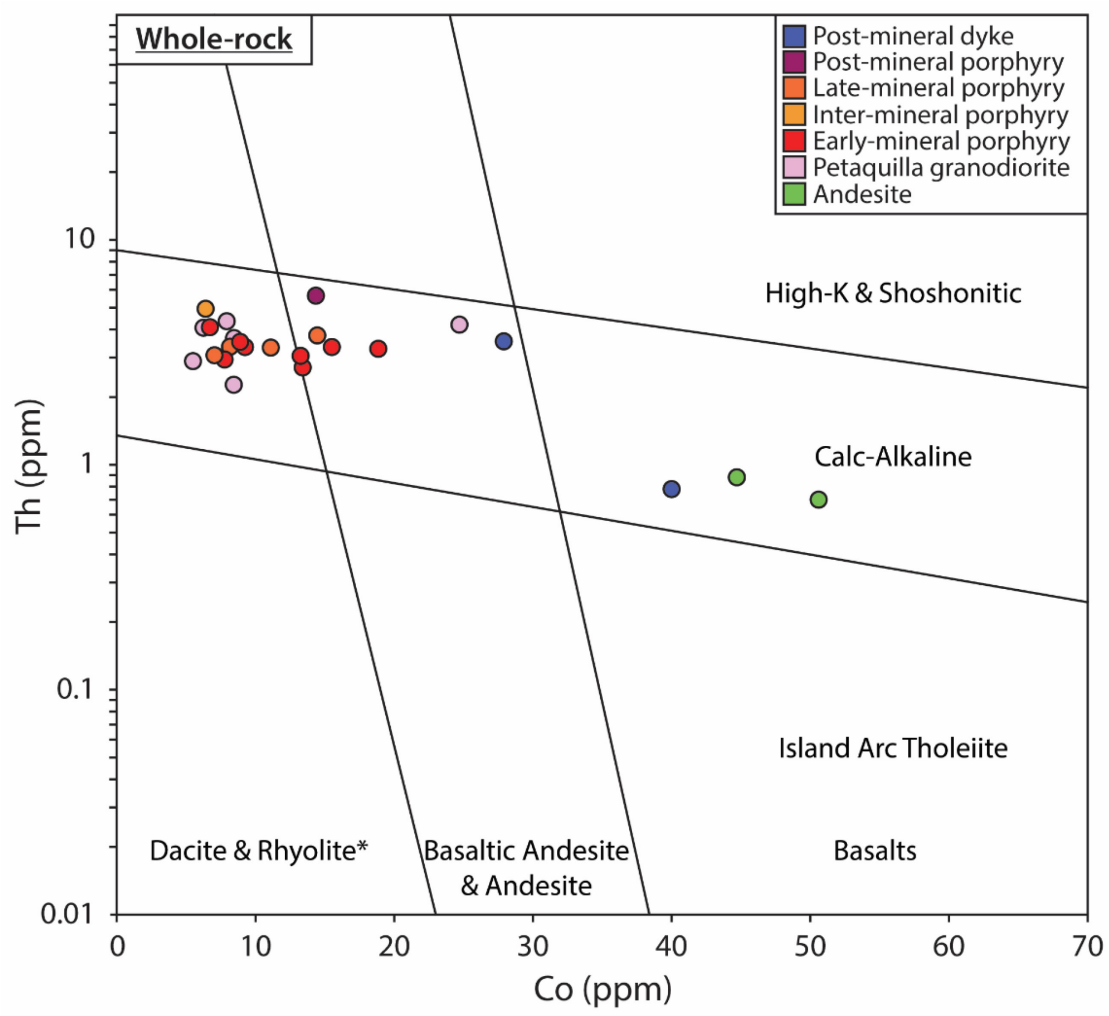


Figure 6.6. Thorium-cobalt immobile element classification diagram (Hastie *et al.*, 2007). Analytical error was estimated to be ~2% for Co and 6% for Th.

of the batholith, with a progressive HREE depletion and Eu anomaly suppression, through time and from north to south. Comparisons between porphyry REE compositions determined in this study and literature data reveals that nearly all porphyries have a similar REE pattern, which itself is identical to that from the southern portion of the batholith. Despite its uniqueness within the studied sample suite, REE patterns which are equivalent to post-mineral porphyry sample IMP021 can be identified in the literature (Fig. 6.7F).

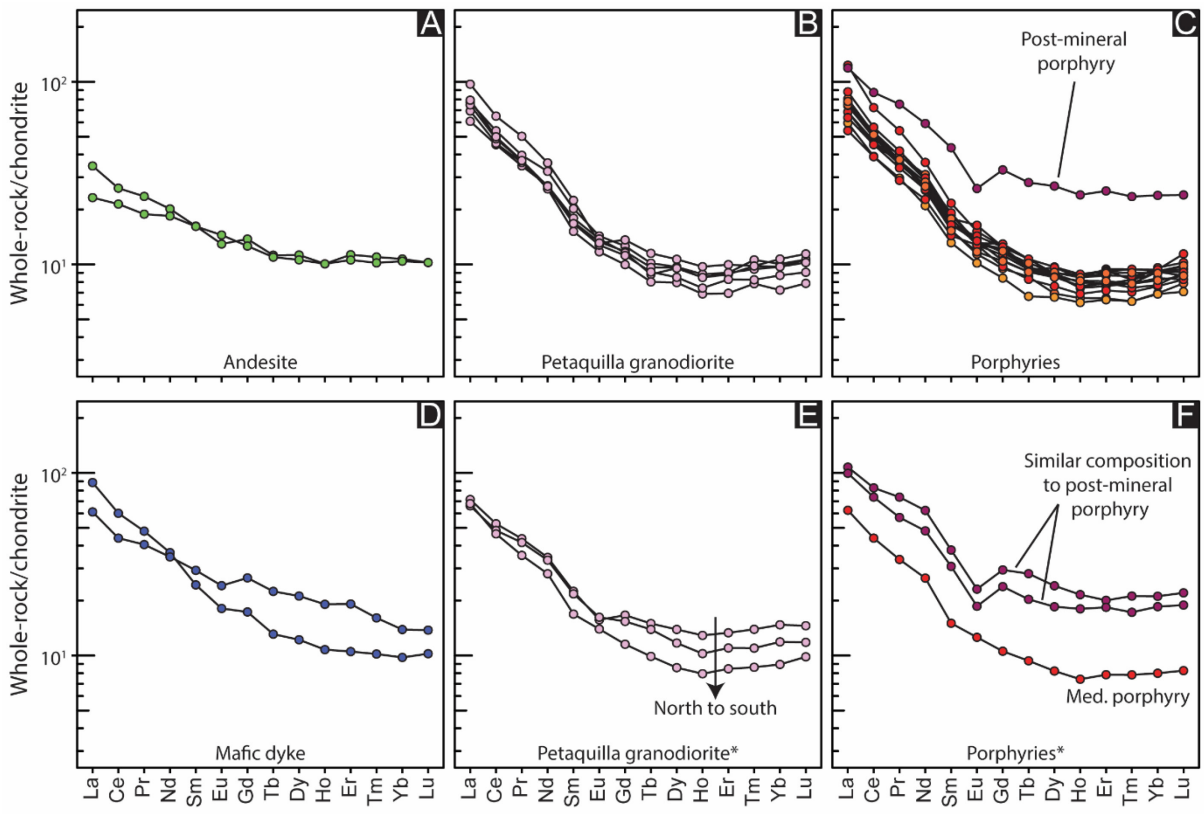


Figure 6.7. Whole-rock chondrite-normalised (Boynton, 1984) REE patterns for samples collected in this study (**A-D.**) and for literature data (**E-F.**; Baker *et al*. 2016). Median compositions are displayed for the north, central and southern portions of the batholith (**E.**), as well as all porphyries (**F.**). *Indicates literature data, taken from Baker *et al.* (2016). Designation of batholith samples as north, central and southern is based on Baker *et al.* (2016) and Sepp and Dilles (2018). Also shown are compositions of porphyritic intrusions that are similar to the post-mineral porphyry. Average 2σ errors are smaller than symbol size.

Titanite

Titanite chondrite-normalised REE patterns show differences between and within units (Fig. 6.8). Only a few successful titanite analyses (vein-hosted and replacement) were possible in the andesite, which dominantly has a shallowly, negatively sloping REE pattern with a slightly positive Eu anomaly (Fig. 6.8A). Concentrations of individual REEs in the Petaquilla granodiorite vary over 2 orders of magnitude. However, observed REE patterns are much more consistent, dominantly showing a negatively sloping REE pattern with a moderately negative Eu anomaly (Fig. 6.8B). With decreasing REE concentrations, Eu/Eu* increases in Petaquilla granodiorite titanite, which also develops a listric pattern. Additionally, a minor proportion of LREE-depleted titanite is also present in the Petaquilla granodiorite (Fig. 6.8B). Early-mineral porphyry titanite, like those from the Petaquilla granodiorite, displays a range of individual REE concentrations, varying over approximately three orders of magnitude (Fig. 6.8C). The overwhelming majority of titanite from the early-mineral porphyry displays positively sloping REE patterns, with variable Eu anomalies (both strongly negative and positive). Two dominant REE signatures are observed in late-mineral

porphyry, with titanite from sample IMP012 typically showing a negatively sloping REE pattern with a moderately to weakly negative Eu anomaly (Fig. 6.8D). Other late-mineral porphyry

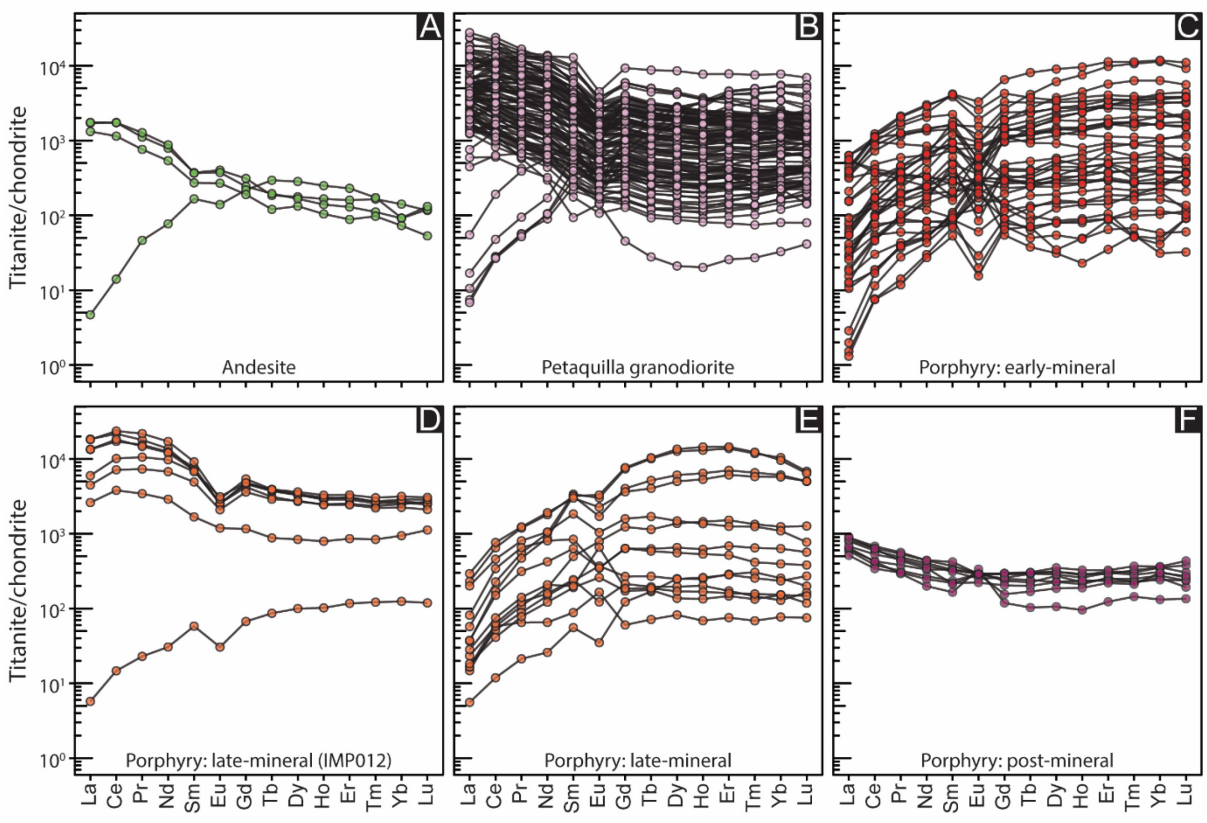


Figure 6.8. Chondrite normalised (Boynton, 1984) REE plots for titanite from the Cobre Panama district. Average 2σ errors are smaller than symbol size.

samples, however, show LREE-depletion (Fig. 6.8E) like those observed in the early-mineral porphyries. Finally, post-mineral porphyry titanite exhibits a unique, flat to slightly concave-upward REE pattern (Fig. 6.8F).

Zircon

Zircon trace element data are shown in relation to those of the 'porphyry indicator zircons' fields of Lu *et al.* (2016) and Pizarro *et al.* (2020). Most zircons have characteristics in common with zircons from porphyry systems, with elevated Eu/Eu* and (Ce/Nd)/Y, as well as low Dy/Yb and Th/U (Figs. 6.9A-C). Low crystallisation temperatures and a moderately elevated magmatic oxidation state were determined, with the majority estimated to have crystallised at temperatures less than 800 °C (Ferry & Watson, 2007) and between FMQ+1 and +3 (Loucks *et al.*, 2020).

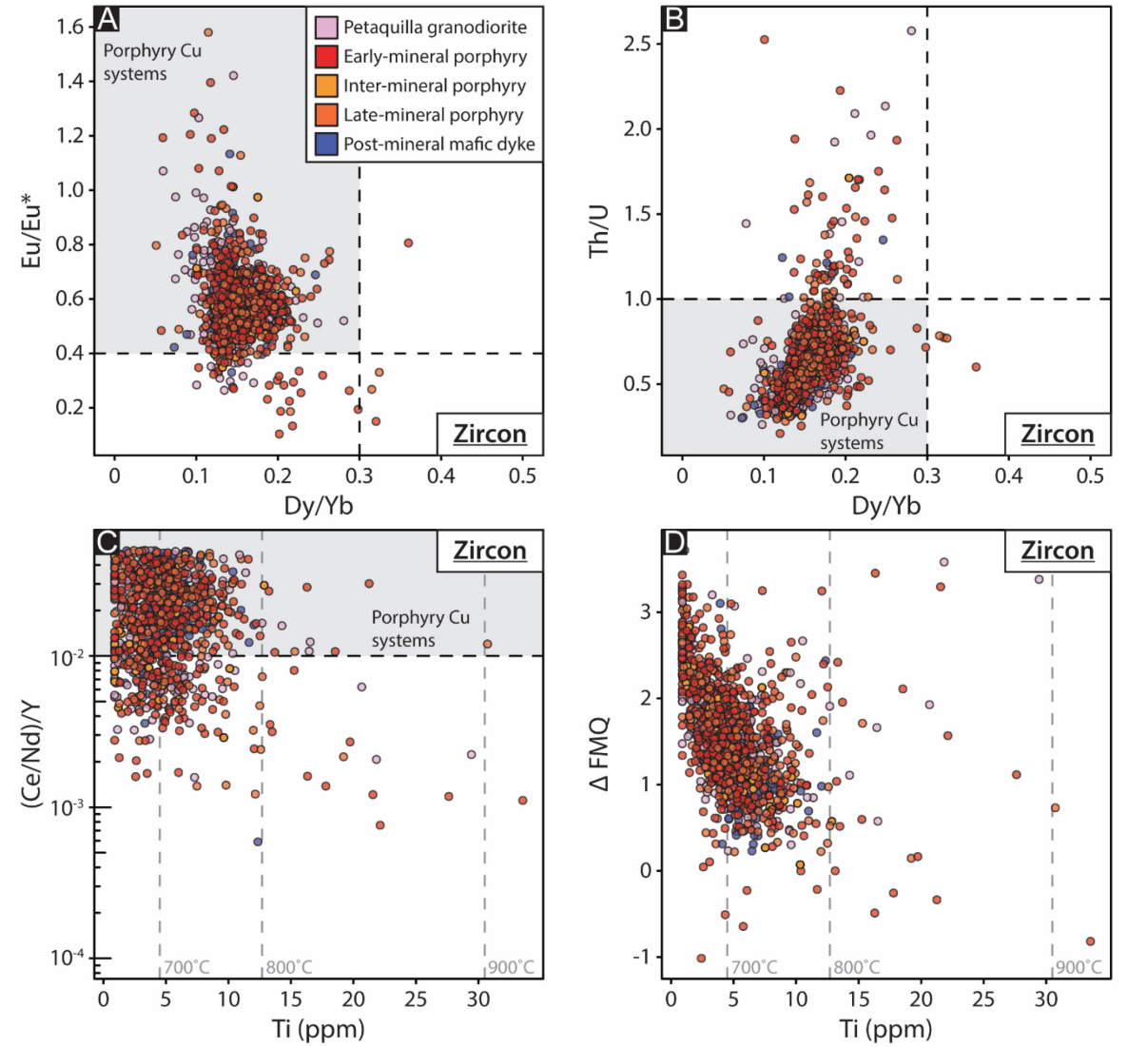


Figure 6.9. Zircon trace element compositions from the Cobre Panama district. **A.** Eu/Eu* vs Dy/Yb. Eu/Eu* is calculated using chondrite normalised REEs (Boynton, 1984). **B.** Th/U vs Dy/Yb. **C.** (Ce/Nd)/Y vs Ti. **D.** FMQ vs Ti. Also shown are fields for zircons from porphyry Cu systems (A-C; Lu *et al.*, 2016; Pizarro *et al.*, 2020), approximate Ti-in-zircon crystallisation temperatures (**C-D.**) assuming $\alpha SiO_2 = 1$ and $\alpha TiO_2 = 0.7$ (Ferry & Watson, 2007) and log fO_2 (ΔFMQ) using the zircon oxybarometer (Loucks *et al.*, 2020). Average 2σ errors are smaller than symbol size.

6.5 Discussion

6.5.1 Titanite Geochronology

Besides Petaquilla granodiorite sample IMP007 (~8%), all samples returned errors that were around 4% of the titanite lower intercept age. Titanite U-Pb data are consistent within uncertainty with zircon data from the same samples (Fig. 6.10). Moreover, nearly all samples, including post-mineral mafic dykes, overlap within uncertainty, returning an age of ~29 Ma which is consistent with literature data from the south of the district (Fig. 6.10; Baker *et al*. 2016). The exception to this is early-mineral porphyry sample IMP019, from the Colina deposit, which returns an age (~28-

27 Ma) that is younger than titanite and zircon ages from several batholith samples (IMP001, IMP005 and IMP010). Despite this, similar ages are observed in both batholith samples and porphyritic intrusions, in the latter case at the Balboa deposit (Fig. 6.10; Baker *et al*. 2016). This suggests that although crystallisation took place over a relatively short time window at the Botija deposit, more protracted crystallisation may have taken place elsewhere in the district. Unfortunately, no zircons were separated from samples IMP003 (andesite) and IMP021 (post-

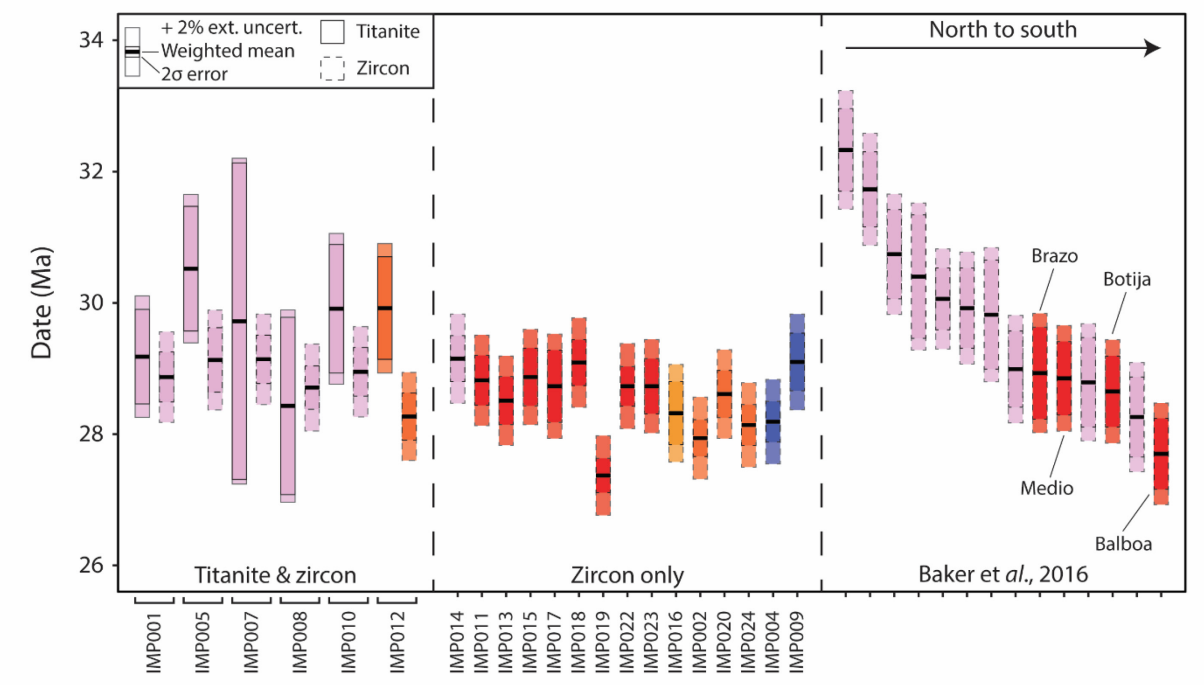


Figure 6.10. Plot comparing titanite lower intercept ages with zircon Concordia ages. Also shown is 2σ uncertainty with ±2% external uncertainty. Shown for comparison are ages determined by Baker *et al.* (2016).

mineral porphyry), and only two successful zircon analyses were possible in IMP006 (andesite). Consequently, the age of these rocks is unclear, though a late-Eocene biostratigraphic age has been suggested for volcanics in the Cobre Panama district (Redwood *et al.*, 2021).

6.5.2 Differentiating igneous and replacement titanite

Variable titanite REE signatures within a single sample (e.g. IMP012; Fig. 6.8D) are identified in samples that contain both igneous and replacement titanite. To group these titanite data into multiple populations, principal component analysis (PCA) was conducted. PCA is an unsupervised machine learning technique that is commonly used for dimensionality reduction (James *et al.*, 2013). Applying statistical techniques to geochemical data is made challenging by its compositional nature, in that elemental concentrations must sum to a constant value (e.g. 100%). This phenomenon, known as the constant sum effect, means that increasing concentrations of one component necessitate decreasing concentrations of another, potentially resulting in spurious

correlations (Aitchison, 1982). To overcome the constant sum effect, centred-log-ratio (clr) transformations of each component were conducted. Centred-log-ratio transformations allow data to vary in real number space without constraint, ensuring that all variables are statistically independent (Buccianti & Grunsky, 2014; Grunsky & Caritat, 2020). Prior to PCA, all censored data (i.e. observations containing element concentrations below LOD) and elements with concentrations that were consistently below LOD were removed. PCA was then undertaken on clr-transformed data, with both conducted in the free programming software R using the clr (Hotelling package; Curran, 2021) and prcomp (Base R) functions respectively. PCA was performed on Cobre Panama titanite to i) identify which elements are important in differentiating igneous and replacement titanite, and ii) understand the controls on titanite trace element composition. Elements included in the PCA were V, Sc, Mn, Sr, Zr, Nb, REEs, Hf, Ta, Th and U.

Results of the PCA (Appendix 10) are compared to titanite groupings (i.e. whether igneous, replacement or vein-hosted), allowing elements which are characteristic of the groupings to be easily identified. Most variables which are included partially discriminate between igneous and replacement titanite (Fig. 6.11A). Indeed, igneous titanite is characterised by high LREE and Th concentrations, whereas replacement titanite displays two end member compositions (Fig. 6.11A). One that is controlled by HREE enrichments, and another that is controlled by enrichments in Sc, Al, F and V (Fig. 6.11A). Hence, PCA highlights the fractionation of REEs between titanite types, as is evident in chondrite-normalised REE patterns (Fig. 6.8).

It is interesting to note that an igneous signature is retained in samples where minerals around titanite are being altered (e.g. IMP005; Fig. 6.4). For example, igneous titanite in sample IMP005 shares ~40% of grain boundaries with chlorite, compared to <10% in sample IMP001, reflecting an increased degree of hydrothermal alteration (as chloritisation). In spite of this, titanite geochemical signatures are almost identical between samples (Fig. 6.11B), implying that titanite and its geochemical signatures are more resistant to alteration than amphibole (which is altering to chlorite). Compositions of post-mineral porphyry titanite (IMP021) are also highlighted, which was identified to show unique signatures compared to replacement titanite in other samples. Vein-hosted titanite does not show a consistent signature, instead showing both igneous and replacement-like signatures (Fig. 6.11B). Further analysis is likely required to ascertain factors controlling vein-hosted titanite compositions.

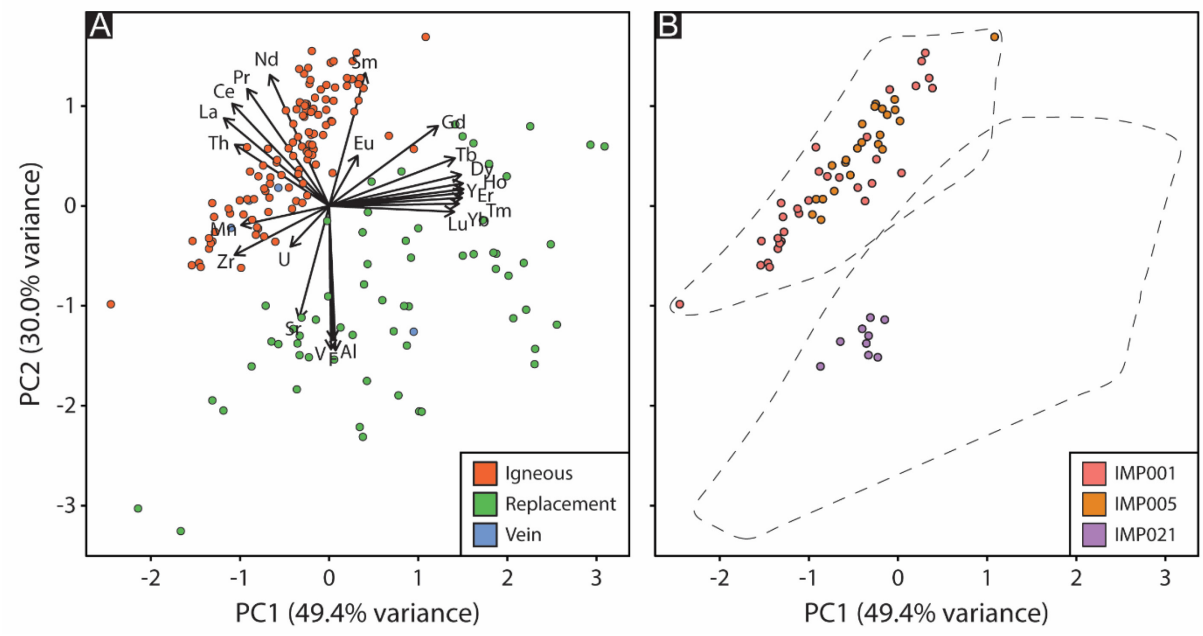


Figure 6.11. Results of principal component analysis on titanite from the Cobre Panama district. Observations are colour-coded by whether they classified as igneous, replacement or vein-hosted. PC1 vs PC2 is displayed, in addition to PC loadings for each element, which is represented by vectors. **A.** All data. **B.** Samples that are discussed in the text, with boxes indicating fields of igneous and replacement titanite.

Through combining PCA results with previous work, bivariate plots can be constructed which better illustrate compositional differences between igneous and replacement titanite (Fig. 6.12). Several studies have identified the utility of plotting F against Fe/Al ratios to identify titanite formed in different environments (Nakada, 1991; Enami *et al.*, 1993; Kontonikas-Charos *et al.*, 2019). Additionally, ΣREE concentrations and Th/U ratios have been used to differentiate titanite types (Li *et al.*, 2010; Cao *et al.*, 2015; Kontonikas-Charos *et al.*, 2019). Selected element concentrations and ratios in bivariate space are subsequently employed to highlight compositional differences between the groups (Fig. 6.12).

Replacement titanite is enriched in F (up to 2.5 wt.%) but has low Fe/Al (mostly 0-1), whereas igneous titanite exhibits low F (sometimes below the LOD) with a higher but restricted range of Fe/Al (1.5-3.5). Vein-hosted titanite is enriched in Fe/Al but contains low concentrations of F (Fig. 6.12A). Igneous titanite has high ΣREEs and Zr relative to replacement titanite, with estimated Zr-in-titanite crystallisation temperatures of ranging from in excess of 800 °C down to the solidus (~650°C; Fig. 6.12B). Additionally, igneous titanite is also enriched in Mn and displays higher Th/U ratios (Fig. 6.12C) relative to replacement titanite but contains lower concentrations of V and Sc (Fig. 6.12D). Vein-hosted titanite shows significant variability between grains for these elements.

After successfully delineating the characteristics of igneous and replacement titanite, inferences can be made on the factors controlling these signatures. Igneous mineral chemistry is linked to corresponding melt compositions through mineral-melt partition coefficients, unless

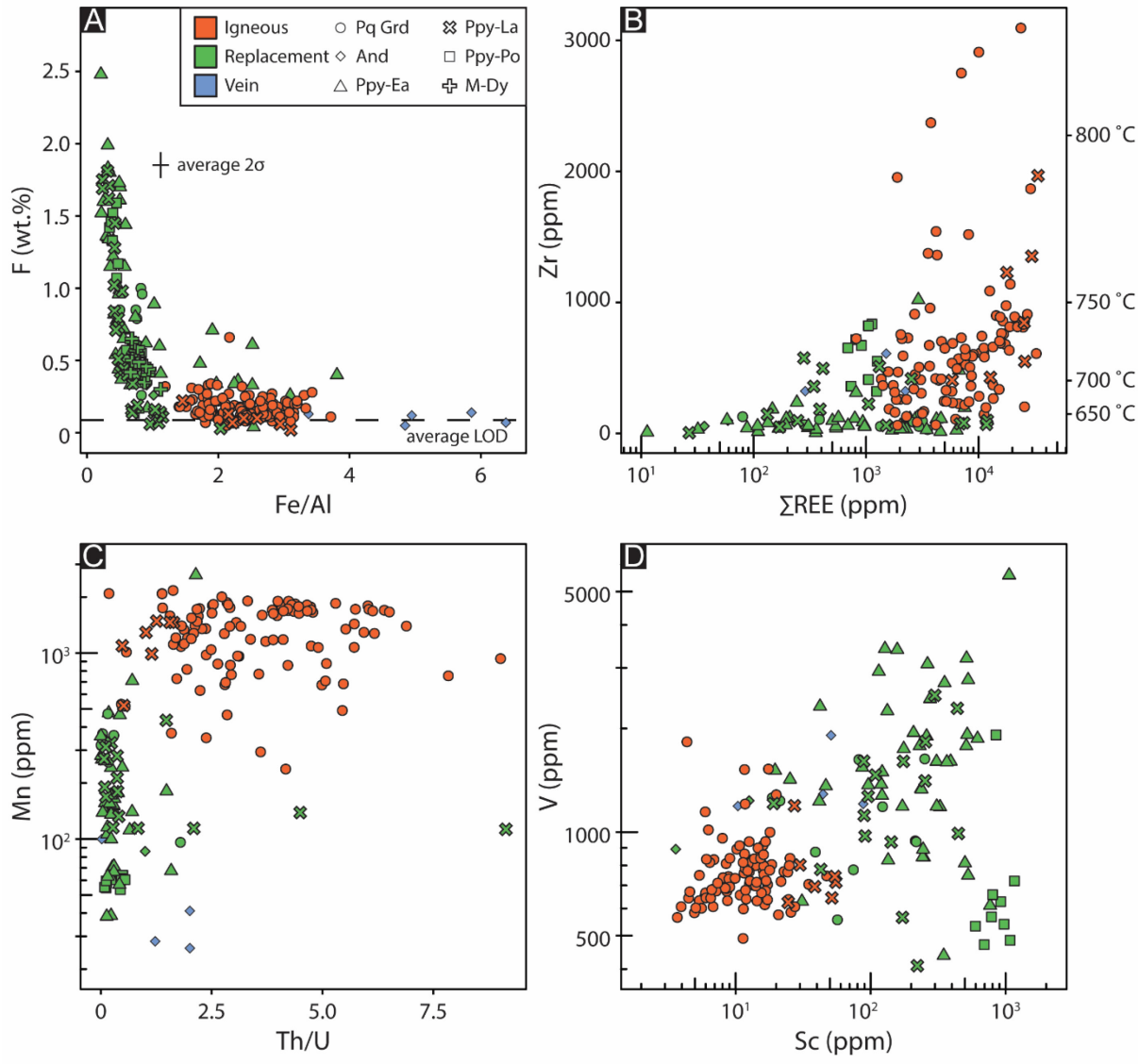


Figure 6.12. Titanite minor and trace element chemistry , as determined by EPMA (**A.**) and laser-ablation ICP-MS (**B-D.**). Colours indicate whether titanite was classified as igneous, replacement or vein-hosted, and symbols indicate the host lithology. **A.** F vs Fe/Al. **B.** Zr vs ΣREE. Approximate crystallisation temperatures for igneous titanite (Hayden *et al.*, 2008) are also shown, assuming $a\mathrm{SiO_2}$ =1, $a\mathrm{TiO_2}$ =0.7 and pressure = 1.5 kb. **C.** Mn vs Th/U. **D.** V vs Sc. Where not specified, 2σ uncertainty is smaller than the symbols.

Trace element incorporation is temperature dependent (e.g. Zr-in-titanite thermometer; Hayden *et al.*, 2008). Partition coefficients for a range of trace elements, including REEs and HFSEs, are extremely high for titanite ($D^{Ttn/melt}$ >100; Bachmann *et al.*, 2005; Prowatke & Klemme, 2005; Colombini *et al.*, 2011), resulting in high elemental concentrations in igneous titanite. Such factors control the signatures of igneous titanite, which will be further discussed later.

Relative to igneous titanite, controls on compositions of replacement, or hydrothermal titanite are much more variable, with a range of potential factors including element mobility in hydrothermal fluids, equilibration with other phases and inheritance from precursor igneous minerals. Elevated F and Al (resulting in low Fe/Al ratios) characterise replacement titanite (Fig. 6.12A), a signature which has been noted by several studies (Enami *et al.*, 1993; Kontonikas-Charos *et al.*, 2019). These elemental enrichments are related to an increasing vuagnatite component, $CaAlSiO_4(OH, F)$, in which Al substitutes for Ti (Sarp *et al.*, 1976; Oberti *et al.*, 1991). Several publications have been devoted to the origins of Al-rich titanite, with increased stability favoured by high host-rock Al/Ti ratios, high pressures, low temperatures and high F activities (Enami *et al.*, 1993; Markl & Piazolo, 1999). Of these, high pressures can be disregarded, as porphyry systems occupy the uppermost portion (~1-6 km, Seedorff *et al.*, 2005; Sillitoe, 2010) of the crust, and hence one or more of the other factors are probably responsible.

Zirconium, with its temperature-dependent partitioning into igneous titanite (Hayden *et al.*, 2008), is an element which is considered to be relatively immobile in aqueous fluids (Halley, 2020). Hence, if replacement titanite were to inherit Zr from precursor minerals, as was shown in Chapter 5 for rutile Ce contents, then titanite Zr contents would be strongly dependent on the igneous mineral that was being altered. Titanite is observed in association with altered amphibole in some samples (e.g. Fig. 6.3F), which could potentially explain low Zr contents in replacement titanite, with Zr contents for example of ~35 ppm common for igneous amphibole from Strontian (Appendix 4). Rare earth elements are also typically considered to be immobile (Williams-Jones *et al.*, 2012). Higher REE concentrations are generally observed for igneous titanite, however, REE concentrations may actually reach 1 wt.% in replacment titanite (Fig. 6.12B). Considering the REE patterns of igneous and replacement titanite (Fig. 6.8), it is clear that HREEs are preferentially incorporated into replacement titanite relative to LREEs. Based both on experimental studies (Williams-Jones *et al.*, 2012) and by comparing elemental concentrations in altered and unaltered samples (isocon method; Ulrich & Heinrich, 2002), LREEs are generally thought to be more mobile than HREEs in the porphyry environment and hence the relative enrichment in HREE for replacement titanite could be explained by mobilisation of LREEs to distal parts of the system. However, the consistency in REE patterns between unaltered and altered samples suggests, at least at the same scale, that no meaningful fractionation of LREEs from HREEs was taking place. Instead, it seems more likely REEs are being mobilised at a local scale. Replacement titanite is commonly associated with allanite (Fig. 6.4), a LREE-rich epidote, suggesting that the two phases may be in equilibrium, with allanite preferentially incorporating LREEs and titanite taking in HREEs.

Previous studies have noted the tendency of hydrothermal titanite to exhibit lower Th/U ratios than igneous titanite (Li *et al.*, 2010; Deng *et al.*, 2015; Zhang *et al.*, 2022). Such ratios may also result from equilibration with allanite, which prefers Th over U (Hermann, 2002), or may simply represent immobility of Th, relative to U (Langmuir, 1978; Langmuir & Herman, 1980). Similarly, relative Mn depletion and enrichment in V and Sc in replacement titanite relative to igneous titanite may be explained by the mobility of these elements after liberation from the breakdown of mafic phases. Manganese is considered to be one of the most mobile transition elements, with V and Sc progressively more immobile (Halley, 2020). For example, chlorite compositions from the propylitic environment often show enrichment in V proximally, whereas Mn contents of chlorite are generally higher further from the centre of the deposit (Xiao *et al.*, 2018; Wilkinson *et al.*, 2020). Alternatively, any available Mn may be preferentially incorporated into chlorite, which is almost always associated with titanite. Few studies have determined Sc contents of chlorite in porphyry systems, but limited research that has been conducted suggests that Sc, like V, tends to be enriched more proximally (Xiao *et al.*, 2018).

The trace element compositions of replacement titanite are mosly consistent between different units (Fig. 6.8). However, titanite signatures from IMP021 are unique, characterised by flat REE patterns, as well as strong enrichments in F and Sr (see Appendix 2). Percentage mineral associations with titanite differ from those found in association with replacement titanite from other units (e.g. higher magneite and K-feldspar). It is unclear what is responsible for the unusual titanite signature, although potential factors include lower temperatures (due to the post-mineral timing of the intrusion) or host-rock influence (as similarly unique REE signatures are observed for whole-rock chemistry).

In summary, replacement tianite (relative to igneous titanite) is characterised by enrichments in F, Sc, V, and depletions in LREEs and Fe/Al ratios. These characteristics are interpreted to reflect fluid composition at the time of titanite precipitation, which in turn may be influenced by i) liberation after alteration of primary igneous phases, as well as ii) prior or co-precipitation of other mineral phases.

6.5.3 Cobre Panama magmatic system

Whole-rock literature data (Baker *et al.*, 2016) highlights the evolution of the Cobre Panama magmatic system through time. In the older, northern portion of the Petaquilla batholith, whole-rock REE patterns show a more negative Eu anomaly and are less depleted in mid to heavy-REEs (Fig. 6.7E). As the batholith gets younger, towards the south, the negative whole-rock Eu anomaly is eradicated and mid- to heavy-REEs become progressively more depleted (Fig. 6.7E). Such a

temporal evolution is noted in multiple porphyry districts, including Chuquicamata (Ballard, 2001), Quellaveco (Nathwani *et al.*, 2021) and Yerington (Carter et al., 2022), and is widely believed to represent protracted deep, and hydrous fractionation in the lower crust (Rohrlach & Loucks, 2005; Richards, 2011; Loucks, 2014). Unfortunately, no samples were collected from older portions of the batholith, so it is unclear whether titanite was present in these rocks. However, it is postulated that if titanite is present in older sections of the batholith, then titanite compositions would evolve through time (as seen in Chapter 5), with high Dy/Yb and more negative Eu anomalies in the north.

Despite the variety of morphologies and textures observed in the porphyries, compositions of the various porphyry intrusions and the southern part of the batholith are indistinguishable, based on whole-rock, zircon and (igneous) titanite geochemistry, as well as geochronology (e.g. Figs. 6.7-10). Such an observation has been noted in other porphyry systems, such as the Quellaveco district in Peru (Nathwani *et al.*, 2021). Only the post-mineral porphyry, sample IMP021, showed a different whole-rock signature (Fig. 6.7E), which in addition to an inability to separate zircons, make this intrusion unique compared to the rest of the porphyry sample suite. Interestingly, similar HREE-enriched, Eu-depleted whole-rock signatures are identified in the literature data (Fig. 6.7F), with all samples occurring in the north-west of the district, either in the Colina deposit or Lata prospect. Further delineation of the extent and geometry of this unmineralised intrusion is required, with important considerations for estimating grade.

6.5.4 Inferring porphyry titanite compositions

To date, there has been an enormous amount of zircon compositional data collected worldwide, not only from porphyry systems but also from a range of other unmineralised systems, allowing for studies to characterise compositions of porphyry zircons (Lu *et al.*, 2016; Pizarro *et al.*, 2020). Using trace element concentrations and ratios in bivariate space (e.g. Eu anomaly vs (Ce/Nd)/Y), these studies have constructed fields that encompass chemistries of porphyry zircons, proposing particular values (e.g. $Eu/Eu^* > 0.4$) that separate porphyry from non-porphyry zircons. These studies are naturally of use to exploration, allowing for mineral chemistry to be readily applied to recognise intrusions which may be prospective for porphyry mineralisation. Undertaking a similar approach for titanite would be ideal; however, there are major difficulties, given the current paucity of titanite trace element data from porphyry deposits. One approach to estimate what the composition of a porphyry-associated titanite might look like, in spite of the scarceness of titanite data, is to invert titanite compositions from porphyry zircon fields using mineral-melt partition coefficients (Colombini *et al.*, 2011). This approach assumes that titanite and zircon were crystallising at a similar time, which is evidenced in the Cobre Panama system by comparable zircon and titanite crystallisation temperatures (Fig. 6.13).

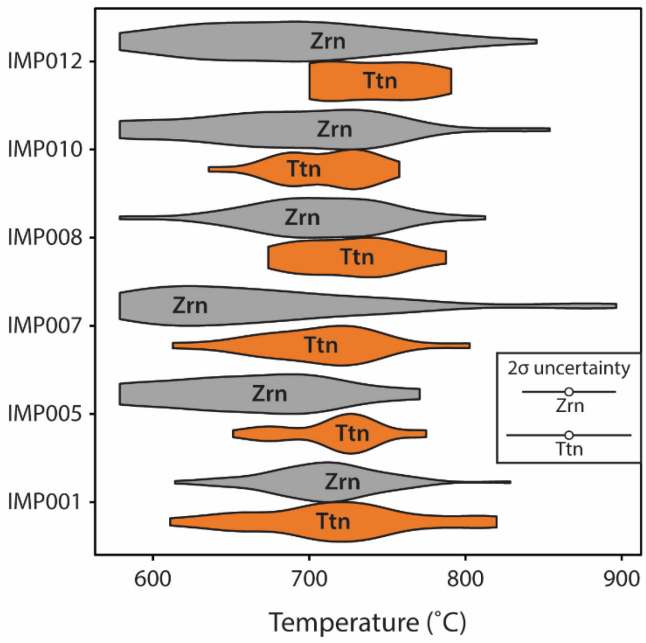


Figure 6.13. Comparison of titanite and zircon crystallisation temperatures from the Cobre Panama district (Ferry & Watson, 2007; Hayden *et al.*, 2008). Assumptions are the same as in Figs 6.9. and 6.12.

For simplicity, zircon-melt partition coefficients are not varied as a function of temperature. Although the temperature-dependence of zircon-melt partitioning is noted, the utilisation of trace element ratios, rather than elemental concentrations should minimise its impacts on the modelled titanite signatures. Cobre Panama zircon chemistry is also inverted (Appendix 11) to show compositions of hypothetical zircon-equilibrated titanites, which are compared to determined titanite compositions (Fig. 6.14). Given that Eu^{2+} is incompatible in both titanite and zircon, and that both minerals were assumed to crystallise at the same magmatic oxidation state, $D_{Eu/Eu^*}^{Zr/Ttn}$ is approximately equal to 1, meaning that titanite and zircon Eu/Eu* can be directly compared (Wilke & Behrens, 1999; Burnham *et al.*, 2015).

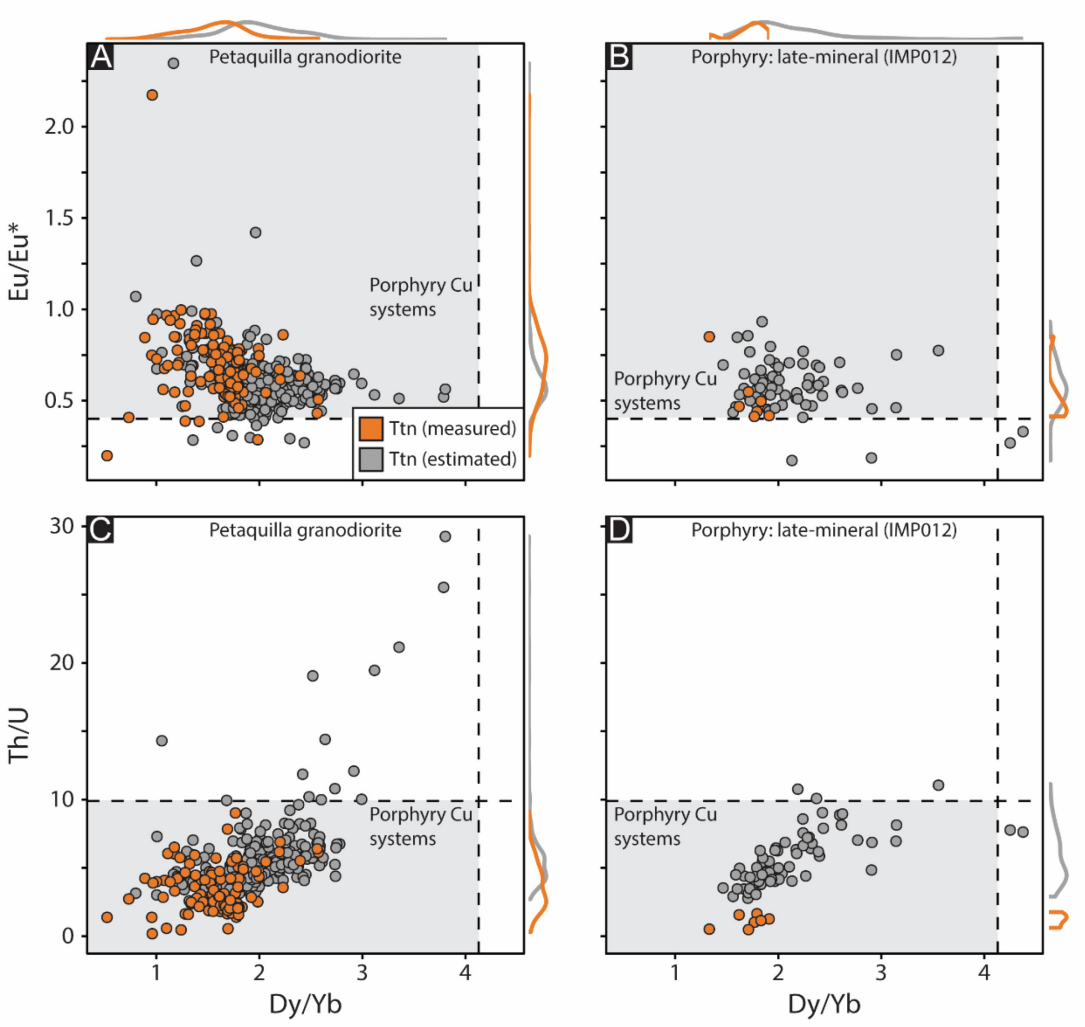


Figure 6.14. Trace element compositions of titanite and hypothetical titanite that would be in equilibrium with zircon. **A-B.** Eu/Eu* vs Dy/Yb for the Petaquilla granodiorite (**A.**) and late-mineral porphyry sample IMP012 (**B.**). **C-D.** Th/U vs Dy/Yb for the Petaquilla granodiorite (**C.**) and late-mineral porphyry sample IMP012 (**D.**). Only lithologies in which titanite was analysed are displayed. Measured and estimated titanite compositions are shown, with reference to porphyry-associated zircon fields derived from Lu *et al.* (2016) and Pizarro *et al.* (2020). Estimated titanite denotes Cobre Panama zircons from the same samples. Porphyry-associated zircon fields, and estimated titanite compositions are related through mineral-melt partition coefficients, which are derived from Colombini *et al.* (2011). For the calculation of Eu/Eu*, chondrite-normalised values are utilised (Boynton, 1984). See text for further discussion. Average 2σ uncertainty for measured titanite is smaller than the symbols.

Igneous titanite from Cobre Panama shows compositions that are consistent with porphyry-associated zircons (Fig. 6.14), which is to be expected as Cobre Panama is a mineralised system. These trace element ratios, Dy/Yb, Eu/Eu* and Th/U, may provide the basis for classification diagrams which can discriminate between titanite from mineralised and unmineralized systems, as is well characterised for zircon (Lu *et al.*, 2016; Pizarro *et al.*, 2020). Such a classification is at this stage preliminary but could be improved in the future either by i) building up a large enough titanite database such that inverting zircon compositions is not necessary, or ii) gaining an enhanced understanding of how trace elements partition into titanite as a function of temperature- allowing for the inversion to be fully temperature corrected. At this stage, such an approach seems to provide

a good first order approximation on the values which separate titanite from mineralised and unmineralised systems, with further study required to constrain the location of the boundaries more accurately.

Broadly, trace element compositions of Cobre Panama titanite and zircon are comparable, with similar Dy/Yb ratios and Eu anomalies (Fig. 6.14). On average, titanite from the Petaquilla granodiorite shows lower Dy/Yb and Th/U, and higher Eu/Eu* ratios, compared to zircon (Fig. 6.14). In late-mineral porphyry sample IMP012, titanite exclusively shows lower Th/U ratios than corresponding zircon, with the presence of low Th/U titanite also in the Petaquilla granodiorite (Fig. 6.14C). Such low Th/U titanite, reflecting high U contents, was also noted at Chuquicamata (see Chapter 5), although it is unclear what is responsible for this signature. Nonetheless, minor differences in trace element composition are observed between titanite and zircon. Estimated crystallisation temperatures are comparable between the two phases (Fig. 6.13), suggesting that these differences are unlikely to be related to crystallisation at different stages of melt evolution. Yet, it is unclear whether this represents crystallisation from different melt batches, or whether this is simply due to partitioning-related uncertainty derived from the inversion.

6.6 Conclusions

Textural, mineralogical and geochemical data have been utilised to understand the occurrence, and explain the chemical signatures, of titanite from the Cobre Panama porphyry deposit. Firstly, titanite was classified as either igneous, replacement or vein-hosted, depending on mineral associations, crystal habit and intra-grain zonation. Such classification allowed for the identification of trace element signatures of titanite from the groups. Igneous titanite is characterised by i) negatively sloping REE patterns, ii) higher Fe/Al and Th/U ratios, and iii) higher REE, Zr and Mn concentrations. Oppositely, replacement titanite generally exhibited i) positively sloping REE patterns, ii) low Fe/Al and Th/U ratios, and iii) higher V and Mn concentrations. Such elemental discriminators are best explained by mineral-melt partitioning behaviour, temperature, mobility in aqueous solutions and equilibration with trace element compatible phases.

Focussing only on the magmatic part of the system, it is clear that whole-rock, zircon and titanite trace element compositions are remarkably similar for the studied samples. Literature data, however, defines a distinct magmatic evolution through space and time, culminating in the high zircon and whole-rock Eu anomalies, and low Dy/Yb ratios that are characteristic of porphyry magmatism. Through combining mineral-melt partitioning data and zircon fertility studies, it is possible to estimate the composition of porphyry-associated titanites. Estimates of porphyry-

associated titanites are consistent with titanite compositions from Cobre Panama, potentially providing a basis for classification diagrams that are able to discriminate between mineralised and unmineralised systems.

Chapter 7. Geochronology and geochemistry of hydrothermal titanite from the Oyu Tolgoi district

7.1 Introduction

The Oyu Tolgoi porphyry copper district is located in the South Gobi Desert, within the Gurvansayhan volcanic arc terrane of the Central Asian Orogenic Belt, approximately 650 km south of Ulaanbaatar (Crane & Kavalieris, 2012). To date, nine deposits have been discovered along a 26 km NNE-trending zone known as the OT trend (Crane & Kavalieris, 2012): Ulaan Khuud, Hugo Dummett North, Hugo Dummett South, Central, Southwest, South, Heruga North, Heruga and Javkhlant (Fig. 7.1). As of 2014, the total measured, indicated and inferred resources and reserves are estimated at 6,382 Mt at 0.67% Cu and 0.29 g/t Au (Porter, 2016), making Oyu Tolgoi one of the largest and highest-grade deposits in the world. Mineralisation at Oyu Tolgoi is associated with the intrusion of porphyritic quartz monzodiorite (QMD) stocks and dykes, which are dated at ~ 372 Ma (Wainwright *et al.*, 2011b). The mine is currently owned by Rio Tinto (66%, through Turquoise Hill Resources) and the Government of Mongolia (Hook, 2022).

Although the modern day discovery is attributed to a 1996 BHP reconnaissance programme, partial exposure of the South Oyu deposit, as well as the occurrence of minor pits and stone tools, suggest that copper mineralisation was exploited during the Bronze Age (Perello *et al.*, 2001; Crane & Kavalieris, 2012). Prior to the discovery of Oyu Tolgoi, Tsagaan Suvarga, which is located approximately 150 km to the east and is dated at ~370 Ma (Watanabe & Stein, 2000), was the only known porphyry deposit in the region.

Chapters 5 and 6 demonstrated that U-Pb isotopes and trace element compositions can be determined simultaneously for igneous titanite, providing useful geochronological and geochemical data. This chapter aims to assess whether a similar approach can be applied to non-igneous titanite, which often contains much lower initial concentrations of U, without compromising the quality of titanite isotopic data. Also central to this chapter is utilising the wide range of ages, as well as physical and chemical conditions to better understand factors that determining non-igneous titanite compositions. Data of this kind would be of particular use in areas that have experienced multiple phases of deformation, magmatism and hydrothermal alteration.

The present study builds on work from Hart-Madigan (2019), who combined titanite U-Pb geochronology with major element chemistry, potentially revealing the presence of several age populations of hydrothermal titanite in the Oyu Tolgoi porphyry Cu-Au district.

7.2 Geologic setting

7.2.1 Regional geology

The Oyu Tolgoi district is located within the Central Asian Orogenic Belt, or Altaids, one of the world's largest orogenic belts, which extends across Mongolia, China, Russia, Kazakhstan, Uzbekistan and Kyrgyzstan. Formation of this belt took place between the Neoproterozoic and the Permian (~1000-250 Ma), involving the accretion of accretionary wedges, oceanic plateaux, ophiolites and island arcs (Khain *et al.*, 2003; Windley *et al.*, 2007; Kröner *et al.*, 2014). In the Permian, closure of the Paleo-Asian Ocean marked the termination of the final orogenic event, represented today by the Solonker Suture (Xiao *et al.*, 2003). Oyu Tolgoi is located within the Gurvansayhan terrane, an arcuate island arc terrane comprising marine to subaerial volcanic and sedimentary units. Following assembly, the terrane was intruded by granites of Carboniferous to Permian age (Lamb & Badarch, 1997; Badarch *et al.*, 2002; Crane & Kavalieris, 2012).

7.2.2 District geology

Cretaceous and younger cover sequences blanket much of the Oyu Tolgoi district, making it difficult to map and understand the relationship between units; hence, most of what is understood about the area has been interpreted from diamond drill core (Crane & Kavalieris, 2012). Consequently, little is known about how the units in the district relate to others in the South Gobi, necessitating an informal local grouping into the Heruga and Oyu Tolgoi sequences. Mineralisation is hosted by the Oyu Tolgoi sequence, in particular porphyritic augite basalt (Da1b), and is associated with the intrusion of stocks and dykes of late Devonian porphyritic quartz monzodiorite (Crane & Kavalieris, 2012; Porter, 2016). The Oyu Tolgoi and Heruga sequences are separated by a major fault, the Contact Fault, which thrust rocks of the Heruga sequence over those of the Oyu Tolgoi sequence, covering mineralisation. The allochthonous Heruga sequence is believed to be mostly overturned (Ayush, 2006) with an inferred Devonian age (Minjin *et al.*, 2005), although this is not well constrained. Unconformably overlying the Devonian rocks is the Carboniferous Sainshandhudag Formation (CS), comprising volcano-sedimentary rocks that are divided into the Ulgii, Tsagaan Suvarga and Aman-Us Members (Minjin *et al.*, 2005; Porter, 2016).

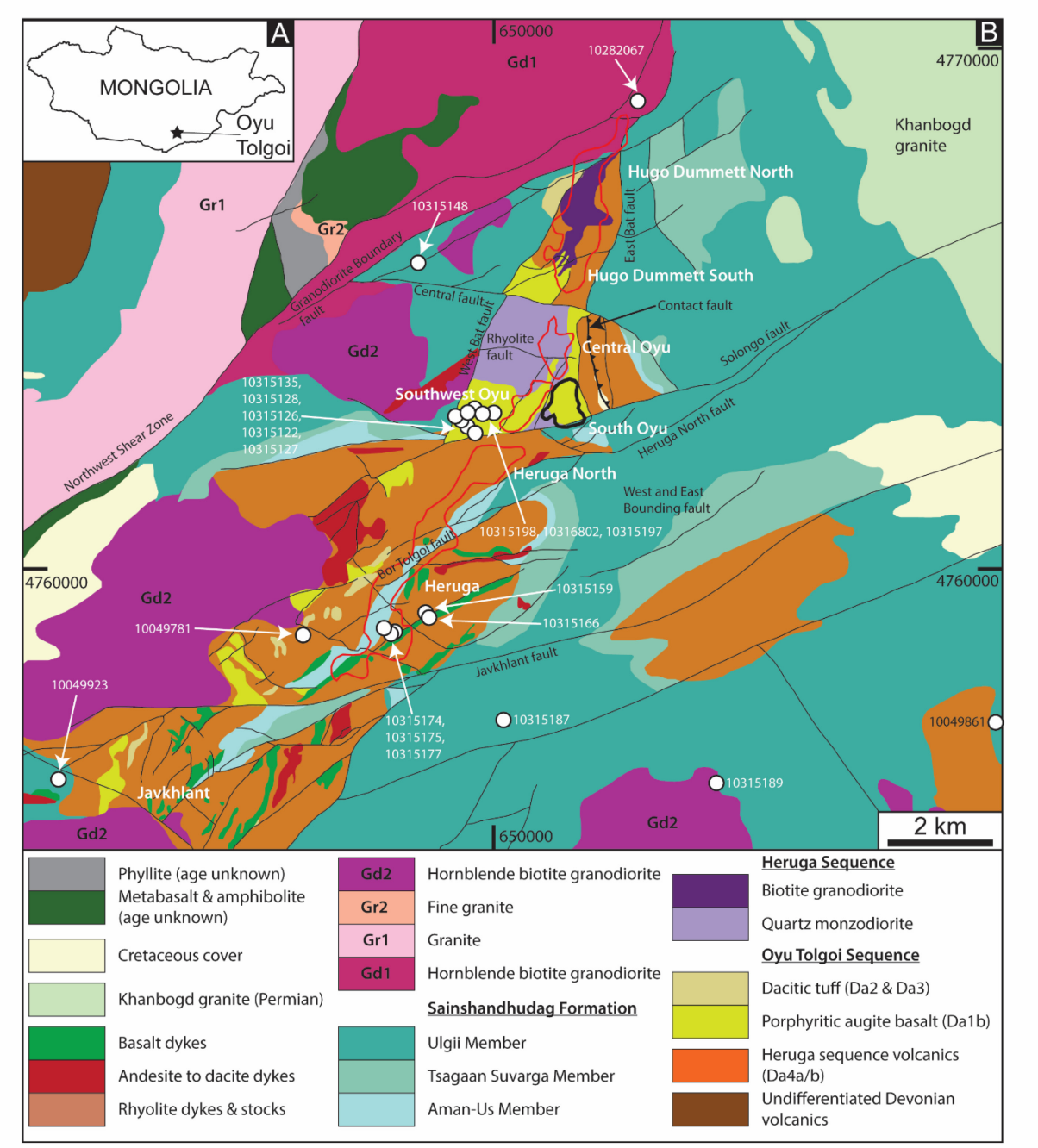


Figure 7.1. Location and geology of the Oyu Tolgoi district. **A.** Inset showing location of Oyu Tolgoi within Mongolia. **B.** Geological map of the Oyu Tolgoi district. Modified from Hart-Madigan (2019), after Porter (2016).

Post-mineral intrusions in the Oyu Tolgoi district were emplaced in three main time periods. Spatially coincident with mineralisation are a series of biotite granodiorite dykes of late Devonian age, within error of the age of mineralisation. A series of granodiorite (Gd1 and Gd2) and granite (Gr1 and Gr2) plutons were then emplaced during the early- (~350 Ma: Wainwright *et al.*, 2011b) and mid-Carboniferous (~320-310 Ma: Amar-Amgalan, 2008; Wainwright *et al.*, 2011b), surrounding the deposits to the north, west and south. A series of hornblende-biotite andesite dykes are interpreted to be of a similar age (Hart-Madigan *et al.*, 2020). Lastly, the circular,

~35 km-wide, alkaline Khanbogd Granite was intruded during the early Permian (Kovalenko *et al.*, 2006; Vaglio, 2007). Exhibiting concentric zonation, this alkaline granite is found relatively close (~ 5 km east) to the Hugo Dummett deposit. It contains zirconium mineralisation in the form of zirconosilicates and zircon (Kovalenko *et al.*, 2006; Kynicky *et al.*, 2011). Strong hornfelsing is observed up to 1 km away from the edge of the Khanbogd Granite and this has affected porphyry mineralisation at the Ulaan Khuud deposit to the north of Hugo Dummett (Crane & Kavalieris, 2012).

Several generations of faults and folds, formed during multiple deformation events, characterise the structurally complex Oyu Tolgoi district. A key structure is the West Bat Fault, a steeply dipping, NNE-trending Carboniferous fault that cuts both the Heruga and Oyu Tolgoi sequences. Other important structures include the Javkhlant, Solongo and Granodiorite Boundary faults, all of which displace Carboniferous granodiorites, and hence must be younger (Crane & Kavalieris, 2012).

7.3 Samples, previous work and methods

7.3.1 Samples

Data presented here come from 23 samples (Table 7.1), collected during Lisa Hart-Madigan's PhD study of the Oyu Tolgoi porphyry Cu-Au district (Hart-Madigan, 2019). Twenty of these samples had been previously investigated by Hart-Madigan (2019) and Hart-Madigan et al. (2020) as part of a propylitic geochronology study, with titanite-bearing samples initially selected to span a wide age range. The reused blocks were polished down and re-analysed *in-situ*, meaning that some of the analytical sites which were utilised during the previous study were polished away, reducing the number of available analytical sites. In addition to the previous titanite U-Pb geochronology and chemistry, whole-rock and chlorite chemistry (Hart-Madigan, unpublished data) are also utilised herein. An additional three samples were selected for this study, with the aim of documenting any mineralogical variability that was not captured during the initial study.

Table 7.1. Sample information, alteration assemblages, analytical techniques and number of analyses. Da1b = porphyritic augite basalt, UN = lithic tuff/ crystal tuff, CS? = porphyritic basalt, Gd1 = hornblende biotite granodiorite, HbBiAnd = hornblende biotite andesite, LQMD = quartz monzodiorite, Da4a = basaltic volcanic breccia, Da1c? = basalt.

Sample	Unit	Grid reference (Z)	Alteration assemblage (type)	TIMA	No. of ttn analyses (*)	Chlorite
10049781	Da1b	646054, 4758284 (-195)	Chl-Epi-Cc-Ab-Qz-Kfs-Bt±Ttn (Propylitic - epidote)	Y	20 (16)	Y
10049809_A	Da1b	648940, 4762351 (957)	Epi-Kfs-Cc-Bt-Chl (Propylitic after potassic?)	Y	N	N
10049861	Unknown	660042, 4756454 (1125)	Ab-Epi-Qz-Chl-Kfs±Ttn (Propylitic after potassic)	Y	40 (33)	N
10049923	CS3?	640977, 4755258 (1212)	Plg-Kfs-Qz-Act-Ab-Bt±Ttn (Propylitic - actinolite)	Y	11 (2)	N
10282067	Gd1?	652990, 4769453 (1177)	Epi-Pmp-Act-Kfs±Ttn (Propylitic - actinolite)	Y	18 (12)	Y
10315121	Da1b	649388, 4762690 (1043)	Epi-Qz-Chl-Cc (Propylitic - epidote)	Y	N	N
10315122	HbBiAnd	649389, 4762690 (1043)	Qz-Epi-Ab-Chl (Propylitic - epidote)	Y	22 (13)	Y
10315126	Da1b	649436, 4762639 (934)	Chl-Ab-Epi-Cc-Plg (Propylitic - epidote)	Y	N	N
10315127	LQMD	649446, 4762629 (912)	Chl-Ab-Qz-Kfs-Epi-Plg±Ttn (Propylitic - epidote)	Y	6 (0)	Y
10315128	Da1b	649453, 4762621 (896)	Epi-Chl-Cc-Qz (Propylitic - epidote)	Y	N	N
10315135	Da1b	649495, 4762572 (803)	Epi-Cc-Qz±Ttn (Propylitic - epidote)	Y	3 (0)	N
10315148	Da1b	648236, 4766045 (565)	Chl-Plg-Epi-Qz-Ab±Ttn (Propylitic- epidote)	Y	6 (0)	Y
10315159	Da1b	648527, 4759046 (-80)	Ser-Qz-Chl±Ttn (Sericite)	Y	25 (23)	Y
10315166	Da4a	648684, 4758839 (529)	Qz-Kfs-Ser±Ttn (Sericite)	Y	11 (5)	Y
10315174	HbBiAnd	647684, 4758454 (159)	Chl-Ab-Cc-Kfs-Qz-Pmp-Epi-Plg±Ttn (Propylitic- epidote)	Y	19 (9)	Y
10315175	Da1b	647661, 4758467 (86)	Epi-Act-Qz ±Ttn (Propylitic - actinolite)	Y	7 (2)	N
10315177	Da1b	647646, 4758476 (40)	Epi-Chl-Qz-Ab-Pmp±Ttn (Propylitic - epidote)	Y	14 (8)	N
10315184	Da1b	646178, 4758225 (218)	Epi-Chl-Qz (Propylitic - epidote)	Y	N	N
10315187	Da1c	650020, 4756880 (1146)	Kfs-Chl-Bt (Propylitic - epidote)	Y	N	N
10315189	Gd2	654511, 4754922 (1147)	Epi-Qz-Pmp-Chl±Ttn (Propylitic - epidote)	Y	42 (41)	Y
10315197	Da1b	649729, 4763199 (1067)	Cc-Qz-Py-Chl-Kfs-Ab±Ttn (Propylitic - chlorite)	Y	12 (1)	Y
10315198	Da1b	649735, 4763199 (1054)	Chl-Py-Kfs-Ab-Qz±Ttn (Propylitic - chlorite)	Y	10 (2)	Y
10316802	Da1b	649870, 4763186 (799)	Chl-Kfs-Epi-Ab-Cc-Qz-Py±Ttn (Propylitic - epidote)	Y	21 (11)	Y

* LA-ICP-MS analyses.

All studied samples apart from 10315159 and 10315166 (which are sericitically altered) have been propylitically altered. Protoliths to these rocks were dominantly volcanic, with the porphyritic augite basalt the most common, although intrusive rocks, including a hornblende biotite granodiorite and the ore-bearing quartz monzodiorite, are also represented. Epidote is often the most abundant mineral in propylitically altered rocks, although one or several or the following minerals may also be present: chlorite, actinolite, calcite, albite, pumpellyite and titanite (Fig. 7.2).

Where possible, propylitic alteration was further subclassified into chlorite, epidote and actinolite subtypes (Norman *et al.*, 1991; Holliday & Cooke, 2007; Cooke *et al.*, 2014), based on the alteration mineral assemblage. Pyrite is typically the most abundant sulphide, although minor chalcopyrite is present in some samples (10315177, 10315198 and 10316802). Samples are variably veined but generally contain at least one, if not multiple generations of veinlets (e.g. 101315166).

Porphyritic augite basalt (Da1b/c)

The original mineralogy of the porphyritic augite basalt has been obscured by variable types and intensities of hydrothermal alteration. Wainwright *et al.* (2011a) described unaltered porphyritic basalt as containing phenocrysts of augite (≤ 10 mm) and plagioclase (≤ 1 mm) in a groundmass of plagioclase, augite, magnetite and apatite. Depending on the sample, augite phenocrysts have been altered to one or more of: chlorite, calcite, actinolite or epidote (Figs. 7.2A, G, I). The groundmass of the altered porphyritic augite basalt mostly comprises plagioclase, chlorite and epidote in propylitically altered samples, but may contain quartz and sericite in sericitically altered samples (Fig. 7.2D). Finely interbedded (on a metre scale) with the porphyritic augite basalt are plagioclase-rich bands, which may (Da1c) or may not be classified as a separate unit (Hart-Madigan, 2019).

Basaltic volcanic breccia (Da4a)

Basaltic volcanic breccia sample 10315166 (Fig. 7.2E) has been intensely altered and veined such that original textures and mineralogy are difficult to discern. However, Porter (2016) described this lithology as a green basaltic volcanic breccia containing vesicular, porphyritic basaltic clasts, interlayered with volcanogenic sediments.

Porphyritic basalt (CS3?)

The studied porphyritic basalt sample (10049923) contains plagioclase (≤ 3 mm) and epidote-actinolite (≤ 3 mm, possibly after amphibole) phenocrysts in a plagioclase- and quartz-rich groundmass.

Hornblende biotite granodiorite (Gd1 and Gd2)

Samples of Carboniferous hornblende biotite granodiorite (Gd1 and Gd2) were also studied. These samples exhibit pervasive epidote alteration, with additional contributions from chlorite, K-feldspar, quartz, pumpellyite, and actinolite.

Hornblende biotite andesite dykes (HbBiAnd)

The hornblende biotite andesite dykes (Figs. 7.2C and F) comprise phenocrysts of skeletal plagioclase (50%, 2-5 mm), amphibole (~20%, 2 mm) and biotite (5-10%, 1-2 mm), with accessory zircon and magnetite in a fine-grained, red groundmass (Wainwright *et al.*, 2011a).

Quartz monzodiorite (LQMD)

The ore-bearing quartz monzodiorite occurs both in porphyritic and equigranular textural varieties. This exhibits a crowded porphyritic texture, with phenocrysts of plagioclase (~15%, ≤ 2mm), K-feldspar (~45%), amphibole (20%) and quartz (< 10%) in a fine-grained groundmass of K-feldspar, zircon, apatite, titanite and magnetite (Wainwright *et al.*, 2011a; Crane & Kavalieris, 2012; Porter, 2016; Hart-Madigan, 2019).

7.3.2 Previous work

The main findings of previous work on titanite U-Pb geochronology in the Oyu Tolgoi district (Hart-Madigan, 2019; Hart-Madigan *et al.*, 2020) are summarised here (Table 7.2). Hart-Madigan *et al.* (2020) concluded that titanite ages are consistent with three phases of hydrothermal activity, related to periods of magmatism in the region. Titanite ages are found to span more than 100 million years, with Devonian (samples 10315175, 10315197, 10315198), Carboniferous (10049923, 10315122, 10315148) and Permian (10315159, 10315166) ages calculated for individual samples. Importantly, samples that returned Devonian ages were within error of the inferred timing of porphyry mineralisation in the Oyu Tolgoi district, and hence were considered to be related to the mineralising event.

Hart-Madigan *et al.* (2020) suggested that only sample 10315189 contained multiple titanite age populations, which they interpreted to represent both igneous and hydrothermal titanite populations of differing ages, in addition to variable Pb or U loss (explaining an MSWD of 11). Hart-Madigan (2019) proposed that Permian titanite, identified on the basis of detectable fluorine (using SEM-EDS), was present in many samples (10049861, 10049781, 10282067, 10315122, 10315166 and 10315189). In this interpretation, F-rich titanite is believed to be related to the Permian, alkaline Khanbogd Granite, with late-stage F-rich fluids inferred based on the occurrence of rare earth fluorocarbonates (Kynicky *et al.*, 2011).

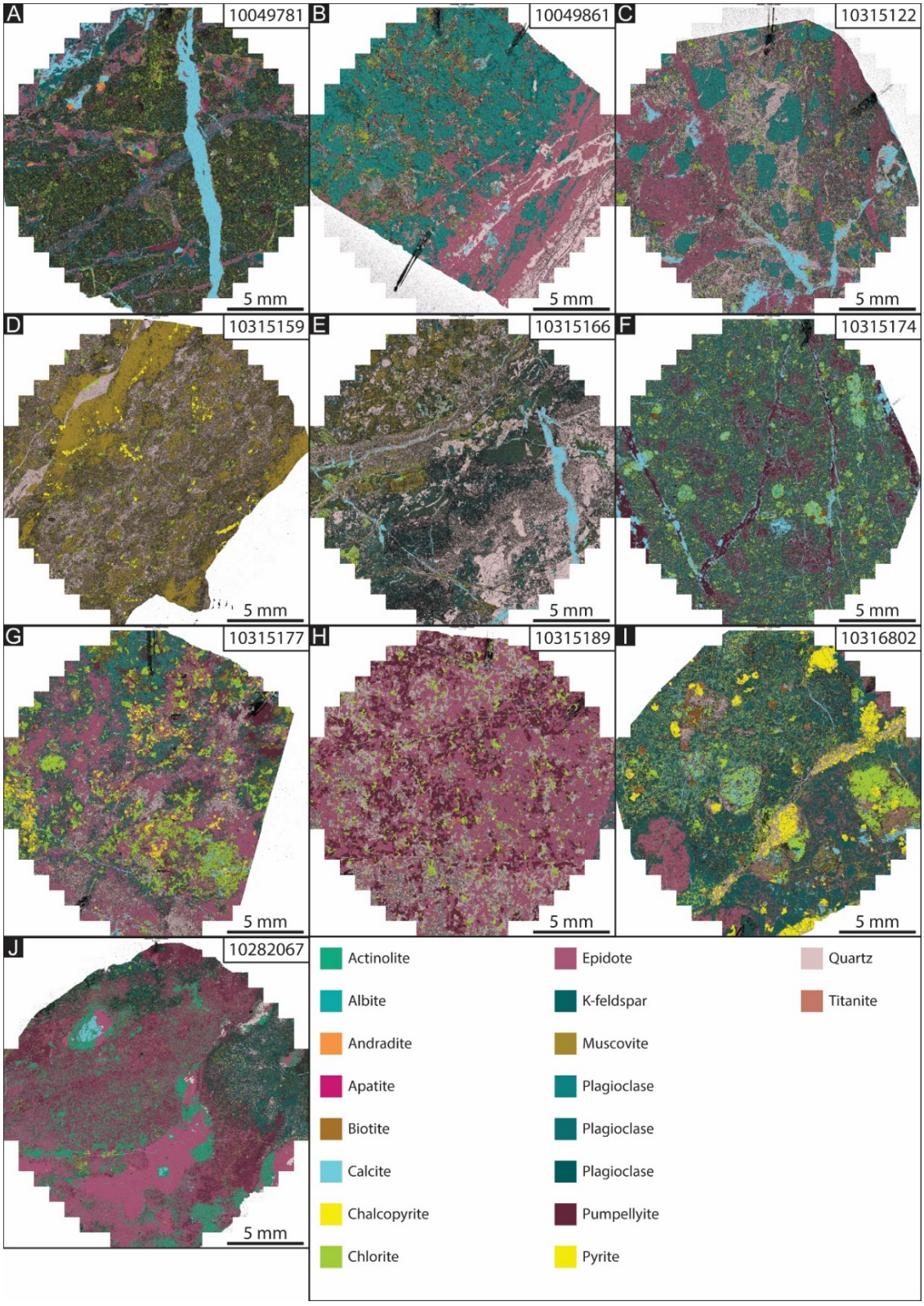


Figure 7.2. Selected TESCAN TIMA phase maps of the Oyu Tolgoi sample suite. **A.** Porphyritic augite basalt. **B.** Lithic tuff/ crystal tuff. **C.** Hornblende biotite andesite. **D.** Porphyritic augite basalt. **E.** Basaltic volcanic breccia. **F.** Hornblende biotite andesite. **G.** Porphyritic augite basalt. **H.** Hornblende biotite granodiorite. **I.** Porphyritic augite basalt. **J.** Hornblende biotite granodiorite.

Table 7.2. Titanite U-Pb dates for the same samples as reported by Hart-Madigan *et al.* (2020).

Sample	Unit	n	Age (Ma)	2σ error	MSWD	Acceptable MSWD*
10049781	Da1b	14	339 (Carb)	16	5.2	1.8
10049861	Unknown	29	408 (NA)	360	0.9	1.5
10049923	CS3?	26	317 (Carb)	18	1.2	1.6
10282067	Gd1?	0	-	-	-	-
10315122	HbBiAnd	36	325 (Carb)	20	1.9	1.5
10315126	Da1b	16	242 (NA)	59	1.1	1.8
10315127	LQMD	14	282 (NA)	98	1.1	1.8
10315128	Da1b	18	291 (NA)	52	0.9	1.7
10315135	Da1b	4	340 (NA)	88	0.9	3.0
10315148	Da1b	42	320 (Carb)	16	1.4	1.4
10315159	Da1b	13	260 (Perm)	32	2.1	1.9
10315166	Da4a	35	288 (Perm)	14	1.2	1.5
10315174	HbBiAnd	36	327 (NA)	100	1.1	1.5
10315175	Da1b	22	380 (Dev)	16	3.3	1.6
10315177	Da1b	22	365 (Dev/Carb)	15	3.2	1.6
10315187	Da1c	16	377 (Dev)	11	0.7	1.8
10315189	Gd2	27	338.4 (Carb)	9.9	13	1.6
10315197	Da1b	8	398 (Dev)	22	1.7	2.2
10315198	Da1b	16	384.5 (Dev)	9	5.1	1.8
10316802	Da1b	16	357 (Dev/Carb)	29	3.0	1.8

7.3.3 Methods

Titanite trace elements and U-Pb isotopes were determined according to the methodology outlined in Chapter 3. Whole-rock and chlorite chemistry from the same samples were also utilised (Hart-Madigan, unpublished data), with whole-rock geochemistry determined at ALS and chlorite chemistry determined at the NHM.

7.4 Results

7.4.1 Titanite textures

Titanite was identified in seventeen samples, occurring in a variety of assemblages and textures (Table 7.3). In terms of crystal morphology, irregular internal zonation and anhedral crystal forms are often encountered (Fig. 7.3). Exceptions to this rule are samples 10049781 and 10315189, which contain titanite that displays euhedral forms (Figs. 7.3A and F). Titanite morphology in sample 10282067 is unique in the sample set, displaying a bladed crystal habit, in addition to exhibiting zonation that is almost akin to the 'fir-tree' sector zoning commonly observed in igneous titanite (Paterson & Stephens, 1992). A minor proportion of analyses were conducted on crystals that contain rutile inclusions (sample 10315189).

Table 7.3. Titanite textural features and mineral associations from the Oyu Tolgoi district.

Sample	Unit	Titanite textures
10049781	Da1b	Found in epidote-K-feldspar-pumpellyite-chlorite-andradite±albite veinlets
10049861	Unknown	Either associated with calcite, chlorite, quartz, epidote and magnetite in either i) an albitic groundmass or ii) epidote veinlets
10049923	CS3?	Found in phenocrysts that have been altered to i) epidote-actinolite or ii) quartz-chlorite-magnetite
10282067	Gd1?	Either in i) an epidote-rich groundmass, ii) at the contact of the epidote-rich groundmass with actinolite-calcite altered phenocrysts or iii) in calcite veins
10315122	HbBiAnd	Associated with i) massive epidote-quartz or ii) along cleavage planes in chlorite
10315127	LQMD	Associated with pervasive chlorite alteration
10315135	Da1b	Within augite phenocrysts that have been altered to calcite, epidote, chlorite and actinolite
10315148	Da1b	Found associated with quartz, epidote, chlorite and calcite either i) in veinlets or ii) with altered phenocrysts
10315159	Da1b	Found in quartz or chlorite veinlets
10315166	Da4a	In quartz-calcite-chlorite veinlets
10315174	HbBiAnd	Associated with pervasive chlorite-calcite alteration, both i) in the groundmass and ii) also replacing amphibole phenocrysts
10315175	Da1b	Found either i) within massive epidote or ii) with actinolite-altered augite phenocrysts
10315177	Da1b	Associated with i) massive epidote or ii) chlorite-calcite-epidote altered phenocrysts
10315189	Gd2	Associated with i) massive epidote, quartz and pumpellyite and ii) partially-rutile altered titanite
10315197	Da1b	Found in either i) with chlorite-epidote-pyrite altered phenocrysts or within ii) chlorite-altered groundmass
10315198	Da1b	In chlorite and calcite altered groundmass
10316802	Da1b	In association with chlorite, calcite and magnetite either i) in the groundmass or ii) replacing phenocrysts

All of the studied samples have been intensely hydrothermally altered, resulting in either propylitic or sericitic alteration assemblages. Hydrothermal alteration has completely transformed the mineralogy of the rock, and in some instances has completely destroyed pre-existing textures. Indeed, titanite dominantly occurs with typical porphyry-alteration minerals (e.g. chlorite, epidote, sericite etc.), rather than primary igneous minerals (see Chapter 6). Moreover, the probable basaltic to andesitic protolith compositions of many studied samples are inconsistent with the occurrence of primary igneous titanite, suggesting that Oyu Tolgoi titanite is mostly non-igneous in origin (i.e. replacement or vein-hosted). Of the studied rocks, sample 10282067 displays the most igneous-like titanite textures, showing both euhedral crystal forms and igneous-like zonation. Nevertheless, textural evidence suggests that titanite in this sample occurs either in veins or has replaced phenocryst or groundmass minerals. This, when coupled with the paucity of fluid inclusion trails which are common in primary titanite that has interacted with hydrothermal fluids (see Chapters 5 and 6), indicates that titanite in this sample is also probably not igneous.

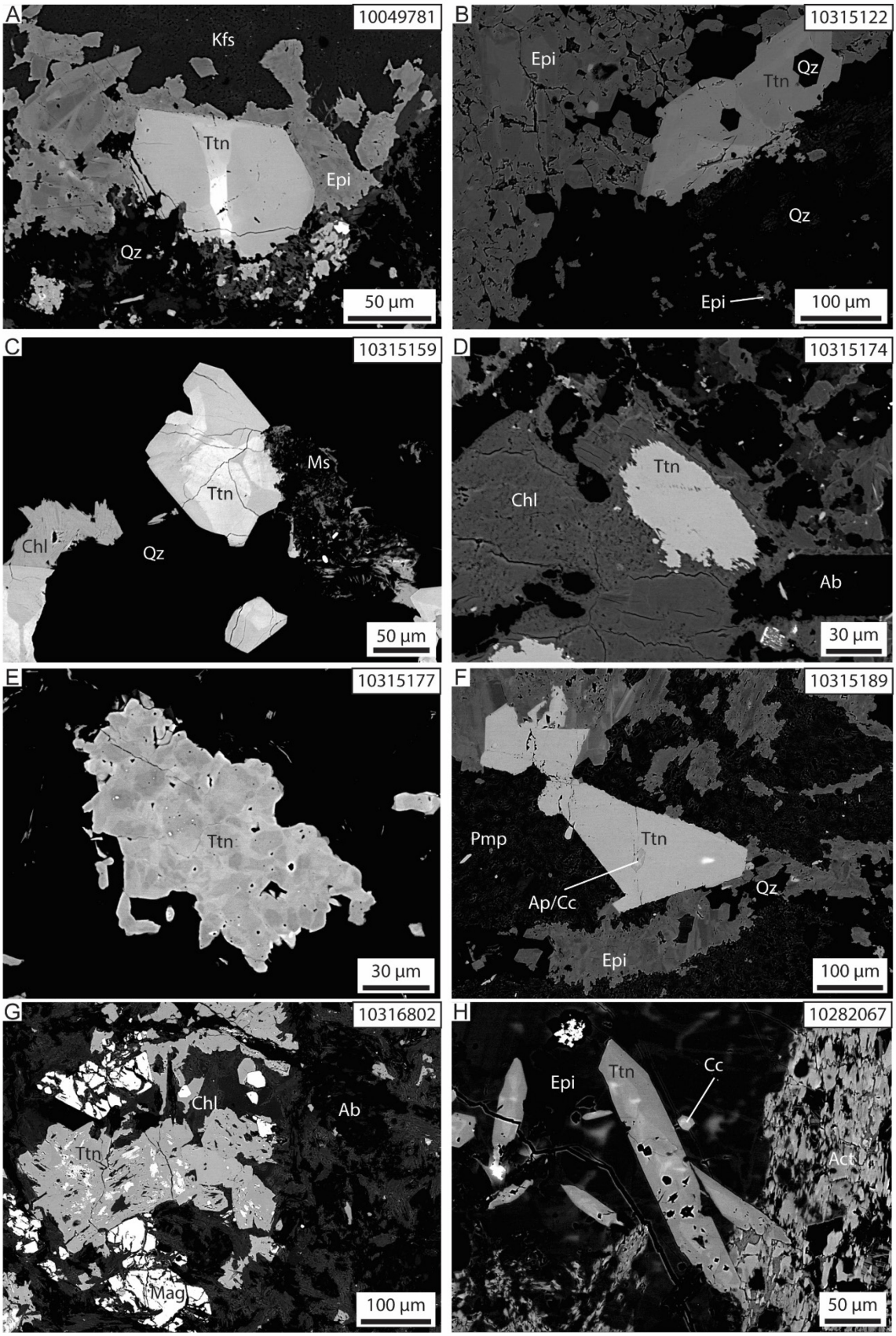


Figure 7.3. Titanite SEM-BSE images from the Oyu Tolgoi district. **A.** Epidote-associated titanite from the porphyritic augite basalt. **B.** Epidote and quartz-associated titanite from the hornblende biotite andesite. **C.** Quartz and muscovite (sericite)-associated titanite from porphyritic augite basalt. **D.** Chlorite-associated titanite from the hornblende biotite andesite. **E.** Titanite from the porphyritic augite basalt. **F.** Epidote, pumpellyite, quartz, apatite and calcite-associated titanite from the

hornblende biotite granodiorite. **G.** Magnetite, chlorite and albite-associated titanite from the porphyritic augite basalt. **H.** Bladed, almost sector-zoned titanite associated with epidote, calcite and actinolite, from the hornblende biotite granodiorite.

Minerals that are texturally associated with titanite are dominated by chlorite and epidote (Fig. 7.4), which occupy over 50% of the volume (assuming grains are circular) of grain boundaries shared with it (Fig. 7.4). Other typical green rock minerals are also commonly associated with titanite, such as: calcite, actinolite, albite, pumpellyite and pyrite (Figs. 7.3 and 7.4). Minor amounts of biotite, plagioclase and K-feldspar are also associated with titanite in various samples. Samples 10315159 and 10315166, however, are sericitically-altered (Figs. 7.2D and E), in which titanite is found in association with quartz and muscovite. Other atypical mineral associations include sample 10049861, where titanite often occurs with magnetite; and sample 10315175, where it is associated with actinolite.

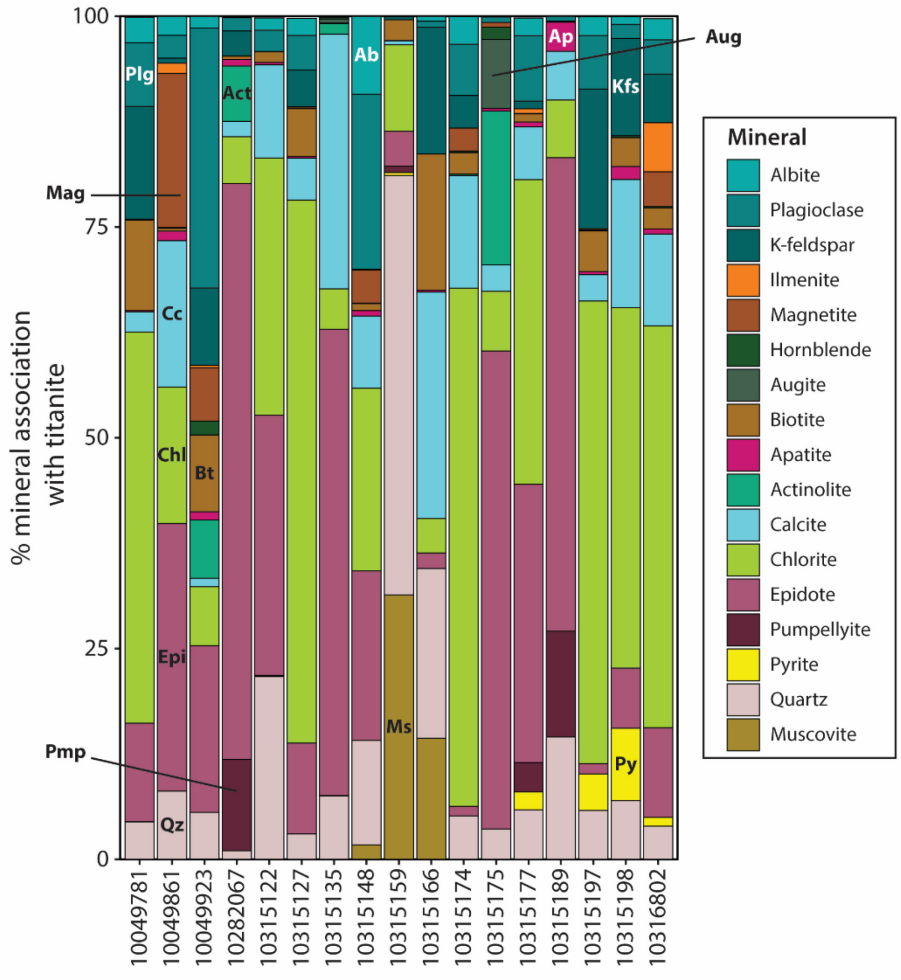


Figure 7.4. Percentages of minerals sharing grain boundaries with titanite in different samples, as determined by automated SEM analysis.

7.4.2 U-Pb geochronology

A total of 287 titanite spot analyses from 23 samples were attempted. Following the removal of contaminated analyses and those with high errors, 170 successful analyses remained (Table 7.4) with a sufficient number of successful spot analyses for geochronology in 9 samples.

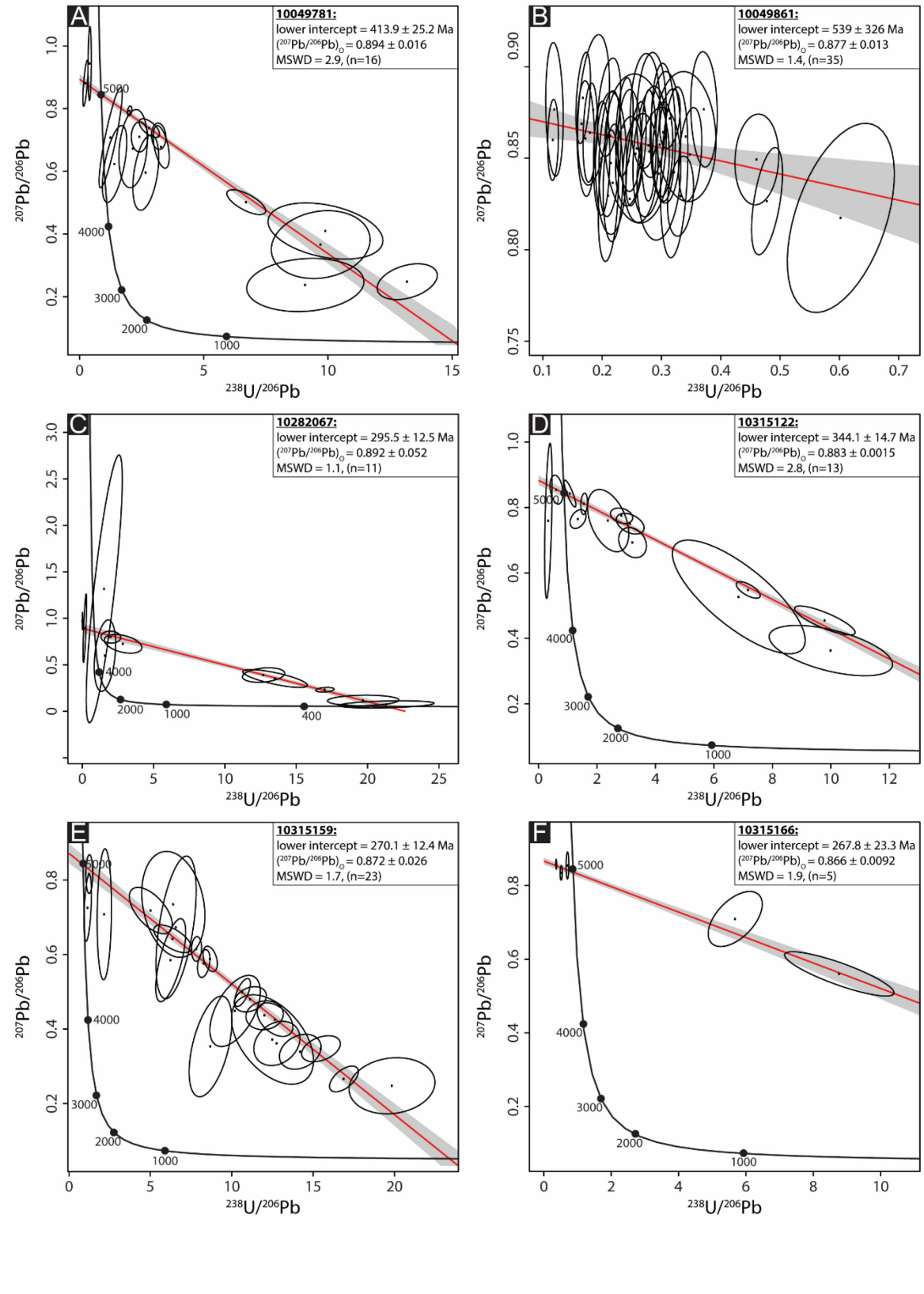
Table 7.4. Titanite U-Pb isotopic data for the Oyu Tolgoi district. Titanite lower intercept ages, 2σ error and an additional propagated 2% external uncertainty, as well as MSWD and acceptable MSWD are shown. Acceptable MSWD is calculated using the equation of Wendt and Carl (1991).

Sample	Unit	n	Age (Ma)	2σ error	Preliminary age	MSWD	Acceptable MSWD*
10049781	Da1b	16	414	27	Dev/Carb	2.9	1.7
10049861	Unknown	35	539	326	NA	1.4	1.5
10049923	CS3?	2	-	-	NA	-	-
10282067	Gd1?	11	296	14	Carb/Perm	1.1	1.9
10315122	HbBiAnd	13	344	16	Carb	2.8	1.8
10315126	Da1b	-	-	-	NA	-	-
10315127	LQMD	-	-	-	NA	-	-
10315128	Da1b	-	-	-	NA	-	-
10315135	Da1b	-	-	-	NA	-	-
10315148	Da1b	1	-	-	NA	-	-
10315159	Da1b	23	270	14	Perm	1.7	1.6
10315166	Da4a	5	268	24	Perm	1.9	2.4
10315174	HbBiAnd	9	-	-	NA	-	-
10315175	Da1b	2	-	-	NA	-	-
10315177	Da1b	7	362	15	Dev/Carb	2.4	2.2
10315187	Da1c	-	-	-	NA	-	-
10315189	Gd2	41	336	7	Carb	3.4	1.4
10315197	Da1b	1	-	-	NA	-	-
10315198	Da1b	2	-	-	NA	-	-
10316802	Da1b	10	374	18	Dev	1.9	1.9

Titanite U-Pb data were plotted on Tera-Wasserburg diagrams (Fig. 7.5), with an MSWD and acceptable MSWD calculated for each sample (Wendt & Carl, 1991). Of the studied samples, three (10049781, 10315122 and 10315189) returned MSWDs which were much higher than expected based on the number of analyses (Table 7.4), implying that these samples may contain multiple age populations.

7.4.3 Titanite chemistry

Chondrite-normalised titanite REE patterns are shown with compositions colour coded by preliminary U-Pb ages, with samples that only contained a sufficient number of analyses (i.e. >5) shown. Where preliminary ages were not determined in this study they are taken from Hart-Madigan (2019) and Hart-Madigan et al. (2020). Titanite chondrite-normalised REE patterns are extremely variable between samples, even where titanite U-Pb ages are similar (Fig. 7.6). Indeed, the only consistency between titanite REE patterns of a particular age is in samples 10315122 and 10315189, which exhibit La and Ce depletion relative to middle REEs (e.g. Sm; Figs. 7.6F and G). Despite this, titanite REE patterns are generally consistent within a sample, although patterns


A
10049781:
lower intercept = 413.9 ± 25.2 Ma
(207Pb/206Pb)o = 0.894 ± 0.016
MSWD = 2.9, (n=16)
B
10049861:
lower intercept = 539 ± 326 Ma
(207Pb/206Pb)o = 0.877 ± 0.013
MSWD = 1.4, (n=35)
C
10282067:
lower intercept = 295.5 ± 12.5 Ma
(207Pb/206Pb)o = 0.892 ± 0.052
MSWD = 1.1, (n=11)
D
10315122:
lower intercept = 344.1 ± 14.7 Ma
(207Pb/206Pb)o = 0.883 ± 0.0015
MSWD = 2.8, (n=13)
E
10315159:
lower intercept = 270.1 ± 12.4 Ma
(207Pb/206Pb)o = 0.872 ± 0.026
MSWD = 1.7, (n=23)
F
10315166:
lower intercept = 267.8 ± 23.3 Ma
(207Pb/206Pb)o = 0.866 ± 0.0092
MSWD = 1.9, (n=5)
207Pb/206Pb
238U/206Pb

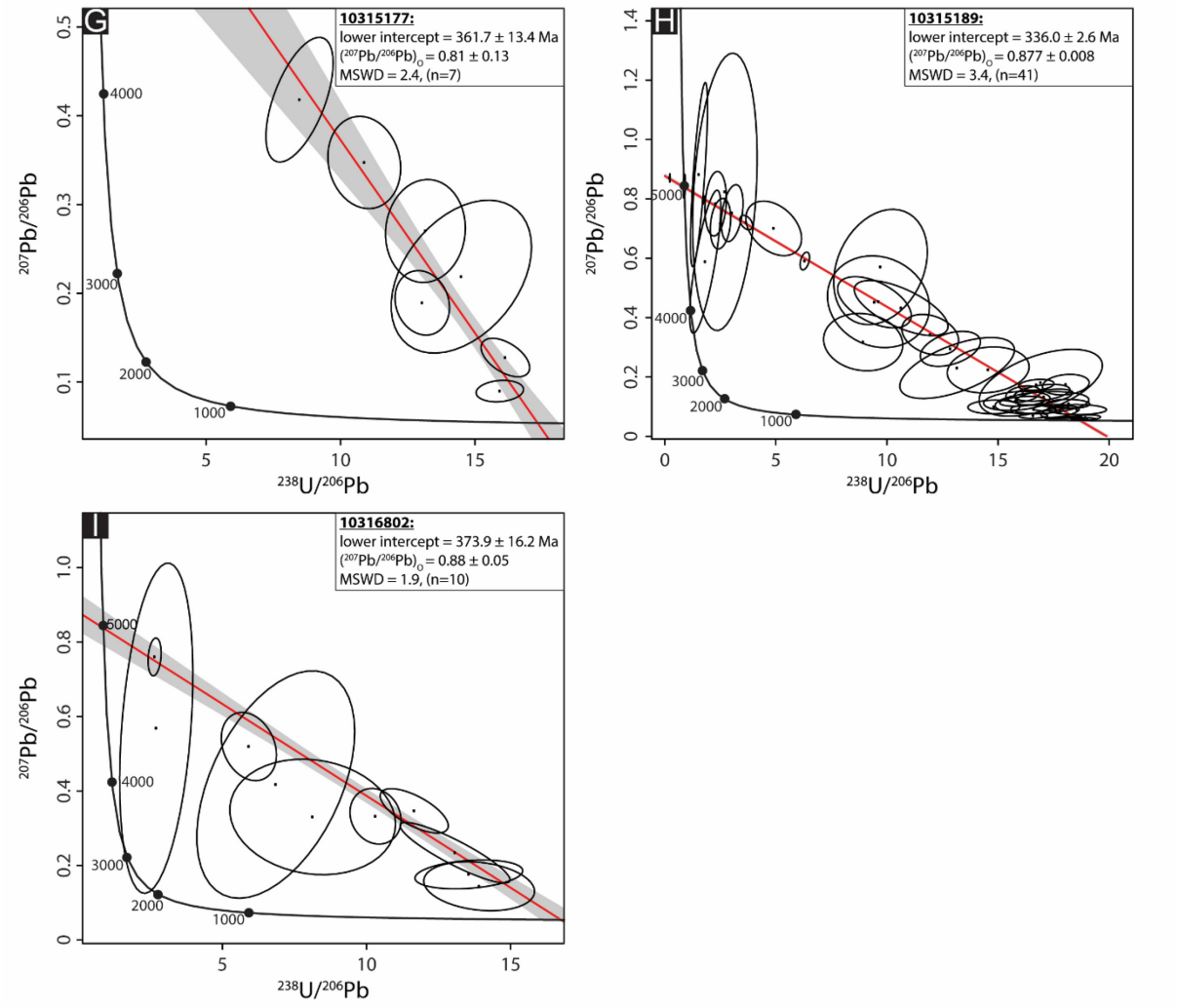


Figure 7.5. Tera-Wasserburg concordia diagrams for titanite age data from the Oyu Tolgoi district. 2σ error ellipses are shown, in addition to the 2σ uncertainty associated with the regression. Crystallisation ages are presented with error, which is derived from the regression, with an additional propagated external uncertainty of 2%.

generally differ from those of their host rock, which are, in all instances, weakly negatively sloping (Hart-Madigan, unpublished data; Fig. 7.6). This implies that titanite is not a major host of the total REE in the rock (cf. Chapter 4; Fig. 4.14).

Titanite REE patterns in samples 10315159, 10315189 and 10316802 are characterised by LREE depletion with consistent shapes observed within each sample, though absolute REE concentrations may vary by up to three orders of magnitude (Figs. 7.6D, G and I). Similarly, Permian titanite in sample 10315166 displays concave-downward patterns with variable concentrations of MREEs (Fig. 7.6J). Sample 10049861 exhibits an unusual sinuous REE pattern, with a positive Eu anomaly (Fig. 7.6A), whereas sample 10315174 exhibits a relatively flat REE pattern with a slight depletion in HREEs (Fig. 7.6B). In spite of the overall consistency of titanite

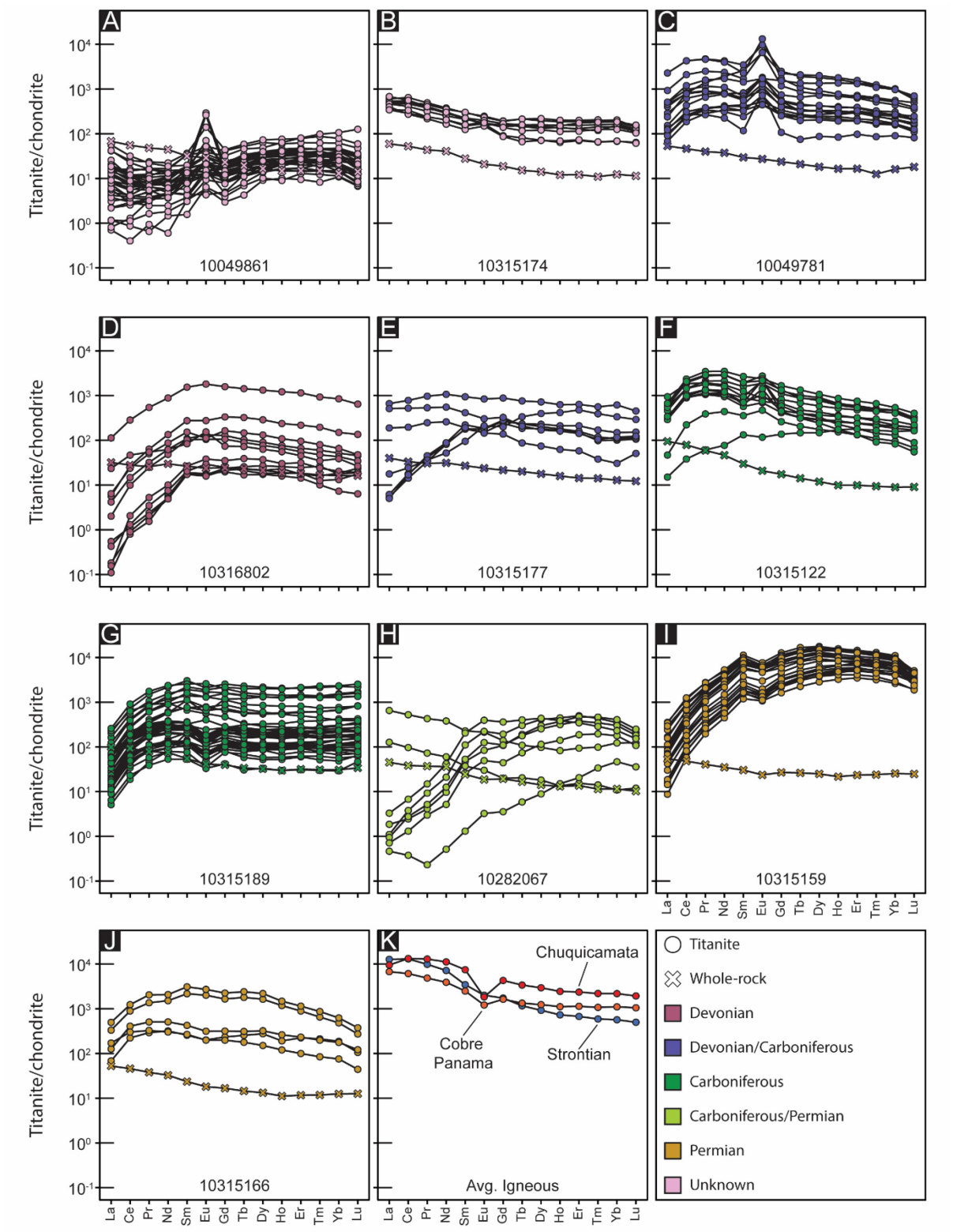


Figure 7.6. Chondrite-normalised (Boynton, 1984) REE plots for titanite from the Oyu Tolgoi district. Samples are colour coded by alteration style. Also shown are average igneous titanite compositions from the Chuquicamata, Cobre Panama and Strontian study sites. Average 2σ errors are smaller than symbol size.

REE patterns within samples, 10282067 and 10315177, and to a lesser extent 10049781 and 10315122, display multiple signatures within a sample (Figs. 7.6C, E, F and H). Titanite from sample 10049781 broadly shows a consistent REE pattern, though the Eu anomaly varies

significantly (Fig. 7.6C). Ranging from 1 to 7.5, the Eu anomaly of titanite in this sample can be used to classify analyses into two groups: a low Eu/Eu* group (1.2-1.8) and a high Eu/Eu* group (2.4-7.5). Titanite from sample 10315122 overwhelmingly displays weakly negatively sloping patterns, with a pronounced LREE hump, though two analyses are LREE depleted relative to the other analyses (Fig. 7.6F). Titanite from samples 10315177 and 10282067 dominantly shows LREE depletion, though a minor proportion of analyses show flat REE patterns (Figs. 7.6E and H).

Titanite minor and trace element compositions can vary both between and within samples (Fig. 7.7). The smaller spot size utilised on the electron microprobe (5 μm) meant that more successful analyses were possible compared to laser-ablation ICP-MS (which employed a 20 μm spot size), hence titanite fluorine contents are shown for more samples. Generally, titanite fluorine contents are <1 wt.%, but samples 10315166, 10282067, 10315122, 10315159 and 10315135 contain a significant proportion of analyses with >1 wt.% F (Fig. 7.7A). Vanadium contents of titanite are chiefly <1000 ppm, except for samples 10049861, 10315174, 10316802, 10315177 and 10049781 (Fig. 7.7B). Concentrations of Mn in titanite generally vary between 30 and 870 ppm, although titanite sample 10049861 contains up to 3500 ppm (Fig. 7.7C). Titanite Sr contents in sample 10315174 (215-300 ppm) are significantly higher than those in other samples (2-92 ppm; Fig. 7.7D). Concentrations of Sn in titanite mostly range between 10 and 200 ppm, although Sn in sample 10315189 is as high as 3000 ppm (Fig. 7.7E). Titanite Th contents vary over several orders of magnitude, with concentrations of less than 0.01 ppm in sample 10282067 but up to 140 ppm in samples 10315189 and 10315159 (Fig. 7.7F).

Titanite compositions can be compared with preliminary ages and host units (Fig. 7.7). Whole-rock V contents do not seem to strongly correlate with those in titanite, with the lowest whole-rock V concentration (sample 10315122; Fig. 7.7B) observed in a sample which contains unremarkable (e.g. all analyses but three in the second quartile) titanite V contents. Chiefly, titanite and whole-rock trace element contents are uncorrelated. However, extreme (e.g. lowest or highest values) whole-rock and titanite trace element concentrations may correlate, such as: i) Mn contents of sample 10315166, ii) Sn contents of sample 10315189 or iii) Th contents of samples 10315159 (Fig. 7.7). In terms of comparing titanite trace element compositions with U-Pb ages, there are few consistent correlations (Fig. 7.7). However, fluorine contents may be partially linked to age, with Permian ages (as well as sample 10315135 which has no known age) exhibiting over 1 wt.% F (Fig. 7.7A).

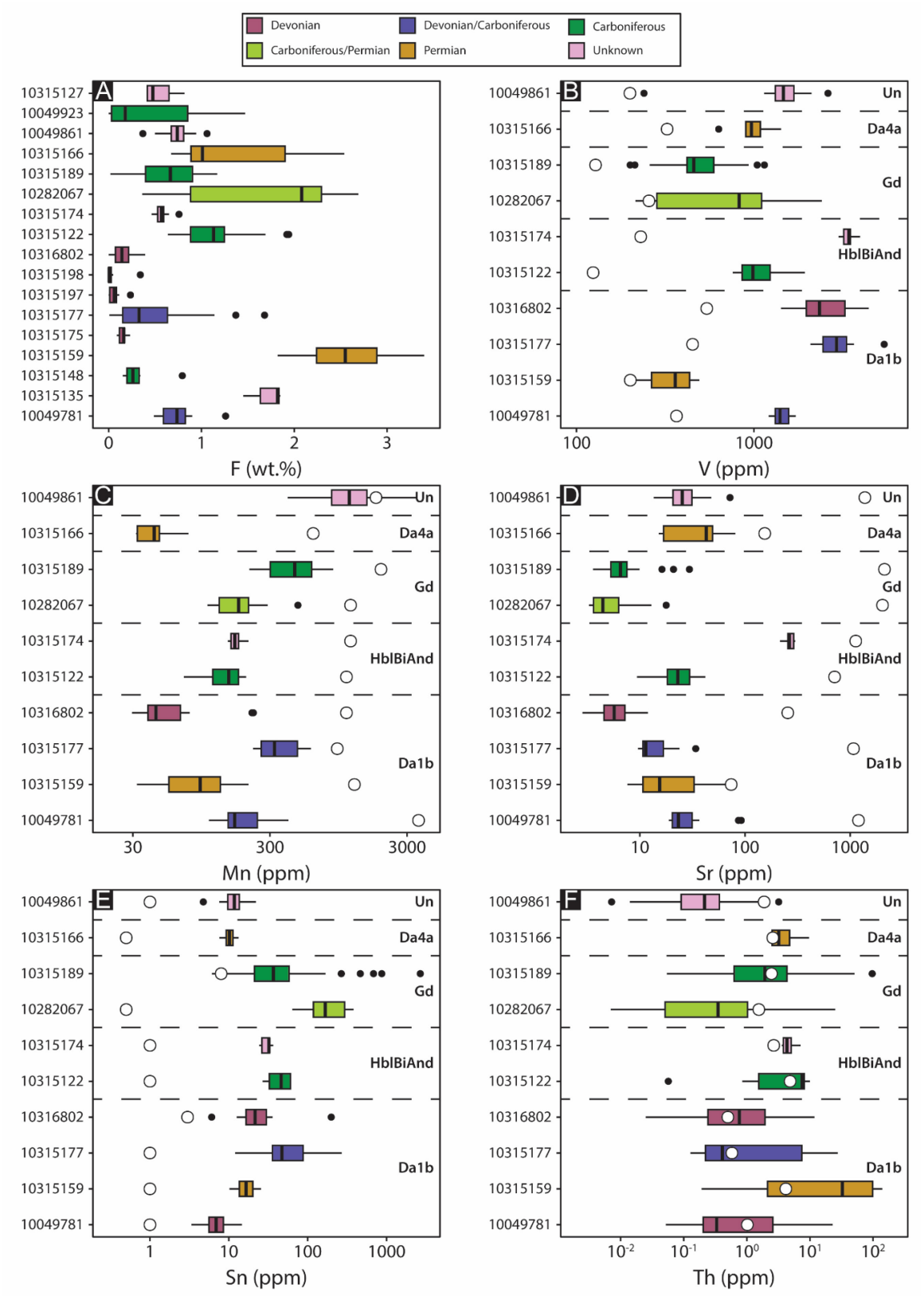


Figure 7.7. Box plots illustrating titanite compositions for different samples. Samples are arranged in terms of host rock and are coloured based on alteration assemblage. **A.** F (wt.%). **B.** V (ppm). **C.** Mn (ppm). **D.** Sr (ppm). **E.** Sn (ppm). **F.** Th (ppm). White circles indicate whole-rock concentrations in the same samples (Hart-Madigan, unpublished data).

7.5 Discussion

7.5.1 Titanite geochronology and the presence of multiple populations

Of the samples in which a suitable number of successful analyses were possible (i.e. ≥ 5), one returned an age with an extremely large error (10049861), and several returned MSWDs which are significantly higher than would be expected based on the number of analyses. This means that isotopic data are more scattered than would be expected for a single age population based on uncertainties, possibly due to geological uncertainty (i.e. multiple populations or disturbance to the isotopic system). Primarily utilising U-Pb isotopic data, Hart-Madigan (2019) proposed that multiple populations of titanite may be present in the same rock, particularly in samples 10315122 and 10315189.

Here, titanite rare earth element compositions – which show distinct bimodality in some samples – are utilised to identify multiple populations, with an age subsequently calculated for each population assuming a suitable number of analyses were conducted (≥ 5). Where too few analyses were conducted in a titanite population, then the population was removed, and an age calculated for the residual population. Firstly, considering samples 10315189 and 10315122, which Hart-Madigan (2019) proposed contained multiple age populations, rare earth element compositions are generally consistent within a sample. However, two groups may be inferred from ΣREE contents in 10315189 (Fig. 7.6C); and in sample 10315122, two analyses exhibit a different signature to the overwhelming majority (Fig. 7.6J). However, samples 10282067 and 10315177 showcase the most obvious examples of multiple titanite rare earth element signatures (Figs. 7.6G and I); in addition to sample 10049781, in which two groups are distinguished by Eu anomaly (Figs. 7.6A).

Comparing ages of the various titanite populations, calculated ages of low-REE and high-REE groups in sample 10315189 are within error of each other (Table 7.5). However, calculated MSWDs vary significantly between populations, with a much lower MSWD in the low-REE (1.6), compared to the high-REE population (8). Hart-Madigan *et al.* (2020) suggest the high MSWD of this sample can be attributed to U and Pb mobility, as well as the occurrence of both igneous and hydrothermal titanite. However, based on likely protolith compositions and the pervasive nature of alteration, it is inferred here that all titanite encountered in the samples studied at Oyu Tolgoi has a non-igneous origin. The high-REE population is also enriched in U and Pb relative to the low-REE population, with an average U content of ~88 ppm compared to ~4 ppm, and an average Pb content of 19 ppm relative to 4.4 ppm (Table 7.5). Using all available evidence, variable MSWDs of the two groups in 10315189 are attributed to minor U or Pb mobility, although the exact mechanism (U loss or Pb gain) remains unclear.

Removal of the two outliers in sample 10315122 does not change the calculated age but does reduce the MSWD to 2. Conversely, removal of the two outliers in 10282067 increases the MSWD to 1.4, with a slightly higher calculated age that is still within error. Removal of the three analyses with the flat REE pattern in sample 10315177 leaves only four analyses remaining, which does not change the calculated age but increases the MSWD to 3.5 (Table 7.5). However, sample 10049781 contains two titanite populations with distinct ages. In this rock, titanite is grouped by Eu anomaly, with Silurian/Devonian or Carboniferous ages returned for the high Eu/Eu* and low Eu/Eu* populations respectively (Table 7.5).

Table 7.5. Titanite U-Pb isotopic for five samples which possibly contained multiple titanite populations. Information as in Table 1.4. Preferred ages are indicated by green text, where these differ from those which included all analyses.

Sample	Group	n	Age (Ma)	2σ error	MSWD	Acceptable MSWD*	Avg. ^{206}Pb content (ppm)	Avg. U content (ppm)
10049781	All analyses	16	414	27	2.9	1.7	8.5	6.8
10049781	Low Eu/Eu*	5	342	49	0.26	2.4	0.90	1.8
10049781	High Eu/Eu*	11	441	34	2.5	1.9	12.0	9.1
10282067	All analyses	11	296	14	1.1	1.9	1.36	3.6
10282067	Removed two analyses	9	304	21	1.4	1.9	1.10	2.1
10315122	All analyses	13	344	16	2.8	1.8	13.3	13.6
10315122	Removed two analyses	11	345	15	2	1.9	15.1	15.9
10315177	All analyses	7	362	15	2.4	2.2	2.28	8.7
10315177	Removed three analyses	4	352	19	3.5	2.6	1.28	4.3
10315189	All analyses	41	336	7	3.4	1.4	8.37	26.6
10315189	High REE	11	335	8	8	1.9	19.2	87.8
10315189	Low REE	30	331	9	1.6	1.5	4.40	4.2

Titanite ages determined in this study are compared to the results of Hart-Madigan *et al.* (2020), as well as major magmatic events in the Oyu Tolgoi district (Fig. 7.8). For sample 10049781, both age populations are plotted, whereas displayed ages for all other samples include all analyses, given that the removal of various geochemical groups did not influence calculated ages. Generally, reliable ages were determined in the same samples in both studies, although more samples were dated by Hart-Madigan *et al.* (2020). Hart-Madigan *et al.* (2020) did not obtain an age for sample 10282067, which they found to showcase large, propagated errors for each analysed titanite. However, a Carboniferous/Permian age (296 ± 14 Ma) was obtained in the present study, significantly younger than the Carboniferous emplacement age obtained via zircon U-Pb (350 ± 4 Ma; Wainwright *et al.*, 2011b), indicating that the rock was either stratigraphically misclassified or that the propylitic alteration in the sample is related to a phase of late Carboniferous granodiorite intrusion, or even possibly the Khanbogd Granite.

Where reliable ages were determined in the present study, Hart-Madigan *et al.* (2020) and by Hart-Madigan (2019), calculated titanite ages are consistent in all samples apart from the high

Eu/Eu* subgroup in 10049781 (Fig. 7.8). It is considered likely that one of these low or high Eu/Eu* populations represents a disturbance to the isotopic system, rather than two distinct age populations of titanite with similar geochemical signatures, separated by 10's of millions of years. In this instance, it is thought that the high Eu/Eu* population has gained Pb, perhaps via partial re-equilibration of pre- to inter-mineral titanite with later hydrothermal fluids. Although uncommon, such processes have been suggested for titanite in metamorphic settings (Kirkland *et al.*, 2016), where isotopically disturbed titanite also exhibits distinct trace element compositions. This interpretation is favoured here, as the Silurian age indicated for the high Eu/Eu* is older than the age of the host rock based on stratigraphic evidence.

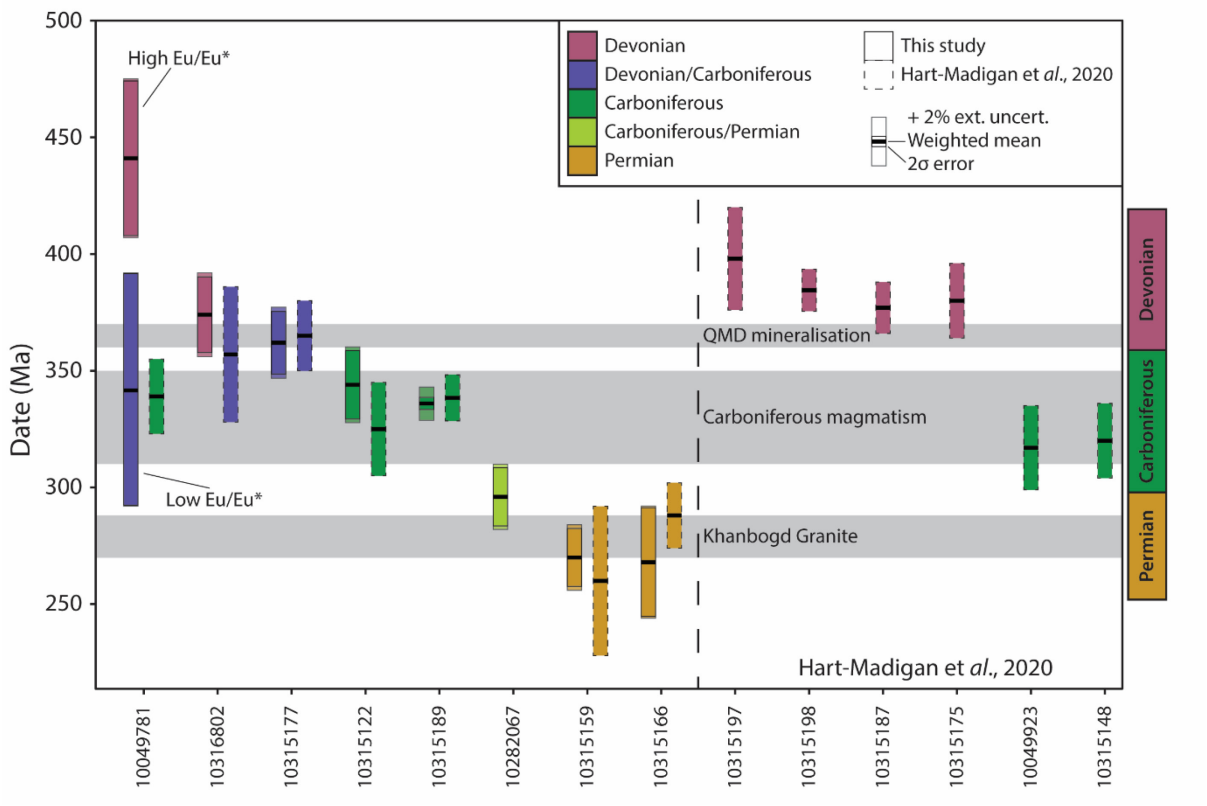


Figure 7.8. Plot comparing titanite lower intercept ages in the Oyu Tolgoi district determined in this study with those of Hart-Madigan *et al.* (2020). 2σ error with ±2% external uncertainty are also shown for ages determined during this study, whilst it is unclear whether the 2σ error reported by Hart-Madigan *et al.* (2020) includes 2% external uncertainty. Also shown are ages of mineralisation based on zircon U-Pb data from the causative QMD intrusion (Wainwright *et al.*, 2011b; Crane & Kavalieris, 2012; Dolgopolova *et al.*, 2013; Loader, 2017), the age range of Carboniferous arc magmatism (Amar-Amgalan, 2008; Wainwright *et al.*, 2011a; Wainwright *et al.*, 2011b) and the age of magmatism associated with the alkaline Khanbogd Granite (Kovalenko *et al.*, 2006; Vaglio, 2007).

7.5.2 Occurrence of fluorine-bearing Permian titanite

Hart-Madigan (2019) also hypothesised that fluorine-rich titanite, as determined by SEM-EDS, was Permian in age, and represented alteration associated with the Permian, alkaline Khanbogd Granite. Indeed, alkaline granites often contain an abundance of fluorine (Bailey, 1977), and the

fluorine-rich nature of the Khanbogd Granite itself can be inferred from the presence of F-rich primary phases (e.g. arfvedsonite), as well as secondary phases that formed during autometasomatism (e.g. rare earth element fluorocarbonates; Kynicky *et al.*, 2011). In the study of Hart-Madigan (2019), only samples 10315159 and 10315166 returned a Permian age, though it was suggested that a minor proportion of F-rich, and hence Permian titanite, was also present in multiple samples, including: 10049861, 10049781, 10282067, 10315189 and 10315122.

Although the study of Hart-Madigan (2019) determined titanite fluorine contents by SEM-EDS (compared to determination by EPMA-WDS in the present study), samples that contained detectable fluorine in titanite are generally consistent with those identified in the present study with > 1 wt.% fluorine (Fig. 7.7A), the exceptions being 10315189 and 10049861 (in which F-rich titanite was almost absent), as well as 10315135 (which wasn't reliably dated in either study). Indeed, of the five samples that contain median titanite F contents of over 1 wt.%, three have a definite or possible Permian age (10315159, 10292067 and 10315159) and another (10315135) wasn't reliable dated by Hart-Madigan *et al.* (2020) or this study (Figs. 7.7A and 7.8). From this, it is interpreted that F-rich titanite in the Oyu Tolgoi district is mostly related to the Khanbogd Granite. However, titanite in sample 10315122 also contains median fluorine contents of >1 wt.% and is unlikely to be related to the Khanbogd Granite given the Carboniferous age (Fig. 7.8). In this sample, elevated F contents may relate to one or combination of several factors which have been demonstrated to result in high titanite F concentrations, such as low temperatures and high pressures, in addition to high host rock Al/Ti ratios and high F activities of the fluid (Enami *et al.*, 1993; Markl & Piazolo, 1999).

Assuming titanite from samples 10315159, 10315166 and 10282067 is related to the Khanbogd Granite, then it raises the question: are there are other geochemical characteristics of titanite which are inherited from an alkaline granite? Kynicky *et al.* (2011) found that units within the Khanbogd Granite are variably enriched in LREEs, Zr, Nb, Hf, Th and U, but are likely to be depleted in Sr. To test whether such geochemical characteristics are inherited by titanite, concentrations of these trace elements are plotted against fluorine contents. Of the Permian-aged

samples, variable correlations are observed between fluorine and the HFSE (apart from U) that are enriched in the Khanbogd Granite (Fig. 7.9) but not in a consistent way.

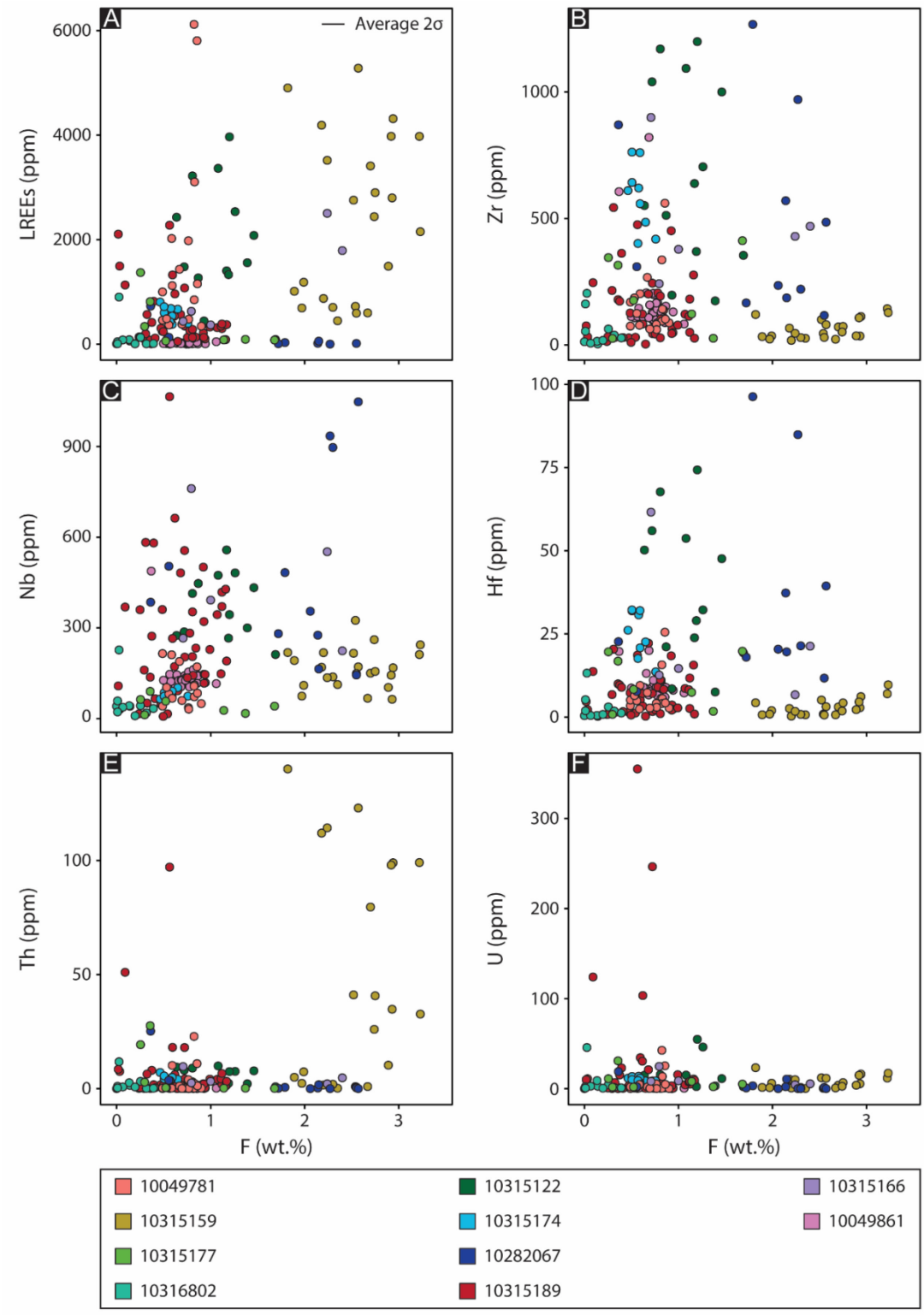


Figure 7.9. Bivariate plots illustrating titanite F contents against various trace elements for different samples. **A.** Sum LREEs. **B.** Zr. **C.** Nb. **D.** Hf. **E.** Th. **F.** U. Average 2σ for trace elements is smaller than symbol size.

An important consideration is how Permian aged samples are distributed in relation to the Khanbogd Granite. As identified by Hart-Madigan (2019) and Hart-Madigan *et al.* (2020), Permian samples 10315159 and 10315166 are up to 10 km away from the boundary of the Khanbogd Granite (Fig. 7.1). These authors, however, did not identify that sample 10282067 may also be of Permian age, which is indeed much closer to the Khanbogd Granite (~ 3 km), but still extends considerably further than the zone of hornfelsing (~ 1 km) associated with granite emplacement (Kovalenko *et al.*, 2006; Hart-Madigan, 2019; Hart-Madigan *et al.*, 2020). One important observation is that these Permian samples are all located near to major structures (Fig. 7.1), which may have facilitated fluid transport over significant distances. It is also interesting to note that of the group of samples located close to the West Bat fault, none were definitively dated as Permian, and only sample 10315135 could speculatively be classified as Permian (based on high F contents). This group of samples is indeed much closer to the Khanbogd Granite than samples 10315159 and 10315166, also lying at the intersection of several major structures, which could have migrated fluids away from the granite (Fig. 7.1). Within this group was 10315122, which was dated as Carboniferous, although reliable ages were not obtained for the other samples. One potential explanation for there may have been some kind of lithological control on fluid flow, with sample 10315122 being classified as a hornblende biotite andesite dyke, and samples 10315159 and 10315166 classified as a porphyritic augite basalt and a basaltic volcanic breccia, respectively.

Another potential consideration is how crystallisation temperatures may vary spatially and temporally. Although the Zr-in-titanite thermometer of Hayden *et al.* (2008) is readily utilised for magmatic titanite, the thermometer is calibrated in the temperature range of 600-1000°C, rendering it invalid for calculating temperatures of propylitic titanite. In all the studied samples, titanite is found in association with chlorite, a mineral which has been utilised to estimate temperatures of formation. Chlorite compositions from the same samples are available (Hart-Madigan, unpublished data), meaning that titanite temperatures of formation in the Oyu Tolgoi district can be estimated, on the predication that titanite and chlorite are coeval. A variety of chlorite thermometers have been postulated, often based on the incorporation of Al into the chlorite structure. In a study of propylitic chlorite from the Northparkes porphyry Cu-Au system, Pacey (2016) compared estimated temperatures from several chlorite thermometers (Walshe, 1986; Kranidiotis & MacLean, 1987; Cathelineau, 1988; Jowett, 1991) with temperatures obtained using oxygen isotope thermometry. Pacey (2016) observed that temperatures obtained using the equation of Jowett (1991) most closely matched those obtained by oxygen isotope thermometry. Hence, chlorite temperatures presented here are calculated using the equation of Jowett (1991). However, it should be noted that no error analysis was conducted by Jowett (1991), hence crystallisation temperatures should be taken as indications rather than absolute values.

For Oyu Tolgoi, chlorite crystallisation temperatures are between 210 and 380°C (Fig. 7.10), which are consistent with temperature ranges estimated using thermodynamics for propylitic alteration assemblages (Reed *et al.*, 2013). Overwhelmingly, chlorite thermometry indicates temperatures between 250 and 350°C. The highest temperatures are found in samples 10282067 and 10315159, which mostly display temperatures greater than 350°C. Both these samples are potentially Permian in age, implying that crystallisation temperatures vary depending on the alteration event. Generally, chlorite temperatures correlate with titanite U-Pb ages, with Devonian samples clustering in a narrow temperature window, and Carboniferous samples in a slightly larger window (Fig. 7.10). Also displayed in Figure 7.10 is the prevailing alteration assemblage, although there appears to be no correlation with chlorite temperatures (Fig. 7.10).

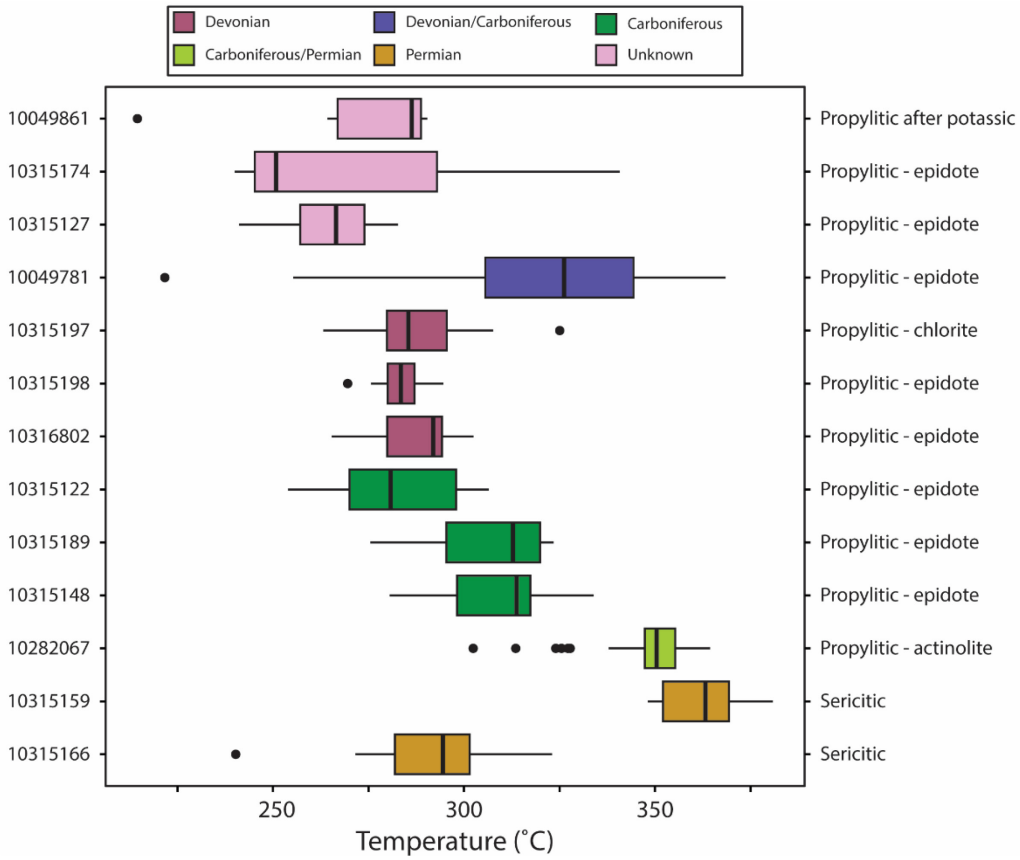


Figure 7.10. Estimated chlorite formation temperatures in the studied samples , colour coded by titanite U-Pb ages from this study and Hart-Madigan *et al.* (2020). Calculated using the equation of Jowett (1991).

Again, an important consideration is how these factors vary spatially, which is shown by Figure 7.11. Generally, estimated temperatures in neighbouring samples are consistent with one another; however, differing crystallisation ages may be observed (e.g. 10315122 and 10315197; Fig. 7.11). This is interpreted to indicate that chlorite temperatures may be prone to re-equilibration where titanite ages are not.

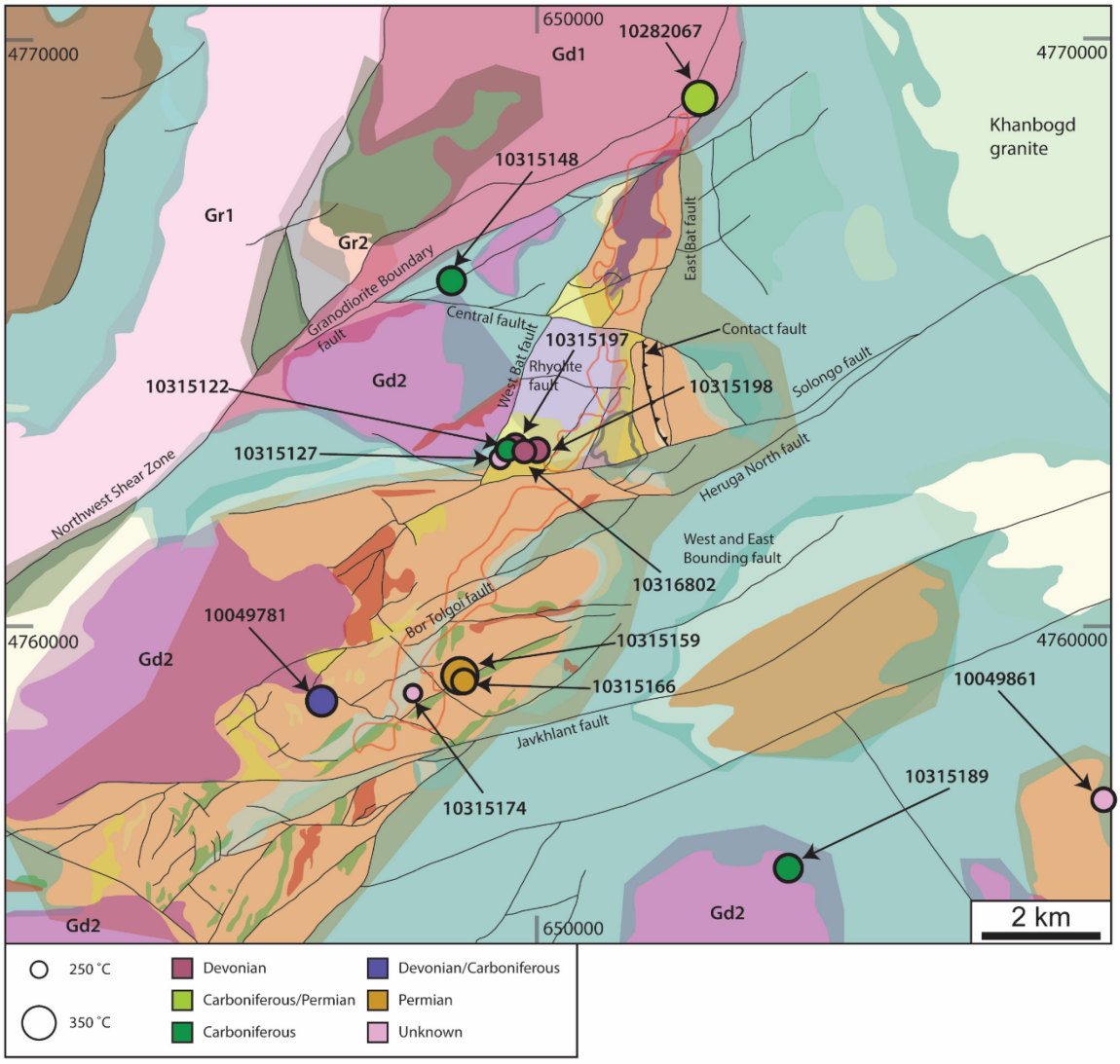


Figure 7.11. Map of the Oyu Tolgoi district showing titanite U-Pb ages, from this study and (Hart-Madigan *et al.*, 2020), as well as chlorite temperatures ; with increasing circle sizes indicating higher chlorite temperatures. Temperatures were calculated using the thermometer of Jowett (1991).

7.5.3 Controls on titanite composition

In spite of the regular occurrence of titanite in propylitically-altered rocks, little is known about the controls on propylitic titanite compositions, relative to more well-studied green rock minerals like chlorite and epidote. Titanite geochemical signatures may be controlled by a variety of factors, including host rock composition, fluid composition, the nature of co-crystallising phases, as well as temperature and pressure. The broad correlation between titanite composition (e.g. F-rich titanite), crystallisation age and chlorite thermometry suggests that alteration event, through bulk fluid composition and intensive parameters, may exert a key control. In order to assess this, principal component analysis was conducted. Again (see Chapter 6), prior to PCA all censored data was removed and clr transformations were carried out. Elements included in the PCA were as follows: F, Al, Fe, Sc, V, Sr, Y, Zr, Nb, Sn, REEs, Hf, Ta, Pb, Th and U.

Results of the principal component analysis are shown in comparison to titanite ages and sample numbers (Fig. 7.12). A variety of elements are observed to impact PC1, with the most important represented by positive loadings for MREEs and HREEs, as well as negative loadings for HFSEs and transition elements. Principal component 2, however, is mostly controlled by LREEs (Fig. 7.12). Assuming that titanite compositions are dominantly controlled by the alteration event, then comparable signatures should be observed in different samples of the same age, with distinct compositions for distinct alteration events. In addition to exhibiting distinct F contents (as discussed earlier), Permian samples 10315159 and 10315166 generally differ in composition (Fig. 7.12). Furthermore, titanite compositions in Carboniferous/Permian sample 10282067 clearly differ from those in Permian samples (Fig. 7.12). Intriguingly, samples with the most consistent titanite signatures are dated to be Carboniferous in age, with several samples including 10315122 and 10315189 clustering at mid values for PC1 and low values for PC2 (Fig. 7.12). For Devonian and Devonian/Carboniferous samples there are a range of titanite compositions (Fig. 7.12). Finally, samples with unknown ages also exhibit their own distinct compositions and are distinct from the compositions observed for samples whose ages are constrained.

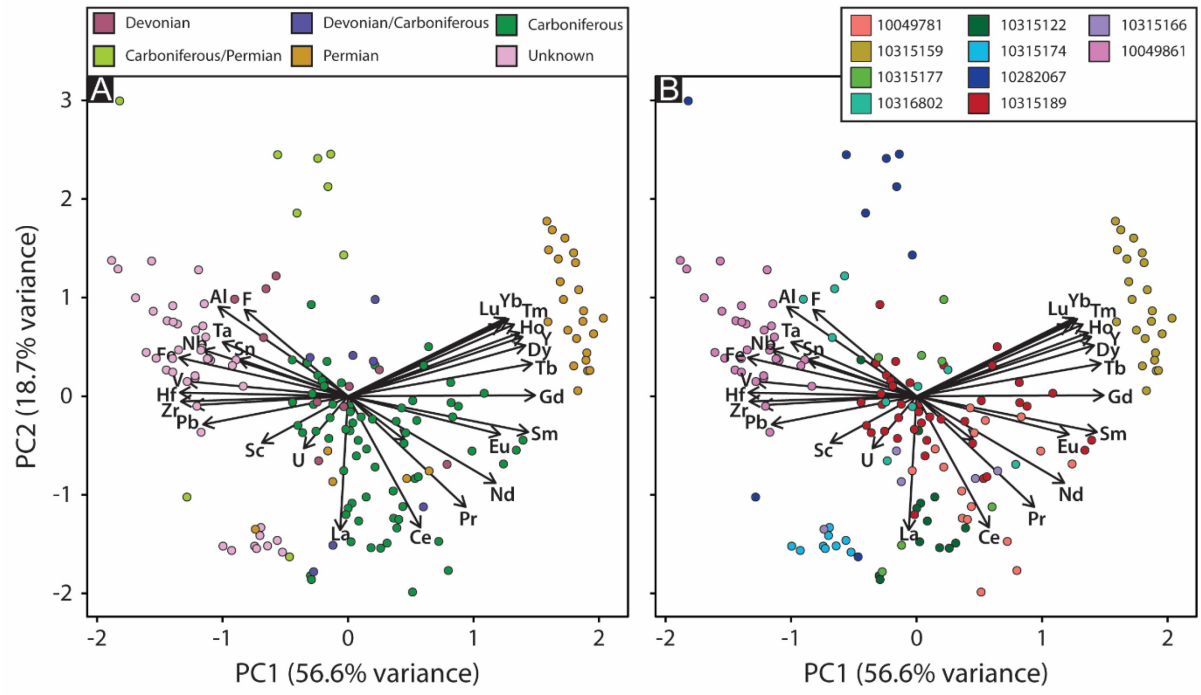


Figure 7.12. PCA biplot showing titanite compositions from OT compared to crystallisation age (**A.**) and sample number (**B.**).

Considering the relative importance of alteration event in controlling titanite compositions, it can be concluded that the various pulses of hydrothermal activity exert some control, particularly for Carboniferous aged samples (Fig. 7.12). However, there are clearly other significant factors, as highlighted by variable titanite compositions (Figs. 7.12) and chlorite temperatures (Figs. 7.10 and

7.11) in neighbouring Permian samples 10315159 and 10315166. Another factor which could potentially influence titanite chemistry is the host rock composition, although it can be concluded that generally is not important; in spite of its potential influence in some samples (e.g. Figs. 7.6G, 7.7C and 7.7E).

Overall, titanites in different samples with overlapping U-Pb ages are more likely to exhibit similar geochemical signatures, likely reflecting fluid composition. Fluid composition itself may be influenced by the chemistry of the bulk fluid, and any processes which may act locally to alter the composition of the bulk fluid. Whole-rock mass transfer (isocon) analysis may be a means to untangle the influence of bulk fluid chemistry with factors that operate on a local scale. Hart-Madigan (2019) conducted isocon analysis on the same sample set (Hart-Madigan, 2019), with results indicating that LREEs are generally to the rocks added during hydrothermal alteration. This LREE addition contrasts with the dominant titanite REE signature at Oyu Tolgoi (Fig. 7.6), which is characterised by either relatively flat REE patterns, or depletion in LREEs relative to HREEs. Such an observation suggests that REE compositions of non-igneous titanite are probably strongly influenced by the local fluid composition; in this case, probably due to the preferential incorporation of LREEs into other mineral phases (see Chapter 6). At Oyu Tolgoi, it is inferred that LREEs may often reside in epidote. For example, sample 10315184 contains approximately 30% epidote (as estimated from automated SEM analysis), which contained median La concentrations of ~10 ppm. In this rock, the whole-rock La concentration is ~9 ppm, meaning that about 30% of all La in that rock is estimated to be located within epidote. As well as epidote, allanite, which is sometimes associated with titanite, or apatite could contribute to the whole-rock LREE budget. Moreover, minor thorite (0.6-1%) is associated with titanite in samples 10049861 and 10316802, which exhibit lower titanite Th concentrations compared to samples 10315159 and 10315189 (Fig. 7.7F) which contain limited thorite (~0.05 %). As is the case in igneous rocks (see Chapter 4), the timing of mineral precipitation is likely to strongly impact mineral compositions, such that titanite which precipitates before or after epidote may potential exhibit different rare earth element signatures.

Locally, the fluid composition may also be influenced by the composition of precursor igneous phases. As highlighted in Chapter 5, primary mineral compositions may be partly inherited by the minerals that replace them, particularly for fluid immobile elements such as REEs and HFSEs. It was difficult to discern precursor igneous minerals in all cases at Oyu Tolgoi, given the intense, pervasive nature of hydrothermal alteration in many samples. However, future study should seek to compare titanite signatures in the same samples where the precursor igneous can be clearly identified.

7.6 Conclusions

This work has demonstrated that trace element concentrations of hydrothermal vein-type or replacement titanite can be determined without compromising the quality of U-Pb isotopic data that are collected simultaneously. Isotopic data collected in this manner can be used to identify either multiple age populations of titanite or grains where the isotopic system has been disturbed. Such an approach has the potential to delineate multiple generations of titanite in complex, poly-deformed and mineralised districts. Indeed, combining titanite geochemistry and geochronology could be a very powerful tool, allowing for the isolation of titanite which is related to mineralisation. Various authors have highlighted that chlorite and epidote compositions vary systematically away from mineralised centres, allowing for their use in exploration targeting or assessment. However, these minerals either do not incorporate radiogenic lead or incorporate a high common lead component, meaning there is uncertainty around whether alteration is related to porphyry mineralisation or another alteration event. Through combining titanite U-Pb geochronology with chlorite and epidote chemistry, there lies the potential to screen out alteration that is unrelated to porphyry mineralisation, ensuring that targeting or assessment studies focus only on spatial geochemical variations that are related the mineralising event.

Using such a small sample suite it was not possible to assess whether spatial zoning of titanite compositions exists around porphyry centres exists, especially given the structural dismemberment and multiple pulses of hydrothermal alteration that the Oyu Tolgoi district has experienced. Nevertheless, compositions of non-igneous titanite are inferred to be controlled by a range of factors, including bulk fluid chemistry, inheritance from primary igneous minerals and also timing of precipitation in relation to other mineral phases.

Chapter 8. Titanite compositions and their application to porphyry exploration

8.1 Introduction

Earlier chapters (see Chapters 4-7) have described titanite textures, mineral associations and compositions from four, variably mineralised, study sites (Strontian, Chuquicamata, Cobre Panama and Oyu Tolgoi), encompassing titanite formed in a range of environments. Data from these study sites includes titanite with both igneous and non-igneous origins, as well as whole-rock and ancillary mineral data (amphibole, zircon). In this thesis, the impact of titanite crystallisation on late-stage melt chemistry has been shown (Chapter 4); titanite compositional evolution in the lead up to formation of a world class porphyry copper deposit has been examined (Chapter 5); compositions of igneous and non-igneous titanite from a major porphyry deposit have been discussed (Chapter 6); and trace element chemistry and geochronology were combined for non-igneous titanite (Chapter 7). In this chapter, these results will be synthesised, together with data from a global sample suite provided by Rio Tinto, and literature data (Table 8.1), providing a more robust indication of whether the geochemical signatures identified can be applied to other systems and environments. Samples from the Rio Tinto global sample suite were selected to originate from a range of unmineralised and mineralised systems of varying size.

Central to the present study is understanding compositional variation with respect to: (1) igneous and non-igneous titanite; and (2) porphyry and non-porphyry titanite. This chapter is split into three parts, with the first part assessing the key controls on titanite composition in these environments. Attempts are then made to characterise and classify titanite composition according to (1) and (2); firstly using conventional methods, as well as unsupervised and supervised learning techniques. Finally, recommendations are made as to the ways in which titanite could be useful in porphyry exploration, and how it could be implemented in an exploration workflow.

8.2 Controls on titanite composition: non-igneous

A variety of factors are likely to control the incorporation of trace elements into non-igneous titanite including temperature and pressure conditions, the host rock composition, fluid composition, pH and salinity. Unpicking these factors and assessing their relative importance is difficult at the present time because of a lack of experimental data and constraints on the conditions of titanite precipitation. Nonetheless, some potential controls that can be addressed are considered below.

Table 8.1. Sample information for the Rio Tinto sample suite and literature data.

Sample No.	Country	Unit	Alteration?	Mineralised?	No. of igneous ttn analyses	No. of non-igneous ttn analyses
Escondida Norte-Zaldivar	Chile					
21223	-	Late Llamo Porphyry	Propylitic	N	-	25
Gravestones	Australia					
21233	-	Porphyritic granite	Propylitic?	N	-	36
21237	-	Granite	Chlorite-sericite?	N	-	10
Yauricocha	Peru					
21624A	-	Quartz monzonite	Potassic	Y	21	-
Little Cottonwood Stock	USA					
22400A	-	Porphyritic bt-hbl granite	-	N	32	-
Alta Stock	USA					
22403A	-	Granodiorite	-	N	41	-
Clayton Peak Stock	USA					
22405A	-	Granodiorite/monzodiorite	-	N	34	-
Valeo Stock						
22407A	USA -	Granodiorite porphyry	Propylitic	N	-	12
Tsagaan Suvarga	Mongolia					
R03557A	-	Monzonite	Sericite	Y	22	-
Santa Clara	Chile					
R08221A	-	Float	Propylitic	?	-	13
R08222A	-	Float	Propylitic	?	-	13
Kneeling Nun[1]	USA					
DS1402	-	Rhyolitic tuff	-	N	74	-
Rat Creek[2]	USA					
RCTD	-	Dacite-rhyolite tuff	-	N	8	-
X17DF01	-	Rhyolite	-	N	15	-
X17DF11	-	Rhyolite	-	N	12	-
X17DF12	-	Dacite	-	N	15	-
X17DF13	-	Dacite	-	N	15	-
Nelson Mountain[2]	USA					
17SJ02	-	Dacite	-	N	18	-
17SJ03	-	Dacite	-	N	19	-
17SJ04	-	Rhyolite	-	N	20	-
17SJ09	-	Dacite	-	N	20	-
17SJ16	-	Rhyolite	-	N	20	-
17SJ19	-	Rhyolite	-	N	20	-
Highland Range[3]	USA					
HRL12a	-	Rhyolite porphyry	-	N	4	-

HRL14a	-	Mingled capping lava	-	N	5	-
HRL19	-	Rhyolitic tuff	-	N	5	-
HRL21	-	Tuff	-	N	5	-
Black Mountain[4]	Philippines					
BA08GS013	-	Synmineral diorite porphyry	Propylitic		8	-
Pebble[5]	USA					
11528-1412	-	Kaskanak granodiorite	?	?	12	-
11530-923	-	Kaskanak granodiorite	?	?	20	-
11532-393	-	Kaskanak granodiorite	?	?	13	-
Tuolumne[6]	USA					
TLM15A15	-	Kuna Crest granodiorite	-	N	36	-
TLM0415	-	Transitional	-	N	33	-
TLM1615	-	Transitional	-	N	23	-
TLM0715	-	Equigranular Half Dome granodiorite	-	N	14	-
TLM1115	-	Equigranular Half Dome granodiorite	-	N	20	-
TLM1715	-	Equigranular Half Dome granodiorite	-	N	35	-
TLM2615	-	Equigranular Half Dome granodiorite	-	N	33	-
TLM1915	-	Porphyritic Half Dome granodiorite	-	N	33	-
Alumbrera[7]	Argentina					
EP3	-	Early porphyry 3	?	Y	32	-
LP3	-	Late porphyry 3	?	Y	28	-
P4	-	Post-mineral porphyry 4	?	N	2	-
SR73	-	Crystal poor pumice	?	N	37	-
SR65	-	Dacite pumice	?	N	34	-
SR63	-	Pumice	?	N	38	-
SR62	-	Crystal rich pumice	?	N	29	-
Bingham Canyon[8]	USA					
QLP2	-	Quartz latite porphyry	?	Y	18	-
QLP1	-	Quartz latite porphyry	?	Y	14	-

[1]Szymanowski *et al.* (2017), [2]Sliwinski *et al.* (2019), [3]Colombini *et al.* (2011), [4]Cao *et al.* (2020), [5]Olson *et al.* (2017), [6](Werts, 2019), [7]Buret (unpublished data), [8]Large *et al.* (2021)✖

8.2.1 Bulk rock controls on non-igneous titanite composition

An intuitive starting point for considering controls on non-igneous titanite composition is a comparison of titanite and whole-rock compositions (Fig. 8.1). It is important to consider here that host rock compositions reflect a combination of precursor rock chemistry and signatures imparted metasomatically (either by addition or removal of components) by hydrothermal fluids, which cannot be untangled without detailed isocon analysis of individual rock samples. Nevertheless, compositions of titanite generally do not correlate with those of their host rock (Fig. 8.1).

Other elements that could be impacted by host rock composition include F and Al; of which understanding the behaviour of halogens (including F) is extremely important in porphyry systems as these elements act as ligands for copper and gold (Candela & Holland, 1984; Ulrich *et al.*, 1999).

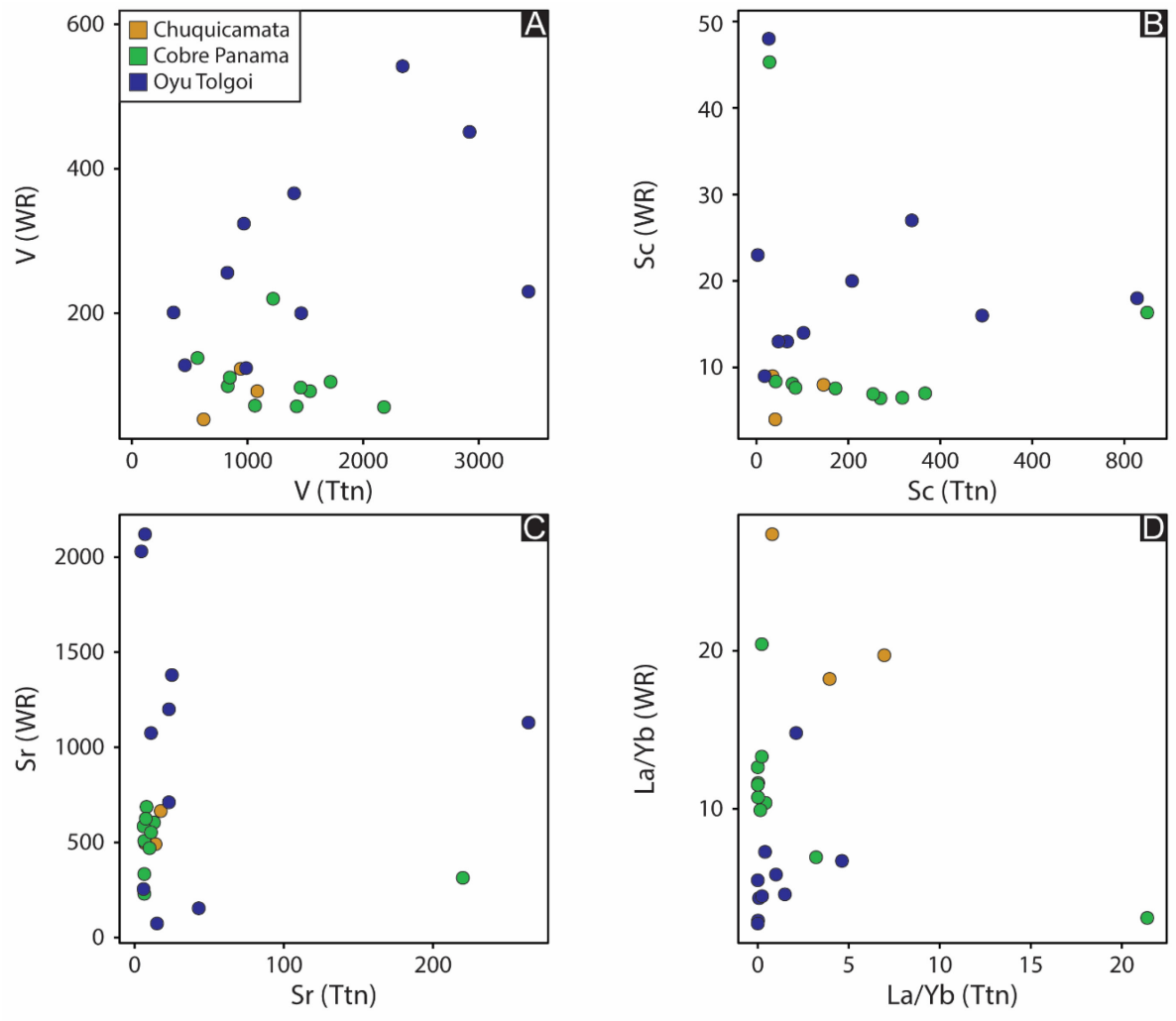


Figure 8.1. Comparison of median non-igneous titanite compositions with the same parameter in their host rocks. **A.** V. **B.** Sc. **C.** Sr. **D.** La/Yb. Average 2σ errors for whole-rock analyses are smaller than symbol size.

A study by Markl and Piazolo (1999) found that host rock Al/Ti ratios are important in controlling incorporation of Al into titanite, which may have implications for F given its incorporation in a coupled substitution mechanism with Al (Fig. 8.2A). However, a lack of any discernible correlation between host rock Al/Ti and titanite F concentrations indicates that Al is likely always in excess, with F incorporation instead controlled by other factors.

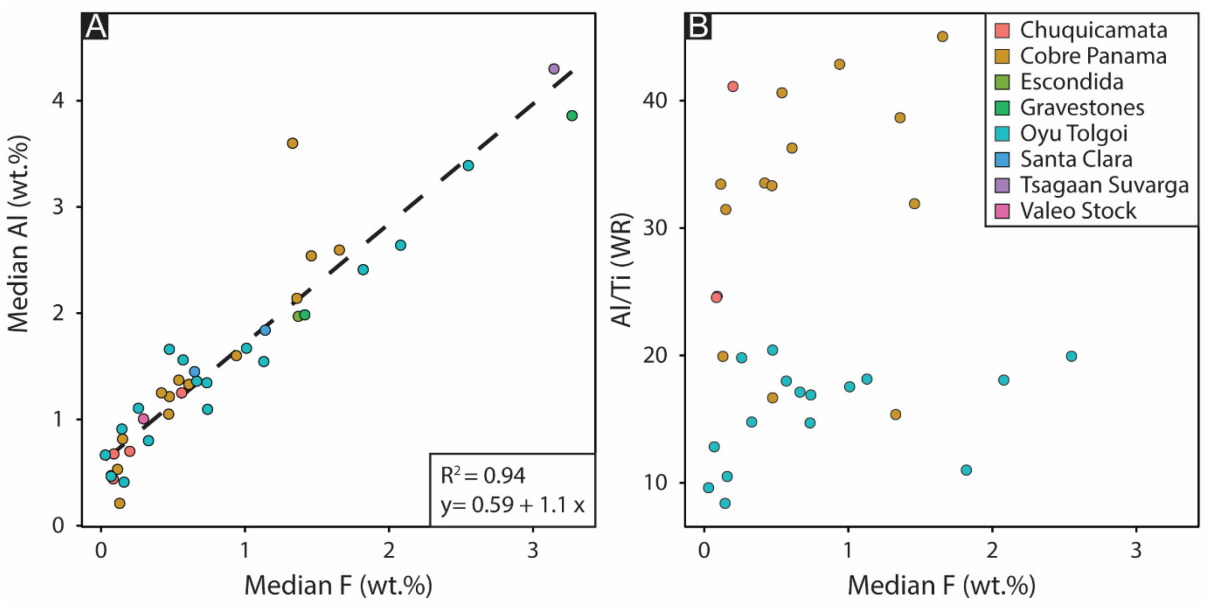


Figure 8.2. Median titanite F contents plotted against Al contents (**A.**) and whole-rock Al/Ti ratios (**B.**).

8.2.2 Fluid compositional controls on non-igneous titanite composition

Another key factor is likely to be fluid composition. In Chapter 7, the association of F-rich titanite with F-rich fluids was inferred, where Permian titanite was interpreted to be related to the Khanbogd Granite, an alkaline intrusion that displays evidence for sourcing F-rich fluids. This, when coupled with the range of titanite F concentrations encountered during the present study, in addition to the limited pressure-temperature variability, indicates that titanite F contents are mostly controlled by fluid composition.

In Chapter 7, the importance of fluid composition was also highlighted with respect to Carboniferous titanite from Oyu Tolgoi (Fig. 7.12). Here, titanite of Carboniferous age exhibited similar trace element signatures, despite the fact that they were: hosted in different samples and units, displayed different mineral assemblages and were up to 10km away from one another; indicating that Carboniferous fluids were distinct and controlled the titanite trace element signature. However, compositional variations within a single hydrothermal system (e.g. Fig. 6.8), and even within the same sample (Fig. 7.6), suggest that more localised factors are also at play.

8.2.3 Mineral assemblage controls on non-igneous titanite composition

Another potential control that can be investigated concerns how titanite compositions relate to the prevailing alteration assemblage, which has been demonstrated to influence potassic and propylitic titanite in porphyry systems (Xiao *et al.*, 2021). No unequivocal potassic titanite was encountered during the present study. In fact, in moderately potassically altered samples, titanite is observed to

be partially or completely replaced. Nevertheless, the possible influence of sericitic alteration at Oyu Tolgoi can be assessed.

Thermodynamic studies indicate that fluids responsible for sericitic, compared to propylitic or potassic alteration, are more acidic (Hemley & Jones, 1964; Montoya & Hemley, 1975; Reed *et al.*, 2013), meaning that a pH control may influence differences in the compositions of titanite from these assemblages. However, chondrite-normalised REE patterns of sericitic titanite do not appear to be unique and Eu anomalies do not significantly differ (Figs. 7.6B and E). This contrasts with sericitic apatite which has been shown to exhibit elevated Eu anomalies (Ma *et al.*, 2021), thought to be due to the liberation of Eu during alteration of plagioclase to sericite. In this regard, it is unclear what is causing the behaviour of titanite and apatite to diverge, although timing of precipitation, or complexation may play a role.

Generally, the most commonly encountered chondrite-normalised REE patterns are positively sloping (e.g. Figs. 6.8 and 7.6). Transport of REEs in aqueous fluids is facilitated by a variety of complexing agents, with Cl, F and OH likely to be the most important in hydrothermal systems (Haas *et al.*, 1995). Rare earths can potentially be fractionated from one another in hydrothermal systems, with mobility controlled by temperature, as well as fluid pH and composition. At propylitic conditions (i.e. temperatures of 300-400 ºC and a fluid pH of ~5-5.5; Reed *et al.*, 2013) experimental studies suggest that REEs are likely transported as F and Cl complexes (Williams-Jones *et al.*, 2012; Migdisov *et al.*, 2016), with LREEs expected to be mobilised preferentially relative to HREEs. This could explain the LREE depletion of propylitic titanite. However, mass transfer analysis indicates that at the hand sample scale, LREEs either remain constant or are even added during propylitic alteration (Ulrich & Heinrich, 2002; Pacey, 2016; Loader, 2017), with resultant flat to negatively-sloping REE patterns assuming metasomatic addition. Another possible explanation could be that local fluid compositions are impacted by the co-precipitation of mineral phases that partition LREEs preferentially, such as allanite and monazite, and potentially even apatite. Although partition coefficients will differ in the hydrothermal environment, allanite-melt partition coefficients indicate that La is over fifty times more compatible than Lu (Mahood & Hildreth, 1983), illustrating how allanite precipitation could potentially fractionate LREEs from HREEs. As shown by Table 8.2, non-igneous titanite is often associated with a LREE-rich phase such as allanite or monazite, but the presence of these phases does not preclude the formation of titanite with elevated La/Yb ratios. This observation suggests that the timing of titanite precipitation in relation to the growth of LREE-rich phases is likely to be important.

Table 8.2. Titanite La/Yb ratios and whether titanite was associated with LREE-rich phases.

Sample	Location	Median La/Yb	Associated with LREE-rich phase? (allanite, monazite)	Sample	Location	Median La/Yb	Associated with LREE-rich phase? (allanite, monazite)
CH003	Chuquicamata	0.25	Y	10049861	Oyu Tolgoi	0.40	Y
CH005	Chuquicamata	17.8	Y	10315159	Oyu Tolgoi	2.11	N
FC002	Chuquicamata	3.95	Y	10315166	Oyu Tolgoi	1	N
FC008	Chuquicamata	6.95	Y	10315174	Oyu Tolgoi	4.63	Y
FC009	Chuquicamata	0.79	Y	10315177	Oyu Tolgoi	0.070	Y
IMP006	Cobre Panama	21.4	Y	10315189	Oyu Tolgoi	0.23	N
IMP011	Cobre Panama	0.22	Y	10049781	Oyu Tolgoi	1.49	Y
IMP013	Cobre Panama	0.43	Y	10316802	Oyu Tolgoi	0.026	Y
IMP014	Cobre Panama	0.0024	Y	10282067	Oyu Tolgoi	0.0028	Y
IMP015	Cobre Panama	0.015	Y	21223	Escondida	300	Y
IMP020	Cobre Panama	0.021	Y	21233	Gravestones	0.12	Y
IMP021	Cobre Panama	3.20	Y	21237	Gravestones	0.0013	Y
IMP022	Cobre Panama	0.14	Y	22407A	Valeo Stock	6.91	Y
IMP023	Cobre Panama	0.0086	Y	R08221A	Santa Clara	3.49	Y
IMP024	Cobre Panama	0.22	Y	R08222A	Santa Clara	4.63	Y

Other important characteristics of non-igneous titanite are their relative enrichment in Sc and V, elements whose speciation is relatively unknown in hydrothermal systems, particularly in propylitic environments (Williams-Jones & Vasyukova, 2018). Mass transfer analyses of propylitically altered rocks suggest that both elements are broadly conserved (Ulrich & Heinrich, 2002; Pacey, 2016; Hart-Madigan, 2019). Studies of propylitic chlorite and epidote often show elevated V contents for samples relatively proximal to porphyry centres (Wilkinson *et al.*, 2015; Hart-Madigan, 2019; Pacey *et al.*, 2020b; Wilkinson *et al.*, 2020) implying a temperature or other fluid property control on substitution into these minerals. In Chapter 6, the association of V- and Sc-rich replacement titanite with alteration products of primary minerals that readily partition Sc and V (e.g. amphibole and magnetite) was taken to indicate that these elements were inherited from precursor igneous minerals. Such a model is consistent with mass transfer studies which indicate that Sc and V are unlikely to be mobilised beyond the hand sample scale.

8.3 Controls on titanite composition: igneous

8.3.1 Extrusive vs intrusive

Although only titanite from intrusive rocks was analysed during the present study, incorporation of literature data from volcanic rocks allows for interesting comparisons to be made. A key factor potentially affecting titanite compositions in extrusive vs. intrusive rocks concerns melt extraction, with extrusive magmas being erupted before rheological lockup has been reached, i.e. before magmas are too crystal-rich to be erupted. Magma crystallinity at rheological lockup is generally believed to be around 50% (Marsh, 1996; Hildreth, 2004; Bachmann & Bergantz, 2006).

Conversely, intrusive magmas crystallise until reaching the solidus (i.e. 100% crystallinity). Hence, titanite compositions from the two environments may represent differences in temperature and melt evolution (cf. Szymanowski *et al*., 2017).

Extrusive and intrusive titanite compositions are compared using cumulative frequency plots (Fig. 8.3). Estimated crystallisation temperatures are consistent with the early extraction of

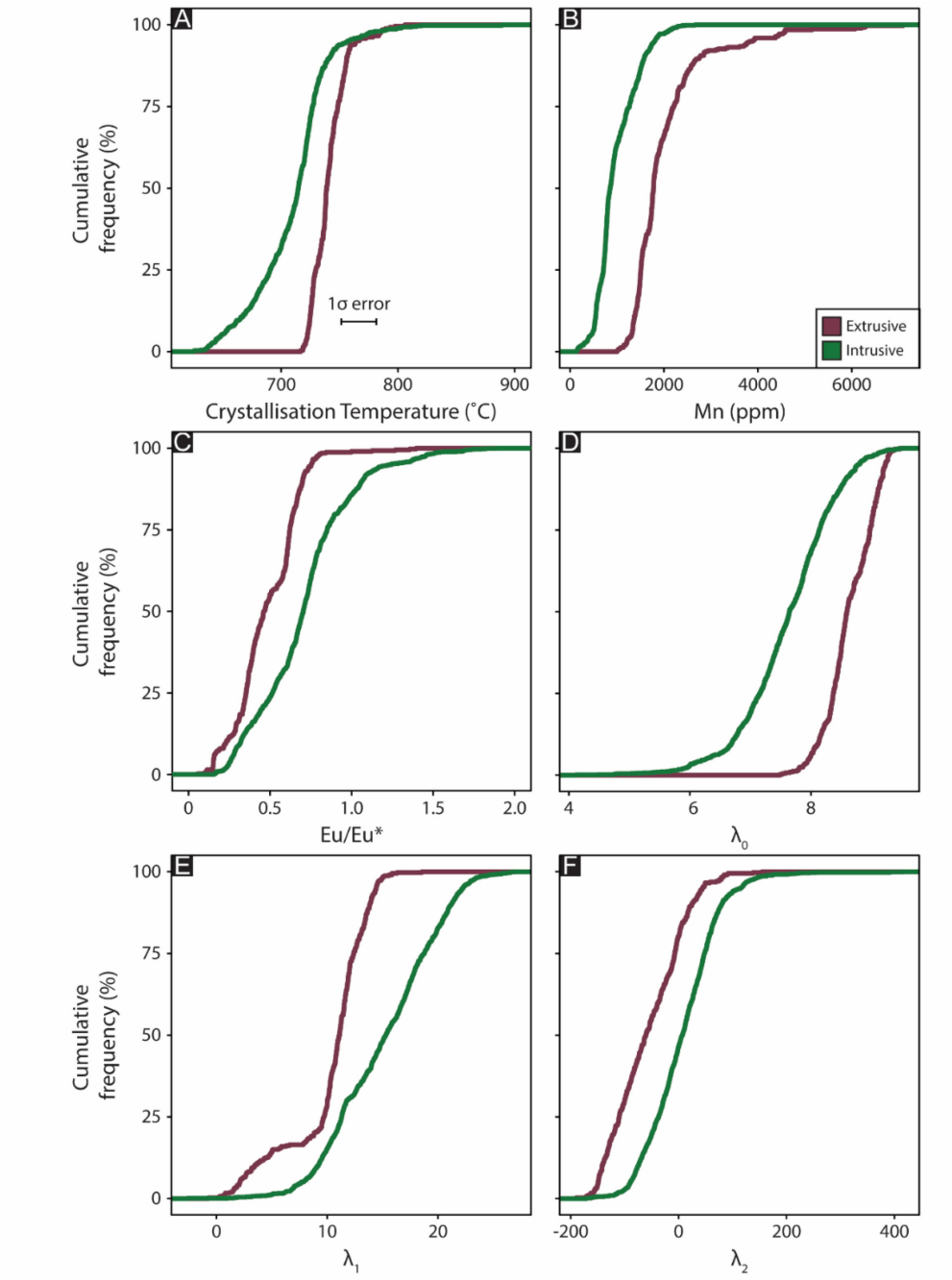


Figure 8.3. Comparison of extrusive and intrusive titanite compositions. **A.** Crystallisation temperature (Hayden *et al.*, 2008). **B.** Mn. **C.** Eu/Eu*. **D.** λ_0. **E.** λ_1. **F.** λ_2. Typical 2σ errors for Mn and Eu/Eu* were 2% and 5% respectively.

titanite-bearing magmas in extrusive systems, evidenced by the absence of near-solidus crystallisation temperatures compared to plutonic titanite (Fig. 8.3A). This has important

implications for trace element concentrations and ratios in titanite, including those which are important in delineating whole-rock compositions of porphyry magmas (e.g. Mn, Eu/Eu*). For example, manganese concentrations are higher, on average, in titanite from extrusive rocks relative to intrusive rocks (Fig. 8.3B). Compositional differences are also observed for the Eu anomaly (Fig. 8.3C), as well as lambda values λ_0, λ_1 and λ_2, all of which likely reflect the fact that a significant proportion of intrusive titanite crystallises at a later stage of melt evolution compared to extrusive titanite (Figs. 8.3D-F). Lambda values provide a means to quantify the shapes of REE patterns (O'Neill, 2016), with λ_0 signifying total REE content, λ_1 indicating the slope of the REE pattern (e.g. La/Yb) and λ_2 representing the concavity of the REE pattern. In exploration, high La/Yb ratios and concave, spoon shaped REE patterns (e.g. high λ_1 and λ_2), are observed for porphyry magmas (e.g. Fig. 6.7), and are considered to indicate derivation from a melt that has fractionated significant amounts of amphibole ± titanite ± garnet (Müntener *et al.*, 2001; Richards, 2011; Loucks, 2014).

8.3.2 Redox

Titanite incorporates several multivalent trace elements, including Fe, Mn and V, as well as the rare earth elements Ce and Eu. For the transition elements, it is plausible that multiple valences of the same element may partition into titanite but relatively little is known about how different valences impact mineral-melt partitioning and the abundances of different transition metal valences in the melt at titanite saturation. More is known, however, about Ce and Eu partitioning and also about the relative abundance of their valence states in typical melts (Burnham & Berry, 2012; Burnham *et al.*, 2015). This allows for inferences about magmatic redox based on the magnitude of Ce and Eu anomalies (Ballard *et al.*, 2002; Smythe & Brenan, 2015). Though Eu^{2+} and Eu^{3+} are both abundant in silicic magmas, Ce^{3+} is much more abundant than Ce^{4+} (Smythe & Brenan, 2015). In titanite, Ce anomalies are unlikely to be sensitive to redox because (i) Ce^{3+} and Ce^{4+} abundances do not vary significantly and (ii) the ionic radius of Ce^{4+} means that it is too large to fit into the titanite Ti-site and too small to fit into the Ca-site (Shannon, 1976). Europium anomalies, however, are potentially redox sensitive, although both positive and negative Eu anomalies can also be generated in a residual melt by *in-situ* crystallisation of titanite and other rock-forming minerals. In Chapter 5, magmatic oxidation state was estimated for evolving magmas in the Chuquicamata district using the zircon oxybarometer of Loucks *et al.* (2020). Using the estimated magmatic fO_2, titanite Eu/Eu* ratios were inverted to give melt Eu/Eu* ratios. From this, it was concluded that variation in melt chemistry, rather than oxidation state alone, was chiefly responsible for progressive increases in titanite (and potentially also zircon; Ballard *et al.*, 2002) Eu/Eu* through time.

8.3.3 Melt chemistry

An obvious control on igneous titanite composition is likely to be melt chemistry, given that the two will be linked through mineral-melt partition coefficients. One means to demonstrate this is by inverting residual melt compositions (using partition coefficients; Colombini *et al.*, 2011) from titanite, and compare them to those of their host rock. In this scenario, whole-rock compositions are treated as the parental liquids prior to the onset of crystallisation, and the inverted melts are reflecting the composition of the melt at the time of (and during) titanite crystallisation (Fig. 8.4).

Textural evidence and typical Zr-in-titanite crystallisation temperatures (e.g. 750 °C; Hayden *et al.*, 2008) indicate that titanite saturation occurs relatively late, potentially when 50-60% of crystallisation has already taken place (Marxer & Ulmer, 2019). It is most likely therefore that the divergence of the melt composition from that of the bulk rock is likely to reflect the crystallisation of the other rock minerals prior to titanite saturation. In the case of Sr, this would mean significant prior plagioclase crystallisation; which is consistent with the crystallisation sequence determined for intermediate composition magmas in experimental studies (Nandedkar *et al.*, 2014; Marxer & Ulmer, 2019) and observations of plagioclase phenocrysts with no titanite inclusions (see Chapter 4).

Another key observation is that titanite from a single rock may record a wide range of compositions. For example, La/Yb and Dy/Yb ratios may vary by greater than an order of magnitude (Figs. 8.4D and E). Additionally, although whole-rock and median melt Eu/Eu* ratios strongly correlate (suggesting a partial bulk magma control), minimum and maximum melt ratios regularly differ by more than 50% of the median, and sometimes by more than a factor of two in some samples (Fig. 8.4C). Differences in magmatic fO_2 could explain this divergence, but it has been demonstrated by several authors (Loader *et al.*, 2017; Nathwani *et al.*, 2021) that a deviation in melt composition is more likely. Ultimately, the controls on igneous titanite composition are perhaps best illustrated by the Eu anomaly, which clearly shows evidence for being controlled by both deep (e.g. bulk magma) and shallow (e.g. *in-situ* crystallisation) processes.

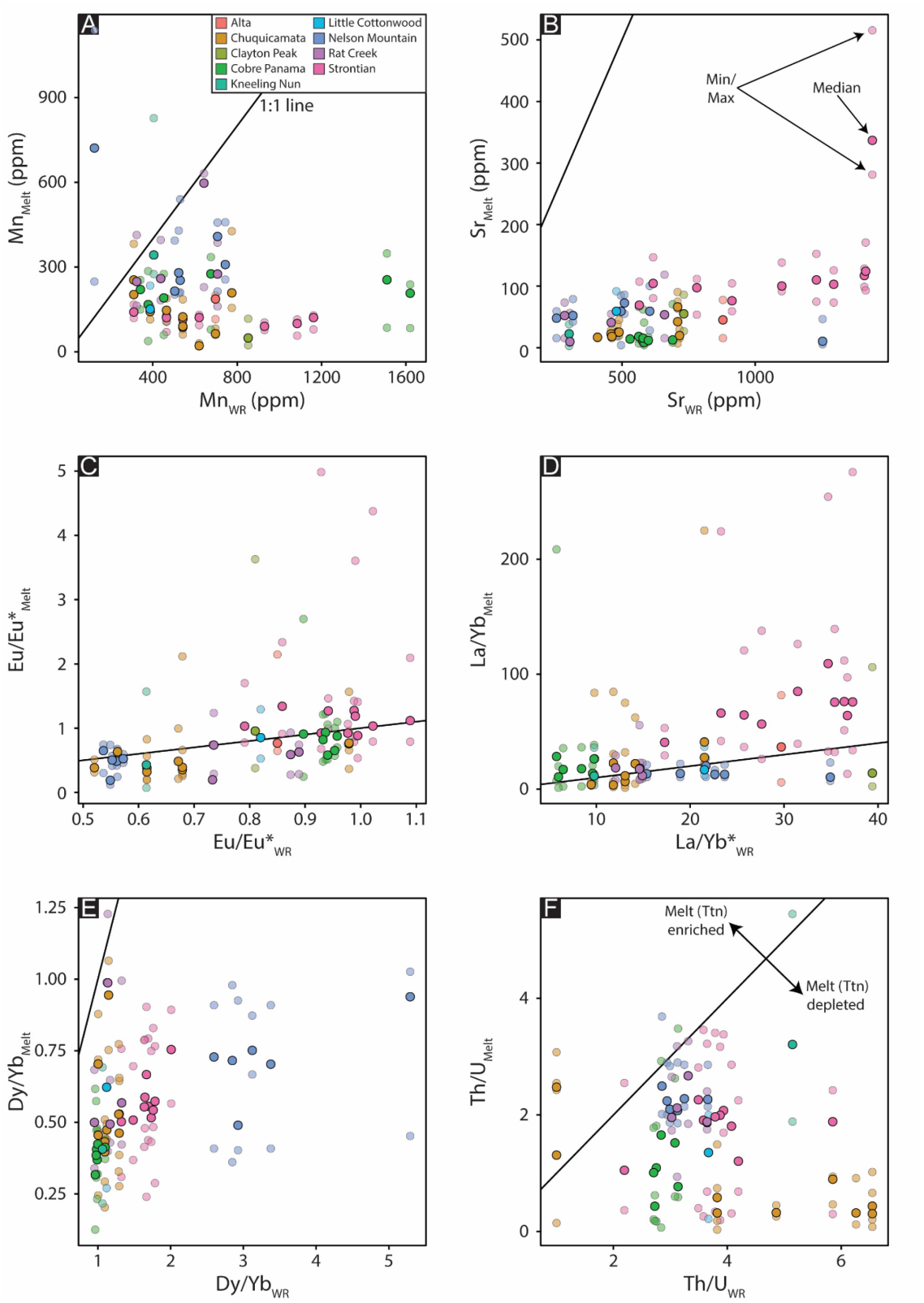


Figure 8.4. Comparison of whole-rock trace element compositions with median, minimum and maximum melt compositions inverted from titanite. 1:1 lines are indicated, with points below the line representing melts (that would be in equilibrium with titanite) that are depleted relative to the bulk rock, and those above the line representing melts that are enriched relative to the bulk rock. Partition coefficients applied are from Colombini *et al.* (2011). Average 2σ errors are smaller than symbol size.

8.4 Classification using conventional techniques

Critical to research into the geochemistry of mineral deposits is characterising and understanding signatures related to mineralisation. In the exploration for porphyry deposits, whole-rock geochemical signatures associated with mineralisation such as high Sr/Y, Eu/Eu* and La/Yb ratios (Rohrlach & Loucks, 2005; Richards, 2011; Loucks, 2014) have been known for several years, with implications for deep crustal processes. The aim of the present study was to understand how titanite, an important trace element-bearing accessory mineral that occurs in both igneous and hydrothermal portions of porphyry systems, could be applied to exploration. To assess whether titanite can be classified using compositional data as igneous or non-igneous (model 1), and porphyry or non-porphyry (model 2), conventional (e.g. bivariate plots) and machine learning techniques are applied. The effectiveness of conventional methods is considered first.

8.4.1 Model 1 (Igneous vs non-igneous)

Figure 8.5 displays geochemical characteristics that have been identified during this study to potentially differentiate igneous and non-igneous titanite. In Chapter 6, it was found that one of the most effective means of discriminating these groups was the F vs Fe/Al diagram. This is validated after integrating all available datasets, with non-igneous titanite mostly exhibiting Fe/Al ratios of <1 and with generally elevated F concentrations that may reach 4 wt.% (Fig. 8.5A). Additionally, non-igneous titanite is also characterised by: i) high V (mostly >400 ppm) and Sc contents (mostly > 10; Fig. 8.5B); ii) variable Zr (1-3000 ppm) and LREE concentrations (mostly <10000 ppm; Fig. 8.5C); iii) low Th/U ratios (mostly <1) and variable Mn (10-3000 ppm; Fig. 8.5D); iv) variable Eu/Eu* (<0.1 to >10) and low La/Sm ratios (mostly <1; Fig. 8.5E); and v) low Th/Sc ratios (mostly <10; Fig. 8.5F). Using these bivariate plots it can be concluded that igneous and non-igneous groups are generally distinct, although there is some minor compositional overlap.

8.4.2 Model 2 (Porphyry vs non-porphyry)

For porphyry systems, the use of indicator minerals could focus on either magmatic or hydrothermal components of the system. However, for hydrothermal titanite, sufficient data are not currently available to differentiate it from non-porphyry environments, hence the following section will attempt to distinguish igneous porphyry-associated titanite from igneous titanite not associated with porphyry systems (non-porphyry). In order to be classed as porphyry-associated titanite, a rock (and hence the titanite within the rock) needed to be plutonic, and originate from a system that produced porphyry mineralisation, with geochronological and textural evidence indicating that the rock crystallised within two million years of the mineralising event; a timescale that is supported

by geochronologic data and numerical modelling (Chiaradia & Caricchi, 2017; Nathwani *et al.*, 2021; Nathwani *et al.*, 2022). Classification as porphyry or non-porphyry is naturally a simplified

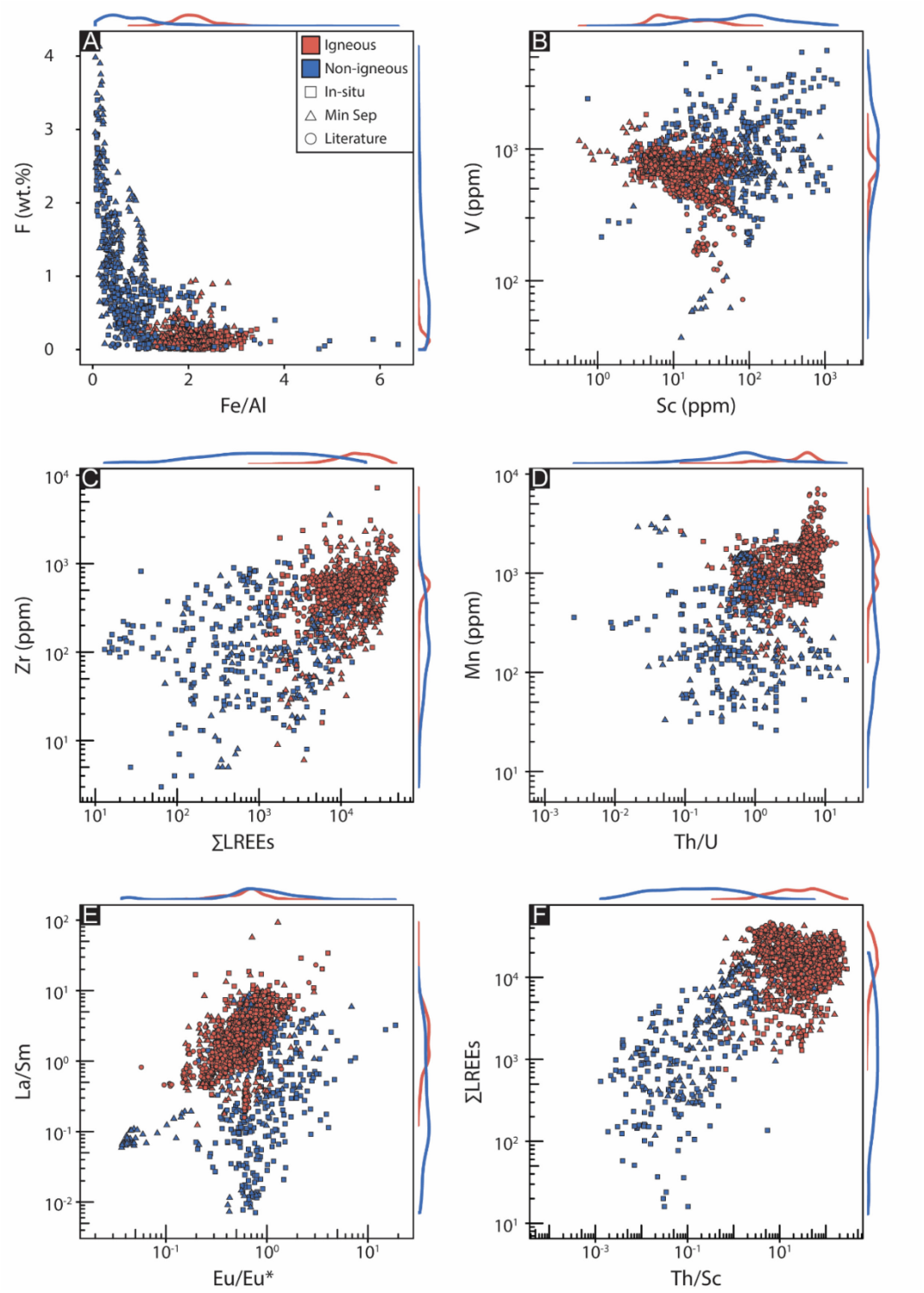


Figure 8.5. Titanite compositional data collected during this study and from the literature, colour coded by interpreted igneous or non-igneous origin. Bivariate plots are shown, with half violin plots to illustrate full data distribution for the two groups. **A.** F vs Fe/Al. **B.** V vs Sc. **C.** Zr vs ΣLREEs. **D.** Mn vs Th/U. **E.** La/Sm vs Eu/Eu*. **F.** ΣLREEs vs Th/Sc. Average 2σ errors are smaller than symbol size.

view of geological systems, which vary in terms of time, size and space. For example, the Los Picos-Fortuna Complex, which is precursor to one of the largest porphyry deposits in the world, would be classified as non-porphyry using a binary classification scheme. Similarly, the Strontian Intrusive Complex, which displays many whole-rock characteristics of a porphyry magma, would be classified as similar to the Kneeling Nun Tuff. One approach to capture some of these subtleties is to give titanite from each sample a 'porphyry score' from one to three, with one representing derivation from a known porphyry deposit, and three designating a rock unrelated to any known porphyry system. Titanite compositions are compared to these porphyry scores (Fig. 8.6), with datasets included in each class and reasons for classification outlined in Table 8.3.

Table 8.3. Porphyry score, reasons for classification and datasets included.

Porphyry score	Reasons for classification	Datasets
1	Intrusive rock from mineralised porphyry district. Within 2 m.y. of mineralisation.	Chuquicamata, Cobre Panama, Yauricocha, Tsagaan Suvarga, Black Mountain, Pebble, Alumbrera, Bingham Canyon
2	Precursor batholith to mineralisation Volcanics coeval with mineralisation Barren altered porphyries Rocks that exhibit fertile whole-rock signature (e.g. high Sr/Y, La/Yb)	Strontian, Chuquicamata (Los Picos-Fortuna Complex), Little Cottonwood, Alta, Clayton Peak, Alumbrera (volcanic)
3	Unrelated to any known porphyry mineralisation	Kneeling Nun, Rat Creek, Nelson Mountain, Highland Range, Tuolumne

Magmatic volatile concentrations are an important variable that has not yet been considered. In addition to anomalous metal contents, porphyry deposits also require an abundance of volatiles, which act as key complexing agents for copper and gold. Volatiles may either be sourced from atypically volatile rich magmas, or by large volumes of magma with typical volatile concentrations (Wilkinson, 2013). One approach to answer this question has been to estimate melt volatile contents from igneous minerals such as apatite and amphibole (Chelle-Michou & Chiaradia, 2017). Titanite, like these minerals, incorporates halogens into its structure and hence may provide a window into the melt volatile content. Only the study of Li *et al.* (2018) has attempted to investigate fluorine partitioning into titanite. They proposed $D^{F}_{Ttn/melt}$ values of 0.5-1.2 for metaluminous melts, at temperature close to 900 °C and pressures between 50 and 200 MPa and indicated that partition coefficients should be corrected using the ASI.

At Cobre Panama, the ASI is dominantly close to one, such that the $D^{F}_{Ttn/melt}$ is estimated to be ~1.2. In the Petaquilla granodiorite, average F contents of igneous titanite are 0.17 wt.%, which would correlate to 0.14 wt.% F in the melt. Such melt F contents are consistent with those determined in melt inclusions in volcanic rocks (Webster *et al.*, 2009). Maximum F contents in

igneous titanite are ~0.75, appearing to indicate high melt F contents, although this may imply that these D values are not appropriate for the lower temperatures at which titanite commonly crystallises. Nevertheless, maximum titanite F contents analysed during the present study are lower than 1 wt.%, which was observed by Price *et al.* (1999) to represent the point at which fluorite saturates instead of titanite in A-type granites.

No literature data are available for major element chemistry of igneous titanite, and hence only data from this study are shown in Figure 8.6A. Comparing titanite fluorine contents for the two porphyry scores, it appears that titanite with a higher porphyry score may exhibit higher F contents, however these differences are within typical analytical error (Fig. 8.6A). In Chapter 5, it was postulated that titanite crystallisation temperatures (Hayden *et al.*, 2008) progressively increased through time towards the mineralising event. This is in contrast to zircon, which commonly exhibits low Ti contents in porphyry rocks, implying lower temperatures of crystallisation according to the thermometer of Ferry and Watson (2007). Unfortunately, for systems where the crystallisation pressure, $a\mathrm{TiO_2}$ and $a\mathrm{SiO_2}$ of the system are not well characterised (e.g. some literature data and the Rio Tinto sample suite) then it is difficult to determine the exact crystallisation temperature. Hence, only systems where these parameters were well characterised are shown. Nevertheless, differences between the groupings are, for the most part, within error, with the exception being that titanite from systems with a porphyry score of 3 does not appear to crystallise to low temperatures (Fig. 8.6B). It is worth noting, however, that this may reflect a high proportion of volcanic titanite.

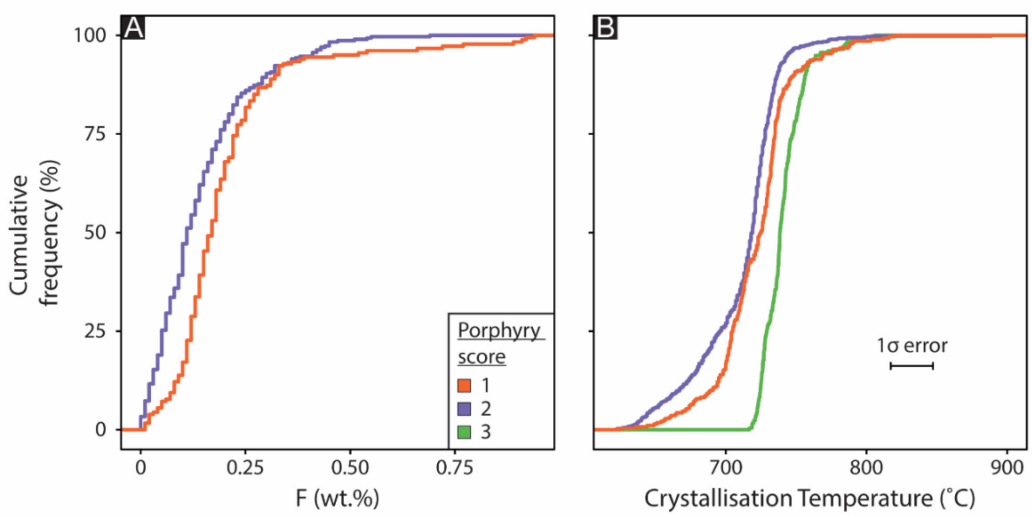


Figure 8.6. Cumulative frequency plots comparing compositions of titanite with different porphyry scores. **A.** F. **B.** Crystallisation temperature (Hayden *et al.*, 2008).

One potential approach to assess trace element characteristics of porphyry titanite was proposed in Chapter 6, which involved back-calculating hypothetical titanite compositions that

would be in equilibrium with porphyry zircons. This method circumvents the problem of a scarcity of porphyry titanite data and instead takes advantage of the wealth of zircon indicator mineral studies. In Chapter 6, it appeared that this approach may have merits, with titanite from the giant Cobre Panama porphyry Cu district identified as being porphyry-associated on this basis. As in Chapter 6, values which divide porphyry and non-porphyry titanite are derived from Pizarro *et al.* (2020) and are related to titanite through partition coefficients (Colombini *et al.*, 2011). All igneous titanite data are displayed in Figure 8.7. According to the Th/U and Dy/Yb classification, all titanite with a porphyry score of 1 (i.e. from a porphyry system) was classified as such (Fig. 8.7A). However, 99% of titanite from rocks with a porphyry score of 2 was also classified as being from a porphyry system and even ~93% of titanite with a porphyry score of 3 (i.e. completely unrelated to mineralisation) was classified as porphyry-like (Fig. 8.7A). Hence, this plot is not useful in identifying porphyry associated titanite. Focussing instead on Figure 8.7B, it is clear that Eu/Eu* is a better discriminant of porphyry associated titanite than other trace element ratios. For instance, 92.1% of titanite with a porphyry score of 1 is classified as porphyry, whereas only 63.9% of titanite from rocks unrelated to mineralisation (porphyry score = 3) is classified as porphyry. Based on this, it may be inferred that utilising a cut-off value of 0.4 may be a useful starting point in filtering out titanite compositions that are completely unrelated to mineralisation.

Within-group comparisons may also be informative, allowing for the identification of any anomalous samples or locations. Key localities are highlighted for the same plot (Fig. 8.8). As identified in Chapter 5, it appears that Th/U ratios may delineate distinct titanite populations both within a single magmatic system and between different magmatic systems, as evidenced by general clustering of data, but also by the presence of multiple Th/U populations – both at Chuquicamata and also at Alumbrera in coeval volcanics (porphyry score = 2). It is also evident that a significant proportion of analyses that are classified as porphyry in the porphyry-related group are from Strontian, with Eu anomalies that are in fact significantly higher than those observed for porphyry titanite. The impact of *in-situ* titanite crystallisation on residual melt chemistry was discussed in Chapter 4; with the absence of extreme Eu/Eu* values in porphyry titanite suggesting that its own impact on residual melt chemistry is being buffered in porphyry systems. This may either relate to *in-situ* crystallisation of abundant plagioclase, which is almost ubiquitously present as a phenocryst phase in porphyry magmas (Seedorff *et al.*, 2005), or oxidation state. Porphyry magmas are generally perceived to be relatively oxidised, which as identified in Chapter 4, means that most Eu would be present in the 3+ oxidation state and hence it would be difficult to fractionate Eu from neighbouring REEs. Overall, it is concluded that conventional methods are unable to unequivocally identify an association with porphyry magmas, suggesting that more sophisticated techniques are required.

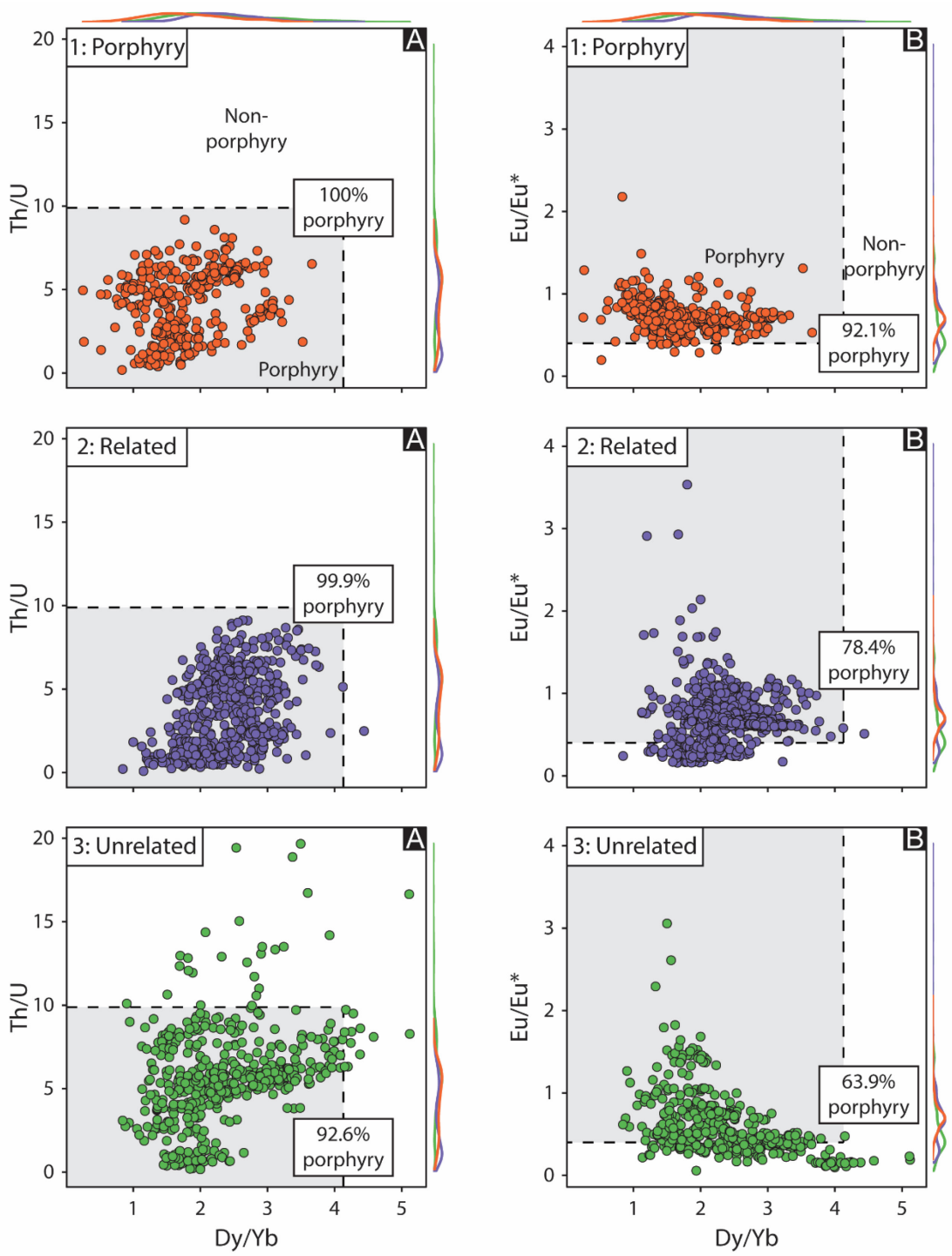


Figure 8.7. Bivariate plots showing various potentially important indicators of magmatic fertility, colour coded by porphyry score. Fields of porphyry magmas are inverted from zircon compositions proposed by Pizarro *et al.* (2020). Partition coefficients are derived from Colombini *et al.* (2011). Average 2σ errors are smaller than symbol size.

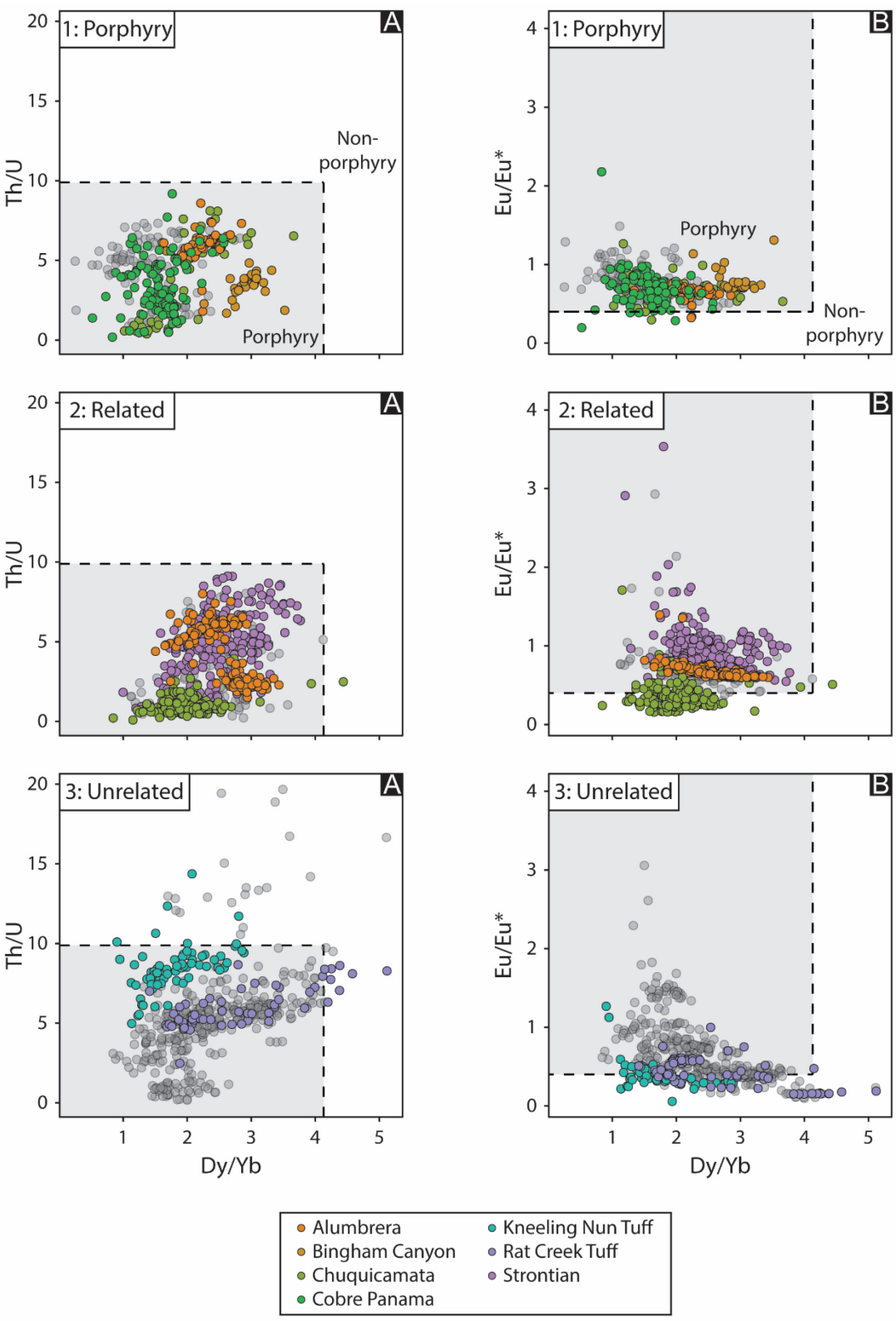


Figure 8.8. Bivariate plots showing various potentially important indicators of magmatic fertility, colour coded by location. Grey points represent data from literature sources and the Rio Tinto global sample suite. Information is the same as Figure 8.7. Average 2σ errors are smaller than symbol size.

8.5 Classification of titanite using unsupervised and supervised learning techniques

8.5.1 Background

Statistical learning involves the use of a variety of techniques to learn from, understand and model large, complex datasets. Statistical learning tools are classified as supervised or unsupervised, differentiated on whether the input data were given a class label or not. For supervised learning techniques, input (training) data with class labels (e.g. mineralised or unmineralized) are used to develop models that can predict class labels for unseen (test) data. Unsupervised techniques, however, are not trained using class labels, and instead describe variance, trends and patterns within the dataset (Hastie *et al.*, 2009; James *et al.*, 2013). Statistical learning techniques are now being increasingly applied in the field of mineral deposit research (Rodriguez-Galiano *et al.*, 2015; Grunsky & Caritat, 2020; Nathwani *et al.*, 2022), using geochemical, geophysical and image data.

Although three 'porphyry scores' were used to explore compositional differences between porphyry and non-porphyry titanite by conventional methods, a binary approach (i.e. non-porphyry represents scores of 2 and 3) is favoured here because it allows unsupervised and supervised learning techniques to be easily applied. For the two models, slightly different variables and datasets were used; these are discussed below.

8.5.2 Unsupervised learning (PCA and K-means clustering)

Cluster analysis is a popular unsupervised learning technique that is used to group data into particular subsets or clusters. One of the most common approaches to clustering is the K-means, which separates the data into a pre-specified (K) number of clusters around the nearest mean (Hastie *et al.*, 2009; James *et al.*, 2013). Figure 8.9 illustrates the impact of varying K. This technique is well suited to the present study, which aims to identity whether compositions of igneous and non-igneous, as well as porphyry and non-porphyry titanite are distinct.

For datasets containing many variables, a dimensionality reduction technique can be advantageous prior to cluster analysis. In Chapter 6, compositional differences between igneous, replacement and vein-hosted titanite were highlighted effectively by PCA. Hence, the approach taken here was to undertake K-means clustering on important principal components for the two models in question. Furthermore, as in Chapter 6, variables were transformed according to the centre-log-ratio transformation prior to PCA, in order to overcome the problems of closure and log-normal distributions in compositional data (Aitchison, 1982). All censored data was removed prior to PCA.

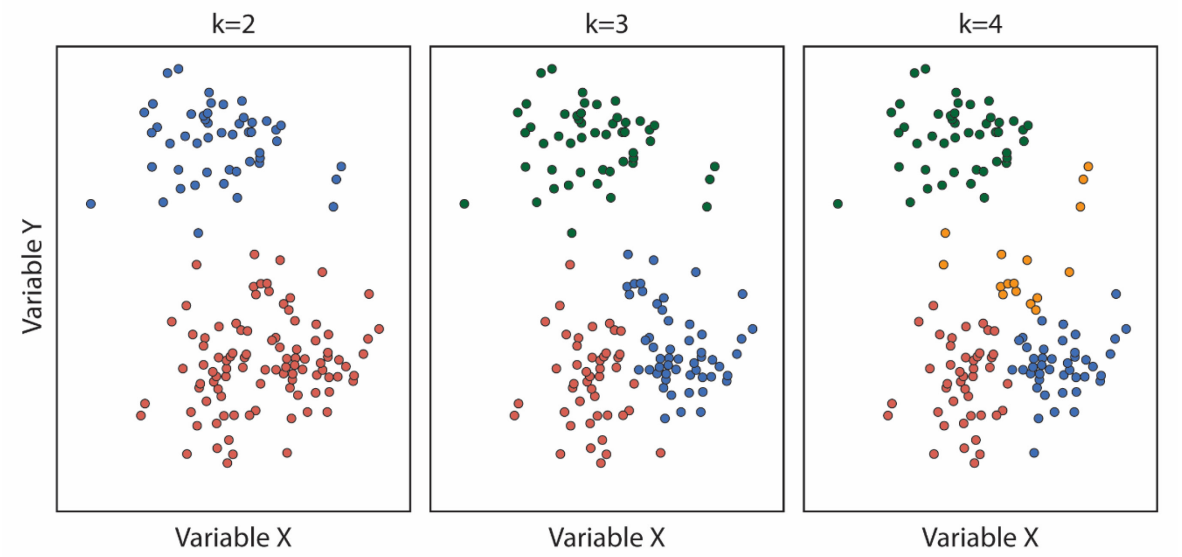


Figure 8.9. Impact of varying K on K-means clustering outputs. Adapted from James *et al.* (2013).

8.5.3 Supervised learning (Random Forest)

Compared to unsupervised learning, supervised learning techniques are more applicable to mineral exploration as they can use a training dataset containing multiple variables from mineralised and unmineralised settings to predict whether an unseen (test) dataset is likely to be related to mineralisation. A variety of techniques could be applied to this problem, including logistic regression, random forest, support vector machines and artificial neural networks. Of these techniques, random forest (Breiman, 2001) was chosen as it is non-parametric (i.e. does not require pre-analysis data transformation) and works well 'off-the-shelf', meaning that algorithms can be applied easily without significant tuning. Previous studies have demonstrated that random forest is a powerful predictive tool that can be applied to geochemical data generally (Harris & Grunsky, 2015; Kirkwood *et al.*, 2016), yielding meaningful results when applied to porphyry exploration specifically (Carranza & Laborte, 2015; Nathwani *et al.*, 2022).

The random forest algorithm is a decision tree-based approach that aggregates multiple decision trees in an ensemble, with each decision tree comprising multiple decision nodes that ultimately lead to a classification (Fig. 8.10). Each decision tree is independently trained on a random subset of the training dataset (a bootstrap) and only uses some variables within the bootstrapped dataset, meaning that random forest is less sensitive to the training data and more able to generalise. Ultimately, an observation is classified by each decision tree, with the overall classification based on the majority vote or an average of all the individual tree results (Fig. 8.10; Hastie *et al.*, 2009). One consideration for supervised learning techniques is whether classes contain varying numbers of observations. Though class imbalance is commonly encountered for a range of

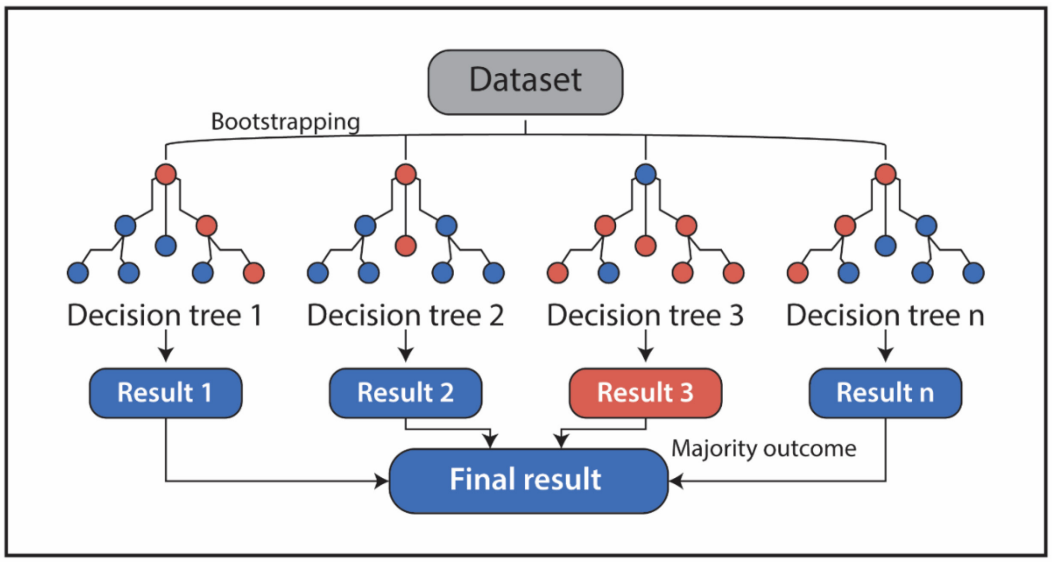


Figure 8.10. Illustration explaining how random forest works.

data types, it can result in a classifier tending to favour the majority class, reducing the performance (Japkowicz & Stephen, 2002). For the Model 1 dataset, approximately 60% of analyses were igneous and 40% non-igneous. Although this is a relatively minor class imbalance, oversampling of the minority class and undersampling of the majority class was conducted using the R function 'ovun.sample' (Lunardon *et al.*, 2014) for good practice to ensure that classes were perfectly balanced. The class imbalance is more problematic for Model 2, given that there are double the number of observations for non-porphyry compared to porphyry titanite. Consequently, simultaneous oversampling and undersampling of the dataset were again conducted prior to training using random forest. Data which were utilised in the training and test datasets for both models are outlined in Table 8.4.

Table 8.4. Datasets that were included in the training and test datasets for Models 1 and 2.

Location	Model 1: Training	Model 1: Test	Model 2: Training	Model 2: Test
Strontian	Y		Y	
Chuquicamata	Y		Y	
Cobre Panama	Y		Y	
Oyu Tolgoi	Y			
Escondida Norte-Zaldivar		Y		
Gravestones		Y		
Yauricocha		Y	Y	
Little Cottonwood Stock	Y		Y	
Alta Stock		Y		Y
Clayton Peak Stock	Y		Y	
Valeo Stock		Y		
Tsagaan Suvarga		Y	Y	
Santa Clara		Y		
Kneeling Nun				Y
Rat Creek			Y	
Nelson Mountain			Y	
Alumbrera				Y
Bingham Canyon			Y	

Cross validation of the training datasets were performed to train the model and assess performance before testing on unseen datasets. The approach taken here involved splitting the datasets into ten subsets (folds), with nine folds used for training and one-fold held back for testing. This was repeated ten times such that each fold appears once as a test dataset, with an average taken at the end to assess model performance. Cross validation was conducted using the 'train' function in R (Kuhn, 2008). Ultimately, model performance is tested using the test dataset, which contains data from locations and deposits that are not included within the training dataset. This is important, as the inclusion of data from the same deposit in both training and test datasets can lead to overfitting.

A variety of metrics are used to assess model performance, which take into account the number of true positives (TP), false positives (FP), true negatives (TN) and false negatives (FN). Such metrics include: true positive rate (TPR; Eqn. 8.1), false positive rate (FPR; Eqn. 8.2), precision (Eqn. 8.3) and F1 (Eqn. 8.4).

$$TPR = \frac{TP}{TP + FN} \qquad \textbf{(Eq. 8. 1)}$$

$$FPR = \frac{FP}{FP + TN} \qquad \textbf{(Eq. 8. 2)}$$

$$Precision = \frac{TP}{TP + FP} \qquad \textbf{(Eq. 8. 3)}$$

$$F1 = 2 \times \left(\frac{Precision \times TPR}{Precision + TPR}\right) \qquad \textbf{(Eq. 8. 4)}$$

Another means to assess model performance is the receiver operating characteristic (ROC) curve. As well as assigning a class label, the model will estimate a probability that an observation belongs to a particular class. For example, if the probability is greater than 0.5, then an observation will be assigned the positive class (e.g., in Model 1, non-igneous). Higher probabilities represent observations that have been more confidently assigned to the positive class. ROC curves represent a plot of the TPR against the FPR and, from these, another performance metric known as area under the curve (AUC) can be calculated. For a model that has no success in classifying observations (essentially random), the AUC will be 0.5, whereas a model that perfectly classifies observations will have an AUC of 1. Training and testing of the random forest algorithm were conducted using the 'randomForest' and 'predict' functions in R, respectively (Liaw & Wiener, 2002; Kuhn, 2008). In addition to classification, valuable information can be extracted from the random forest, including the relative importance of different variables in determining the classification. In this study, the mean decrease in node impurity (Gini Index) was utilised (Liaw & Wiener, 2002), which

measures how well each variable splits the dataset, with high values corresponding to variables of greater importance.

Two separate models were created to tackle the problem of classifying porphyry and non-porphyry titanite, the first of which employed the same element list used in the unsupervised learning technique (Model 2a). In order to compare performance, another model was created which parameterised REEs as lambda values (λ_0, λ_1, λ_2 etc.; O'Neill, 2016) and Eu as Eu/Eu* instead of including all REEs individually; elements that were identified to be unimportant based on clustering were also removed (Model 2b).

8.6 Results of Model 1 (Igneous vs non-igneous) – unsupervised learning

The importance of fluorine and aluminium in differentiating igneous from non-igneous titanite was highlighted earlier in the Chapter (as Fe/Al; Fig. 8.5A). As fluorine contents are determined by electron microprobe only (and not laser-ablation ICP-MS), datasets which did not include electron microprobe and laser ablation analyses on the same spots were excluded. This, coupled with an absence of textural data for literature and ex-situ grain mount data, meant that only analyses conducted in the present study could be utilised. Elements used in the statistical learning techniques for Model 1 were as follows: Sc, V, Mn, Sr, Y, Zr, La, Ce, Pr, Nd, Sm, Eu, Gd, Tb, Dy, Ho, Er, Tm, Yb, Lu, Th, U, F and Al.

Results of the PCA (see Appendix 12) are displayed as PCA biplots (Fig. 8.11A). For Model 1, principal components 1 and 2 capture most of the variance within the dataset, representing ~45% and 33% respectively, with later PCs all capturing <10% of the variance. Chiefly, PC1 is controlled by positive loadings for the HREEs, and negative loadings for the LREEs, Th and U. PC2 is controlled by positive loadings for MREEs, and negative loadings for V, Al, Sc, F (Fig. 8.11A). Igneous titanite compositions group at low PC1 and high PC2 values, indicating enrichment in LREEs and MREEs, Th and U, whereas non-igneous compositions scatter quite widely but tend to display elevated HREE and/or F, Al, Sc and V contents (Fig. 8.11A).

Cluster analysis was carried out in R using the 'fviz_cluster' function (Kassambara & Mundt, 2017), with K initially defined as two on the assumption that compositions are likely to predominantly reflect non-igneous and igneous origins. It is important to note that although the axes have been rotated, the datapoints are located in the same position in the PCA biplot and the cluster plots (Fig. 8.11).

The cluster analysis is fairly successful in splitting the data into igneous and non-igneous types, with cluster 1 primarily representing non-igneous and cluster 2 representing primarily igneous titanite types respectively (Fig. 8.11B). Based on this observation, the accuracy of the cluster analysis in grouping titanite into igneous and non-igneous types can be assessed (Table 8.5).

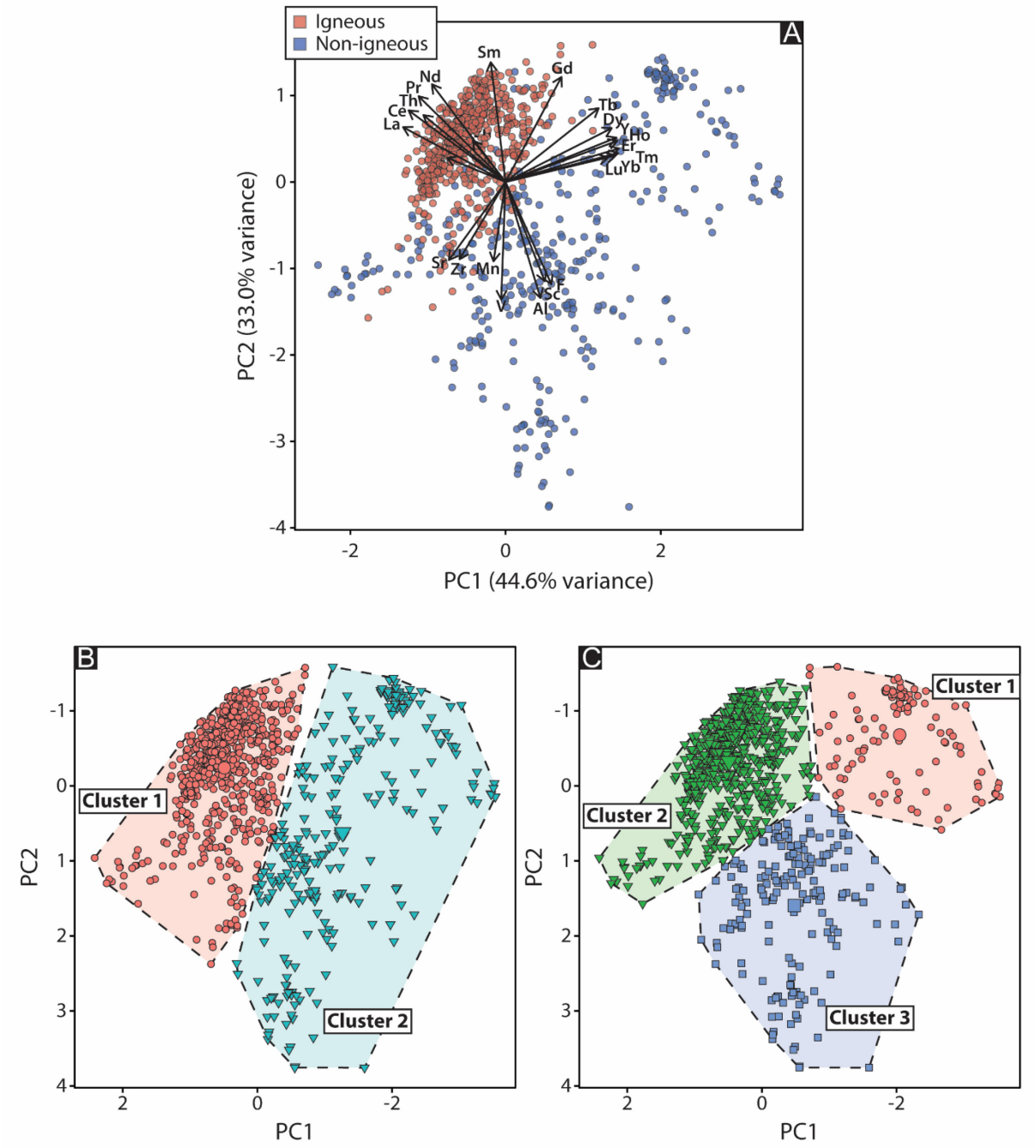


Figure 8.11. Results of PCA and cluster analysis for Model 1. **A.** PCA biplot. **B.** Cluster analysis where k=2. **C.** Cluster analysis where k=3.

Although K was initially defined as two, given the textural classification of titanite into igneous and non-igneous groups, it is possible to objectively determine the optimal number of clusters independent of the sample labels by calculating the total within-sum of squares (Hastie *et*

al., 2009), with a break in slope indicating the ideal number of clusters. Total within-sum of squares was determined using the 'fviz_nbclust' function in R (Kassambara & Mundt, 2017). Based on this, the optimal number of clusters in the dataset for Model 1 was found to be three. For K=3 (Fig. 8.11C), a high accuracy is still retained in identifying igneous titanite (Table 8.5) and the number

Table 8.5. Correlation matrix showing cluster analysis performance for Model 1, compared to textural classification.

Type	K	Igneous	Non-igneous
Cluster 1	2	0.5%	70.0%
Cluster 2	2	99.5%	30.0%
Cluster 1	3	0.9%	29.0%
Cluster 2	3	0.5%	47.9%
Cluster 3	3	98.6%	23.1%

of misclassified non-igneous titanites is also reduced (~23%; assuming cluster 3 = igneous). Interestingly, this also highlights compositional variability within non-igneous titanite, potentially indicating two main geochemical signatures: one which is characterised by high HREE contents, and another that is characterised by high F, Al , Sc and V contents (Fig. 8.11C). These two non-igneous populations are not texturally distinct, nor do they exhibit unique mineral associations.

Of the 965 analyses included, it can be concluded that this unsupervised learning technique performed reasonably well at identifying non-igneous titanite, accurately identifying 70% of analyses classified as non-igneous on textural grounds (cluster 1). However, the imperfect separation implies that there is compositional overlap between igneous and non-igneous titanite, possibly reflecting the partial or progressive alteration of primary igneous titanite. Nevertheless, the technique was extremely adept at identifying unaltered magmatic titanite, correctly identifying 99.5% (cluster 2). Consequently, it can be concluded that titanite origin, from either silicate melt or hydrothermal fluids, is the most important source of variance in the dataset.

8.7 Results of Model 1 (Igneous vs non-igneous) – Supervised learning

Training and testing of the random forest algorithm was conducted using the 'randomForest' and 'predict' functions in R, respectively (Liaw & Wiener, 2002; Kuhn, 2008). The random forest algorithm performed extremely well in identifying whether titanite is likely to be igneous or non-igneous (Table 8.6). Indeed, an AUC of nearly 0.99 means that the algorithm nearly always correctly classified titanite in the test dataset as igneous or non-igneous (Fig. 8.12). The effectiveness of the algorithm in correctly classifying titanite should not be a surprise, given that

Table 8.6. Results of random forest predictions of test dataset for Models 1, 2a and 2b.

Model	Accuracy	F1	Precision	TPR	FPR	AUC
1	0.94	0.93	0.88	0.99	0.10	0.99
2a	0.87	0.81	0.89	0.74	0.05	0.87
2b	0.85	0.80	0.81	0.79	0.11	0.92

conventional and unsupervised learning techniques were also generally effective at predicting whether titanite had an igneous or non-igneous origin, but the marked improvement in accuracy is noteworthy.

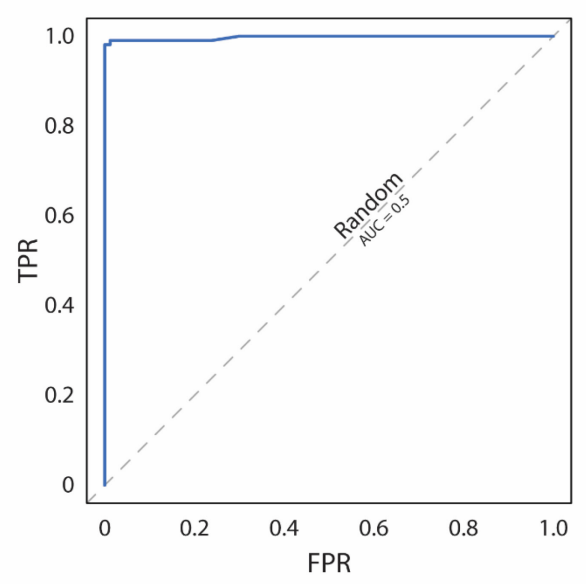


Figure 8.12. ROC curve for Model 1.

The most important variables, as determined by the Gini Index, are LREEs and Th, with lesser contributions from Sc, V, Al and F (Table 8.7). This observation is supported by outcomes from the unsupervised learning techniques, which showed that although Sc, V, Al and F contents may be elevated in non-igneous titanite, differences in LREEs and Th were likely to provide the most powerful discriminants.

Table 8.7. Gini indices for Model 1.

Element	Gini	Element	Gini	Element	Gini
Sc	22.20	Pr	34.97	Er	1.37
V	4.70	Nd	16.92	Tm	1.32
Mn	12.24	Sm	5.88	Yb	1.28
Sr	1.81	Eu	4.47	Lu	1.02
Y	1.28	Gd	1.76	Th	64.01
Zr	6.25	Tb	1.51	U	6.91
La	72.21	Dy	1.45	Al	33.35
Ce	57.45	Ho	1.42	F	15.63

8.8 Results of Model 2 (Porphyry vs non-porphyry) – unsupervised learning

Prior to PCA and K-means clustering, all analyses classified as non-igneous on textural grounds were removed from the dataset to isolate magmatic processes which might be responsible for differences in titanite composition. From Figure 8.6A and also Chapter 6, it is inferred that fluorine and aluminium are unlikely to be important discriminators, given that these elements do not vary significantly within igneous titanite (S.D = 0.14 and 0.11, respectively). Additionally, removal of these variables allows for LA-ICP-MS alone to be considered, meaning that literature data can be incorporated. However, an important drawback of incorporating literature data is that the number of analytes may be limited relative to those determined in the present study, necessitating striking a balance between the volume of data and the number of variables included. Elements included within the PCA and cluster analysis are as follows: Sc, V, Mn, Sr, Y, Zr, Nb, La, Ce, Pr, Nd, Sm, Eu, Gd, Tb, Dy, Ho, Er, Tm, Yb, Lu, Hf, Ta, Th and U. As with Model 1, element concentrations were transformed by clr prior to PCA and cluster analysis.

From the principal component analysis, PC1 represented ~50% of variance, and PC2 ~17%, with subsequent components capturing less than 10% of the variance of the dataset. PC1 is dominantly controlled by positive loadings for the HREEs, and negative loadings for the LREEs, as well as HFSEs and Sr (Fig. 8.13A). Importantly, PC2 is controlled by positive loadings for Mn, and to a lesser extent Sc, as well as negative loadings for the middle REEs (Fig. 8.13A). As with Model 1, K was initially defined as 2 for cluster analysis based on the two known groups, porphyry and non-porphyry. In terms of identifying porphyry and non-porphyry titanite, it is clear that clustering using dimensionally-reduced PCA data is unable to conclusively separate the two groups (Fig. 8.13A). In fact, approximately equal proportions of porphyry and non-porphyry titanite are classified in each cluster (Table 8.8). Again, as with Model 1, the optimal number of clusters is

Table 8.8. Correlation matrix showing cluster analysis performance for Model 2.

Type	K	Porphyry	Non-porphyry
Cluster 1	2	64.0%	52.4%
Cluster 2	2	36%	47.6%
Cluster 1	3	18.6%	45.6%
Cluster 2	3	57.4%	51.0%
Cluster 3	3	24%	3.4%

determined to be 3, based on the total within-sum of squares. After defining K as 3, cluster 3 is found to mostly contain porphyry titanite and cluster 1 mostly non-porphyry titanite. Cluster 2 contains a roughly equal proportion of both groups (Fig. 8.13C; Table 8.8). From this, it can be

inferred that unsupervised learning techniques are unable to discriminate porphyry-associated titanite compositions with high accuracy, suggesting that there is significant compositional overlap.

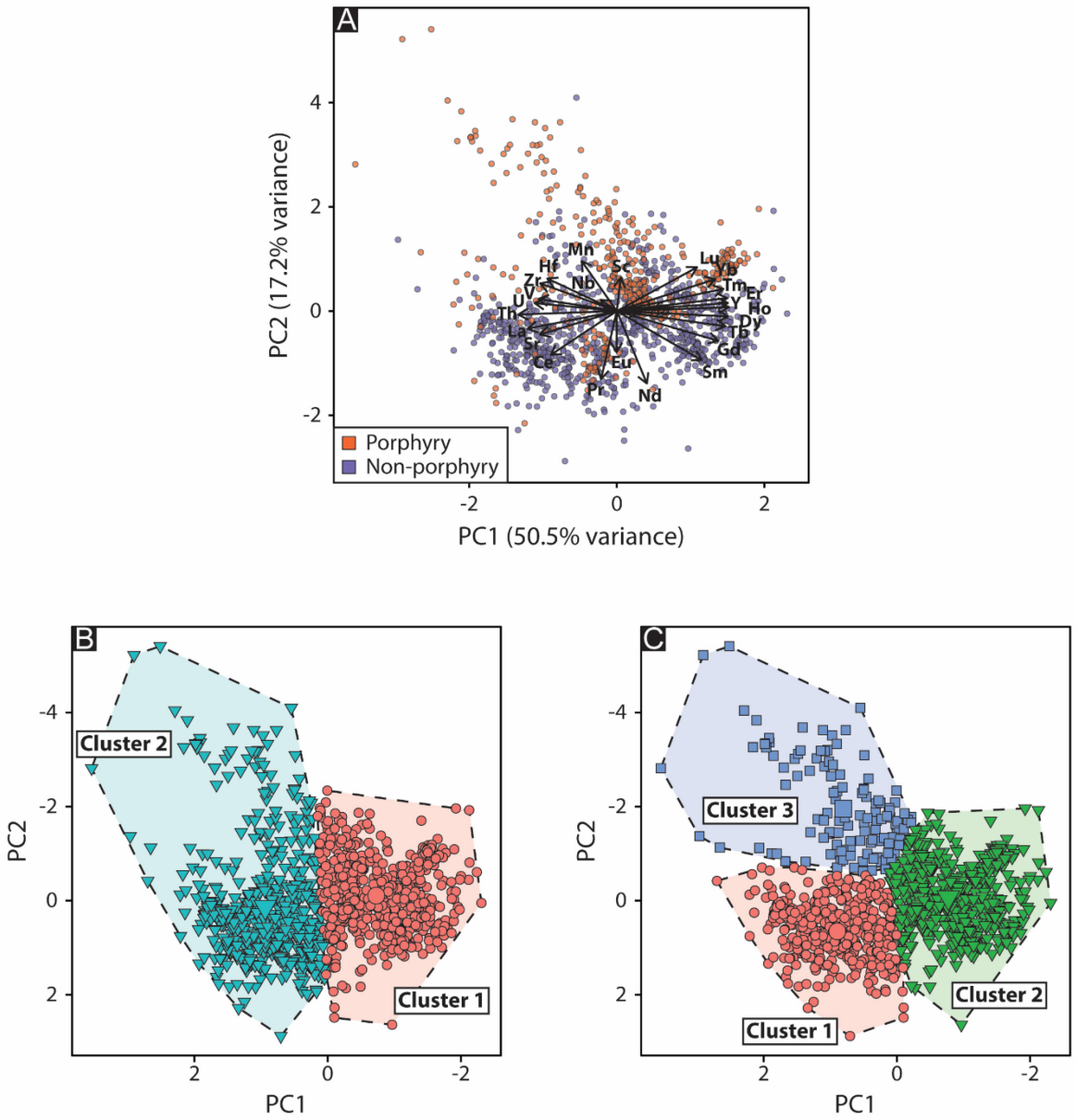


Figure 8.13. Results of PCA and cluster analysis for Model 2. **A.** PCA biplot. **B.** Cluster analysis where k=2. **C.** Cluster analysis where k=3.

8.9 Results of Model 2 (Porphyry vs non-porphyry) – supervised learning

Cross validation of both Model 2a and 2b returned accuracy scores of 0.96. Testing of the two random forest models on an unseen test dataset demonstrates that both were generally able to identify porphyry titanite (Table 8.6). However, Model 2b generally performs slightly better than

Model 2a (Table 8.6; Fig. 8.14), with AUC values of 0.92 and 0.87 respectively. The Gini Indices for Models 2a and 2b indicate that Mn, Sr, and REEs, particularly the lambda values and Eu/Eu* for Model 2b, were important in discriminating porphyry from non-porphyry titanite (Table 8.9).

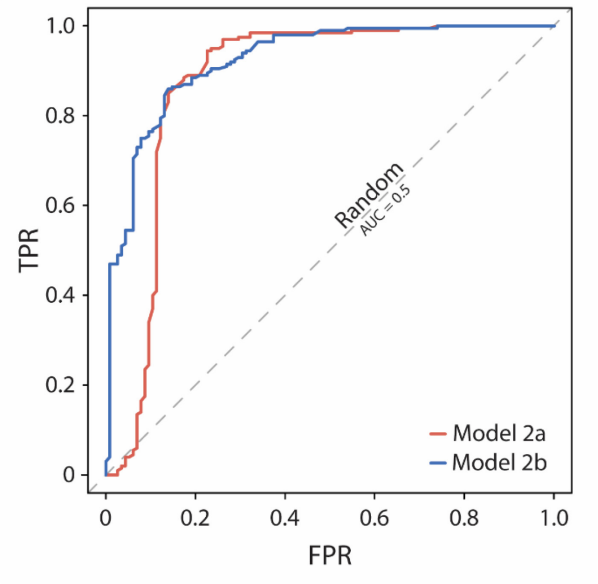


Figure 8.14. ROC curve for Models 2a and 2b.

Both models are a considerable improvement on those based on unsupervised learning techniques, which were misclassifying a much larger proportion of titanite. Model outcomes could be improved by utilising a larger dataset with more training data, which would reduce the likelihood of overfitting and allow the model to generalise more effectively. Additionally, this study only focussed on applying a single machine learning technique, random forest, whilst there are several additional techniques which may have yielded more accurate results.

Table 8.9. Gini index for Models 2a and 2b.

Model 2a					
Variable	Gini	Variable	Gini	Variable	Gini
Sc	18.17	Pr	33.40	Tm	8.55
V	10.98	Nd	26.06	Yb	9.83
Mn	52.91	Sm	22.76	Lu	10.03
Sr	37.83	Eu	12.24	Hf	19.87
Y	10.92	Gd	12.70	Ta	8.80
Zr	16.19	Tb	10.18	Th	8.05
Nb	9.92	Dy	9.62	U	9.39
La	12.46	Ho	7.78		
Ce	13.52	Er	7.29		
Model 2b					
Variable	Gini	Variable	Gini	Variable	Gini
Sc	29.07	Y	29.12	λ_1	42.00
V	25.37	Th	17.29	λ_2	35.15
Mn	63.77	U	19.27	Eu/Eu*	51.90
Sr	47.61	λ_0	36.43		

8.10 Use of titanite in exploration

8.10.1 Titanite occurrence in porphyry systems

Although a common igneous accessory mineral, the particular association of titanite with porphyry systems worldwide, whether in coeval volcanics, the precursor batholith or in the porphyritic intrusions themselves, suggests that titanite may to some extent indicate that a magma is of suitable composition to form a porphyry deposit. In Chapters 5 and 6, the occurrence of fluid inclusion trails in titanite from the Chuquicamata and Cobre Panama porphyry deposits was interpreted to represent the passage of hydrothermal fluids. Hence, the presence of magmas of a suitable composition, which have produced hydrothermal fluids can be inferred using textures of detrital titanite. However unlike zircon, a commonly used porphyry indicator mineral (Pizarro *et al.*, 2020), primary titanite is susceptible to hydrothermal alteration and may be completely destroyed in rocks that have been strongly altered by potassic or acidic fluids. In some cases, the presence of precursor titanite may be inferred if titanite has been pseudomorphically replaced (see Chapters 5 and 6), though important geochemical signatures will be lost.

In the hydrothermal portion of the porphyry system, the occurrence of propylitic titanite has been noted by several authors (Seedorff *et al.*, 2005; Wilkinson *et al.*, 2015; Hart-Madigan *et al.*, 2020; Xiao *et al.*, 2021) and this is confirmed by this study which found widespread titanite in such rocks at Cobre Panama and Oyu Tolgoi. Additionally, titanite is noted to occur in rocks that have been subjected to sodic-calcic alteration (Carten, 1986), as well as in potassically (Celis, 2015) and sericitically altered rocks (see Chapter 7). However, the utility of titanite in targeting these alteration zones remains to be seen, given that sodic-calcic alteration is generally poorly preserved (Sillitoe, 2010) and that, despite the volume of publications on porphyry alteration zones, few have highlighted the occurrence of potassic and sericitic titanite.

8.10.2 Effects of hydrothermal alteration

Another key consideration is understanding how robust geochemical signatures are to hydrothermal alteration. As observed in Chapters 5 and 6, titanite is susceptible to hydrothermal alteration and may be partially or completely destroyed. Where titanite has been completely destroyed, certain geochemical characteristics may be retained by secondary rutile, although this requires investigation. One important thing to note is that Eu/Eu* may be impacted by hydrothermal alteration. In Chapter 5, it was demonstrated that altered igneous titanite displayed anomalously high Eu/Eu*, necessitating the filtering out of non-igneous titanite data prior to undertaking assessments of exploration potential. As demonstrated during this chapter, non-igneous titanite,

which includes altered igneous crystals, is easily distinguished from unaltered magmatic titanite by both unsupervised and supervised learning techniques using F, Al, Sc, and LREE concentrations.

8.10.3 Comparison of titanite with other mineral indicators

Utilisation of a variety of minerals has been postulated for porphyry exploration, including zircon, apatite, chlorite and epidote; so in what circumstances might the analysis of titanite be advantageous?

Chlorite and epidote

Spatial variation in chlorite and epidote compositions in the green rock environment may be utilised to infer i) the presence of a nearby porphyry system, ii) the potential endowment of that system and potentially even iii) vector towards the core of the system (Wilkinson *et al.*, 2015; Cooke *et al.*, 2020b; Pacey *et al.*, 2020b). However, geochemical signatures become obscured when there have been multiple pulses of hydrothermal activity, as genuine porphyry-related geochemical signatures are overprinted by signatures which are completely unrelated to mineralisation. Hart-Madigan *et al.* (2020) highlighted that titanite can be used to date alteration events in the propylitic environment, whereas epidote and chlorite only incorporate minor amounts of initial U. Through combining U-Pb dating of propylitic titanite with chlorite and epidote compositional data, signatures which are only related to the mineralising event can be isolated, meaning that the mineralising potential of the hydrothermal system can be accurately assessed.

Furthermore, in this study it has been demonstrated that U-Pb isotopes and chemical compositions of propylitic titanite can be simultaneously determined without compromising the quality of the geochronological data. Although requiring further study, the ability to obtain U-Pb dates, when coupled with geochemical diversity, means there is the potential to utilise titanite alone as an indicator mineral in the green rock environment. However, care should be exercised when working in districts that have experienced multiple pulses of hydrothermal activity, as reactivity of titanite may cause the isotopic system to be disturbed, or where multiple titanite generations may exist.

Zircon

When it comes to understanding the magmatic part of the porphyry system, whether via U-Pb geochronology (Chelle-Michou *et al.*, 2014; Buret *et al.*, 2016), thermobarometry (Large *et al.*, 2021) or mineralising potential (Pizarro *et al.*, 2020; Nathwani *et al.*, 2021), zircon remains the gold standard. Key to the utility of zircon in understanding porphyry magmatic systems is its resistance to hydrothermal alteration, with magmatic signatures retained even in intensely acid altered samples. Titanite is clearly not completely resistant to hydrothermal alteration, as evidenced

by the occurrence of pseudomorphs in rocks that have been subjected to potassic, acid and even propylitic alteration at Chuquicamata and Cobre Panama (see Chapters 5 and 6). However, it has been demonstrated during the present study that magmatic titanite still retains an igneous signature when subjected to weak to moderate alteration. Importantly, titanite incorporates several petrogenetically important species that are not incorporated into zircon. Halogen contents, for example, could provide important information about critical ore forming processes such as fluid exsolution, as has been demonstrated for apatite (Nathwani *et al.*, 2023); whilst LILE e.g. Sr, can be a useful discriminant between porphyry and non-porphyry magmas. Hence, in rocks that haven't been subjected to intense hydrothermal alteration, titanite can constrain some aspects of the magmatic system that zircon cannot. Alternatively, zircon may be absent in more mafic porphyry intrusions where titanite may be present. For these rocks, analysis of titanite can be utilised for U-Pb geochronology, thermobarometry and mineral prospectivity studies.

Apatite

Of the minerals which can potentially be used as indicators of porphyry mineralisation, only apatite (Loader, 2017; Brugge, 2021) and titanite are commonly observed in both magmatic and hydrothermal domains. The occurrence of apatite throughout the porphyry system is more widespread, however the analysis of titanite over apatite may be advantageous for several reasons. As has been demonstrated in this chapter, titanite compositions can be readily utilised to determine a hydrothermal or magmatic origin. This ability to differentiate igneous and non-igneous compositions, when combined with U-Pb geochronology (Frost *et al.*, 2001) means that timings of both magmatic and hydrothermal events can be constrained, and compared to known mineralising events in the prospective district. Additionally, preliminary work has indicated that igneous, porphyry titanite compositions can be identified using machine learning techniques. When taking into account these characteristics, it appears that analysis of titanite over apatite would be preferable in detrital studies, potentially providing geochronological, mineral prospectivity and even thermobarometric information (Hayden *et al.*, 2008).

8.10.4 Exploration workflow

A recommended workflow that could be applied to utilise titanite compositions in the exploration for new deposits is presented in Figure 8.15. Initial steps of the workflow are dependent on whether sampling of stream sediments or whole-rocks has been conducted, which, in Chapter 5, was identified to potentially influence whether igneous or non-igneous titanite is sampled. Sampling of rocks, which are assumed to be igneous, is recommended to allow for whole-rock compositions to be determined. Use of whole-rock chemistry is beneficial as it is relatively easy, cheap and may

save time in filtering out any igneous rocks that are distinctly unrelated to mineralisation. However, analysis of titanite in stream sediments may be of more use practically, where the chemical context of the host rock has been lost.

If whole-rock analysis is possible, then the first step is to screen out rocks that are unsuitable for the assessment of magma fertility (i.e. rocks that are too mafic or too altered). Thereafter, commonly employed whole-rock ratios are applied to remove rocks that are highly unlikely to be related to mineralisation. If rocks display a geochemical characteristic of a fertile magma (e.g. high Sr/Y) then titanite can be attempted to be located. Titanite can be analysed *in-situ*, after preparing thin sections or polished blocks, or following mineral separation. At least 30 analytical sites are recommended per sample in order to characterise titanite trace element chemistry and to carry out U-Pb geochronology. A suitable number of sites may be present *in-situ* or may require mineral separation. If no titanite is identified either *in-situ* or during mineral separation, then the application of other mineral indicators is recommended; either zircon (which is well characterised) or potentially rutile, which may inherit titanite geochemical signatures (see Chapter 5).

Assuming that a suitable number of titanite analyses are possible, then the next step is to conduct trace (± major) element and U-Pb analysis. Titanite compositions are first filtered based on whether they are igneous or non-igneous, which involves utilising F, V, or LREE concentrations, or Fe/Al and Th/Sc ratios. Elevated F contents, or low Th/Sc ratios for example, indicate that titanite is non-igneous in origin. For igneous titanite, it is recommended that a supervised learning technique, such as the random forest algorithm that is applied here, are utilised to assess the likelihood of derivation from a porphyry system. The utility of such an approach has been demonstrated in this study using a relatively small dataset, with improved performance likely arising from the development of a larger dataset incorporating a wider range of environments.

The final stages of the assessment involve conducting textural observations, with the presence of fluid inclusion trails likely to indicate that separation of a magmatic volatile phase has occurred. Finally, U-Pb geochronologic data should be processed, which can be conducted for both igneous and non-igneous titanite, in addition to porphyry and non-porphyry titanite. A combination of both titanite classification, and U-Pb data is proposed, with a final decision based on whether U-Pb ages compared to known periods of mineralisation for a given district (for both igneous and non-igneous titanite), in addition to predictions based on supervised learning techniques.

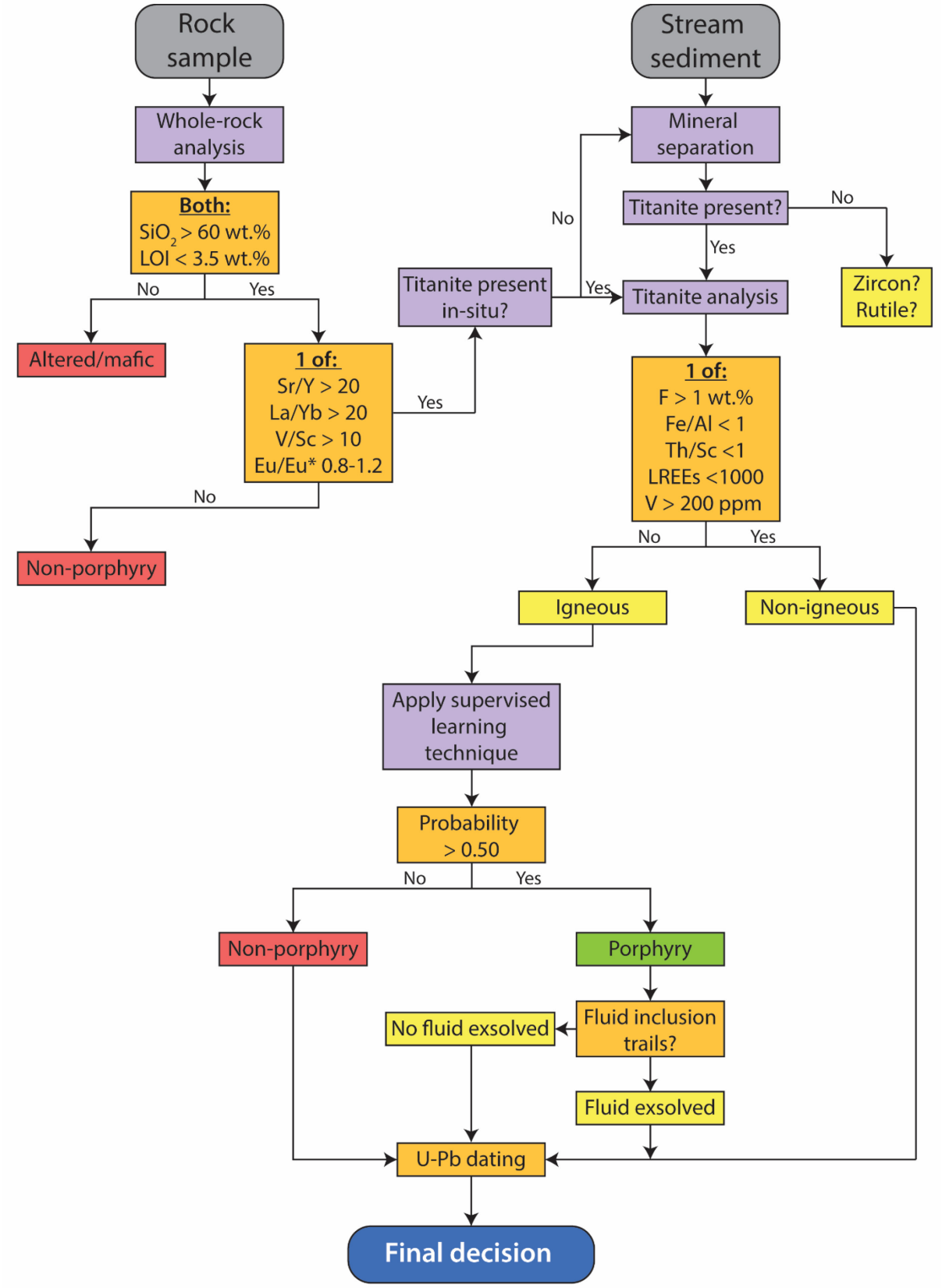


Figure 8.15. Recommended exploration workflow.

8.11 Conclusions

Through applying unsupervised and supervised machine learning techniques, it has been demonstrated that titanite compositions can be applied to fingerprint different environments of formation. Non-igneous titanite, which in a porphyry system may commonly be found in the green rock environment, is characterised by high F and Al, as well and Sc (and V), with characteristically low LREE contents relative to igneous titanite. Both unsupervised and supervised learning techniques are readily able to differentiate igneous from non-igneous titanite. It is concluded that compositions of non-igneous titanite are mostly controlled by fluid chemistry, inheritance from precursor igneous minerals and by co-precipitating minerals.

For igneous titanite, it is demonstrated that their characteristics mostly reflect those of the residual melt chemistry, which in part reflects bulk magma composition, but is also strongly impacted by late-stage *in-situ* fractional crystallisation. In particular, late titanite compositions may be strongly impacted by the earlier crystallisation of titanite, with important implications for key trace element parameters in titanite and also other minerals.

Considering solely igneous titanite, it is demonstrated conventional methods, such as bivariate plots, are unable to effectively discriminate between titanite formed in porphyry and non-porphyry environments. This is because signatures that often characterise porphyry magmas, such as positive Eu anomalies, can also be generated by unrelated processes. Supervised learning techniques, however, are better applied to porphyry titanite as these incorporate many geochemical parameters simultaneously. Finally, a workflow is proposed for the application of titanite to mineral exploration, which firstly involves screening suitable rocks based on their whole-rock composition, before using trace elements to identify firstly whether titanite is igneous or not, and then whether titanite is likely to be from a porphyry system or not. In such a scenario, it is suggested that U-Pb geochronology also plays a valuable role.

Chapter 9. Conclusions and future work

9.1 Main conclusions

This study aimed to catalogue the occurrence, textures and compositions of titanite in mineralised and unmineralised systems. Detailed study of titanite was conducted in four particular locations: Strontian, Chuquicamata, Cobre Panama and Oyu Tolgoi, encompassing both igneous and non-igneous titanite. Titanite compositions are examined in the context of other geochemical data from the same systems, including whole-rock, amphibole and zircon chemistry. Through this, as well as consideration of literature data and a global sample suite, the ways in which titanite could influence, and be utilised in mineral prospectivity studies are evaluated. This had the ultimate aim of assessing the usefulness of titanite as an indicator mineral, with the generation of a classification scheme that could identify titanite from mineralised systems. The main findings of this work are outlined below.

9.1.1 The influence of titanite on residual melt chemistry

Saturation of titanite from a crystallising magma has implications not only in terms of the application of titanite to porphyry prospectivity studies, but also for the trace element evolution of the residual melt, and hence other mineral phases.

- At Strontian, the late-stage evolution of the residual melt was tracked using amphibole and titanite compositions. This revealed a distinct core to rim evolution in terms of Y, as well as Sr/Y, Eu/Eu* and Ta/Nb ratios.
- Using textural, thermometric, modal abundance and geochemical data, titanite was demonstrated to i) co-crystallise with amphibole rims, but not cores, and ii) host a significant percentage of the whole-rock trace element budget.
- Modelling of Rayleigh fractional crystallisation was consistent with a titanite control on late-stage residual melt (and hence amphibole and titanite) chemistry.
- These results are pertinent, not least for porphyry deposits, where abundant titanite crystallisation could generate false positive signatures in unmineralised systems, but also for provenance studies generally involving late-stage granitoid melts.

9.1.2 The occurrence of titanite in porphyry systems

In porphyry environments, titanite occurs in the both the magmatic and hydrothermal domains, exhibiting a range of occurrences and textures.

- Titanite mainly occurs as a primary igneous mineral and in the propylitic environment.

- It is rarely found in sericitically altered rocks and has also been suggested to occur in the (often poorly preserved) sodic-calcic and potassic zones. However, no potassic titanite was identified in samples encountered during this study, which also did not analyse any rocks that were subjected to sodic-calcic alteration.
- Primary igneous titanite may be completely destroyed in rocks that have been subjected to intense potassic, sericitic or acidic alteration, and is commonly replaced by rutile ± Fe-Ti oxides ± REE-bearing phases.
- Where titanite has been completely destroyed, magmatic signatures may be preserved by secondary rutile.
- The ubiquity of fluid inclusion trails in primary titanite from altered rocks suggests that this may be a useful indicator of whether a crystallising magma saturated in a volatile phase.

9.1.3 Differentiating igneous and non-igneous titanite

One of the main aims of this study was to characterise textural and geochemical differences between igneous and non-igneous titanite, of which the latter includes altered igneous, replacement and vein-hosted types.

- Igneous titanite is i) generally larger, ii) often more euhedral, iii) displays internal zonation (core to rim or sector zoning) as identified by SEM-BSE mode, and iv) is associated with common igneous minerals (e.g. zircon, amphibole).
- Propylitic titanite is often associated with typical green rock minerals: chlorite, epidote, calcite etc.
- Separating titanite from a rock containing both igneous and non-igneous titanite may result in sampling bias, preferentially separating crystals with an igneous origin.
- Altered primary titanite may be identified texturally by an intimate association with rutile ± Fe-Ti oxides ± REE-bearing phases. Altered igneous titanite compositions are variable, some of which retain a predominantly igneous signature, although others may be overprinted, taking on a new hydrothermal composition.
- Non-igneous titanite (encompassing replacement, vein-hosted and altered igneous types) is characterised by elevated F, Al and Sc contents, but low LREE and Th contents.
- Compositions of igneous and non-igneous types are distinct enough that they can be readily distinguished by simple bivariate plots (e.g. F vs Fe/Al), as well as more sophisticated methods (e.g. machine learning techniques).
- Consequently, an igneous or non-igneous origin may be inferred solely on the basis of compositional data.

9.1.4 Controls on compositions of non-igneous titanite

A range of factors were investigated to understand what controls the compositions of non-igneous titanite, including host-rock composition, temperature and fluid composition.

- Generally, it is inferred that non-igneous titanite compositions are primarily controlled by i) fluid composition, ii) inheritance from primary igneous minerals and iii) by co-precipitating minerals.

9.1.5 Controls on compositions of igneous titanite

Factors responsible for governing the composition of igneous titanite were also considered.

- Broadly, igneous titanite compositions (e.g. Sr, Eu anomaly) are demonstrated to reflect residual melt compositions which partially reflect, but may also diverge from, those of the bulk magmas at near-solidus temperatures.

9.1.6 Identifying igneous titanite from porphyry systems

Compositions of igneous titanite from a range of mineralised and unmineralised systems were determined to investigate whether signatures of igneous titanite from porphyry systems are unique.

- Many false positive signatures are likely to result from applying conventional methods to recognise porphyry titanite. For example, elevated Eu/Eu* ratios, which characterise zircons in porphyry systems, can be generated by unrelated processes; including abundant crystallisation of titanite itself.
- The potential in utilising supervised learning techniques is highlighted, which are demonstrated to accurately identify porphyry titanite.

9.1.7 Using titanite in mineral exploration

Overall, it is interpreted that there is significant potential for titanite to be used in exploration due to its compositional variability in both magmatic and hydrothermal environments. This variability could be combined with textural observations and U-Pb geochronology, to assess whether magmas are: i) a suitable composition to form a porphyry system; ii) whether there was significant hydrothermal alteration; and iii) whether rocks the same age as known mineralising events.

9.2 Recommendations for future work

From this work, several additional avenues of research could be pursued, focussing on either magmatic or hydrothermal portions of the porphyry system.

9.2.1 Magmatic titanite

One area of potential further research involves estimated crystallisation temperatures in titanite and zircon. In the Chuquicamata district, calculated zircon crystallisation temperatures decrease through time towards the mineralising event, an observation that is consistent with zircons from porphyry deposits worldwide. On average, titanite crystallisation temperatures in the same rocks are observed to increase. Both the Zr-in-titanite and Ti-in-zircon thermometers are reliant upon on accurate estimation of $a\mathrm{TiO_2}$, which is often assumed to be 0.7, but can introduce uncertainty into thermometric estimates. One way to estimate $a\mathrm{TiO_2}$ is to determine zircon Ti concentrations, and Zr concentrations in titanite that is included within zircon. As titanite is included in zircon, the titanite-zircon pairs can be assumed to be in equilibrium, and hence crystallised at the same temperature, meaning that $a\mathrm{TiO_2}$ can be estimated. Titanium-in-zircon temperatures generally imply that porphyry magmas crystallise at low temperatures, something which could be better understood by accurately estimating $a\mathrm{TiO_2}$ for a range of magma compositions.

Analysis of titanite inclusions in zircon could also inform on other processes, such as volatile saturation. Titanite volatile contents are another interesting avenue of research that was considered during this study. However, differences in F content were difficult to resolve, and would require more precise determination. A comparison of titanite F contents included in zircon with those in the groundmass could be informative, providing valuable information on whether titanite F contents are subject to re-equilibration following interaction with hydrothermal fluids.

It was also not possible during the present study to fully investigate how magmatic redox impacted titanite compositions, particularly for transition elements. Further study could investigate how concentrations of these elements vary in magmas of variable oxidation state, which could be constrained by several independent methods including zircon oxybarometry and Fe-Ti oxide pairs.

In terms of research focussed on particular study sites, further work should focus on how titanite compositions vary within the precursor batholith to the Cobre Panama deposit, the Petaquilla batholith. Whole-rock signatures in the southern portion of the batholith are indistinguishable from those of the porphyritic intrusions, whereas signatures in the northern, older portion of the batholith are distinctly less porphyry-like. It is suggested that titanite trace element compositions, and even potentially titanite occurrence, would vary systematically from north to south and through time. Study of titanite from throughout the batholith could be informative on temperature, volatile and compositional variation through time.

A pilot study which tests the application of titanite compositions to assessing mineral prospectivity in stream sediments is also proposed. Such a study would involve collecting

sediments from streams that drain several variably mineralised districts, before conducting blind testing to potentially identify catchments associated with mineralised deposits.

9.2.2 Hydrothermal titanite

Another potential study involves systematically sampling and determining titanite compositions from throughout a mineralised porphyry district. Spatial variation in chlorite and epidote chemistry, for example, is well characterised, indicating that the compositions of these minerals are sensitive to variations in temperature, salinity, pH and oxidation related to dispersion of a fluid away from a mineralised centre. Undertaking a similar approach for titanite could be informative and would involve collecting many samples from a well characterised system, such as Batu Hijau. If successful, additional complexities such as the presence of multiple hydrothermal pulses could be factored in, with the application of geochronology to discern different hydrothermal events.

In Chapter 5, it was identified that rutile may inherit trace element contents from precursor titanite. If rutile were to completely inherit trace element compositions of titanite, or did so in a consistent manner, then it would be possible to estimate the composition of primary titanite which has been subsequently replaced, which may be particularly useful in rocks that have been subjected to intense hydrothermal alteration where precursor titanite is likely to have been completely destroyed. For example, comparing signatures of rutile pseudomorphs after titanite, with titanite included within zircon could aid in understanding how faithfully rutile records precursor titanite compositions.

References

Ackerson, M. (2011). Trace element partitioning between titanite and groundmass in silicic volcanic systems. University of North Carolina at Chapel Hill.

Ahmed, A., Crawford, A. J., Leslie, C., Phillips, J., Wells, T., Garay, A., Hood, S. B. & Cooke, D. R. (2020). Assessing copper fertility of intrusive rocks using field portable X-ray fluorescence (pXRF) data. *Geochemistry: Exploration, Environment, Analysis* **20**, 81-97.

Aitchison, J. (1982). The statistical analysis of compositional data. *Journal of the Royal Statistical Society: Series B (Methodological)* **44**, 139-160.

Aleinikoff, J. N., Wintsch, R. P., Fanning, C. M. & Dorais, M. J. (2002). U–Pb geochronology of zircon and polygenetic titanite from the Glastonbury Complex, Connecticut, USA: an integrated SEM, EMPA, TIMS, and SHRIMP study. *Chemical geology* **188**, 125-147.

Alt, J. C., Shanks III, W. C. & Jackson, M. C. (1993). Cycling of sulfur in subduction zones: The geochemistry of sulfur in the Mariana Island Arc and back-arc trough. *Earth and Planetary Science Letters* **119**, 477-494.

Amar-Amgalan, S. (2008). U-Pb geochronology and multi-isotopic systematics of granitoids from Mongolia, Central Asian Orogenic Belt: Implications for granitoid origin and crustal growth during the Phanerozoic.

Andersen, T. (2002). Correction of common lead in U–Pb analyses that do not report 204Pb. *Chemical geology* **192**, 59-79.

Annen, C., Blundy, J. & Sparks, R. (2006). The genesis of intermediate and silicic magmas in deep crustal hot zones. *Journal of Petrology* **47**, 505-539.

Annen, C., Pinel, V. & Burgisser, A. (2023). Re-evaluation of the role of volatiles in the rupture of magma chambers and the triggering of crystal-rich eruptions. *Journal of Volcanology and Geothermal Research*, 107755.

Arribas Jr, A., Hedenquist, J. W., Itaya, T., Okada, T., Concepción, R. A. & Garcia Jr, J. S. (1995). Contemporaneous formation of adjacent porphyry and epithermal Cu-Au deposits over 300 ka in northern Luzon, Philippines. *Geology* **23**, 337-340.

Ashworth, J. & Tyler, I. (1983). The distribution of metamorphic temperatures around the Strontian granodiorite. *Geological Magazine* **120**, 281-290.

Atherton, M. & Ghani, A. (2002). Slab breakoff: a model for Caledonian, Late Granite syn-collisional magmatism in the orthotectonic (metamorphic) zone of Scotland and Donegal, Ireland. *Lithos* **62**, 65-85.

Atkinson, W. & Einaudi, M. T. (1978). Skarn formation and mineralization in the contact aureole at Carr Fork, Bingham, Utah. *Economic geology* **73**, 1326-1365.

Ayers, J. C., Flanagan, D., Miller, C., Watson, E., Ryerson, F., Wallrich, B. & Ackerson, M. (2022). The solubility of titanite in silicate melt determined from growth and dissolution experiments. *Contributions to Mineralogy and Petrology* **177**, 1-15.

Ayush, O. (2006). Structure, stratigraphy, petrography, and whole-rock geochemistry of Upper Devonian Alagbayan Group volcanic and sedimentary rocks comprising the hanging wall to the Hugo Dummett deposit, Southern Gobi, Mongolia: Unpublished M. Sc. thesis, Ulan Bator, Mongolia, Mongolian University of Science and Technology ….

Bachmann, O. & Bergantz, G. W. (2006). Gas percolation in upper-crustal silicic crystal mushes as a mechanism for upward heat advection and rejuvenation of near-solidus magma bodies. *Journal of Volcanology and Geothermal Research* **149**, 85-102.

Bachmann, O., Dungan, M. & Bussy, F. (2005). Insights into shallow magmatic processes in large silicic magma bodies: the trace element record in the Fish Canyon magma body, Colorado. *Contributions to Mineralogy and Petrology* **149**, 338-349.

Badarch, G., Cunningham, W. D. & Windley, B. F. (2002). A new terrane subdivision for Mongolia: implications for the Phanerozoic crustal growth of Central Asia. *Journal of Asian Earth Sciences* **21**, 87-110.

Bailey, E. B. & Maufe, H. B. (1916). *The Geology of Ben Nevis and Glen Coe and the Surrounding Country:(Explanation of Sheet 53)*: HM Stationery Office.

Bailey, J. (1977). Fluorine in granitic rocks and melts: a review. *Chemical geology* **19**, 1-42.

Baker, M. J., Hollings, P., Thompson, J. A., Thompson, J. M. & Burge, C. (2016). Age and geochemistry of host rocks of the Cobre Panama porphyry Cu–Au deposit, central Panama: Implications for the Paleogene evolution of the Panamanian magmatic arc. *Lithos* **248**, 40-54.
Ballantyne, G. H. (1983). CHEMICAL AND MINERALOGICAL VARIATIONS IN PROPYLITIC ZONES SURROUNDING PORPHYRY COPPER DEPOSITS.
Ballard, J. R. (2001). A comparative study between the geochemistry of ore-bearing and barren calc-alkaline intrusions. Canberra: The Australian National University.
Ballard, J. R., Palin, J. M., Williams, I. S., Campbell, I. H. & Faunes, A. (2001). Two ages of porphyry intrusion resolved for the super-giant Chuquicamata copper deposit of northern Chile by ELA-ICP-MS and SHRIMP. *Geology* **29**, 383-386.
Ballard, J. R., Palin, M. J. & Campbell, I. H. (2002). Relative oxidation states of magmas inferred from Ce (IV)/Ce (III) in zircon: application to porphyry copper deposits of northern Chile. *Contributions to Mineralogy and Petrology* **144**, 347-364.
Barnes, C. G. & Barnes, M. A. (2020). The western Hayfork terrane: Remnants of the Middle Jurassic arc in the Klamath Mountain province, California and Oregon. *Geosphere* **16**, 1058-1081.
Barra, F., Alcota, H., Rivera, S., Valencia, V., Munizaga, F. & Maksaev, V. (2013). Timing and formation of porphyry Cu–Mo mineralization in the Chuquicamata district, northern Chile: new constraints from the Toki cluster. *Mineralium Deposita* **48**, 629-651.
Barton, M. D. & Young, S. (2002). Non-pegmatitic deposits of beryllium: mineralogy, geology, phase equilibria and origin. *Reviews in Mineralogy and Geochemistry* **50**, 591-691.
Belousova, E., Griffin, W. L., O'Reilly, S. Y. & Fisher, N. (2002). Igneous zircon: trace element composition as an indicator of source rock type. *Contributions to Mineralogy and Petrology* **143**, 602-622.
Birt, E. A. (2019). The generation of high Sr/Y in the Strontian Intrusive Complex. Imperial College London.
Blundy, J. D. & Wood, B. J. (1991). Crystal-chemical controls on the partitioning of Sr and Ba between plagioclase feldspar, silicate melts, and hydrothermal solutions. *Geochimica et Cosmochimica Acta* **55**, 193-209.
Boehnke, P., Watson, E. B., Trail, D., Harrison, T. M. & Schmitt, A. K. (2013). Zircon saturation re-revisited. *Chemical geology* **351**, 324-334.
Bouzari, F., Hart, C. J., Bissig, T. & Barker, S. (2016). Hydrothermal alteration revealed by apatite luminescence and chemistry: A potential indicator mineral for exploring covered porphyry copper deposits. *Economic geology* **111**, 1397-1410.
Boynton, W. V. (1984). Cosmochemistry of the rare earth elements: meteorite studies. *Developments in geochemistry*: Elsevier, 63-114.
Breiman, L. (2001). Random forests. *Machine learning* **45**, 5-32.
Brown, G. & Fyfe, W. (1970). The production of granitic melts during ultrametamorphism. *Contributions to Mineralogy and Petrology* **28**, 310-318.
Brown, P., Ryan, P., Soper, N. & Woodcock, N. (2008). The Newer Granite problem revisited: a transtensional origin for the Early Devonian trans-suture suite. *Geological Magazine* **145**, 235-256.
Bruand, E., Storey, C. & Fowler, M. (2014). Accessory mineral chemistry of high Ba–Sr granites from northern Scotland: constraints on petrogenesis and records of whole-rock signature. *Journal of Petrology* **55**, 1619-1651.
Brugge, E. (2021). Apatite in porphyry systems and its applications in mineral exploration. Imperial College London.
Buccianti, A. & Grunsky, E. (2014). Compositional data analysis in geochemistry: Are we sure to see what really occurs during natural processes? : Elsevier, 1-5.
Buchs, D. M., Arculus, R. J., Baumgartner, P. O., Baumgartner-Mora, C. & Ulianov, A. (2010). Late Cretaceous arc development on the SW margin of the Caribbean Plate: Insights from the Golfito, Costa Rica, and Azuero, Panama, complexes. *Geochemistry, Geophysics, Geosystems* **11**.
Buret, Y., von Quadt, A., Heinrich, C., Selby, D., Wälle, M. & Peytcheva, I. (2016). From a long-lived upper-crustal magma chamber to rapid porphyry copper emplacement: Reading the

geochemistry of zircon crystals at Bajo de la Alumbrera (NW Argentina). *Earth and Planetary Science Letters* **450**, 120-131.
Buret, Y., Wotzlaw, J.-F., Roozen, S., Guillong, M., von Quadt, A. & Heinrich, C. A. (2017). Zircon petrochronological evidence for a plutonic-volcanic connection in porphyry copper deposits. *Geology* **45**, 623-626.
Burnham, A., Berry, A., Halse, H., Schofield, P., Cibin, G. & Mosselmans, J. (2015). The oxidation state of europium in silicate melts as a function of oxygen fugacity, composition and temperature. *Chemical geology* **411**, 248-259.
Burnham, A. D. & Berry, A. J. (2012). An experimental study of trace element partitioning between zircon and melt as a function of oxygen fugacity. *Geochimica et Cosmochimica Acta* **95**, 196-212.
Burnham, C. W. (1979). Magmas and hydrothermal fluids. In: Barnes, H. L. (ed.) *Geochemistry of Hydrothermal Ore Deposits.* New York: John Wiley & Sons, 71-136.
Cabrera, J. M., Rabbia, O. & Parra, A. (2010). Caracterización Petrológica de la Fuente Magmática del Depósito Radomiro Tomic. *CODELCO Norte Biennial Conference of Geosciences. Calama*, 1-14.
Campbell, I. H., Ballard, J. R., Palin, J. M., Allen, C. & Faunes, A. (2006). U-Pb zircon geochronology of granitic rocks from the Chuquicamata-El Abra porphyry copper belt of northern Chile: Excimer laser ablation ICP-MS analysis. *Economic geology* **101**, 1327-1344.
Candela, P. A. & Holland, H. D. (1984). The partitioning of copper and molybdenum between silicate melts and aqueous fluids. *Geochimica et Cosmochimica Acta* **48**, 373-380.
Cao, M., Hollings, P., Evans, N. J., Cooke, D. R., McInnes, B. I., Zhao, K., Qin, K., Li, D. & Sweet, G. (2020). In situ elemental and Sr isotope characteristics of magmatic to hydrothermal minerals from the Black Mountain porphyry deposit, Baguio district, Philippines. *Economic geology* **115**, 927-944.
Cao, M., Qin, K., Li, G., Evans, N. J. & Jin, L. (2015). In situ LA-(MC)-ICP-MS trace element and Nd isotopic compositions and genesis of polygenetic titanite from the Baogutu reduced porphyry Cu deposit, Western Junggar, NW China. *Ore Geology Reviews* **65**, 940-954.
Carmichael, I. S. (1991). The redox states of basic and silicic magmas: a reflection of their source regions? *Contributions to Mineralogy and Petrology* **106**, 129-141.
Carranza, E. J. M. & Laborte, A. G. (2015). Random forest predictive modeling of mineral prospectivity with small number of prospects and data with missing values in Abra (Philippines). *Computers & Geosciences* **74**, 60-70.
Carten, R. B. (1986). Sodium-calcium metasomatism; chemical, temporal, and spatial relationships at the Yerington, Nevada, porphyry copper deposit. *Economic geology* **81**, 1495-1519.
Carter, L. C., Tapster, S. R., Williamson, B. J., Buret, Y., Selby, D., Rollinson, G. K., Millar, I. & Parvaz, D. B. (2022). A rapid change in magma plumbing taps porphyry copper deposit-forming magmas. *Scientific reports* **12**, 1-20.
Cashman, K. V., Sparks, R. S. J. & Blundy, J. D. (2017). Vertically extensive and unstable magmatic systems: a unified view of igneous processes. *Science* **355**, eaag3055.
Castro, A. (2020). The dual origin of I-type granites: the contribution from experiments. *Geological Society, London, Special Publications* **491**, 101-145.
Cathelineau, M. (1988). Cation site occupancy in chlorites and illites as a function of temperature. *Clay minerals* **23**, 471-485.
Celis, A. (2015). Titanite as an indicator mineral for alkalic porphyry Cu-Au deposits in south-central British Columbia. *UBC Library, doi* **10**.
Černý, P., Novák, M. & Chapman, R. (1995). The Al (Nb, Ta) Ti (in− 2) substitution in titanite: the emergence of a new species? *Mineralogy and Petrology* **52**, 61-73.
Chakhmouradian, A. R. (2004). Crystal chemistry and paragenesis of compositionally unique (Al-, Fe-, Nb-, and Zr-rich) titanite from Afrikanda, Russia. *American Mineralogist* **89**, 1752-1762.
Chakhmouradian, A. R. & Zaitsev, A. N. (2002). Calcite–amphibole–clinopyroxene rock from the Afrikanda complex, Kola Peninsula, Russia: mineralogy and a possible link to carbonatites. III. Silicate minerals. *The Canadian Mineralogist* **40**, 1347-1374.
Chang, Z., Hedenquist, J. W., White, N. C., Cooke, D. R., Roach, M., Deyell, C. L., Garcia Jr, J., Gemmell, J. B., McKnight, S. & Cuison, A. L. (2011). Exploration tools for linked porphyry

and epithermal deposits: Example from the Mankayan intrusion-centered Cu-Au district, Luzon, Philippines. *Economic geology* **106**, 1365-1398.
Chelle-Michou, C. & Chiaradia, M. (2017). Amphibole and apatite insights into the evolution and mass balance of Cl and S in magmas associated with porphyry copper deposits. *Contributions to Mineralogy and Petrology* **172**, 105.
Chelle-Michou, C., Chiaradia, M., Béguelin, P. & Ulianov, A. (2015). Petrological evolution of the magmatic suite associated with the Coroccohuayco Cu (–Au–Fe) Porphyry–skarn deposit, Peru. *Journal of Petrology* **56**, 1829-1862.
Chelle-Michou, C., Chiaradia, M., Ovtcharova, M., Ulianov, A. & Wotzlaw, J.-F. (2014). Zircon petrochronology reveals the temporal link between porphyry systems and the magmatic evolution of their hidden plutonic roots (the Eocene Coroccohuayco deposit, Peru). *Lithos* **198**, 129-140.
Chelle-Michou, C. & Rottier, B. (2021). Transcrustal Magmatic Controls on the Size of Porphyry Cu Systems: State of Knowledge and Open Questions. In: Sholeh, A. & Wang, R. (eds.) *Special Publications Series 24*: Society of Economic Geologists, 87-100.
Chen, Y.-X. & Zheng, Y.-F. (2015). Extreme Nb/Ta fractionation in metamorphic titanite from ultrahigh-pressure metagranite. *Geochimica et Cosmochimica Acta* **150**, 53-73.
Cherniak, D. (1993). Lead diffusion in titanite and preliminary results on the effects of radiation damage on Pb transport. *Chemical geology* **110**, 177-194.
Cherniak, D. (1995). Sr and Nd diffusion in titanite. *Chemical geology* **125**, 219-232.
Cherniak, D. (2006). Zr diffusion in titanite. *Contributions to Mineralogy and Petrology* **152**, 639-647.
Cherniak, D. (2010). Diffusion in accessory minerals: zircon, titanite, apatite, monazite and xenotime. *Reviews in Mineralogy and Geochemistry* **72**, 827-869.
Chew, D., O'Sullivan, G., Caracciolo, L., Mark, C. & Tyrrell, S. (2020). Sourcing the sand: Accessory mineral fertility, analytical and other biases in detrital U-Pb provenance analysis. *Earth-Science Reviews* **202**, 103093.
Chiaradia, M. (2020). Gold endowments of porphyry deposits controlled by precipitation efficiency. *Nature Communications* **11**, 1-10.
Chiaradia, M. & Caricchi, L. (2017). Stochastic modelling of deep magmatic controls on porphyry copper deposit endowment. *Scientific reports* **7**, 44523.
Claiborne, L. L., Miller, C. F. & Wooden, J. L. (2010). Trace element composition of igneous zircon: a thermal and compositional record of the accumulation and evolution of a large silicic batholith, Spirit Mountain, Nevada. *Contributions to Mineralogy and Petrology* **160**, 511-531.
Clark, A., Farrar, E. & Kents, P. (1977). Potassium-argon age of the Cerro Colorado porphyry copper deposit, Panama. *Economic geology* **72**, 1154-1158.
Cline, J. S. & Bodnar, R. J. (1991). Can economic porphyry copper mineralization be generated by a typical calc-alkaline melt? *Journal of Geophysical Research: Solid Earth* **96**, 8113-8126.
Cloos, M. (2001). Bubbling magma chambers, cupolas, and porphyry copper deposits. *International geology review* **43**, 285-311.
Colombini, L. L., Miller, C. F., Gualda, G. A., Wooden, J. L. & Miller, J. S. (2011). Sphene and zircon in the Highland Range volcanic sequence (Miocene, southern Nevada, USA): elemental partitioning, phase relations, and influence on evolution of silicic magma. *Mineralogy and Petrology* **102**, 29-50.
Cooke, D., Agnew, P., Hollings, P., Baker, M., Chang, Z., Wilkinson, J., White, N., Zhang, L., Thompson, J., Gemmell, J., Fox, N., Chen, H. & Wilkinson, C. C. (2017). Porphyry indicator minerals (PIMS) and porphyry vectoring and fertility tools (PVFTS)–indicators of mineralization styles and recorders of hypogene geochemical dispersion halos. *Journal of Geochemical Exploration* **190**, 109-129.
Cooke, D. R., Agnew, P., Hollings, P., Baker, M., Chang, Z., Wilkinson, J. J., Ahmed, A., White, N. C., Zhang, L. & Thompson, J. (2020a). Recent advances in the application of mineral chemistry to exploration for porphyry copper–gold–molybdenum deposits: detecting the geochemical fingerprints and footprints of hypogene mineralization and alteration. *Geochemistry: Exploration, Environment, Analysis* **20**, 176-188.

Cooke, D. R., Hollings, P. & Walshe, J. L. (2005). Giant porphyry deposits: characteristics, distribution, and tectonic controls. *Economic geology* **100**, 801-818.
Cooke, D. R., Hollings, P., Wilkinson, J. J. & Tosdal, R. (2014). Geochemistry of Porphyry Deposits. In: Holland, H. D. & Turekian, K. K. (eds.) *Treatise on geochemistry*. Oxford: Elsevier, 357-381.
Cooke, D. R., Wilkinson, J. J., Baker, M., Agnew, P., Phillips, J., Chang, Z., Chen, H., Wilkinson, C. C., Inglis, S. & Hollings, P. (2020b). Using mineral chemistry to aid exploration: A case study from the Resolution porphyry Cu-Mo deposit, Arizona. *Economic geology* **115**, 813-840.
Crane, D. & Kavalieris, I. (2012). Geologic overview of the Oyu Tolgoi porphyry Cu-Au-Mo deposits, Mongolia.
Curran, J. (2021). Package 'Hotelling'. *R package version 1.0-8*.
Dahlström, S. I., Cooper, F. J., Blundy, J., Tapster, S., Yáñez, J. C. & Evenstar, L. A. (2022). Pluton exhumation in the Precordillera of northern Chile (17.8–24.2 S): Implications for the formation, enrichment, and preservation of porphyry copper deposits. *Economic geology* **117**, 1043-1071.
Deer, W., Howie, R. & Zussman, J. (2013). An Introduction to the Rock-Forming Minerals.
Deng, X.-D., Li, J.-W., Zhou, M.-F., Zhao, X.-F. & Yan, D.-R. (2015). In-situ LA-ICPMS trace elements and U–Pb analysis of titanite from the Mesozoic Ruanjiawan W–Cu–Mo skarn deposit, Daye district, China. *Ore Geology Reviews* **65**, 990-1004.
Dilles, J., Tomlinson, A., Martin, M. & Blanco, N. (1997). El Abra and Fortuna Complexes: A porphyry copper batholith sinistrally displaced by the Falla Oeste. *Congreso Geológico Chileno*, 1883-1887.
Dilles, J. H. (1987). Petrology of the Yerington Batholith, Nevada; evidence for evolution of porphyry copper ore fluids. *Economic geology* **82**, 1750-1789.
Dilles, J. H., Kent, A. J., Wooden, J. L., Tosdal, R. M., Koleszar, A., Lee, R. G. & Farmer, L. P. (2015). Zircon compositional evidence for sulfur-degassing from ore-forming arc magmas. *Economic geology* **110**, 241-251.
Dilles, J. H., Tomlinson, A. J., García, M. & Alcota, H. (2011). The geology of the Fortuna Granodiorite Complex, Chuquicamata district, northern Chile: Relation to porphyry copper deposits. *SGA Biennial Meeting, 11 th*.
Dohmen, R. & Blundy, J. (2014). A predictive thermodynamic model for element partitioning between plagioclase and melt as a function of pressure, temperature and composition. *American Journal of Science* **314**, 1319-1372.
Dolgopolova, A., Seltmann, R., Armstrong, R., Belousova, E., Pankhurst, R. & Kavalieris, I. (2013). Sr–Nd–Pb–Hf isotope systematics of the Hugo Dummett Cu–Au porphyry deposit (Oyu Tolgoi, Mongolia). *Lithos* **164**, 47-64.
Duffy, J. A. (1993). A review of optical basicity and its applications to oxidic systems. *Geochimica et Cosmochimica Acta* **57**, 3961-3970.
Enami, M., Suzuki, K., Liou, J. & Bird, D. K. (1993). Al-Fe3+ and F-OH substitutions in titanite and constraints on their PT dependence. *European Journal of Mineralogy*, 219-232.
Ferry, J. & Watson, E. (2007). New thermodynamic models and revised calibrations for the Ti-in-zircon and Zr-in-rutile thermometers. *Contributions to Mineralogy and Petrology* **154**, 429-437.
Finlayson, T. (2002). DISTRIBUTION, MINERALOGY, AND POTENTIAL RECOVERY OF RUTILE FROM THE CHUQUICAMATA PORPHYRY COPPER DEPOSIT OF NORTHERN CHILE.
Fournier, R. O. (1999). Hydrothermal processes related to movement of fluid from plastic into brittle rock in the magmatic-epithermal environment. *Economic geology* **94**, 1193-1211.
Fowler, M. & Henney, P. (1996). Mixed Caledonian appinite magmas: implications for lamprophyre fractionation and high Ba-Sr granite genesis. *Contributions to Mineralogy and Petrology* **126**, 199-215.
Fowler, M., Kocks, H., Darbyshire, D. & Greenwood, P. (2008). Petrogenesis of high Ba–Sr plutons from the northern highlands Terrane of the British Caledonian Province. *Lithos* **105**, 129-148.

Franz, G. & Spear, F. S. (1985). Aluminous titanite (sphene) from the eclogite zone, south-central Tauern Window, Austria. *Chemical geology* **50**, 33-46.
Frost, B. R., Chamberlain, K. R. & Schumacher, J. C. (2001). Sphene (titanite): phase relations and role as a geochronometer. *Chemical geology* **172**, 131-148.
Gao, X.-Y., Zheng, Y.-F., Chen, Y.-X. & Guo, J. (2012). Geochemical and U–Pb age constraints on the occurrence of polygenetic titanites in UHP metagranite in the Dabie orogen. *Lithos* **136**, 93-108.
Garber, J., Hacker, B., Kylander-Clark, A., Stearns, M. & Seward, G. (2017). Controls on trace element uptake in metamorphic titanite: Implications for petrochronology. *Journal of Petrology* **58**, 1031-1057.
Geostats. (2022). GIOP96 Certified Reference Material, 2022. http://www.geostats.com.au/certs/GIOP-96.pdf.
Gray, D., Lawlor, M. & Stone, R. (2019). Cobre Panamá Project, Colón Province, Republic of Panamá. NI 43-101 Technical Report: Report by First Quantum Minerals Ltd., effective ….
Green, T. & Pearson, N. (1986). Rare-earth element partitioning between sphene and coexisting silicate liquid at high pressure and temperature. *Chemical geology* **55**, 105-119.
Green, T. & Pearson, N. (1987). An experimental study of Nb and Ta partitioning between Ti-rich minerals and silicate liquids at high pressure and temperature. *Geochimica et Cosmochimica Acta* **51**, 55-62.
Gromet, L. P. & Silver, L. T. (1983). Rare earth element distributions among minerals in a granodiorite and their petrogenetic implications. *Geochimica et Cosmochimica Acta* **47**, 925-939.
Grunsky, E. & Caritat, P. d. (2020). State-of-the-art analysis of geochemical data for mineral exploration. *Geochemistry: Exploration, Environment, Analysis* **20**, 217-232.
Gualda, G. A., Ghiorso, M. S., Lemons, R. V. & Carley, T. L. (2012). Rhyolite-MELTS: a modified calibration of MELTS optimized for silica-rich, fluid-bearing magmatic systems. *Journal of Petrology* **53**, 875-890.
Günther, D. & Hattendorf, B. (2005). Solid sample analysis using laser ablation inductively coupled plasma mass spectrometry. *TrAC Trends in Analytical Chemistry* **24**, 255-265.
Gustafson, L. B. & Hunt, J. P. (1975). The porphyry copper deposit at El Salvador, Chile. *Economic geology* **70**, 857-912.
Haas, J. R., Shock, E. L. & Sassani, D. C. (1995). Rare earth elements in hydrothermal systems: estimates of standard partial molal thermodynamic properties of aqueous complexes of the rare earth elements at high pressures and temperatures. *Geochimica et Cosmochimica Acta* **59**, 4329-4350.
Halley, S. (2020). Mapping magmatic and hydrothermal processes from routine exploration geochemical analyses. *Economic geology* **115**, 489-503.
Halley, S., Dilles, J. H. & Tosdal, R. M. (2015). Footprints: Hydrothermal alteration and geochemical dispersion around porphyry copper deposits. *SEG Discovery*, 1-17.
Harris, J. & Grunsky, E. C. (2015). Predictive lithological mapping of Canada's North using Random Forest classification applied to geophysical and geochemical data. *Computers & Geosciences* **80**, 9-25.
Harrison, T. M. & Watson, E. B. (1984). The behavior of apatite during crustal anatexis: equilibrium and kinetic considerations. *Geochimica et Cosmochimica Acta* **48**, 1467-1477.
Harrison, T. M., Watson, E. B. & Aikman, A. B. (2007). Temperature spectra of zircon crystallization in plutonic rocks. *Geology* **35**, 635-638.
Hart-Madigan, L. (2019). Mineral transformations and element fluxes during propylitic alteration in porphyry ore systems: A case study of the Oyu Tolgoi porphyry Cu-Au deposits, Mongolia. Imperial College London.
Hart-Madigan, L., Wilkinson, J. J., Lasalle, S. & Armstrong, R. N. (2020). U-Pb DATING OF HYDROTHERMAL TITANITE RESOLVES MULTIPLE PHASES OF PROPYLITIC ALTERATION IN THE OYU TOLGOI PORPHYRY DISTRICT, MONGOLIA. *Economic geology* **115**, 1605-1618.

Hastie, A. R., Kerr, A. C., Pearce, J. A. & Mitchell, S. (2007). Classification of altered volcanic island arc rocks using immobile trace elements: development of the Th–Co discrimination diagram. *Journal of Petrology* **48**, 2341-2357.
Hastie, T., Tibshirani, R. & Friedman, J. (2009). An introduction to statistical learning.
Hawthorne, F. C., Oberti, R., Harlow, G. E., Maresch, W. V., Martin, R. F., Schumacher, J. C. & Welch, M. D. (2012). Nomenclature of the amphibole supergroup. *American Mineralogist* **97**, 2031-2048.
Hayden, L. A., Watson, E. B. & Wark, D. A. (2008). A thermobarometer for sphene (titanite). *Contributions to Mineralogy and Petrology* **155**, 529-540.
Heaman, L. M. (2009). The application of U–Pb geochronology to mafic, ultramafic and alkaline rocks: an evaluation of three mineral standards. *Chemical geology* **261**, 43-52.
Hedenquist, J. W., Simmons, S. F., Giggenbach, W. F. & Eldridge, C. S. (1993). White Island, New Zealand, volcanic-hydrothermal system represents the geochemical environment of high-sulfidation Cu and Au ore deposition. *Geology* **21**, 731-734.
Heinrich, C. A. & Candela, P. A. (2014). Fluids and ore formation in the Earth's crust. In: Holland, H. D. & Turekian, K. K. (eds.) *Treatise on geochemistry*. Oxford: Elsevier, 1-28.
Heinrich, C. A., Driesner, T., Stefánsson, A. & Seward, T. M. (2004). Magmatic vapor contraction and the transport of gold from the porphyry environment to epithermal ore deposits. *Geology* **32**, 761-764.
Hemley, J., Cygan, G., Fein, J., Robinson, G. & d'Angelo, W. (1992). Hydrothermal ore-forming processes in the light of studies in rock-buffered systems; I, Iron-copper-zinc-lead sulfide solubility relations. *Economic geology* **87**, 1-22.
Hemley, J. J. & Jones, W. (1964). Chemical aspects of hydrothermal alteration with emphasis on hydrogen metasomatism. *Economic geology* **59**, 538-569.
Henze, P. K., Christiansen, E. H., Kowallis, B. J., Dorais, M. J., Mosher, H. D., Franzen, L. M., Martin, A. J. & Nabelek, P. I. (2023). Titanite geochemistry and textures: Implications for magmatic and post-magmatic processes in the Notch Peak and Little Cottonwood granitic intrusions, Utah. *American Mineralogist: Journal of Earth and Planetary Materials* **108**, 226-248.
Hermann, J. (2002). Allanite: thorium and light rare earth element carrier in subducted crust. *Chemical geology* **192**, 289-306.
Hildreth, W. (2004). Volcanological perspectives on Long Valley, Mammoth Mountain, and Mono Craters: several contiguous but discrete systems. *Journal of Volcanology and Geothermal Research* **136**, 169-198.
Hildreth, W. & Moorbath, S. (1988). Crustal contributions to arc magmatism in the Andes of central Chile. *Contributions to Mineralogy and Petrology* **98**, 455-489.
Hirata, T. & Ohno, T. (2001). In-situ isotopic ratio analysis of iron using laser ablation-multiple collector-inductively coupled plasma mass spectrometry (LA-MC-ICP-MS). *Journal of Analytical Atomic Spectrometry* **16**, 487-491.
Holden, P., Halliday, A. & Stephens, W. (1987). Neodymium and strontium isotope content of microdiorite enclaves points to mantle input to granitoid production. *Nature* **330**, 53-56.
Holden, P., Halliday, A. N., Stephens, W. E. & Henney, P. J. (1991). Chemical and isotopic evidence for major mass transfer between mafic enclaves and felsic magma. *Chemical geology* **92**, 135-152.
Holland, T. & Blundy, J. (1994). Non-ideal interactions in calcic amphiboles and their bearing on amphibole-plagioclase thermometry. *Contributions to Mineralogy and Petrology* **116**, 433-447.
Holliday, J. & Cooke, D. (2007). Advances in geological models and exploration methods for copper±gold porphyry deposits. *Proceedings of exploration*, 791-809.
Hook, L. (2022). Rio Tinto prevails in $3.3bn takeover of Turquoise Hill. *Financial Times*.
Horie, K., Hidaka, H. & Gauthier-Lafaye, F. (2008). Elemental distribution in apatite, titanite and zircon during hydrothermal alteration: Durability of immobilization mineral phases for actinides. *Physics and Chemistry of the Earth, Parts A/B/C* **33**, 962-968.

Horn, I., Rudnick, R. L. & McDonough, W. F. (2000). Precise elemental and isotope ratio determination by simultaneous solution nebulization and laser ablation-ICP-MS: application to U–Pb geochronology. *Chemical geology* **164**, 281-301.
Horstwood, M. S., Košler, J., Gehrels, G., Jackson, S. E., McLean, N. M., Paton, C., Pearson, N. J., Sircombe, K., Sylvester, P. & Vermeesch, P. (2016). Community-derived standards for LA-ICP-MS U-(Th-) Pb geochronology–Uncertainty propagation, age interpretation and data reporting. *Geostandards and Geoanalytical Research* **40**, 311-332.
Hunt, J. & Kerrick, D. (1977). The stability of sphene; experimental redetermination and geologic implications. *Geochimica et Cosmochimica Acta* **41**, 279-288.
Hutton, D. H. (1988). Igneous emplacement in a shear-zone termination: The biotite granite at Strontian, Scotland. *Geological Society of America Bulletin* **100**, 1392-1399.
Ito, E., Harris, D. M. & Anderson Jr, A. T. (1983). Alteration of oceanic crust and geologic cycling of chlorine and water. *Geochimica et Cosmochimica Acta* **47**, 1613-1624.
Jackson, M., Blundy, J. & Sparks, R. (2018). Chemical differentiation, cold storage and remobilization of magma in the Earth's crust. *Nature* **564**, 405-409.
Jackson, S. E., Pearson, N. J., Griffin, W. L. & Belousova, E. A. (2004). The application of laser ablation-inductively coupled plasma-mass spectrometry to in situ U–Pb zircon geochronology. *Chemical geology* **211**, 47-69.
Jahns, R. H. & Burnham, C. W. (1969). Experimental studies of pegmatite genesis; l, A model for the derivation and crystallization of granitic pegmatites. *Economic geology* **64**, 843-864.
James, G., Witten, D., Hastie, T. & Tibshirani, R. (2013). *An introduction to statistical learning*: Springer.
Japkowicz, N. & Stephen, S. (2002). The class imbalance problem: A systematic study. *Intelligent data analysis* **6**, 429-449.
Jefferies, N. (1985). The distribution of the rare earth elements within the Carnmenellis pluton, Cornwall. *Mineralogical magazine* **49**, 495-504.
Jennings, E. S., Marschall, H., Hawkesworth, C. & Storey, C. (2011). Characterization of magma from inclusions in zircon: Apatite and biotite work well, feldspar less so. *Geology* **39**, 863-866.
Jochum, K. P., Nohl, U., Herwig, K., Lammel, E., Stoll, B. & Hofmann, A. W. (2005). GeoReM: a new geochemical database for reference materials and isotopic standards. *Geostandards and Geoanalytical Research* **29**, 333-338.
Jochum, K. P., Weis, U., Stoll, B., Kuzmin, D., Yang, Q., Raczek, I., Jacob, D. E., Stracke, A., Birbaum, K. & Frick, D. A. (2011). Determination of reference values for NIST SRM 610–617 glasses following ISO guidelines. *Geostandards and Geoanalytical Research* **35**, 397-429.
Jowett, E. C. (1991). Fitting iron and magnesium into the hydrothermal chlorite geothermometer. *Geological Association of Canada/Mineralogical Association of Canada/Society of Economic Geologists Joint Annual Meeting Program with Abstracts* **16**, A82.
Jugo, P. J. (2009). Sulfur content at sulfide saturation in oxidized magmas. *Geology* **37**, 415-418.
Kassambara, A. & Mundt, F. (2017). Package 'factoextra'. *Extract and visualize the results of multivariate data analyses* **76**.
Kennedy, A. K., Kamo, S. L., Nasdala, L. & Timms, N. E. (2010). Grenville skarn titanite: potential reference material for SIMS U–Th–Pb analysis. *The Canadian Mineralogist* **48**, 1423-1443.
Kerr, A. C. & Tarney, J. (2005). Tectonic evolution of the Caribbean and northwestern South America: The case for accretion of two Late Cretaceous oceanic plateaus. *Geology* **33**, 269-272.
Kesler, S., Sutter, J., Issigonis, M., Jones, L. & Walker, R. (1977). Evolution of porphyry copper mineralization in an oceanic island arc; Panama. *Economic geology* **72**, 1142-1153.
Kesler, S. E. & Wilkinson, B. H. (2006). The role of exhumation in the temporal distribution of ore deposits. *Economic geology* **101**, 919-922.
Khain, E., Bibikova, E., Salnikova, E., Kröner, A., Gibsher, A., Didenko, A., Degtyarev, K. & Fedotova, A. (2003). The Palaeo-Asian ocean in the Neoproterozoic and early Palaeozoic: new geochronologic data and palaeotectonic reconstructions. *Precambrian Research* **122**, 329-358.

Kirkham, R. & Dunne, K. P. (2000). *World Distribution of Porphyry, Porphyry-associated Skarn and Bulk-tonnage Epithermal Deposits and Occurrences*: Natural Resources Canada, Geological Survey of Canada.
Kirkland, C., Hollis, J., Danišík, M., Petersen, J., Evans, N. & McDonald, B. (2017). Apatite and titanite from the Karrat Group, Greenland; implications for charting the thermal evolution of crust from the U-Pb geochronology of common Pb bearing phases. *Precambrian Research* **300**, 107-120.
Kirkland, C. L., Spaggiari, C., Johnson, T., Smithies, R. H., Danišík, M., Evans, N., Wingate, M., Clark, C., Spencer, C. & Mikucki, E. (2016). Grain size matters: Implications for element and isotopic mobility in titanite. *Precambrian Research* **278**, 283-302.
Kirkwood, C., Cave, M., Beamish, D., Grebby, S. & Ferreira, A. (2016). A machine learning approach to geochemical mapping. *Journal of Geochemical Exploration* **167**, 49-61.
Kohn, M. J. (2017). Titanite petrochronology. *Reviews in Mineralogy and Geochemistry* **83**, 419-441.
Kohn, M. J. & Corrie, S. L. (2011). Preserved Zr-temperatures and U–Pb ages in high-grade metamorphic titanite: evidence for a static hot channel in the Himalayan orogen. *Earth and Planetary Science Letters* **311**, 136-143.
Kontonikas-Charos, A., Ehrig, K., Cook, N. J. & Ciobanu, C. L. (2019). Crystal chemistry of titanite from the Roxby Downs Granite, South Australia: insights into petrogenesis, subsolidus evolution and hydrothermal alteration. *Contributions to Mineralogy and Petrology* **174**, 1-20.
Kovalenko, V., Yarmoluyk, V., Sal'nikova, E., Kozlovsky, A., Kotov, A., Kovach, V., Savatenkov, V., Vladykin, N. & Ponomarchuk, V. (2006). Geology, geochronology, and geodynamics of the Khan Bogd alkali granite pluton in southern Mongolia. *Geotectonics* **40**, 450-466.
Kowallis, B. J., Christiansen, E. H., Dorais, M. J., Winkel, A., Henze, P., Franzen, L. & Mosher, H. (2022). Variation of Fe, Al, and F substitution in titanite (sphene). *Geosciences* **12**, 229.
Kranidiotis, P. & MacLean, W. (1987). Systematics of chlorite alteration at the Phelps Dodge massive sulfide deposit, Matagami, Quebec. *Economic geology* **82**, 1898-1911.
Kröner, A., Kovach, V., Belousova, E., Hegner, E., Armstrong, R., Dolgopolova, A., Seltmann, R., Alexeiev, D., Hoffmann, J. & Wong, J. (2014). Reassessment of continental growth during the accretionary history of the Central Asian Orogenic Belt. *Gondwana Research* **25**, 103-125.
Kuhn, M. (2008). Building predictive models in R using the caret package. *Journal of statistical software* **28**, 1-26.
Kynicky, J., Chakhmouradian, A. R., Xu, C., Krmicek, L. & Galiova, M. (2011). Distribution and evolution of zirconium mineralization in peralkaline granites and associated pegmatites of the Khan Bogd complex, southern Mongolia. *The Canadian Mineralogist* **49**, 947-965.
Lamb, M. A. & Badarch, G. (1997). Paleozoic sedimentary basins and volcanic-arc systems of Southern Mongolia: new stratigraphic and sedimentologic constraints. *International geology review* **39**, 542-576.
Lang, J. R. & Titley, S. R. (1998). Isotopic and geochemical characteristics of Laramide magmatic systems in Arizona and implications for the genesis of porphyry copper deposits. *Economic geology* **93**, 138-170.
Langmuir, D. (1978). Uranium solution-mineral equilibria at low temperatures with applications to sedimentary ore deposits. *Geochimica et Cosmochimica Acta* **42**, 547-569.
Langmuir, D. & Herman, J. S. (1980). The mobility of thorium in natural waters at low temperatures. *Geochimica et Cosmochimica Acta* **44**, 1753-1766.
Large, S. J., Buret, Y., Wotzlaw, J.-F., Karakas, O., Guillong, M., von Quadt, A. & Heinrich, C. A. (2021). Copper-mineralised porphyries sample the evolution of a large-volume silicic magma reservoir from rapid assembly to solidification. *Earth and Planetary Science Letters* **563**, 116877.
Large, S. J., Quadt, A. v., Wotzlaw, J.-F., Guillong, M. & Heinrich, C. A. (2018). Magma evolution leading to porphyry Au-Cu mineralization at the Ok Tedi deposit, Papua New Guinea: Trace element geochemistry and high-precision geochronology of igneous zircon. *Economic geology* **113**, 39-61.
Leake, B. E., Woolley, A. R., Arps, C. E., Birch, W. D., Gilbert, M. C., Grice, J. D., Hawthorne, F. C., Kato, A., Kisch, H. J. & Krivovichev, V. G. (1997). Nomenclature of amphiboles; report

of the Subcommittee on Amphiboles of the International Mineralogical Association Commission on new minerals and mineral names. *Mineralogical magazine* **61**, 295-310.
Li, J.-W., Deng, X.-D., Zhou, M.-F., Liu, Y.-S., Zhao, X.-F. & Guo, J.-L. (2010). Laser ablation ICP-MS titanite U–Th–Pb dating of hydrothermal ore deposits: a case study of the Tonglushan Cu–Fe–Au skarn deposit, SE Hubei Province, China. *Chemical geology* **270**, 56-67.
Li, X., Zhang, C., Behrens, H. & Holtz, F. (2018). Fluorine partitioning between titanite and silicate melt and its dependence on melt composition: experiments at 50–200 MPa and 875–925° C. *European Journal of Mineralogy* **30**, 33-44.
Liaw, A. & Wiener, M. (2002). Classification and regression by randomForest. *R news* **2**, 18-22.
Lissinna, B. (2005). A profile through the central American landbridge in western Panama: 115 Ma interplay between the Galápagos hotspot and the central American subduction zone. Christian-Albrechts Universität Kiel.
Liu, Z., Wu, F., Guo, C., Zhao, Z., Yang, J. & Sun, J. (2011). In situ U-Pb dating of xenotime by laser ablation (LA)-ICP-MS. *Chinese Science Bulletin* **56**, 2948-2956.
Loader, M. (2017). Mineral indicators of porphyry Cu fertility. Imperial College London.
Loader, M. A., Nathwani, C. L., Wilkinson, J. J. & Armstrong, R. N. (2022). Controls on the magnitude of Ce anomalies in zircon. *Geochimica et Cosmochimica Acta*.
Loader, M. A., Wilkinson, J. J. & Armstrong, R. N. (2017). The effect of titanite crystallisation on Eu and Ce anomalies in zircon and its implications for the assessment of porphyry Cu deposit fertility. *Earth and Planetary Science Letters* **472**, 107-119.
Locock, A. J. (2014). An Excel spreadsheet to classify chemical analyses of amphiboles following the IMA 2012 recommendations. *Computers & Geosciences* **62**, 1-11.
Loucks, R. (2014). Distinctive composition of copper-ore-forming arcmagmas. *Australian Journal of Earth Sciences* **61**, 5-16.
Loucks, R. R., Fiorentini, M. L. & Henríquez, G. J. (2020). New magmatic oxybarometer using trace elements in zircon. *Journal of Petrology* **61**, egaa034.
Lowell, J. D. & Guilbert, J. M. (1970). Lateral and vertical alteration-mineralization zoning in porphyry ore deposits. *Economic geology* **65**, 373-408.
Lu, Y.-J., Loucks, R. R., Fiorentini, M., McCuaig, T. C., Evans, N. J., Yang, Z.-M., Hou, Z.-Q., Kirkland, C. L., Parra-Avila, L. A. & Kobussen, A. (2016). Zircon compositions as a pathfinder for porphyry Cu±Mo±Au deposits.
Luhr, J. F. & Carmichael, I. S. (1980). The colima volcanic complex, Mexico. *Contributions to Mineralogy and Petrology* **71**, 343-372.
Lunardon, N., Menardi, G. & Torelli, N. (2014). ROSE: a package for binary imbalanced learning. *R journal* **6**.
Lynch, G. & Ortega, J. (1997). Hydrothermal alteration and tourmaline-albite equilibria at the Coxheath porphyry Cu-Mo-Au deposit, Nova Scotia. *Canadian Mineralogist* **35**, 79-94.
Ma, Y., Jiang, S.-Y., Frimmel, H. E., Duan, R.-C., Zhu, L.-Y. & Chen, R.-S. (2021). Age and fluid source of the sub-volcanic Zhaiping Ag–Pb–Zn deposit in the eastern Cathaysia Block (Fujian Province, Southeastern China). *Mineralium Deposita*, 1-16.
Mahood, G. & Hildreth, W. (1983). Large partition coefficients for trace elements in high-silica rhyolites. *Geochimica et Cosmochimica Acta* **47**, 11-30.
Markl, G. & Piazolo, S. (1999). Stability of high-Al titanite from low-pressure calcsilicates in light of fluid and host-rock composition. *American Mineralogist* **84**, 37-47.
Marsh, B. D. (1996). Solidification fronts and magmatic evolution. *Mineralogical magazine* **60**, 5-40.
Marxer, F. & Ulmer, P. (2019). Crystallisation and zircon saturation of calc-alkaline tonalite from the Adamello Batholith at upper crustal conditions: an experimental study. *Contributions to Mineralogy and Petrology* **174**, 1-29.
Mattinson, J. M. (1978). Age, origin, and thermal histories of some plutonic rocks from the Salinian block of California. *Contributions to Mineralogy and Petrology* **67**, 233-245.
McAteer, C. A., Daly, J. S., Flowerdew, M. J., Connelly, J. N., Housh, T. B. & Whitehouse, M. J. (2010). Detrital zircon, detrital titanite and igneous clast U–Pb geochronology and basement–cover relationships of the Colonsay Group, SW Scotland: Laurentian provenance and correlation with the Neoproterozoic Dalradian Supergroup. *Precambrian Research* **181**, 21-42.

McClenaghan, M. B. (2005). Indicator mineral methods in mineral exploration. *Geochemistry: Exploration, Environment, Analysis* **5**, 233-245.
McFarlane, C. R. (2016). Allanite UPb geochronology by 193 nm LA ICP-MS using NIST610 glass for external calibration. *Chemical geology* **438**, 91-102.
McLeod, G. W., Dempster, T. J. & Faithfull, J. W. (2011). Deciphering magma-mixing processes using zoned titanite from the Ross of Mull Granite, Scotland. *Journal of Petrology* **52**, 55-82.
Meyer, C. & Hemley, J. (1967). Wall rock alteration. In: Barnes, H. L. (ed.) *Geochemistry of hydrothermal ore deposits* New York: Holt, Rinehart and Winston, 166-235.
Migdisov, A., Williams-Jones, A., Brugger, J. & Caporuscio, F. A. (2016). Hydrothermal transport, deposition, and fractionation of the REE: Experimental data and thermodynamic calculations. *Chemical geology* **439**, 13-42.
Minjin, C., Sersmaa, G., Erdenechuluun, C., Otgonbayar, T., Badamkhatan, Z. & Manchuk, K. (2005). Stratigraphy of Mid-Upper Paleozoic rocks in

South Mongolia. *Mongolian Geoscientist* **27**, 15-20.
Montes, C., Bayona, G., Cardona, A., Buchs, D. M., Silva, C., Morón, S., Hoyos, N., Ramírez, D., Jaramillo, C. & Valencia, V. (2012). Arc-continent collision and orocline formation: Closing of the Central American seaway. *Journal of Geophysical Research: Solid Earth* **117**.
Montoya, J. & Hemley, J. (1975). Activity relations and stabilities in alkali feldspar and mica alteration reactions. *Economic geology* **70**, 577-583.
Morton, A. C. & Hallsworth, C. (2007). Stability of detrital heavy minerals during burial diagenesis. *Developments in sedimentology* **58**, 215-245.
Morton, A. C. & Hallsworth, C. R. (1999). Processes controlling the composition of heavy mineral assemblages in sandstones. *Sedimentary geology* **124**, 3-29.
Müntener, O., Kelemen, P. B. & Grove, T. L. (2001). The role of H2O during crystallization of primitive arc magmas under uppermost mantle conditions and genesis of igneous pyroxenites: an experimental study. *Contributions to Mineralogy and Petrology* **141**, 643-658.
Mutch, E., Blundy, J., Tattitch, B., Cooper, F. & Brooker, R. (2016). An experimental study of amphibole stability in low-pressure granitic magmas and a revised Al-in-hornblende geobarometer. *Contributions to Mineralogy and Petrology* **171**, 1-27.
Nakada, S. (1991). Magmatic processes in titanite-bearing dacites, central Andes of Chile and Bolivia. *American Mineralogist* **76**, 548-560.
Nandedkar, R. H., Hürlimann, N., Ulmer, P. & Müntener, O. (2016). Amphibole–melt trace element partitioning of fractionating calc-alkaline magmas in the lower crust: an experimental study. *Contributions to Mineralogy and Petrology* **171**, 1-25.
Nandedkar, R. H., Ulmer, P. & Müntener, O. (2014). Fractional crystallization of primitive, hydrous arc magmas: an experimental study at 0.7 GPa. *Contributions to Mineralogy and Petrology* **167**, 1-27.
Nathwani, C. L., Large, S. J., Brugge, E. R., Wilkinson, J. J., Buret, Y. & EIMF. (2023). Apatite evidence for a fluid-saturated, crystal-rich magma reservoir forming the Quellaveco porphyry copper deposit (Southern Peru). *Contributions to Mineralogy and Petrology* **178**, 49.
Nathwani, C. L., Loader, M. A., Wilkinson, J. J., Buret, Y., Sievwright, R. H. & Hollings, P. (2020). Multi-stage arc magma evolution recorded by apatite in volcanic rocks. *Geology* **48**, 323-327.
Nathwani, C. L., Simmons, A. T., Large, S. J., Wilkinson, J. J., Buret, Y. & Ihlenfeld, C. (2021). From long-lived batholith construction to giant porphyry copper deposit formation: petrological and zircon chemical evolution of the Quellaveco District, Southern Peru. *Contributions to Mineralogy and Petrology* **176**, 1-21.
Nathwani, C. L., Wilkinson, J. J., Fry, G., Armstrong, R. N., Smith, D. J. & Ihlenfeld, C. (2022). Machine learning for geochemical exploration: classifying metallogenic fertility in arc magmas and insights into porphyry copper deposit formation. *Mineralium Deposita*, 1-24.
Newman, S. & Lowenstern, J. B. (2002). VolatileCalc: a silicate melt–H2O–CO2 solution model written in Visual Basic for excel. *Computers & Geosciences* **28**, 597-604.
Nobel, M. & Benavides, S. (2013). Cobre Panama mapping 2013. *Unpublished report for First Quantum Minerals*, 25.

Norman, D., Parry, W. & Bowman, J. R. (1991). Petrology and geochemistry of propylitic alteration at Southwest Tintic, Utah. *Economic geology* **86**, 13-28.
O'Neill, H. S. C. (2016). The smoothness and shapes of chondrite-normalized rare earth element patterns in basalts. *Journal of Petrology* **57**, 1463-1508.
Oberti, R., Smith, D. C., Rossi, G. & Caucia, F. (1991). The crystal-chemistry of high-aluminium titanites. *European Journal of Mineralogy*, 777-792.
Olierook, H. K., Taylor, R. J., Erickson, T. M., Clark, C., Reddy, S. M., Kirkland, C. L., Jahn, I. & Barham, M. (2019). Unravelling complex geologic histories using U–Pb and trace element systematics of titanite. *Chemical geology* **504**, 105-122.
Olson, N. H., Dilles, J. H., Kent, A. J. & Lang, J. R. (2017). Geochemistry of the Cretaceous Kaskanak batholith and genesis of the Pebble porphyry Cu-Au-Mo deposit, southwest Alaska. *American Mineralogist: Journal of Earth and Planetary Materials* **102**, 1597-1621.
OREAS. (2022a). OREAS 20a Certified Reference Material, 2022. https://www.oreas.com/crm/oreas-20a/.
OREAS. (2022b). OREAS 102a Certified Reference Material, 2022. https://www.oreas.com/crm/oreas-102a/.
OREAS. (2022c). OREAS 681 Certified Reference Material, 2022. https://www.oreas.com/crm/oreas-681/.
OREAS. (2022d). OREAS 920 Certified Reference Material, 2022. https://www.oreas.com/crm/oreas-920/.
Ossandón, G., Fréraut, R., Gustafson, L. B., Lindsay, D. D. & Zentilli, M. (2001). Geology of the Chuquicamata mine: A progress report. *Economic geology* **96**, 249-270.
Pacey, A. (2016). The characteristics, geochemistry and origin of propylitic alteration in the Northparkes porphyry Cu-Au system. Imperial College London.
Pacey, A., Wilkinson, J. J., Boyce, A. J. & Millar, I. L. (2020a). Magmatic fluids implicated in the formation of propylitic alteration: Oxygen, hydrogen, and strontium isotope constraints from the Northparkes porphyry Cu-Au district, New South Wales, Australia. *Economic geology* **115**, 729-748.
Pacey, A., Wilkinson, J. J. & Cooke, D. R. (2020b). Chlorite and epidote mineral chemistry in porphyry ore systems: A case study of the Northparkes district, New South Wales, Australia. *Economic geology* **115**, 701-727.
Padilla, A. J. & Gualda, G. A. (2016). Crystal-melt elemental partitioning in silicic magmatic systems: An example from the Peach Spring Tuff high-silica rhyolite, Southwest USA. *Chemical geology* **440**, 326-344.
Pamukcu, A. S., Carley, T. L., Gualda, G. A., Miller, C. F. & Ferguson, C. A. (2013). The evolution of the Peach Spring giant magma body: Evidence from accessory mineral textures and compositions, bulk pumice and glass geochemistry, and rhyolite-MELTS modeling. *Journal of Petrology* **54**, 1109-1148.
Pan, Y., Fleet, M. E. & MacRae, N. D. (1993). Late alteration in titanite (CaTiSiO5): redistribution and remobilization of rare earth elements and implications for U/Pb and Th/Pb geochronology and nuclear waste disposal. *Geochimica et Cosmochimica Acta* **57**, 355-367.
Parmigiani, A., Degruyter, W., Leclaire, S., Huber, C. & Bachmann, O. (2017). The mechanics of shallow magma reservoir outgassing. *Geochemistry, Geophysics, Geosystems* **18**, 2887-2905.
Pasteris, J. D. (1996). Mount Pinatubo volcano and "negative" porphyry copper deposits. *Geology* **24**, 1075-1078.
Paterson, B., Rogers, G., Stephens, W. & Hinton, R. (1993). The longevity of acid–basic magmatism associated with a major transcurrent fault. *Geological Society of America, Abstracts with Programs*, A42.
Paterson, B., Stephens, W. & Herd, D. (1989). Zoning in granitoid accessory minerals as revealed by backscattered electron imagery. *Mineralogical magazine* **53**, 55-61.
Paterson, B. A. (1990). Accessory mineral growth histories: implications for granitoid petrogenesis. University of St Andrews.
Paterson, B. A. & Stephens, W. E. (1992). Kinetically induced compositional zoning in titanite: implications for accessory-phase/melt partitioning of trace elements. *Contributions to Mineralogy and Petrology* **109**, 373-385.

Paton, C., Hellstrom, J., Paul, B., Woodhead, J. & Hergt, J. (2011). Iolite: Freeware for the visualisation and processing of mass spectrometric data. *Journal of Analytical Atomic Spectrometry* **26**, 2508-2518.
Peacock, S. M. (1993). The importance of blueschist→ eclogite dehydration reactions in subducting oceanic crust. *Geological Society of America Bulletin* **105**, 684-694.
Peccerillo, A. & Taylor, S. (1976). Geochemistry of Eocene calc-alkaline volcanic rocks from the Kastamonu area, northern Turkey. *Contributions to Mineralogy and Petrology* **58**, 63-81.
Perello, J., Cox, D., Garamjav, D., Sanjdorj, S., Diakov, S., Schissel, D., Munkhbat, T.-O. & Oyun, G. (2001). Oyu Tolgoi, Mongolia: Siluro-Devonian porphyry Cu-Au-(Mo) and high-sulfidation Cu mineralization with a cretaceous chalcocite blanket. *Economic geology* **96**, 1407-1428.
Petersen, G. (2011). *Minería y metalurgia en el antiguo Perú*. Lima: Visadeva.
Petrone, C. M., Mollo, S., Gertisser, R., Buret, Y., Scarlato, P., Del Bello, E., Andronico, D., Ellis, B., Pontesilli, A. & De Astis, G. (2022). Magma recharge and mush rejuvenation drive paroxysmal activity at Stromboli volcano. *Nature Communications* **13**, 7717.
Piccoli, P., Candela, P. & Rivers, M. (2000). Interpreting magmatic processes from accessory phases: titanite—a small-scale recorder of large-scale processes. *Earth and Environmental Science Transactions of the Royal Society of Edinburgh* **91**, 257-267.
Piccoli, P. M. & Candela, P. A. (2002). Apatite in igneous systems. *Reviews in Mineralogy and Geochemistry* **48**, 255-292.
Pizarro, H., Campos, E., Bouzari, F., Rousse, S., Bissig, T., Gregoire, M. & Riquelme, R. (2020). Porphyry indicator zircons (PIZs): Application to exploration of porphyry copper deposits. *Ore Geology Reviews* **126**, 103771.
Porter, T. M. (2016). The geology, structure and mineralisation of the Oyu Tolgoi porphyry copper-gold-molybdenum deposits, Mongolia: A review. *Geoscience Frontiers* **7**, 375-407.
Price, J. D., Hogan, J. P., Gilbert, M. C., London, D. & Morgan, G. B. (1999). Experimental study of titanite-fluorite equilibria in the A-type Mount Scott Granite: Implications for assessing F contents of felsic magma. *Geology* **27**, 951-954.
Prowatke, S. & Klemme, S. (2005). Effect of melt composition on the partitioning of trace elements between titanite and silicate melt. *Geochimica et Cosmochimica Acta* **69**, 695-709.
Prowatke, S. & Klemme, S. (2006). Trace element partitioning between apatite and silicate melts. *Geochimica et Cosmochimica Acta* **70**, 4513-4527.
Read, H. H. (1961). Aspects of Caledonian magmatism in Britain. *Geological Journal* **2**, 653-683.
Redwood, S. D., Bryan, J. R., Buchs, D. M. & Burge, C. (2021). Late Eocene Biostratigraphic Age for Andesitic Volcanic Host Rocks Formed in an Island Environment at the Cobre Panama Porphyry Cu-Mo-Au-Ag Deposit, Panama. *Economic geology* **116**, 199-209.
Reed, M., Rusk, B. & Palandri, J. (2013). The Butte magmatic-hydrothermal system: One fluid yields all alteration and veins. *Economic geology* **108**, 1379-1396.
Rezeau, H., Moritz, R., Wotzlaw, J.-F., Hovakimyan, S. & Tayan, R. (2019). Zircon petrochronology of the Meghri-Ordubad pluton, Lesser Caucasus: Fingerprinting igneous processes and implications for the exploration of porphyry Cu-Mo deposits. *Economic geology* **114**, 1365-1388.
Richards, J. P. (2005). Cumulative factors in the generation of giant calc-alkaline porphyry Cu deposits. In: Porter, T. (ed.) *Super porphyry copper and gold deposits: A global perspective*, 7-25.
Richards, J. P. (2011). High Sr/Y arc magmas and porphyry Cu±Mo±Au deposits: just add water. *Economic geology* **106**, 1075-1081.
Richards, J. P., Boyce, A. J. & Pringle, M. S. (2001). Geologic evolution of the Escondida area, northern Chile: A model for spatial and temporal localization of porphyry Cu mineralization. *Economic geology* **96**, 271-305.
Rivera, S. L., Alcota, H., Proffett, J., Díaz, J., Leiva, G. & Vergara, M. (2012). Update of the geologic setting and porphyry Cu-Mo deposits of the Chuquicamata district, northern Chile. In: Hedenquist, J. W., Harris, M. & Camus, F. (eds.) *Geology and genesis of major copper deposits and districts of the world: a tribute to Richard H. Sillitoe.*: Society of Economic Geologists.

Rodriguez-Galiano, V., Sanchez-Castillo, M., Chica-Olmo, M. & Chica-Rivas, M. (2015). Machine learning predictive models for mineral prospectivity: An evaluation of neural networks, random forest, regression trees and support vector machines. *Ore Geology Reviews* **71**, 804-818.

Rogers, G. & Dunning, G. R. (1991). Geochronology of appinitic and related granitic magmatism in the W Highlands of Scotland: constraints on the timing of transcurrent fault movement. *Journal of the Geological Society* **148**, 17-27.

Rohrlach, B. D. & Loucks, R. R. (2005). Multi-million-year cyclic ramp-up of volatiles in a lower crustal magma reservoir trapped below the Tampakan copper-gold deposit by Mio-Pliocene crustal compression in the southern Philippines. In: Porter, T. (ed.) *Super porphyry copper and gold deposits: A global perspective*, 369-407.

Sabine, P. (1963). The Strontian granite complex, Argyllshire. *Bulletin of the Geological Survey of Great Britain* **20**, 6-42.

Šala, M., Šelih, V. S., Stremtan, C. C., Tămaş, T. & van Elteren, J. T. (2021). Implications of laser shot dosage on image quality in LA-ICP-QMS imaging. *Journal of Analytical Atomic Spectrometry* **36**, 75-79.

Sarp, H., Bertrand, J. & McNear, E. (1976). Vuagnatite, CaAl (OH) SiO1, a new natural calcium aluminum nesosilicate. *American Mineralogist* **61**, 825-330.

Sawka, W. N. (1988). REE and trace element variations in accessory minerals and hornblende from the strongly zoned McMurry Meadows Pluton, California. *Earth and Environmental Science Transactions of the Royal Society of Edinburgh* **79**, 157-168.

Scaillet, B. & Evans, B. W. (1999). The 15 June 1991 eruption of Mount Pinatubo. I. Phase equilibria and pre-eruption P–T–f O2–f H2O conditions of the dacite magma. *Journal of Petrology* **40**, 381-411.

Schiller, D. & Finger, F. (2019). Application of Ti-in-zircon thermometry to granite studies: problems and possible solutions. *Contributions to Mineralogy and Petrology* **174**, 1-16.

Schmitz, M. D. & Bowring, S. A. (2001). U-Pb zircon and titanite systematics of the Fish Canyon Tuff: An assessment of high-precision U-Pb geochronology and its application to young volcanic rocks. *Geochimica et Cosmochimica Acta* **65**, 2571-2587.

Schodde, R. (2017). Recent trends and outlook for global exploration. *PDAC International Convention, Trade Show & Investors Exchange*.

Schoene, B. (2014). 4.10-U–Th–Pb Geochronology. *Treatise on geochemistry* **4**, 341-378.

Scibiorski, E. A. & Cawood, P. A. (2022). Titanite as a petrogenetic indicator. *Terra Nova* **34**, 177-183.

Seedorff, E., Dilles, J. H., Proffett, J. M., Einaudi, M. T., Zurcher, L., Stavast, W. J., Johnson, D. A. & Barton, M. D. (2005). Porphyry deposits: Characteristics and origin of hypogene features.

Seo, J. H., Guillong, M. & Heinrich, C. A. (2009). The role of sulfur in the formation of magmatic–hydrothermal copper–gold deposits. *Earth and Planetary Science Letters* **282**, 323-328.

Sepp, M. D. & Dilles, J. H. (2018). Structural evolution, vein orientation, and paragenesis of the Botija porphyry Cu-Mo-(Au) deposit, Panama. *Economic geology* **113**, 857-890.

Shannon, R. D. (1976). Revised effective ionic radii and systematic studies of interatomic distances in halides and chalcogenides. *Acta crystallographica section A: crystal physics, diffraction, theoretical and general crystallography* **32**, 751-767.

Sillitoe, R. H. (1972). A plate tectonic model for the origin of porphyry copper deposits. *Economic geology* **67**, 184-197.

Sillitoe, R. H. (2010). Porphyry copper systems. *Economic geology* **105**, 3-41.

Sillitoe, R. H. (2018). Why no porphyry copper deposits in Japan and South Korea? *Resource geology* **68**, 107-125.

Simon, A. C., Pettke, T., Candela, P. A., Piccoli, P. M. & Heinrich, C. A. (2006). Copper partitioning in a melt–vapor–brine–magnetite–pyrrhotite assemblage. *Geochimica et Cosmochimica Acta* **70**, 5583-5600.

Singer, D. A., Berger, V. I. & Moring, B. C. (2008). Porphyry copper deposits of the world: Database and grade and tonnage models: USGS Open-File Report 2008-1155. *USGS: Reston, VA, USA*.

Sliwinski, J., Farsky, D., Lipman, P. W., Guillong, M. & Bachmann, O. (2019). Rapid magma generation or shared magmatic reservoir? Petrology and geochronology of the Rat Creek and Nelson Mountain Tuffs, CO, USA. *Frontiers in Earth Science* **7**, 271.

Smythe, D. J. & Brenan, J. M. (2015). Cerium oxidation state in silicate melts: Combined fO2, temperature and compositional effects. *Geochimica et Cosmochimica Acta* **170**, 173-187.

Spear, F. S. & Parrish, R. R. (1996). Petrology and cooling rates of the Valhalla complex, British Columbia, Canada. *Journal of Petrology* **37**, 733-765.

Speer, J. A. & Gibbs, G. (1976). The crystal structure of synthetic titanite, CaTiOSiO4, and the domain textures of natural titanites. *American Mineralogist* **61**, 238-247.

Speidel, F., Faure, S., Smith, M. T. & McArthur, G. F. (2001). Exploration and discovery at the Petaquilla copper-gold concession, Panama. In: Albinson, T. & Nelson, C. E. (eds.) *Special Publications Series 28*: Society of Economic Geologists, 349-362.

Spencer, K., Hacker, B., Kylander-Clark, A., Andersen, T., Cottle, J., Stearns, M., Poletti, J. & Seward, G. (2013). Campaign-style titanite U–Pb dating by laser-ablation ICP: Implications for crustal flow, phase transformations and titanite closure. *Chemical geology* **341**, 84-101.

Stacey, J. t. & Kramers, J. (1975). Approximation of terrestrial lead isotope evolution by a two-stage model. *Earth and Planetary Science Letters* **26**, 207-221.

Stepanov, A., Mavrogenes, J. A., Meffre, S. & Davidson, P. (2014). The key role of mica during igneous concentration of tantalum. *Contributions to Mineralogy and Petrology* **167**, 1-8.

Stephens, W. (2001). Polycrystalline amphibole aggregates (clots) in granites as potential I-type restite: An ion microprobe study of rare-earth distributions. *Australian Journal of Earth Sciences* **48**, 591-601.

Stephens, W. & Halliday, A. (1984). Geochemical contrasts between late Caledonian granitoid plutons of northern, central and southern Scotland. *Earth and Environmental Science Transactions of the Royal Society of Edinburgh* **75**, 259-273.

Storey, C. D., Jeffries, T. E. & Smith, M. (2006). Common lead-corrected laser ablation ICP–MS U–Pb systematics and geochronology of titanite. *Chemical geology* **227**, 37-52.

Streckeisen, A. (1976). To each plutonic rock its proper name. *Earth-Science Reviews* **12**, 1-33.

Szymanowski, D., Wotzlaw, J.-F., Ellis, B. S., Bachmann, O., Guillong, M. & von Quadt, A. (2017). Protracted near-solidus storage and pre-eruptive rejuvenation of large magma reservoirs. *Nature Geoscience* **10**, 777-782.

Tang, M., Lee, C.-T. A., Chen, K., Erdman, M., Costin, G. & Jiang, H. (2019). Nb/Ta systematics in arc magma differentiation and the role of arclogites in continent formation. *Nature Communications* **10**, 1-8.

Tera, F. & Wasserburg, G. (1972). U-Th-Pb systematics in three Apollo 14 basalts and the problem of initial Pb in lunar rocks. *Earth and Planetary Science Letters* **14**, 281-304.

Thiéblemont, D., Triboulet, C. & Godard, G. (1988). Mineralogy, petrology and P–T–t path of Ca–Na amphibole assemblages, Saint-Martin des Noyers formation, Vendée, France. *Journal of Metamorphic Geology* **6**, 697-715.

Tosdal, R. & Richards, J. (2001). Magmatic and structural controls on the development of porphyry Cu±Mo±Au deposits.

Ulrich, T., Günther, D. & Heinrich, C. A. (1999). Gold concentrations of magmatic brines and the metal budget of porphyry copper deposits. *Nature* **399**, 676-679.

Ulrich, T. & Heinrich, C. A. (2002). Geology and alteration geochemistry of the porphyry Cu-Au deposit at Bajo de la Alumbrera, Argentina. *Economic geology* **97**, 1865-1888.

Ulrich, T. & Mavrogenes, J. (2008). An experimental study of the solubility of molybdenum in H2O and KCl–H2O solutions from 500 C to 800 C, and 150 to 300 MPa. *Geochimica et Cosmochimica Acta* **72**, 2316-2330.

Vaglio, D. (2007). Mineralogy, Geochemistry and Geochronology of Pegmatites and Associated Alkaline Granite Rocks of the Khan Bogd Complex, South Mongolia. *Section of Earth Sciences*: Université de Genève.

van Dongen, M., Weinberg, R. F. & Tomkins, A. G. (2010). REE-Y, Ti, and P remobilization in magmatic rocks by hydrothermal alteration during Cu-Au deposit formation. *Economic geology* **105**, 763-776.

van Elteren, J. T., Metarapi, D., Šala, M., Šelih, V. S. & Stremtan, C. C. (2020). Fine-tuning of LA-ICP-QMS conditions for elemental mapping. *Journal of Analytical Atomic Spectrometry* **35**, 2494-2497.
Van Malderen, S. J., van Elteren, J. T., Šelih, V. S. & Vanhaecke, F. (2018). Considerations on data acquisition in laser ablation-inductively coupled plasma-mass spectrometry with low-dispersion interfaces. *Spectrochimica Acta Part B: Atomic Spectroscopy* **140**, 29-34.
Vermeesch, P. (2018). IsoplotR: A free and open toolbox for geochronology. *Geoscience Frontiers* **9**, 1479-1493.
Wainwright, A. J., Tosdal, R. M., Forster, C. N., Kirwin, D. J., Lewis, P. D. & Wooden, J. L. (2011a). Devonian and carboniferous arcs of the Oyu Tolgoi porphyry Cu-Au district, South Gobi region, Mongolia. *Bulletin* **123**, 306-328.
Wainwright, A. J., Tosdal, R. M., Wooden, J. L., Mazdab, F. K. & Friedman, R. M. (2011b). U–Pb (zircon) and geochemical constraints on the age, origin, and evolution of Paleozoic arc magmas in the Oyu Tolgoi porphyry Cu–Au district, southern Mongolia. *Gondwana Research* **19**, 764-787.
Walshe, J. L. (1986). A six-component chlorite solid solution model and the conditions of chlorite formation in hydrothermal and geothermal systems. *Economic geology* **81**, 681-703.
Watanabe, Y. & Stein, H. J. (2000). Re-Os ages for the Erdenet and Tsagaan Suvarga porphyry Cu-Mo deposits, Mongolia, and tectonic implications. *Economic geology* **95**, 1537-1542.
Watson, E. B. & Harrison, T. M. (1983). Zircon saturation revisited: temperature and composition effects in a variety of crustal magma types. *Earth and Planetary Science Letters* **64**, 295-304.
Webster, J. D., Tappen, C. M. & Mandeville, C. W. (2009). Partitioning behavior of chlorine and fluorine in the system apatite–melt–fluid. II: Felsic silicate systems at 200 MPa. *Geochimica et Cosmochimica Acta* **73**, 559-581.
Wegner, W., Wörner, G., Harmon, R. S. & Jicha, B. R. (2011). Magmatic history and evolution of the Central American Land Bridge in Panama since Cretaceous times. *Bulletin* **123**, 703-724.
Wendt, I. & Carl, C. (1991). The statistical distribution of the mean squared weighted deviation. *Chemical Geology: Isotope Geoscience Section* **86**, 275-285.
Werts, K. (2019). Discerning magmatic processes and melt interconnectivity in the Tuolumne Intrusive Complex from hornblende and titanite compositional zoning patterns. Texas Tech University, 323.
Wilke, M. & Behrens, H. (1999). The dependence of the partitioning of iron and europium between plagioclase and hydrous tonalitic melt on oxygen fugacity. *Contributions to Mineralogy and Petrology* **137**, 102-114.
Wilkinson, J. J. (2013). Triggers for the formation of porphyry ore deposits in magmatic arcs. *Nature Geoscience* **6**, 917-925.
Wilkinson, J. J., Baker, M. J., Cooke, D. R. & Wilkinson, C. C. (2020). Exploration targeting in porphyry Cu systems using propylitic mineral chemistry: A case study of the El Teniente deposit, Chile. *Economic geology* **115**, 771-791.
Wilkinson, J. J., Chang, Z., Cooke, D. R., Baker, M. J., Wilkinson, C. C., Inglis, S., Chen, H. & Gemmell, J. B. (2015). The chlorite proximitor: A new tool for detecting porphyry ore deposits. *Journal of Geochemical Exploration* **152**, 10-26.
Williams-Jones, A. E., Migdisov, A. A. & Samson, I. M. (2012). Hydrothermal mobilisation of the rare earth elements–a tale of "ceria" and "yttria". *Elements* **8**, 355-360.
Williams-Jones, A. E. & Vasyukova, O. (2018). The economic geology of scandium, the runt of the rare earth element litter. *Economic geology* **113**, 973-988.
Windley, B. F., Alexeiev, D., Xiao, W., Kröner, A. & Badarch, G. (2007). Tectonic models for accretion of the Central Asian Orogenic Belt. *Journal of the Geological Society* **164**, 31-47.
Wones, D. R. (1989). Significance of the assemblage titanite+ magnetite+ quartz in granitic rocks. *American Mineralogist* **74**, 744-749.
Wotzlaw, J.-F., Schaltegger, U., Frick, D. A., Dungan, M. A., Gerdes, A. & Günther, D. (2013). Tracking the evolution of large-volume silicic magma reservoirs from assembly to supereruption. *Geology* **41**, 867-870.
Wright, A. & Bowes, D. (1979). Geochemistry of the appinite suite. *Geological Society, London, Special Publications* **8**, 699-704.

Xiao, B., Chen, H., Hollings, P., Wang, Y., Yang, J. & Wang, F. (2018). Element transport and enrichment during propylitic alteration in Paleozoic porphyry Cu mineralization systems: Insights from chlorite chemistry. *Ore Geology Reviews* **102**, 437-448.

Xiao, W., Windley, B. F., Hao, J. & Zhai, M. (2003). Accretion leading to collision and the Permian Solonker suture, Inner Mongolia, China: Termination of the central Asian orogenic belt. *Tectonics* **22**.

Xiao, X., Zhou, T., White, N. C., Zhang, L., Fan, Y. & Chen, X. (2021). Multiple generations of titanites and their geochemical characteristics record the magmatic-hydrothermal processes and timing of the Dongguashan porphyry-skarn Cu-Au system, Tongling district, Eastern China. *Mineralium Deposita* **56**, 363-380.

Xiao, Y., Chen, S., Niu, Y., Wang, X., Xue, Q., Wang, G., Gao, Y., Gong, H., Kong, J. & Shao, F. (2020). Mineral compositions of syn-collisional granitoids and their implications for the formation of juvenile continental crust and adakitic magmatism. *Journal of Petrology* **61**, egaa038.

Xie, L., Wang, R.-C., Chen, J. & Zhu, J.-C. (2010). Mineralogical evidence for magmatic and hydrothermal processes in the Qitianling oxidized tin-bearing granite (Hunan, South China): EMP and (MC)-LA-ICPMS investigations of three types of titanite. *Chemical geology* **276**, 53-68.

Yuan, H.-L., Gao, S., Dai, M.-N., Zong, C.-L., Günther, D., Fontaine, G. H., Liu, X.-M. & Diwu, C. (2008). Simultaneous determinations of U–Pb age, Hf isotopes and trace element compositions of zircon by excimer laser-ablation quadrupole and multiple-collector ICP-MS. *Chemical geology* **247**, 100-118.

Yuan, H., Gao, S., Liu, X., Li, H., Günther, D. & Wu, F. (2004). Accurate U-Pb age and trace element determinations of zircon by laser ablation-inductively coupled plasma-mass spectrometry. *Geostandards and Geoanalytical Research* **28**, 353-370.

Zachariasen, W. (1930). II. the crystal structure of titanite. *Zeitschrift für Kristallographie-Crystalline Materials* **73**, 7-16.

Zeiger, K., Gordon, S., Long, S., Kylander-Clark, A., Agustsson, K. & Penfold, M. (2015). Timing and conditions of metamorphism and melt crystallization in Greater Himalayan rocks, eastern and central Bhutan: insight from U–Pb zircon and monazite geochronology and trace-element analyses. *Contributions to Mineralogy and Petrology* **169**, 1-19.

Zentilli, M., Graves, M. C., Mathur, R., Hanley, J. J., Heaman, L. M. & Boric, R. (2021). Locating the "Missing Half" of the Giant Chuquicamata Porphyry Copper Deposit, Chile. In: Sholeh, A. & Wang, R. (eds.) *Special Publications Series 24*: Society of Economic Geologists, 69-85.

Zentilli, M., Maksaev, V., Boric, R. & Wilson, J. (2018). Spatial coincidence and similar geochemistry of Late Triassic and Eocene–Oligocene magmatism in the Andes of northern Chile: evidence from the MMH porphyry type Cu–Mo deposit, Chuquicamata District. *International Journal of Earth Sciences* **107**, 1097-1126.

Zhang, F., Li, W., Fu, T. & Qiao, X. (2022). Late Permian orogenic gold mineralization at Haoyaoerhudong, northern China: Constraints from hydrothermal titanite and apatite chemistry. *Ore Geology Reviews* **144**, 104858.